

# ZnO: Ultrafast photodoping

## Ultrashort and metastable photoinduced metallization of the ZnO(10-10) surface

vorgelegt von

M. Sc.

Lukas Immanuel Gierster

ORCID: 0000-0002-6329-6027

von der Fakultät II - Mathematik und Naturwissenschaften  
der Technischen Universität Berlin  
zur Erlangung des akademischen Grades  
Doktor der Naturwissenschaften

Dr. rer. nat.

vorgelegte Dissertation

### Promotionsausschuss:

Vorsitzender: Prof. Dr. Andreas Knorr

Erstgutachterin: Prof. Dr. Julia Stähler

Zweitgutachterin: Prof. Dr. Ulrike Woggon

Drittgutachter: Prof. Dr. Uwe Bovensiepen

Berlin 2021



This work was performed between April 2015 and January 2021 in the group of Prof. Dr. Julia Stähler in the Department of Physical Chemistry (Director: Prof. Dr. Martin Wolf) at the Fritz Haber Institute of the Max Planck Society.

Berlin, Januar 2021



# Abstract

In recent years, band bending at oxide semiconductor surfaces induced by chemical doping or electric fields has gained considerable attention, because it leads to metallic surfaces with interesting properties not found in the bulk semiconductor. These properties include high electron mobility, magnetism and superconductivity. Optical generation of such surface metals on ultrafast timescales would pave the way for novel high-speed electronics. In this thesis, I investigate the photoresponse of the (10-10) surface of zinc oxide (ZnO) to femtosecond laser pulses using time- and angle-resolved photoelectron spectroscopy. The semiconductor ZnO is widely used in optoelectronics due to its transparency for visible light and its ease of nanostructuring. I show that photoexcitation acts like chemical doping of the ZnO surface and induces band bending on ultrafast time scales. The 'ultrafast photodoping' effect is reached by positive surface charging due to the photoexcitation of deep donor-type defects at the surface. For low photoexcitation densities, surface-confined excitons are formed. At a critical density, an exciton Mott transition occurs, and within only 20 femtoseconds the surface becomes metallic. The surface metal decays on a timescale of few hundred picoseconds, due to reduction of the defect exciton density upon electron-hole recombination.

After the initial decay, a fraction of the photoexcited defect excitons remains and exhibits a lifetime exceeding the inverse laser repetition rate (5 microseconds). In the course of investigating this long-lived defect exciton population, I develop a new mathematical model, which allows for lifetime determination by tuning of the laser repetition rate and facilitates to analyze pump-probe scans in the presence of photostationary states. The long-lived defect exciton lead to metastable doping of the ZnO surface. Complementary to the ultrafast metallization due to short-lived defect excitons described above, a photostationary semiconductor-to-metal transition can be reached upon increasing the density of deep defects at the sample surface by sustained UV illumination. These observations are consistent with the persistent photoconductivity of ZnO reported in literature and provide a microscopic explanation for this phenomenon.

In summary, a novel ultrafast photodoping mechanism is reported that leads to surface metallization of ZnO. Compared to hitherto known photoinduced phase transitions, the ultrafast generation and decay of the surface metal occurs with three- to four orders of magnitude lower laser fluences. Beyond implementations of ZnO as a transparent photoconductive switch, this work is the starting point for studies on optically generated surface metals with emerging properties beyond metallicity in the ultrafast time domain.



# Deutsche Kurzzusammenfassung

Die Bandverbiegung an Oxid-Halbleiteroberflächen, induziert durch chemische Dotierung oder elektrische Felder, hat in den letzten Jahren erhebliche Aufmerksamkeit erlangt. Dies liegt daran, dass sie zu metallischen Oberflächen mit interessanten Eigenschaften führt, die keine Entsprechung im Volumen finden, insbesondere hohe Elektronenbeweglichkeit, Magnetismus und Supraleitung. Die optische Erzeugung solcher Oberflächenmetalle auf ultraschnellen Zeitskalen wäre ein Meilenstein für neuartige Anwendungen im Bereich schneller Elektronik. In dieser Arbeit untersuche ich die Photoreaktion der (10-10)-Oberfläche von Zinkoxid (ZnO) auf Femtosekunden-Laserpulse mittels zeit- und winkel-aufgelöster Photoelektronenspektroskopie. Der Halbleiter ZnO wird aufgrund seiner Transparenz für sichtbares Licht und vielfältigen Möglichkeiten zur Nanostrukturierung häufig in der Optoelektronik eingesetzt. Ich zeige, dass die Photoanregung wie eine chemische Dotierung der ZnO-Oberfläche wirkt und eine Bandverbiegung auf ultraschnellen Zeitskalen induziert. Der 'ultraschnelle Photodotierungs'-Effekt wird durch positive Oberflächenladung aufgrund der Photoanregung von Defekten an der Oberfläche erreicht. Bei einer geringen Anregungsdichte werden Exzitonen an der Oberfläche gebildet. Bei einer kritischen Dichte tritt ein Exzitonen-Mott-Übergang ein, und innerhalb von nur 20 Femtosekunden wird die Oberfläche metallisch. Das Oberflächenmetall zerfällt innerhalb von wenigen hundert Pikosekunden durch die Reduktion der Defekt-Exzitonendichte über Elektron-Loch-Rekombination.

Nach dem anfänglichen Zerfall bleibt ein Teil der photoangeregten Defekt-Exzitonen bestehen und weist eine Lebensdauer auf, die die inverse Laserrepetitionsrate (5 Mikrosekunden) überschreitet. Im Zuge der Untersuchung dieser langlebigen Population entwickle ich ein neues mathematisches Modell, das die Bestimmung der Lebensdauer durch Durchstimmen der Laserrepetitionsrate ermöglicht und es erlaubt, Pump-Probe-Daten in Anwesenheit photostationärer Zustände zu analysieren. Die langlebigen Defekt-Exzitonen führen zu einer metastabilen Dotierung der ZnO Oberfläche. Komplementär zu der oben beschriebenen ultraschnellen Metallisierung durch kurzlebige Defekt-Exzitonen kann ein photostationärer Halbleiter-zu-Metall-Übergang erreicht werden, indem die Dichte der Defekte an der Probenoberfläche mit lange andauernder UV-Beleuchtung erhöht wird. Diese Beobachtungen sind konsistent mit der in der Literatur beschriebenen persistenten Photoleitfähigkeit von ZnO und geben eine mikroskopische Erklärung für dieses Phänomen.

Zusammenfassend wird ein neuartiger ultraschneller Photodotierungsmechanismus beschrieben, der zur Metallisierung der ZnO Oberfläche führt. Im Vergleich zu bisher bekannten photoinduzierten Phasenübergängen erfolgt die ultraschnelle Erzeugung und der Zerfall des Oberflächenmetalls mit drei bis vier Größenordnungen niedrigeren Laserfluenzen. Über Implementierungen von ZnO als transparenter photoleitender Schalter hinaus ist diese Arbeit der Ausgangspunkt für die Erforschung optisch erzeugter Oberflächenmetalle mit Eigenschaften jenseits der Metallizität auf ultraschnellen Zeitskalen.



# Contents

<b>1</b>	<b>Introduction</b>	<b>1</b>
<b>2</b>	<b>Theoretical background</b>	<b>9</b>
2.1	General properties of ZnO . . . . .	9
2.2	Metallization of semiconductors upon doping . . . . .	10
2.2.1	Doping of semiconductors . . . . .	10
2.2.2	The doping-induced Mott semiconductor-to-metal transition . . . . .	13
2.2.3	Semiconductor-to-metal transition in 2D, the example of ZnO/H . . . . .	17
2.2.4	Summary . . . . .	20
2.3	Metallization of semiconductors upon photoexcitation . . . . .	21
2.3.1	Excitons . . . . .	21
2.3.2	Exciton formation - the case of ZnO . . . . .	22
2.3.3	Persistent photoconductivity and photoinduced metallization . . . . .	24
2.3.4	Ultrafast exciton Mott transition . . . . .	30
2.3.5	Photoinduced changes of the electronic band structure . . . . .	32
2.3.6	Summary . . . . .	36
<b>3</b>	<b>Experimental techniques and setup</b>	<b>38</b>
3.1	Photoelectron spectroscopy . . . . .	38
3.1.1	Concept . . . . .	38
3.1.2	Measurement of the workfunction . . . . .	41
3.1.3	Fields between sample and analyzer - part 1 . . . . .	43
3.1.4	Time- and angle-resolved photoelectron spectroscopy . . . . .	45
3.1.5	Fields between sample and analyzer - part 2 . . . . .	47
3.2	Experimental Setup . . . . .	52
3.2.1	The femtosecond laser system . . . . .	53
3.2.2	Characterization of the laser pulses . . . . .	55
3.2.3	The ultrahigh vacuum chamber . . . . .	58
3.2.4	Setup for trARPES measurements . . . . .	60
3.2.5	Data acquisition and analysis . . . . .	60
3.2.6	Sample preparation . . . . .	62
<b>4</b>	<b>Mathematical framework to deal with photostationary states in pump-probe spectroscopy</b>	<b>65</b>
4.1	Lifetime determination . . . . .	66
4.1.1	Very long lifetimes . . . . .	66
4.1.2	Less long lifetimes . . . . .	67

4.2	Pump-probe spectroscopy with photostationary states . . . . .	75
4.2.1	Motivation . . . . .	76
4.2.2	Model for pump-probe spectroscopy . . . . .	81
4.2.3	Exemplary dataset . . . . .	88
4.3	Summary . . . . .	97
<b>5</b>	<b>Metastable photodoping of the ZnO surface</b>	<b>98</b>
5.1	Electronic structure of the ZnO surface in the photostationary state . . . . .	100
5.2	Uncovering the photostationary state and its analogy to surface doping with hydrogen . . . . .	101
5.3	Lifetime of the photostationary state . . . . .	103
5.4	Lateral localization of the photostationary state . . . . .	106
5.5	Lab time change of the photostationary state . . . . .	107
5.6	Photon energy dependent excitation of the photostationary state . . . . .	111
5.7	Angular distribution of the photostationary state after long UV exposure - the onset of delocalization . . . . .	114
5.8	Angular distribution of the photostationary state at high photoexcitation fluences and short UV exposure times . . . . .	116
5.9	Uncovering the true photoinduced work function change . . . . .	120
5.10	Summary and conclusions . . . . .	126
<b>6</b>	<b>Ultrafast generation and decay of a surface metal</b>	<b>128</b>
6.1	Unveiling the ultrafast semiconductor-to-metal transition . . . . .	130
6.1.1	A photoinduced free electron-like band . . . . .	130
6.1.2	Thermalization and cooling of the electron system . . . . .	133
6.1.3	Determination of the threshold fluence . . . . .	137
6.1.4	Rise and decay of the metal phase . . . . .	139
6.1.5	Determination of the time constants . . . . .	142
6.1.6	Temperature dependence . . . . .	144
6.1.7	A transient 2DEG? Comparison of resonant photoexcitation to surface doping with hydrogen . . . . .	145
6.1.8	Summary . . . . .	149
6.2	The mechanism . . . . .	149
6.2.1	Concept of the photodoping mechanism . . . . .	150
6.2.2	Critical behaviour of the effective mass . . . . .	151
6.2.3	Valence band dynamics . . . . .	155
6.2.4	Pump-induced shifts probed at negative delays . . . . .	163
6.2.5	Measuring work function shifts in the ultrafast time domain . . . . .	171
6.2.6	Versus lab time change of the ultrafast photoresponse . . . . .	182

6.2.7 Influence of the annealing temperature on the photoresponse . . . .	184
6.2.8 Summary and discussion . . . . .	187
6.3 Final summary . . . . .	193
<b>7 Summary and conclusions</b>	<b>194</b>
<b>Appendix</b>	<b>201</b>
<b>References</b>	<b>203</b>
<b>Acronyms</b>	<b>218</b>
<b>Thank you</b>	<b>222</b>



---

# 1 Introduction

Chemical doping is a fundamental tool to tailor the conduction properties of semiconductors for device applications. Upon variation of the material composition, previously insulating materials show thermally activated conductivity or even metallic behaviour [Mot74]. In recent years, chemical doping at oxide semiconductor surfaces has gained considerable attention. This is because surface doping can lead to metallic two-dimensional electron gases (2DEGs) with interesting features not found in the bulk semiconductor such as high electron mobility, magnetism or superconductivity [Hwa12]. In general, chemical doping is a process that happens in thermodynamic equilibrium, e.g. during material synthesis. An appealing concept is to replace chemical doping with *photodoping*, a term that expresses that photoexcitation acts alike to chemical doping. As electronic transitions driven by photoexcitation have a certain lifetime, the conductive properties of a semiconductor can be modulated *transiently* and, by means of ultrashort laser pulses, on very short time scales [Yu91, Iwa03, Weg14b]. Up to date, optical generation of 2DEGs was only observed at very long timescales by modification of the chemical composition due to photoexcitation [Mee10, McK14, Röd15]. While it would be groundbreaking to reversibly control the surface doping of oxides on ultrafast time scales for transient 2DEG generation.

Chemical dopants that lead to surface metallization of oxides are often adsorbates, such as hydrogen in case of zinc oxide (ZnO) [Oza10, Dei15] or surface oxygen vacancies, i.e. missing oxygen atoms of the crystal lattice in the topmost layer of the material [Mee10, McK14, Fra17]. The dopant leads to an occupied state within the fundamental band gap, which spontaneously releases an electron into the conduction band (CB). Such a 'shallow donor' dopant has two effects for the material: Firstly, the electron in the CB contributes to electrical conductivity. Secondly, as the electron is donated to the CB, the oxygen vacancies at the surface become positively charged. This leads to downward surface band bending of the valence band (VB) and CB, respectively. Hence, the electrons in the CB are confined to a surface region with a depth of few nanometers only [Dei15]. The confinement leads to the formation of quantized subbands and the above mentioned special properties of 2DEGs [Hwa12].

Interestingly enough, semiconductors doped with shallow donors have a close analogy with photoexcited semiconductors. At low doping densities, the effect of shallow donors on the electronic structure of a semiconductor is understood by the hydrogen model [Cox87]: When a point defect donates an electron to the CB, it orbits around the defect because it is attracted by the Coulomb interaction to the hole. Freeing the electron requires a certain activation energy and only then it contributes to electrical conduction. As a result

the semiconductor shows thermally activated conduction. However, upon increasing the doping density above a critical value, the so-called Mott transition occurs and individual donor electrons form a metallic band [Mot74]. The semiconductor then undergoes a semiconductor-to-metal transition (SMT).

Comparing the concepts of chemical doping with shallow donors to those used in the context of photoexcited semiconductors, one can state that the hydrogen-like shallow donor state matches the definition of an exciton [Zha18]. Excitons are electron-hole pairs bound by the Coulomb interaction, the fundamental quasiparticle in mildly photoexcited semiconductors. Free excitons are formed upon optical transitions from the valence band (VB) to the CB. In addition to free excitons, defect excitons are formed by optical transitions from doping-induced states deep in the band gap, so-called 'deep impurities' or 'deep defects', to the CB. These two cases, free excitons and defect excitons, are illustrated in Figure 1.1 a) and b), respectively. For free excitons the electron-hole pair can move freely throughout the semiconductor. This is different for the defect exciton. Here the hole is fixed in space, exactly as for the hydrogen-like shallow donor state [Zha18]. Thus, the definition of defect excitons and shallow donors overlaps, which suggests that photoexcitation acts in this case alike to chemical doping.

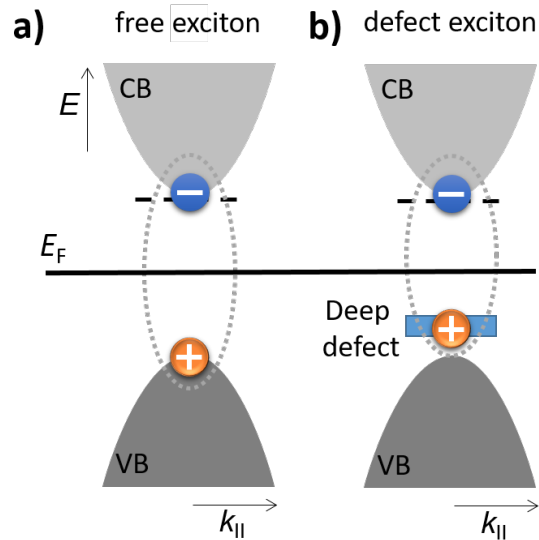


**Figure 1.1:** a) and b) Electronic band structure of a mildly photoexcited semiconductor, where free and defect excitons are formed, respectively.  $E_F$  is the equilibrium Fermi energy.

In a seminal paper regarding this topic, it has been experimentally demonstrated that photodoping due to the photoexcitation of deep defects and chemical doping with shallow donors are in fact identical - at least if the defect excitons have exceedingly long lifetimes. Photodoping was used to fine-tune the number of states that act like shallow donors on timescales of persistent photoconductivity (PPC), i.e. photoinduced conductivity that last

---

up to minutes, hours or even days. With this, a photoinduced Mott SMT was reached in the bulk of a GaAs compound [Kat87]. In ZnO, PPC is also a well-known phenomenon. Theory predicts that this effect stems from the photoexcitation of oxygen vacancies, which form deep defects in ZnO [Lan05]. The photoexcited defect excitons are presumably an important part of the notorious unintentional n-type doping of ZnO [Lan07]. However, so far no clear experimental evidence for this theory exists and it is unknown if long-lived defect excitons are truly the origin of this effect.

Given that photodoping is effective on timescales of PPC, what about ultrashort time scales? It is well known that photoexcited electron-hole pairs can undergo an ultrafast Mott transition within hundreds of femtoseconds [Hub01, Sek17, Den20]. This leads to a metal-like optical response of semiconductors. However, the general properties of this metallic phase are far from understood [Sek17, Gue19]. One important consequence of driving such a transition at ultrafast timescales is that it happens far out of thermodynamic equilibrium. Therefore, upon optical population of the CB a quasi-Fermi level is formed in the band, which is not equal to the equilibrium Fermi level  $E_F$  [Kli12]. This goes hand in hand with the formation of a quasi-Fermi level in the VB, but only upon optical excitation across the fundamental band gap and not when optical excitation addresses deep defects. Without a modification of the electronic band structure beyond simple band filling, a *metal-like* semiconductor is formed instead of a *transient metal* with properties of an equilibrium metal. This difference and its relevance for optically controlled switches is illustrated in the following with a prototypical photoconductive switch, cf. Figure 1.2:

**Metal-like semiconductor:** In equilibrium, the CB of a semiconductor is above  $E_F$  and unoccupied. Upon photoexcitation, either from the VB or a deep defect, the CB becomes populated with electrons up to the quasi-Fermi level. Without further modifications of the equilibrium band structure due to photoexcitation, the CB minimum as well as the quasi-Fermi level of the electrons are above  $E_F$  (cf. Figure 1.2 a)). When such a metal-like semiconductor is placed in between to metal electrodes, an applied voltage would not lead to a current from electrode 1 to 2. This is because an energy gap exists between the electrons residing in the metal electrodes and the semiconductor. The photoinduced current in such a case is limited to the photoinduced electron density in the CB.

**Transient metal:** A transient metal is reached, when photoexcitation leads to density of states at  $E_F$ . This requires a modification of the equilibrium band structure, i.e. a downward shift of the CB minimum below  $E_F$ . In this state a current flows between the two metal electrodes, as long as the transient metal persists. The photoinduced current is not limited to the photoinduced electron density in the CB, because the band is refilled from the metal electrodes (cf. Figure 1.2 b)).

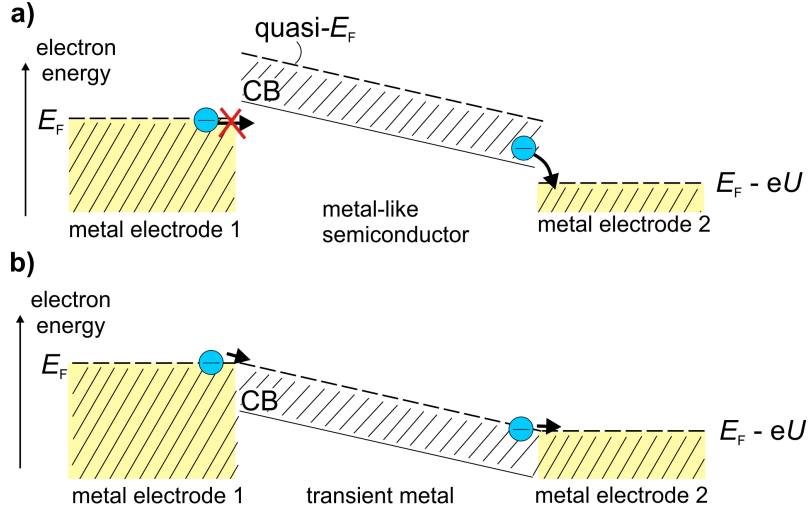


**Figure 1.2:** Driving a current between two metal electrodes using a transient metal.  $eU$  is the potential difference due to an applied voltage  $U$  between two metal electrodes. a) For a metal-like semiconductor, an electron plasma in the CB exists, but the quasi-Fermi level is well above the equilibrium Fermi level  $E_F$ . Electrons in the CB can transfer to electrode 2, but no current between the electrodes is driven. b) A transient metal with density of states at  $E_F$  does the job. Note that Schottky barriers at the semiconductor-metal interfaces are omitted for simplicity.

Hence, with a transient metal and the geometry displayed in Figure 1.2 b), ultrafast currents in information technology or for optoelectronic devices can be driven, for example light emitters in the terahertz regime [Cha]. For ZnO, the ultrafast generation of a transient metal would be especially appealing, as any application would benefit from the ease of nanostructuring and transparency to visible light of this material [Kli10b, Vit17]. However, as explained above, reaching a transient metal as opposed to a metal-like semiconductor goes beyond an exciton Mott transition, as a photoinduced downward shift of the CB with respect to the equilibrium is required. In general, the electronic band structure of semiconductors can be affected by photoexcitation due to three mechanisms:

1. Some semiconductors are at the verge of metallization in equilibrium and a SMT occurs upon slight changes of the system parameters, e.g. the lattice temperature or the band filling. Those changes can be triggered by photoexcitation, resulting in the formation of a transient metal [Iwa03, Mor14, Weg14b, Weg15]. However, the needed photoexcitation density to drive such a transition in inorganic semiconductors is considerable, typically on the order of parts per 10-100 atoms [Iwa03, Weg14b]. This exceeds the Mott density of semiconductors such as Silicon (Si) and ZnO by two to three orders of magnitude [Mot74].
2. In semiconductors such as ZnO, Si and gallium arsenide (GaAs), significant electronic band structure changes cannot be reached upon changes of system parameters such

---

as temperature variation close to ambient conditions. Yet, the band gap shrinks as photoexcited charge carriers change the screening in the system [Kli12]. A complete collapse of the band gap was demonstrated for GaAs [Hua98]. But also in this case the required photoexcitation density is very high, close to the damage threshold of the material.

3. Photoexcitation can also be used to modify the surface potential and create band bending, just like surface doping with shallow donors does [Kro99]. As discussed earlier, in the case of shallow donors an electron is *spontaneously* emitted into the CB due to thermal activation. The left-behind holes lead to positive surface charging and downward band bending at semiconductor surfaces. Equivalently, if photoexcitation ionizes deep defects localized at the surface, *optical excitation* creates positive surface charges and photoinduced downward band bending. However, whether such band bending could be sufficient to bent the CB below  $E_F$  and enable the formation of a transient metal confined to semiconductor surfaces is so far entirely unexplored.

In this thesis I investigate the electronic properties of the ZnO(10-10) surface upon photoexcitation below and above the Mott density, from femtosecond timescales to those of PPC. To do so, I use time- and angle-resolved photoelectron spectroscopy (trARPES) with femtosecond laser pulses. The ultrafast dynamics are accessed with a pump-probe scheme, where a first femtosecond laser pulse (pump) excites the sample and a second one (probe) photoemits the non-equilibrium electronic population. Pump photon energies resonant to as well as slightly below the fundamental band gap are used. Supplementary to the pump-probe scheme I developed a new mathematical model, which allows to investigate photoinduced dynamics on microsecond timescales and longer with repetitive laser pulses. For all experiments, a ZnO surface prepared with sputtering and annealing cycles in an ultrahigh vacuum (UHV) environment is used. This ensures well-defined and clean surface conditions, including the control of the surface defect density.

With this setup I show that ultrafast photoexcitation of the ZnO surface is in remarkable analogy to surface doping with shallow donors. The fundamental building block of all observed effects is the photoexcitation of deep defect levels at the ZnO surface, most likely oxygen vacancies. At low photoexcitation fluence, surface-confined defect excitons are formed. Above a threshold photoexcitation fluence, the defect excitons undergo a Mott transition and a metallic band with a parabolic dispersion evolves. Generation and decay of the metal phase occurs in the ultrafast time domain, within few tens of femtoseconds and few hundred picoseconds, respectively. The population of the photoinduced metallic band is Fermi-Dirac distributed with respect to the *equilibrium* Fermi level, meaning that a transient metal as opposed to a metal-like phase is formed (cf. Figure 1.2). The origin of the electronic band structure change, which is necessary for the formation of the transient

metal, is photoinduced downward band bending caused by positive surface charging due to the photodepletion of deep defects just above the VB maximum. This is evidenced by monitored the energetic position of the VB in the ultrafast time domain, which shifts downward and relaxes in exact temporal correlation with the rise and decay of the metal phase. Moreover, the effective mass of the transient metallic band evolves with a critical form as a function of the photoexcitation density as expected for a semiconductor-to-metal transition induced by shallow donor dopants. I conclude that photoexcitation is equivalent to chemical doping with shallow donors of oxide surfaces on the ultrashort timescale. The resulting photoinduced metallic phase is alike to 2DEGs induced by chemical doping. Remarkably, compared to hitherto known photoinduced SMTs in inorganic semiconductors, the SMT at the ZnO surface is driven with three to four orders of magnitude lower laser fluence.

After the decay of the surface metal phase within few hundred picoseconds, a small fraction of defect excitons remains and survives the inverse laser repetition rate. This long-lived defect exciton population has a multi-component decay that ranges from microsecond to minutes/hours, resulting in metastable n-type doping of the ZnO surface. Also on these timescales a photoinduced SMT can be reached, if a sufficient amount of deep defects at the surface is present. All these observations fit perfectly to the phenomenon of PPC reported in literature. They are a clear experimental evidence for the theoretical prediction that PPC originates from the photoexcitation of deep defects.

In summary, this thesis develops an in-depth understanding of the photoinduced physics at the ZnO surface on multiple time scales. As ZnO is an attractive material for nanotechnology due to its ease of nanostructuring and transparency to visible light, the ultrafast generation and decay of a surface metal in this material could be exploited for novel ultrafast electronics. Similar deep defects exist in many semiconductor compounds, therefore the insights of this work are not ZnO-specific. The discovered mechanism represents a general route to control metallicity confined to semiconductor interfaces on ultrafast timescales.

**Outline of this thesis** The present work focuses on the photoinduced changes of the band structure of the ZnO(10-10) surface upon ultrafast photoexcitation below and above the Mott limit. Chapter 2 elaborates on the physics background. I first summarize basic properties of ZnO. Then, in section 2.2, I review doping of semiconductors with shallow and deep impurities as well as the doping-induced Mott SMT. An important example is the 2DEG formation at ZnO surfaces induced by hydrogen adsorption. Section 2.3 elaborates on how excitons, in particular defect excitons, can be viewed as an analogue to chemical dopants and which photoinduced changes of the electronic band structure can be expected. Subsequently, the third chapter introduces the experimental technique,

---

trARPES, and describes the experimental setup. A part of section 3.1 is dedicated to the electrical field landscape in between sample and analyzer, which plays a fundamental role for the energetic position of spectral features probed by trARPES in the presence of photoinduced surface charges.

The results of this thesis are presented as follows: In chapter 4, I present the mathematical model I developed in order to understand the contribution of long-lived photoexcited populations to spectroscopy with repetitive laser pulses. When the lifetime of such electron populations exceeds the temporal distance between two subsequent laser pulses, a photostationary population builds up. For the case of pump-probe spectroscopy, I show that the photostationary population is, under some conditions, sensitive to the pump-probe delay on ultrafast time scales. Such population changes that can lead to unexpected signal contributions in pump-probe data, as exemplified by trARPES measurements of photoexcited ZnO in section 4.2.2.

In the following chapter 5, I explore defect exciton populations on a time scale of microseconds to minutes/hours leading to photostationary n-type doping of the ZnO(10–10) surface. I show that the defect excitons are surface confined, as they modify the surface potential and lead to a photoinduced work function reduction (section 5.2). Then I show that they arise from the photoexcitation of deep defects, which can be created by UV illumination on a minutes to hours timescale. The energetic position of the deep defect, as well as the rise of the defect density (and hence rise of the density of defect *excitons* upon photoexcitation) is in agreement with observations made in the context of PPC in ZnO (section 5.5 and 5.6). At a critical density, the defect excitons undergo a Mott transition leading to a metallic surface. This occurs exclusively for high defect densities (section 5.7 and section 5.8).

Chapter 6 is dedicated to the ultrafast surface metal generation at the ZnO surface. I show that, for low defect densities, the Mott transition can be driven with a sufficiently strong pump laser pulses *exclusively* on picosecond time scales. The metal phase rises as the defect exciton population is enhanced above the Mott limit, and decays as the defect excitons recombine. The dynamic delocalization and subsequent localization is monitored by the evolution of the effective mass of the surface electrons. The transient metallic phase has striking similarity with the 2DEG induced by hydrogen adsorption at the ZnO(10–10) surface, and the SMT cannot be driven for such hydrogen-terminated ZnO, strongly suggesting that it is a surface phenomenon (section 6.1.7). In section 6.2, the mechanism leading to the ultrafast SMT is unveiled by multiple systematics and test experiments exploiting the capabilities of trARPES. The section starts with the analysis of the effective mass change as a function of photoexcitation fluence, which evolves as predicted from the Mott-Hubbard model for the doping-induced SMT. Then, the VB dynamics that evidence photoinduced downward band bending are presented. A photon

energy dependency of the downward shift of the VB unveils that the photoexcitation of defect states in the ZnO band gap, located less than 0.4 eV above the VB maximum, must be responsible for the SMT. In section 6.2.4, I show that the pump-induced surface charges lead to peculiar shifts of the photoelectron spectra at negative pump-probe delays, as is well-known from literature. This is another independent proof beside the VB downward shift that the surface is positively charged upon photoexcitation. Finally, in sections 6.2.6 and 6.2.7 I show how the ultrafast photoresponse can be tailored by creating deep defects via sustained UV illumination and variation of the sample annealing temperature during the surface preparation.

The thesis also encompasses some technical insights for trARPES regarding the measurement of work function changes due to photoinduced surface charges. Related considerations, measurements and model calculations are contained in section 5.9 (for photostationary work function changes) and section 6.2.5 (for pump-induced work function changes in the ultrafast time domain).

Chapter 7 summarizes all results to draw a consistent picture of the photoinduced dynamics on multiple time scales at clean, but defective and hence common and application-relevant ZnO surfaces.

---

## 2 Theoretical background

This thesis is about ultrafast photodoping in ZnO. The term photodoping expresses that photoexcitation and chemical doping with shallow donors are equivalent. In this chapter I elaborate on the analogy between (localized) excitons and shallow donors. After a short introduction to the general properties of ZnO, doping in semiconductors and the doping-induced Mott SMT are reviewed. A particular example relevant for the present work is the surface metallization of ZnO surface 'doping' via adsorption of Hydrogen (H). Subsequently, excitons in semiconductors, the analogy between excitons and shallow donor dopants, and the Mott transition between photoexcited excitons are introduced. Finally, the changes of the electronic band structure upon photoexcitation, needed to drive a true SMT in semiconductors are reviewed.

### 2.1 General properties of ZnO

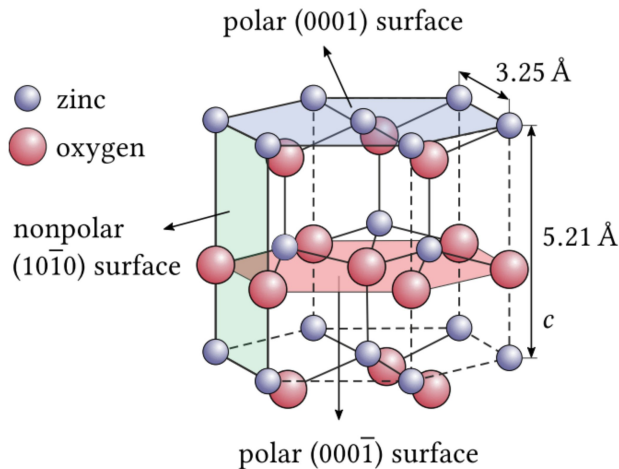


**Figure 2.1:** ZnO crystal structure. Adopted from [Dei16].

This section briefly introduces basic electronic properties of ZnO and crystal structure. Detailed information on the properties of ZnO and application in devices can be e.g. found in ref. [Kli10b] and a review with a focus on the surface chemistry is given by ref. [Wöl07].

**Basic electronic properties** ZnO is a semiconductor with direct gap at the center of the Brillouin zone in the UV (3.44 eV at 0 K, 3.37 eV at 300 K), and a high exciton binding energy of 60 meV. The wide band gap makes it transparent to visible and near UV light. ZnO is intrinsically n-doped (CB 0.2 eV above the Fermi energy), the origin of which is uncertain up to date. Doping can arise from lattice defects such as vacancies

or interstitials or from impurities as introduced in the next section. The intrinsic n-type conductivity and optical transparency make it attractive as a transparent electrode, in particular due to its high electrical and thermal conductivity. Moreover, it can be grown in nanostructures and large single crystals. ZnO has envisioned (and partially existing) applications in light-harvesting applications, thin-film transistors, laser diodes and LEDs in the blue to ultraviolet region.

**Crystal structure** Figure 2.1 shows the crystal structure of ZnO. It grows in a hexagonal crystal system (wurtzite structure), the unit cell is defined by the lattice parameters  $a$  and  $c$ . Also indicated is the non-polar (10-10) surface that consists of alternating rows of zinc and oxygen atoms. This surface is the most thermodynamically stable and thus dominant in nanostructures. For this reason, it is chosen for this work. The polar surfaces with either exclusively zinc (000-1) or oxygen (0001) atoms are also indicated. These surfaces are energetically less favourable because of the dipole moment ensuing from the strong ionic character of the bonds in the ZnO crystal [Wöl07].

## 2.2 Metallization of semiconductors upon doping

### 2.2.1 Doping of semiconductors

Doping of a semiconductor crystal can be achieved by the introduction of impurities, or by point defects, such as lattice vacancies or interstitial atoms. Doping modifies electronic properties such as the conductivity and the alignment of CB and VB relative to the Fermi level, and is thus crucial for the technological applications of semiconductors.

The general idea of doping with impurities is substituting an atom of the semiconductor crystal with another atom of a different valence. This gives rise to additional electronic states in the band gap, from which charge carriers can be freed and may contribute to conduction, upon thermal or optical excitation. Generally, if the substituting atom has a higher (lower) valence, extra electrons (holes) can be excited to the CB (VB), and the impurity acts as donor (acceptor). Point defects have a similar effect. For example, the oxygen vacancy in ZnO is expected to give rise to an electronic level with two extra electrons, on top of the band structure of the host lattice [Jan09]. This is reasonable, because due to the strong electronegativity of oxygen, the lattice constituents can be considered as ionized  $\text{Zn}^{2+}$  and  $\text{O}^{2-}$  [Kli10b], i.e. taking an oxygen atom away should set two electrons free.

One generally distinguishes between 'shallow' and 'deep' impurities on the basis of their position in the band gap. This distinction is typically made by comparing the thermal energy at room temperature to the ionization energy: When the ionization energy is on the order of few tens of meV, the donor is called shallow, and otherwise, it is called deep.

The two instances are reviewed below.

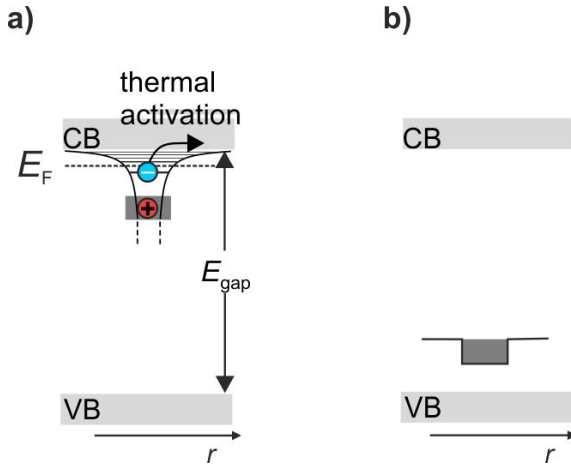


**Figure 2.2:** Shallow donors and deep donors. a) In case of a shallow donor the doping due to an impurity or point defect creates an occupied state in the band gap, very close to the CB minimum. Thermal excitation is sufficient to ionize the defect. However, the electron in the CB will be attracted to the impurity site due to the positive charge, forming a hydrogen-like state. The black line sketches the Coulomb potential energy due to the hole at the impurity site as a function of distance from the site  $r$ :  $U(r) = -\frac{e^2}{4\pi\epsilon r}$ . b) In the case of a deep donor the doping creates an occupied state in the band gap, too far away from the CB to be thermally activated. The electronic wave function is strongly localized, in contrast to the hydrogenic state of the shallow donor.

**Shallow donors** In Figure 2.2 a), a shallow donor is illustrated. The impurity induces an occupied level close to the CB minimum. Due to its proximity to the CB minimum it can be thermally ionized, and the electron is promoted to the CB. However, the electron in the CB is still attracted to the impurity site due to the positive charge, forming a hydrogen-like state. The common approach is to treat the impurity as an extended hydrogen atom.

The hydrogen model is used calculate the ionization energies of shallow donors for a certain host crystal. It does not explicitly take into account the specific chemistry of the impurity, but only the parameters of the host lattice. The idea behind this is that the electronic wave function is extended over many lattice sites, and the far field should be well described by the Coulomb potential of the hole, reduced by the dielectric constant of the host lattice. Close to a symmetry point of the band structure of the host lattice, and assuming that the CB has parabolic dispersion, the problem can be reduced to solving the Schrödinger equation of the hydrogen atom [Shk84]:

$$\left( -\frac{\hbar^2}{2m_{\text{eff}}}\Delta - \frac{e^2}{4\pi\epsilon r} \right) \Psi = E\Psi \quad (2.1)$$

with the effective mass  $m_{\text{eff}}$  of the CB instead of the free electron mass and the dielectric

constant of the material  $\epsilon$ . This gives for the ionization energy  $E_D$  the series

$$E_n = -\frac{m_{\text{eff}}e^4}{8\pi\epsilon^2\hbar^2n^2}, \quad n = 1, 2, 3, \dots, \infty \quad (2.2)$$

where the base line is the CB minimum. The Bohr radius of the ground state 1s orbital is

$$a_H = 4\pi\epsilon\hbar^2/(e^2m_{\text{eff}}) \quad (2.3)$$

Because  $\epsilon$  is larger than  $\epsilon_0$  and the effective mass smaller than one, for many semiconductors the resulting Bohr radius is larger than that for the hydrogen atom and extends over several unit cells (for ZnO:  $a_H=1.56$  nm, the lattice constant is 0.325 nm(0.521 nm) for the a(c) axis [Ell16]). The ionization energy of the ground state is 55.3 meV for ZnO. This energy is approximately in agreement with optical measurements for a few impurities in ZnO [Ell16]. Deviations are expected (and observed, e.g. for shallow acceptors in Si [Zha18]) due to the simplified nature of the model that does not take into account the chemical nature of the impurity. Viewing shallow donors as extended Hydrogen atoms is the starting point for the Mott the metal-insulator transition [Mot74], as will be seen in the subsequent section.

As shallow dopants contribute to the concentration of free carriers, they have the important effect of shifting the energy bands relative to the Fermi level (Fermi level pinning) [Cox87]. An increased electron concentration in the CB due to shallow donors leads to a shift of the Fermi level towards the CB. The technological consequences are exploited e.g. in p-n-junctions.

**Deep donors** In Figure 2.2 b), the electronic band structure of a semiconductor with a deep donor is shown. The energetic position of the occupied level is deep in the band gap, such that it is not thermally ionized at room temperature. The wave function of the electronic state is strongly confined to the impurity site, more like a particle in a box than a hydrogen atom [Cox87]. The determination of ionization energies relies entirely on ab-initio electron band structure calculations [Ell16, Zha18].

**Unifying shallow and deep impurities** The distinction between shallow and deep impurities by their thermal ionization at room temperature is clearly device-oriented. Another definition is based on the localization of the electronic wave function at the impurity site, i.e. whether it is extended hydrogen-like or strongly localized [Zha18]. However, a strict difference between these two types of impurities does not exist, because ab-initio density functional theory (DFT) calculations show that even shallow defects are strongly localized at the lattice site of the impurity when they are neutral, i.e. before forming the hydrogenic state upon thermal excitation of the donor electron into the CB

[Zha18]. On the one hand, this means that the ionization energy  $E_D$  of shallow donors is in this view not entirely correct, because the electron has to be excited from the neutral defect in order to form the hydrogenic-like state, and  $E_D$  is just the ionization energy from the 1s state. On the other hand, there is an important conceptual consequence, namely that a situation where an electron is excited from a deep donor into the conduction band (e.g. optically), and then forms an extended hydrogenic state, cannot be distinguished from a shallow donor [Zha14, Zha18]. I will come back to this later in section 2.3.3.

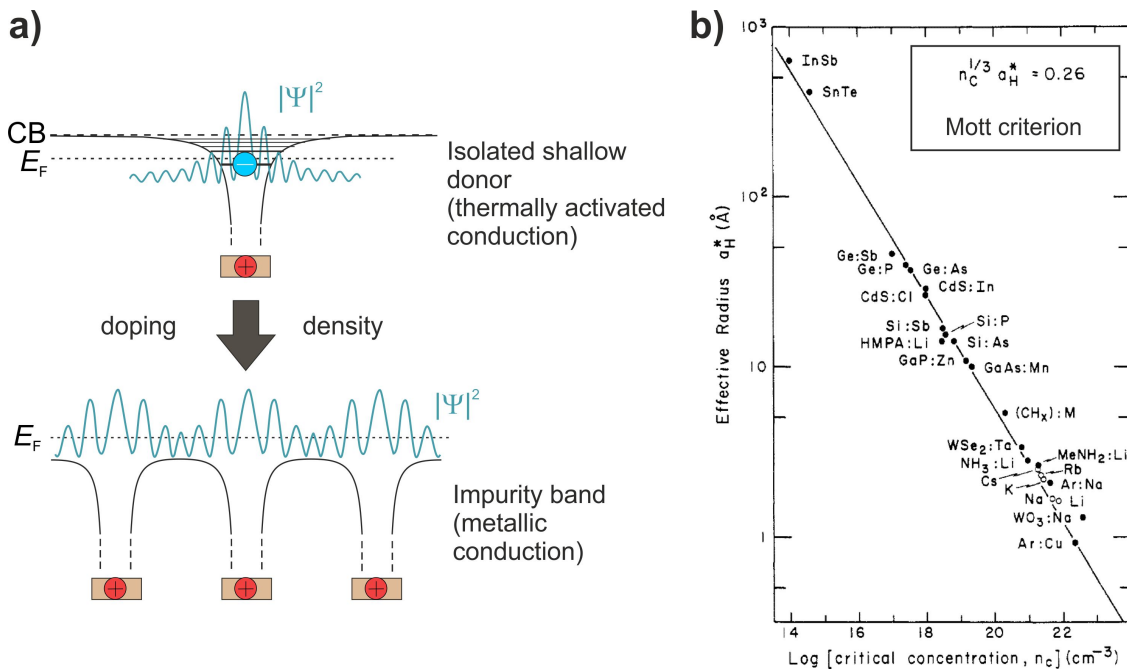


**Figure 2.3:** Doping induced semiconductor-to-metal (Mott) transition. a) Schematic of the transition: Upon reaching a critical density, isolated shallow donors with thermally activated conduction form an impurity band. b) Log-log plot of the estimated Bohr radius  $a_H^*$  of the localized state versus the experimentally determined critical concentration required to yield metallic behaviour. The line is a linear fit to the data, showing that the Mott criterion, equation 2.4, is obeyed quite universally (From ref. [Edw81]).

### 2.2.2 The doping-induced Mott semiconductor-to-metal transition

Shallow donors in low concentration are isolated from each other, and the donor electrons are localized in hydrogenic potentials at the impurity sites. They contribute to conductivity only when they are excited thermally (or by an optical transition) into the CB<sup>1</sup>.

<sup>1</sup>More precisely, above the mobility edge, i.e. the energy of delocalized states in the upper Hubbard band, that arises from moving an electron to a distant donor that is already occupied. The mobility edge is

Thus the conductivity of doped semiconductors decreases with decreasing temperature until approaching the 'freeze-out' region. When the doping density of shallow donors in a semiconductor is increased above a critical value, the wave functions of individual shallow donors overlap enough, such that excess electrons delocalize and form a metallic band, also called impurity band[Mot74]. The transition is illustrated in Figure 2.3 a). The semiconductor is then called 'degenerately doped' and behaves like a metal, allowing for conduction down to 0 Kelvin.

This transition occurs in many compounds. Figure 2.3 b) presents a plot of the radius of the wave function of the donor electron versus the critical concentration  $N_c$  required for metallic behaviour in several systems (experimentally determined). The solid line is a fit that shows that the critical concentration follows remarkably well a linear relationship that is known as the Mott criterion

$$N_c^{1/3} a_H = K. \quad (2.4)$$

$K$  is a constant that is determined by the fit in Figure 2.3 b) to  $0.26 \pm 0.05$ , which is comparable to theoretical predictions by Mott (see below).  $a_H$  is the Bohr radius<sup>2</sup>. Because the wave function of the shallow donors is extended over several lattice sites, the doping-induced semiconductor-to-metal transition (SMT) happens already at low doping densities, for example at parts per  $10^4$  atoms in phosphorous-doped silicon [Cox87]. Instead of varying the doping, the pressure or the applied magnetic field can be varied, thereby changing the distance between the donor sites or the shaping the wavefunctions, respectively [Lim03, Edw85].

**Mott-Hubbard model and critical behaviour** The Mott-Hubbard model is an important concept for the theoretical description of the doping-induced SMT and predicts critical scaling of physical quantities such as the effective mass close to the transition point. From band theory, it follows that a periodic array of one-electron atoms (hydrogen atoms, such as shallow donors in a host) would be metallic, no matter how far their distance is. This results from a tight-binding approach, where the exponential decay of the wave function in the 1s orbitals leads to a finite overlap for all interatomic distances[Shk84]. The band width would become very small and the effective mass of the band would be very large, but still conduction would be allowed, because the band is only half-occupied (as it is two-fold spin degenerate). However, what is missing in this picture is the electron-electron repulsion. Mott [Mot61, Mot74] argued that the band would split into two bands, one fully

---

a concept that is introduced in the context of localization by disorder. It can be below the CB minimum, within the upper Hubbard band [Mot74]. See the definition of the Hubbard bands and the Anderson localization further below.

<sup>2</sup>Note that in Figure 2.3 b), the radius is not exactly the Bohr radius from the Hydrogen model (equation 2.3), but is a 'fine-tuned' value based a more realistic value based on experimental data.

occupied and one unoccupied. The argument is that in order to transit to a neighboring site, an electron has to overcome an activation energy that is approximately the difference between the ionization energy minus the electron affinity  $I - A$  of the neighboring states. In the case of hydrogen atoms, this would be just the difference  $E_2 - E_1$  (cf. equation 2.2). The two bands are called the upper and lower Hubbard, named after Hubbard who first introduced a tight-binding Hamiltonian including the electron-electron repulsion between neighboring lattice sites. The difference  $I - A$  (the Hubbard  $U$ ) can be interpreted as the electron repulsion energy, when two electrons are at the same site [Mot74, Cox87]. The metal-insulator transition occurs when the band width  $W$  (which increases with the interatomic distance) equals the electron repulsion energy

$$U = W.$$

Figure 2.4 illustrates the transition from an insulator or semiconductor with separated Hubbard bands.

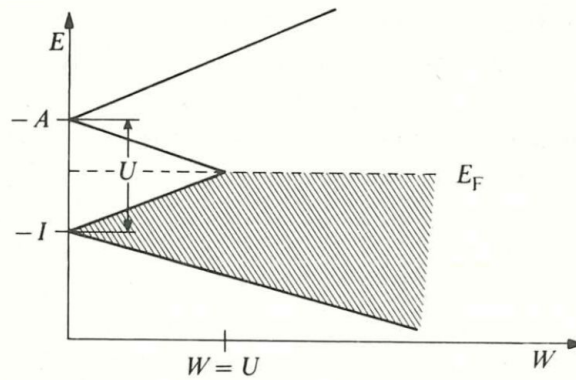


**Figure 2.4:** Schematic of the transition from an insulator or semiconductor to a metal due to the overlap of two separated Hubbard bands. The energy is plotted versus the band width, which increases with decreasing interatomic distance. At  $U = W$  the bands overlap and the system becomes metallic. From ref. [Cox87]

First, the bands are separated due to their low band width (large interatomic distance), and a SMT occurs where the bands overlap at the critical band width  $W = U$ . Mott gave a rough estimate of the interatomic distance at which the SMT occurs, for exponential decaying wave functions [Mot74]. The SMT occurs at a critical density of atoms

$$N_c^{1/3} a_H \cong 0.2. \quad (2.5)$$

As shown above, the Mott criterion is obeyed by many systems.

The Mott-Hubbard model predicts a phase transition of second order, i.e. the change

in conductivity would be continuous according to Mott [Mot74]. A recent application of the Mott-Hubbard model to excitons in semiconductors comes to the conclusion that the transition can be first or second order, depending on the strength of  $U$  [Gue19]. Independent of whether the change in conductivity would be continuous or not, it has been shown that the conductivity scales with a critical form towards the transition point [Lim03], i.e.

$$(\sigma - \sigma_C) \propto (P - P_C)^\delta, \quad (2.6)$$

where  $\delta$  is the critical exponent,  $\sigma_C$  the conductivity at the transition point and  $P$  the parameter to tune through the Mott transition. In the cited reference [Lim03], this is the pressure. Solving the Mott-Hubbard model at 'half-filling' (i.e. one electron per lattice site) in the Gutzwiller approximation indeed predicts such critical behaviour for several quantities including the effective mass[Bri70, Edw85].

When the two Hubbard impurity bands merge, a single metallic band results. It should be noted that this impurity band is formed first below the CB of the host material and merges with the CB only at elevated doping densities [Mot74]. This picture has been corroborated experimentally in Si-doped GaAs by measuring the thermal activation energy required for promoting carriers from the impurity band into the CB and the effective mass of the impurity band as a function of doping density above the Mott limit [Liu93]. Starting with the ionization energy of isolated shallow donors, the thermal activation energy approaches zero at doping densities that are 10-100 times higher than the Mott density. At about at the same density, the effective mass of the impurity band is found to merge with the CB effective mass.

**Anderson localization** The above so far considered a periodic array of shallow donors. In real crystals, doping centers will be randomly distributed. The disorder leads so-called Anderson localization. Within the Anderson model, disorder is accounted for by distributing the electron energies at the individual shallow donor sites randomly within an interval  $V_0$ . Localization occurs when the ratio between  $V_0$  and the band width  $W$  surpasses a critical limit. Just below the critical limit, the electrons become first delocalized within the middle of the band, while the band tails are more likely to be localized. Mott introduced the concept of the mobility edge, which separates localized from delocalized states within the bands [Mot74]. Thus, a certain filling of a band might be necessary to reach metallic conductivity. Due to the contributions of Mott and Anderson, the doping-induced SMT is also called Mott-Anderson transition.

### 2.2.3 Semiconductor-to-metal transition in 2D, the example of ZnO/H

The above introduced SMT between shallow donor dopants was experimentally confirmed for bulk samples. Yet, metallization can also occur in two dimensions (2D). A notable example is the formation of two-dimensional electron gases (2DEGs) at oxide surfaces. The confinement of electrons in a narrow region at the surface can lead to novel properties not found in the bulk material, such as high electron mobility, superconductivity and surface magnetism [Hwa12]. Such 2DEGs can be induced by doping with shallow donor dopants or by electrical fields. In case of doping, the general picture is that shallow donors donate an electron to the conduction band, and the holes at the impurity sites form a layer of positive charges at the surface. The electrical potential of the positive surface charges leads to downward band bending of the VB and CB toward the surface and hence confinement of the CB electrons at the surface [Fra17], cf. Figure 2.5 a).

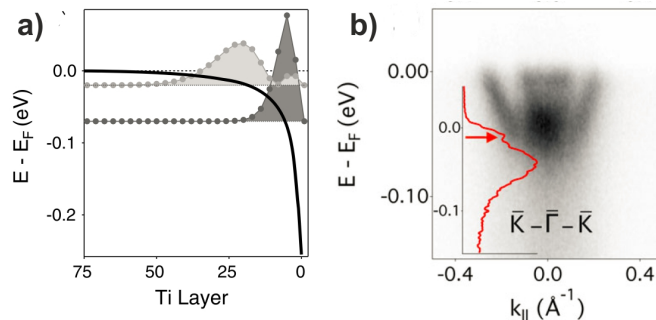


**Figure 2.5:** 2DEG at the SrTiO<sub>3</sub> surface. a) Position of the CB along the surface normal (1 Ti layer = 0.225 nm) and square modulus of the wave function of the lowest two subbands arising from the surface confinement due to the downward band bending. b) Angle-resolved photoelectron spectroscopy (ARPES) spectrum of the free electron-like states. Shown is the photoemission intensity versus wave vector parallel to the surface  $k_{\parallel}$  close to the Fermi energy  $E_F$ . Two parabolic bands are observed, cut by  $E_F$ . From [McK14].

#### UV illumination-induced surface oxygen vacancies at the origin of the 2DEGs at various oxide surfaces

Figure 2.5 presents one of the best known examples, the 2DEG at the SrTiO<sub>3</sub> surface [Fra17, Mee10, McK14]. Figure 2.5 a) shows the calculated band bending of the CB toward the surface by using the Poisson equation, assuming that the surface is positively charged [McK14]. The CB bends downward to the surface and the confinement to few nanometers leads to the formation of quantized states (subbands). The square modulus of the wave function calculated from a tight binding approach for the lowest two subbands is shown. The positive charge is adjusted such that the energetic position of the lowest subband matches the experimental results summarized in the following. Figure 2.5 b) shows the electronic band structure as a function of wave vector parallel to the surface  $k_{\parallel}$  measured with angle-resolved photoelectron spectroscopy, the method of

choice to investigate the surface metallization (for an introduction to the technique see the experimental section 3.1). The ARPES spectrum shows two parabolic bands, in agreement with the two subbands predicted theoretically.

The source of the shallow donors at the surface of  $\text{SrTiO}_3$  are most likely oxygen vacancies. DFT calculations have shown that the oxygen vacancy indeed forms a shallow donor [Jan14]. Moreover, it is possible to form them via UV illumination at oxide surfaces via photolysis, which inherently happens during the ARPES measurement. Indeed, the 2DEG at the  $\text{SrTiO}_3$  surface appears after UV illumination only [Mee10, McK14]. Moreover, the 2DEG can be eradicated by oxygen exposure [McK14]. This UV illumination-controlled formation of 2DEG states is beneficial, because it offers the option to imprint electronic circuits using interference patterns [Mee10].

Similar states are induced at the surface of many oxide surfaces, such as  $\text{In}_2\text{O}_3$  [Zha13],  $\text{TiO}_2$  [Röd15] and  $\text{KTaO}_3$  [Kin12] and have been attributed to surface oxygen vacancies. Also at the  $\text{ZnO}$  surface, a 2DEG can be induced by 'surface doping' via the adsorption of hydrogen (H), see below. Note that in contrast to the above example of  $\text{SrTiO}_3$ , oxygen vacancies are deep donors at the  $\text{ZnO}$  surface [Jan09], and thus should not induce a 2DEG in thermodynamic equilibrium. Oxygen vacancies are the most likely candidate for the photoinduced surface metal formation in this thesis, and the relation between photoexcitation and shallow donor behaviour will be discussed later, in section 2.3.3. For completeness, it should be mentioned that recently a 2DEG at the  $\text{ZnO}$  surface was reported after deposition of Aluminum (Al). Contrary to the wide-spread view that oxygen vacancies form deep donors, the 2DEG formation has been attributed to oxygen vacancies induced by the oxidation of the Al film [Röd18].

**The transition from localized to delocalized states and the example of H-doped ZnO** The metallization of oxide surfaces by shallow donors is commonly described in a surface-averaged picture, i.e. by drawing the downward band bending toward the surface (cf. Figure 2.5). In this picture, the laterally localized character of the doping site is lost. To understand the photoinduced SMT at the  $\text{ZnO}$  surface discovered within this thesis, a surface-averaged picture is not sufficient. The concepts of the Mott transition that are established for three dimensions (3D) systems are necessary.

In the surface averaged picture the effect of the doping of the surface with shallow donors is comparable to applying an electric field. Indeed, external electrical fields can be used to induce band bending and create a 2DEG as well. This is exploited in a metal-oxide semiconductor field-effect transistor (MOSFET). By tuning the electrical field, the CB of the oxide is bent below the Fermi level and is occupied. The strength of the band bending determines how much of the CB can be occupied, and hence determines the electron density in the two-dimensional electron gas (2DEG) [Kra04]. It was found that

metallic behaviour can only be observed above a critical electron density. Moreover, the effective mass shows critical behaviour towards the transition point, as expected from the Mott-Hubbard model. The critical behaviour of the effective mass was also demonstrated for other 2D systems [Cas03]. Note however, that the theory of SMTs in 2D is still in development [Naj19].

In the case of doping, from the concept of the shallow impurities and the Mott transition in 3D, one would expect a localized electronic state at low doping densities, which then evolves into a metallic band. The band structure change induced by the doping would be locally varying across the surface, unlike a simple field effect. This view is corroborated by the study of H adsorption at the mixed-terminated ZnO surface [Dei15, Dei16]. A sufficient amount of adsorption of H at ZnO(10-10) leads to the formation of a 2DEG, evidenced by a parabolic band cut by  $E_F$  in ARPES data, combined with downward band bending [Oza10]. However, as shown in a combined experimental-theoretical study by ref. [Dei15, Dei16], in the low dosing regime, localized (view nm wide) electron pockets are formed that are spatially separated from each other. The results of ref. [Dei15, Dei16] are summarized in the following.

Figure 2.6 a) shows the laterally-resolved potential change induced by H adsorption at the ZnO(10-10) surface, calculated with DFT. It varies strongly on a length scale of nanometers. It should be noted that H can adsorb at the Zn and the oxygen sites of the surface (the structure of the surface is overlaid in Figure 2.6 b)) and acts as an electron donor on oxygen but as an electron acceptor on Zn. Correspondingly, the potential is lowered at the oxygen sites and increased at the Zn sites. Figure 2.6 b) shows the potential change as false color plot versus position along the surface normal (left) and along the surface (bottom). The potential change is not only strongly localized laterally, but as well localized to the surface. In the surface-average, the potential is lowered toward the surface within less than 2 nm, comparable to the band bending shown for SrTiO<sub>3</sub> in Figure 2.5 that was not ab-initio calculation-based. As the CB is downward bent locally, presumably below the Fermi level, localized electron pockets at the ZnO surface are formed, which are independent of each other in the low doping density regime.

The experimental confirmation of this picture is three-fold. Firstly, the picture of independent electron pockets at the surface explains the linear increase of the photoemission signal around  $E_F$  in the low dosing regime. Secondly, the calculated potential change explains quantitatively the work function reduction that is observed experimentally. And thirdly, ref. [Dei15] measured the signal of photoexcited excitons that are bound to the H sites. This exciton signal is detailed in section 2.3.1. The signal increases in the low dosing regime, but in the high dosing regime the signal is quenched. This is interpreted as the increased number of individual, localized electron pockets, which subsequently delocalize, forming a metallic band. The formation of electron-hole pairs is then impeded due to

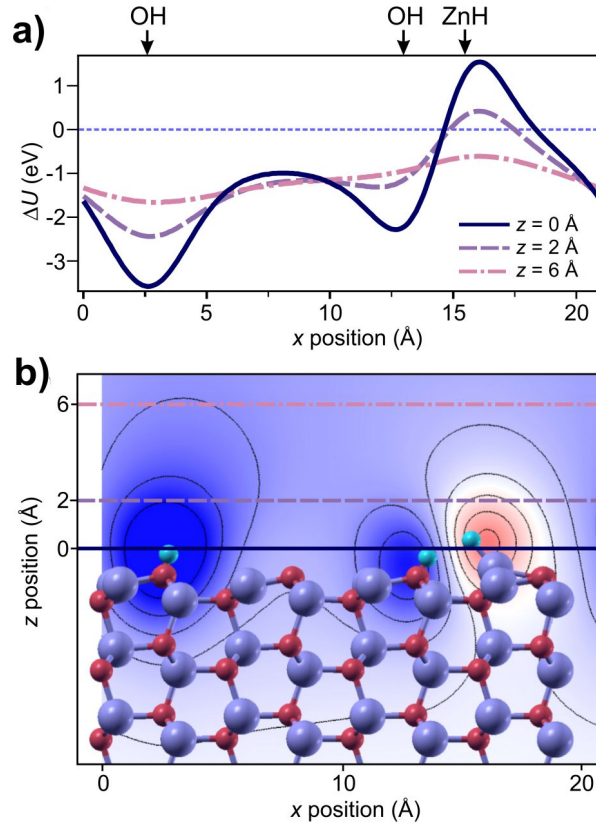


**Figure 2.6:** Lateral corrugation of the potential at the mixed-terminated ZnO surface upon surface doping with H. a) H-adsorption-induced potential change  $\Delta U$  along a specific line at the surface. b) False color plot of  $\Delta U$  as a function of position along the surface (bottom) and along the surface normal (left). The solid lines represent 0.5 eV increments  $\Delta U$ . From [Dei15].

screening of the Coulomb potential. In this view, isolated, confined electron pockets are formed at the surface which then delocalize and form a metallic band, conceptually like the Mott or Mott-Anderson transition in 3D.

#### 2.2.4 Summary

In summary, doping of semiconductors by impurities or defects can lead to shallow and deep donors and acceptor levels. The definition is based on the energetic position of the impurity state within the band gap. While shallow impurities can be activated thermally, deep impurities require an energy larger than the thermal energy to be emitted into the CB. A semiconductor-to-metal transition occurs at a critical doping density, which can be described by the Mott criterion. This SMT would only occur for shallow donors (or acceptors), where the electrons exhibit extended (hydrogenic) wave functions and not for deep donors, where the electrons are strongly localized. Doping-induced SMTs also occur in 2D. 2DEG formation at oxide surfaces results from doping with shallow donors such as

oxygen vacancies or adsorbates such as H in the case of ZnO.

## 2.3 Metallization of semiconductors upon photoexcitation

After having introduced chemical doping in the last section, this section elaborates the extent to which optical excitation of excitons can be viewed as analogous to doping with shallow donors. The description of excitons as extended hydrogen atoms, which finds confirmation by experimental work, is at the origin of this analogy.

### 2.3.1 Excitons

Excitons are bound states of photoexcited electrons and holes attracted by the Coulomb potential. They are essential to the optical properties of semiconductors. The photoexcited carriers can arise from optical excitation across the band gap (free excitons, hole in the VB), or from photoexciting occupied defect states within the band gap (defect excitons, hole localized at the defect<sup>3</sup>). Furthermore, free excitons can also be attracted (or trapped) by a charged or neutral impurity forming a defect-bound exciton.

For free excitons there is the general distinction between Wannier excitons and Frenkel excitons. For Frenkel excitons, electron and hole are held strongly together such that they are localized on the same lattice site. Such states occur in systems with low dielectric constant, such as molecular crystals. The binding energy can reach several 100 meV. For materials with wide bands, such as Si, GaAs or ZnO, Wannier excitons are formed. These excitons have a small binding energy of not more than few tens of meV and are extended over several lattice sites.

Wannier excitons are described as extended H atoms, analogously to shallow donors, cf. section 2.2.1. The exciton energies are given by the hydrogenic formula with respect to the band gap [Cox87]:

$$E_n = E_{\text{gap}} - \frac{\mu e^4}{8\pi\epsilon^2\hbar^2 n^2}, \quad n = 1, 2, 3, \dots, \infty. \quad (2.7)$$

The only difference in the description is that the hole is not localized in the VB. Therefore, in equation 2.7 the reduced effective mass of the electron-hole pair is used instead of the effective mass of the electron (cf. equation 2.2):

$$\mu = \frac{m_{\text{eff}}^e m_{\text{eff}}^h}{m_{\text{eff}}^e + m_{\text{eff}}^h} \quad (2.8)$$

The reduced effective mass  $\mu$  approaches the electron effective mass  $m_{\text{eff}}^e$  when the hole

<sup>3</sup>The state is also called bound exciton [Zha14, Zha18]. Also empty defect states can be populated. If an exciton is formed, the hole would be in the VB and the electron localized at the defect.

is localized, i.e.  $m_{\text{eff}}^h \rightarrow \infty$ . The exciton problem becomes then equivalent to the shallow donor problem [Mah67]. The experimentally determined exciton binding energy of ZnO is  $59 \pm 0.5$  meV [Kli10a].

Experimentally, excitons were first discovered in copper oxide  $\text{CuO}_2$  by optical spectroscopy, see ref. [Kaz] and references therein. The exciton series appears below the fundamental absorption edge. Due to the relatively high exciton binding energy of about 100 meV, states up to  $n=26$  could be observed in high resolution spectroscopy [Kaz]. Remarkably, the exciton energies follow the  $n^{-2}$  dependence predicted by the hydrogenic model precisely.

Defect and defect bound excitons can be identified by additional peaks in photoluminescence data [Kli10a, Fog19]. An overview of the observed transition in ZnO can be found in ref. [Vem12].

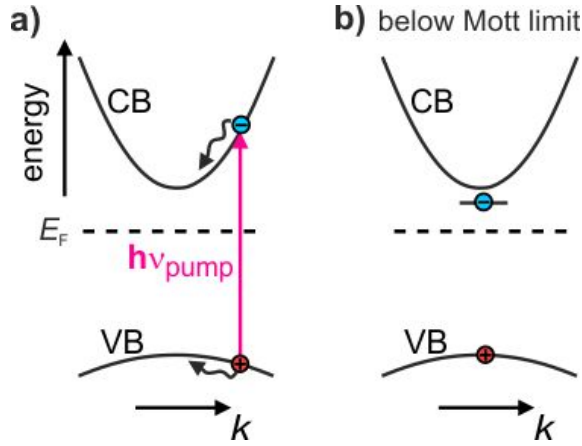


**Figure 2.7:** Simplistic sketch of exciton formation upon optical excitation across the fundamental band gap. a) Optical excitation creates electrons in the CB and holes in the VB which subsequently scatter to the band edges. b) The photoexcited electrons and holes form an exciton at low charge carrier densities (photoexcitation fluences).

### 2.3.2 Exciton formation - the case of ZnO

When a semiconductor is photoexcited above the fundamental band gap, first free electrons and holes are created, which then bind to excitons. Figure 2.7 shows a simplistic picture of what is expected for photoexcitation of a semiconductor across the band gap. In Figure 2.7 a) a photon with energy greater than the band gap creates a non-thermal population of electrons and holes in the CB and VB, respectively, which scatter to the band edges through electron-electron and electron-phonon interaction. At low charge carrier densities below the so-called Mott limit, they bind to excitons (Figure 2.7 b)). In the present sketch the excitonic level is drawn below the CB minimum, representing the ionization energy of this state [Zhu14]. The processes in Figure 2.7 occur on femto- to picosecond timescales,

thus requiring ultrafast pump-probe spectroscopy for their investigation.

Exciton formation has been investigated with optical spectroscopy, e.g. using optical frequencies in the THz regime, which corresponds to photon energies in the meV regime. This way intra-excitonic transitions can be excited and thus the exciton population can be monitored directly [Ul11]. Also time-resolved ARPES (trARPES) has been used to investigate exciton formation, e.g. in  $\text{CuO}_2$  [Tan19], Si [Wei04], in the transition metal dichalcogenide  $\text{WSe}_2$  [Pup17] and in organic semiconductors [Zhu15]. The case of ZnO is summarized in the following, due to this relevance for the present work.

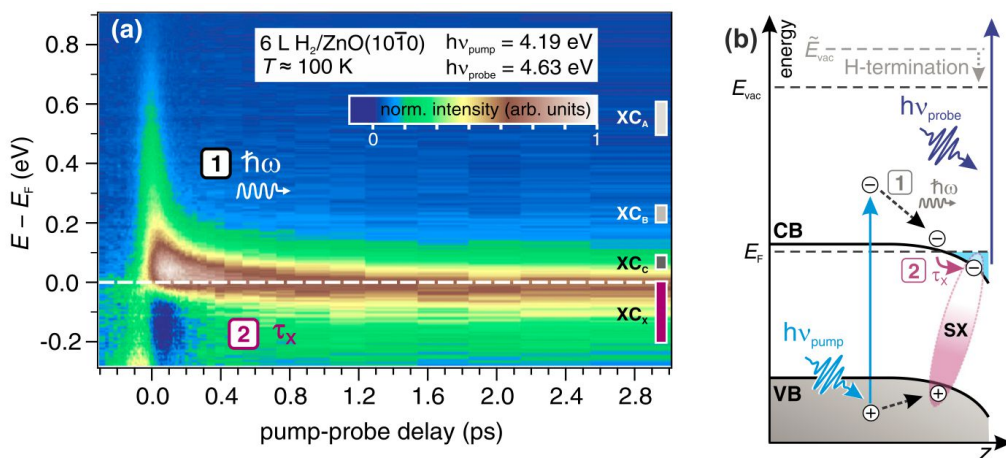


**Figure 2.8:** Exciton formation at the ZnO(10-10) surface probed with trARPES. a) False color plot of the pump-induced photoemission intensity as a function of pump-probe delay. The pump photon energy is 4.19 eV, above the ZnO band gap. The signal at negative delays was subtracted from the data. b) Energy level diagram to interpret the results, see text. From [Dei14].

Figure 2.8 a) show the photoemission intensity of ZnO after dosing 6L H (for the dosing cf. section 3.2.6), as a false color plot versus pump-probe delay (bottom) and energy with respect to the equilibrium Fermi level  $E_F$  (left). The pump photon energy is 4.19 eV, i.e. above the band gap of 3.4 eV, and the excitation density is below the supposed Mott density. Qualitatively, the photoemission intensity consists of a short-lived signal at energies above  $E_F$  and the delayed rise of a signal below  $E_F$  within few hundred fs. Figure 2.8 b) shows a sketch with the interpretation of the observed signal. The electrons at high energies are attributed to hot electrons in the ZnO CB band, which scatter down to the band edge. The lifetime of the electrons with excess energy is on the order of few fs only at high energies, which is attributed to the strong interaction of electrons and optical phonons in ZnO, in accordance with theory [Zhu10].

The signal that rises within few hundred fs below  $E_F$  is attributed to surface excitons. The excitonic binding energy leads to an increase of the energy required to photoemit the electron, such that the signal appears below the CB minimum. Ref. [Dei14] shows that the

signal increases as the H coverage increases, demonstrating that this excitonic species is bound to H sites (cf. the illustration in Figure 2.8 b). Indeed, the exciton binding energy of ZnO is 60 meV and the bulk CB is 200 meV above  $E_F$  for n-type doped ZnO. Hence, a photoelectron signal below  $E_F$  can only occur in regions where the CB is lowered with respect to the bulk value [Dei16]. At H adsorption sites this happens due to downward band bending as discussed in section 2.2.3. Note that at high H coverages the surface exciton signal becomes quenched, likely due to enhanced screening [Dei15], as mentioned in section 2.2.3.

### 2.3.3 Persistent photoconductivity and photoinduced metallization

As discussed above, the description of excitons as extended hydrogen-like atoms is identical to the description of shallow donors but for the fact that free excitons are mobile as the hole mass is finite. For defect excitons with an immobile hole the analogy becomes closest. This section condenses the analogy between photoexcitation of defect excitons and chemical doping. Because some photoexcited defects have a very long lifetime, this leads to a photodoping effect that is intimately related with the phenomenon of persistent photoconductivity (PPC) observed in many semiconductors including ZnO. A Mott-Anderson SMT using the PPC effect has been demonstrated by transport measurements in a GaAs compound.

**Photodoping** The creation of free electrons in the CB and holes in the VB by photoexcitation is often termed 'photodoping'. For example, in strongly correlated materials such as metal oxides that are insulating due to electron-electron repulsion in the Mott-Hubbard sense, additional carriers introduced in the system would change the Mott-Hubbard  $U$ , and hence cause a semiconductor (or insulator)-to-metal transition [Oka11, Eck13]. This so-called filling-controlled Mott transition can be induced by chemical doping. With transient optical spectroscopy it was demonstrated that photoirradiation produces similar spectral features as chemical doping [Oka11] and induces metal-like behaviour on the ultrafast time scale [Oka11, Iwa03]. However, the properties of these photodoped state are far from understood, and recent theoretical work has emphasized the differences between the photodoped and the chemically doped state due to scattering between the photoexcited charge carriers [Eck13].

The perhaps most direct and universal analogy between chemical doping and photoexcitation results upon identifying shallow donors as thermally excited defect excitons. The same state can be excited optically by photoexcitation of a deep donor. To illustrate this, Figure 2.9 summarizes the concept of a shallow donor, deep donor and a defect exciton created by photoexcitation of a deep donor.

The shallow donor state (Figure 2.9 a)) is located energetically just below the CB

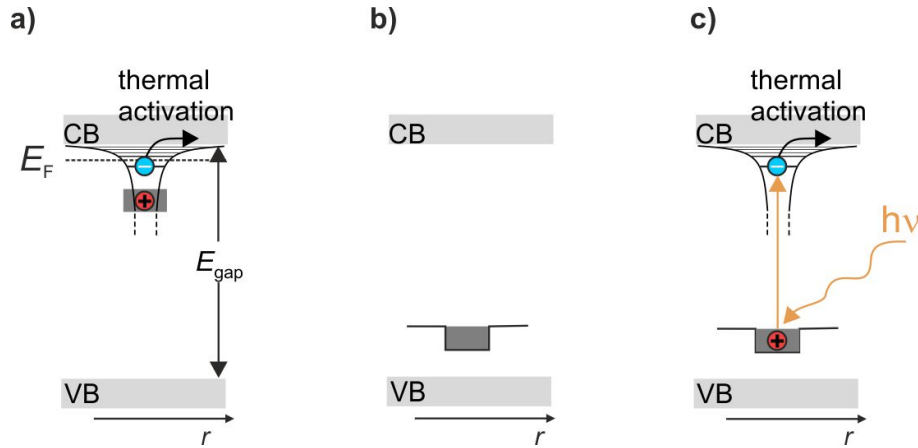


**Figure 2.9:** Shallow donor defect exciton analogy. a) and b) Shallow donor and deep donor, respectively. c) Defect exciton created by photoexciting an electron from a deep donor into the CB. The electron is bound to the photohole in a hydrogenic potential. The resulting state is qualitatively analog to a).

such that an electron can be excited into the CB by thermal activation. The electron then orbits around the hole at the impurity site in a hydrogenic-like state. The deep donor state (Figure 2.9 b)) is located energetically so far away from the CB that thermal activation is not possible. However, upon photoexcitation the electron can be excited to the conduction band (Figure 2.9 c)). Once again, the electron then orbits around the hole at the impurity site in a hydrogenic-like state, analogous to the shallow donor depicted in Figure 2.9 a). Indeed, for photoexcited deep donors, the effective mass of the hole becomes infinitely large and therefore the hydrogen series of the exciton (cf. equation 2.7) becomes equal to the thermally excited shallow donor (cf. equation 2.2).

**Persistent photoconductivity in ZnO** The above described photodoping is supposedly at the origin of a phenomenon called persistent photoconductivity (PPC) in ZnO and other materials. The experimental phenomenon is displayed in Figure 2.10.

Shown is the current through a ZnO nanowire as a function of time. The experimental configuration (see inset) is under vacuum. The current rises as a function of UV illumination time and when the light is switched off, it persists and only slowly decays. When air is introduced, the current decays faster. Due to sensitivity to air or oxygen [Col58, Gur14], the photoconductivity has been related to either the photodesorption of adsorbed oxygen at the ZnO surface or oxygen vacancies. In the first scenario, adsorbed oxygen supposedly causes a depletion region at the surface by capturing electrons [Bao11]. There are doubts that enough oxygen could be adsorbed at the ZnO surface under vacuum conditions to allow for a conductivity rise on the order of hours [Gur14]. In the latter scenario, a continuous rise could be caused by the formation of more and more oxygen vacancies at the

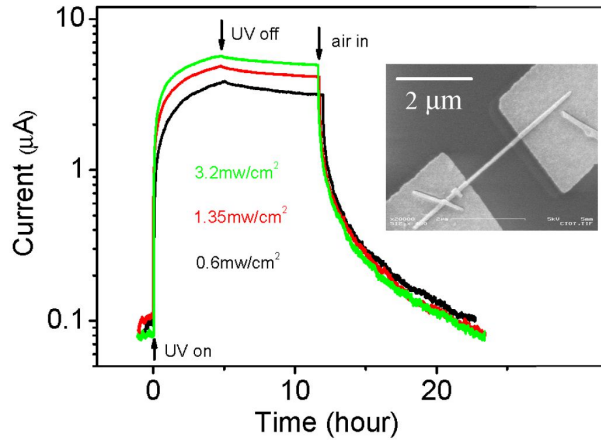


**Figure 2.10:** Persistent photoconductivity of a ZnO nanowire. The current between two electrodes (see inset) rises as a function of UV illumination time, the system is under vacuum. Stronger illumination leads to a larger rise of the current. When the light is switched off, the current is maintained and only decays on a time scale of hours, getting faster as air is provided. Adopted from [Bao11].

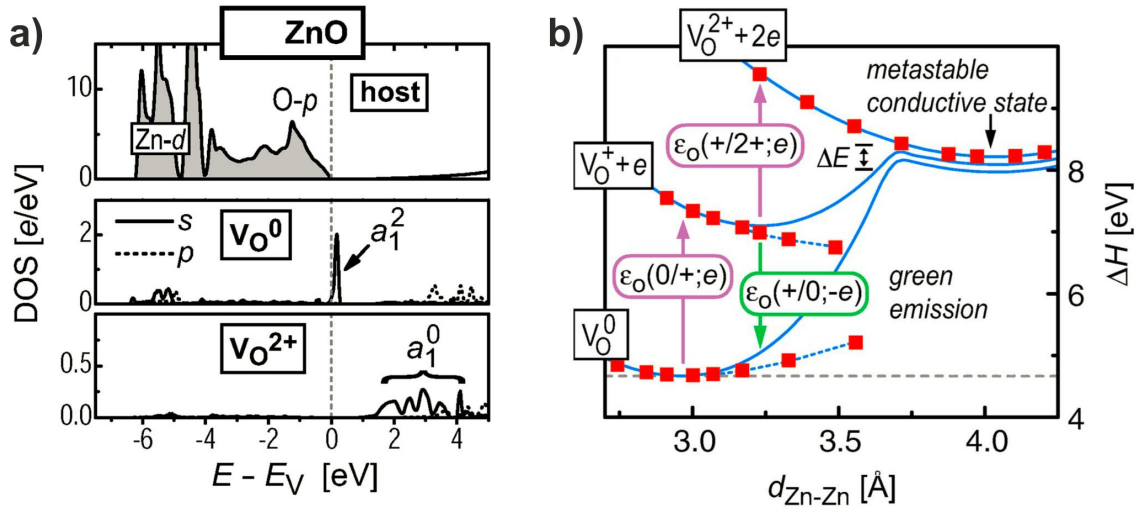
surface by photolysis. This is supported by X-Ray spectroscopy which shows that ZnO becomes Zn-rich after UV illumination [Gur14]. Furthermore, theory supports that the photoexcitation of the oxygen vacancies leads to persistent conductivity as described in the following.

Figure 2.11 shows DFT calculations by Lany and Zunger [Lan05, Lan07]. Figure 2.11 a) shows the calculated electronic density of states of ZnO, ZnO with a neutral oxygen vacancy and with the two-fold charged oxygen vacancy. The neutral oxygen vacancy induces an occupied state just above the VB maximum, i.e. it forms a deep donor, which is not ionized thermally<sup>4</sup>. Two-fold charging of the oxygen vacancy changes the density of states significantly, producing electronic states in the CB region, which were termed 'perturbed host states' by Lany and Zunger.

According to Lany and Zunger, PPC arises due to the one- and two-fold charging of the oxygen vacancy. Figure 2.11 b) shows the calculated formation energies for the one- and two-fold charged oxygen vacancy versus distance of the nearest neighbor Zn atoms. Two-fold charging leads to a distortion of the lattice, creating a thermal barrier that has to be overcome before the excited electron-hole pair can recombine. Lany and Zunger also note that the one-fold charged oxygen vacancy can lead to a defect exciton in the triplet configuration which then has a rather long lifetime<sup>5</sup>. Note that a different

<sup>4</sup>It should be noted that the calculated band gap is much smaller than the experimental band gap of 3.4 eV as a result of the local density approximation used for the DFT calculation in ref. [Lan05]. However, advanced DFT calculation using hybrid functionals confirm that the oxygen vacancy forms deep donor state just above the VB maximum [Pat06]

<sup>5</sup>The one-fold charged oxygen vacancy is supposedly also at the origin of luminescence at higher wavelength than the incoming photon (green luminescence), induced by a large Stokes shift due to the lattice



**Figure 2.11:** DFT calculations to explain persistent photoconductivity in ZnO. a) Electronic density of states of ZnO, ZnO with a neutral oxygen vacancy inducing an occupied state just above the VB maximum, and with the two-fold charged oxygen vacancy which creates states in the CB region. The energy axis is referenced to the VB maximum, the calculated band gap is 1.53 eV. b) Calculated formation energies of the one- and two-fold charged oxygen vacancy versus distance of the nearest neighbor Zn atoms. Adopted from ref. [Lan05].

research team, Janotti and van der Walle [Jan09] also showed that the lattice is locally distorted upon photoexcitation of the oxygen vacancy. Different to Lany and Zunger they deduced a thermal barrier of 0.3 eV also for the one-fold charged oxygen vacancy. They noted, however, that this thermal barrier might be too small to explain persistent photoconductivity at room temperature.

**Fine tuning the density of shallow donors in a semiconductor by photoexciting deep defects** Would photoexcited deep defects behave like shallow donors and undergo a Mott or Mott-Anderson SMT analogous to shallow donor dopants? This question was addressed by measuring the photoinduced conductivity change of another semiconductor, namely Si-doped Al<sub>0.3</sub>Ga<sub>0.7</sub>As [Kat87]. In this compound, the Si dopants form a deep level in the band gap and photoexcitation creates defect excitons with a very long lifetime.

Ref. [Kat87] tested by transport measurements if the material is metallic or not. Metallicity is characterized by a finite conductivity at 0 K. The experimental approach is to measure the conductivity as a function of temperature and then extrapolate to 0 K. This was done by ref. [Kat87] for different illumination times, which correspond to different defect exciton populations. Figure 2.12 shows the extrapolated zero-temperature

deformation as indicated in Figure 2.11 b). Indeed, the luminescence of ZnO in the visible can be most efficiently excited with wavelength that are in the UV, around 3.4 eV [Lei03]. Moreover, the luminescence decay of visible light after photoexcitation of ZnO across the band gap has a lifetime that exceeds the μs range [Fog19].

conductivity as a function of illumination time<sup>6</sup>. Only above a critical illumination dose, does the sample exhibit a finite zero-temperature conductivity. The conductivity then rise further, following a linear trend. The solid line is a fit with the critical form, equation 2.6, which matches the data perfectly with a critical exponent of  $\delta = 1$ . The trend of the conductivity thus follows the expectation from the Mott-Hubbard model. In addition to demonstrating the critical behaviour as a function of UV illumination dose, the authors also repeated the measurements in the presence of an applied magnetic field ( $H=0$  T and  $H=4$  T). The applied magnetic field is found to shift the threshold UV illumination dose to a lower value. This shift is explained by the magnetic field-induced shaping of the wave functions at the photoexcited impurity. As mentioned before in section 2.2.2, magnetic fields can also be used to tune through the Mott transition. This study thus gives evidence for a Mott or Mott-Anderson SMT using the defect exciton - shallow donor analogy.

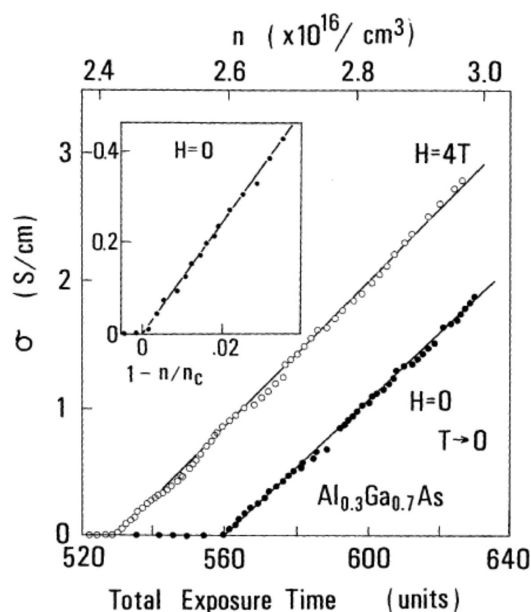


**Figure 2.12:** Mott-Anderson transition in Si-doped  $\text{Al}_{0.3}\text{Ga}_{0.7}\text{As}$  induced by UV illumination. Shown is the extrapolated zero-temperature conductivity versus UV illumination time. At a certain UV dose, the conductivity rises linearly. The solid line is a fit with the critical form expected from the Mott-Hubbard model, see text. From [Kat87].

**Open questions** Two questions related to the above are addressed within this thesis:

- What is the origin of the intrinsic n-type doping in ZnO? It has been long attributed to oxygen vacancies, but theory agrees in that the oxygen vacancy forms a deep

<sup>6</sup>One unit corresponds to an interval of 3 seconds of UV illumination. After each exposure interval the conductivity was measured as a function of temperature. This approach is possible because the lifetime of the defect exciton is immeasurably long in this case.

donor. If the model for PPC in ZnO by Lany and Zunger was correct, it would mean that at least under some sample conditions (those in which ZnO has been exposed to UV light), oxygen vacancies could still lead to an n-doping on a time scale of PPC [Lan07]. This question is tackled in section 5, where I show that photoexcitation generates a shallow donor-like state that is long-lived, with a component that decays within few tens of  $\mu\text{s}$  and a second, even longer lived component. The shallow donor-like state is confined to the ZnO surface. More of these shallow donor-like states are formed as the sample undergoes a UV illumination-induced change of the density of deep donor defects at the surface, which is concordant with the rise of PPC upon UV illumination reported in literature. Moreover, the results show that the state evolves from a spatially localized state into a metallic band with heavy effective mass at long UV exposures, indicative that a Mott-Anderson SMT takes place. It is concluded that ZnO is n-type *photodoped* at the timescales of PPC. This strongly supports the theory of Lany and Zunger for PPC.

- The photoexcitation of deep donor defects at the ZnO surface induces shallow donor-like states at the ZnO surface at times timescales of PPC. But what about ultrafast timescales? At which time scales would photoexcitation lead to an effect that is equivalent to chemical doping, i.e. a process carried out in thermodynamic equilibrium? In section 6.2 I will show using trARPES that photoexcited deep donors at the ZnO surface behave like shallow donor dopands already on femtosecond time scales after optical excitation. Due to the surface localization of the deep donors, photoexcitation induces transient downward band bending toward the surface, as observed for chemical doping, cf. section 2.2.3. While, at low fluence, surface-confined defect excitons are formed, the defect excitons undergo an Mott transition and form a photoinduced metal at the ZnO surface. The occupation of the metallic phase is governed by Fermi-Dirac statistics with respect to the equilibrium Fermi level. Moreover, the fluence-dependent measurement unveil that the effective mass diverges upon approaching the excitonic phase from the metallic phase. This is as predicted from the Mott-Hubbard model and has been observed for chemical doping, see section 2.2.2. While, an ultrafast time scale is actually expected for a Mott transition between photoexcited excitons, the finding that the photoexcitation of defect excitons at the ZnO surface acts in exact analogy to chemical doping with shallow donors already on femtosecond timescales is new. The ultrafast exciton Mott transition and the photoinduced electronic band structure changes that are expected to happen are reviewed in the next two sections.

### 2.3.4 Ultrafast exciton Mott transition

Already on timescales of exciton formation, i.e. femto to picoseconds, a Mott transition between excitons is expected to occur. In literature, the Mott-Hubbard model has also been applied directly to describe the system properties of such an exciton Mott transition [Gue19]. However, the typically used argument that excitons cease to exist at increasing photoexcitation fluence is based on the enhanced screening upon increasing the charge carrier density [Kli12] and not the tuning of bandwidth and electron repulsion. Screening reduces the electron-hole attraction. For the screened Coulomb potential (Yukawa potential)

$$U(r) = \frac{e^2}{4\pi\epsilon r} e^{-r\gamma}, \quad (2.9)$$

where  $\gamma$  is the screening length, it can be shown that no bound states exist in this potential anymore when

$$a_H\gamma > 1.19. \quad (2.10)$$

$a_H$  is the Bohr radius. In the Thomas-Fermi description of the screening length this gives then [Mot74]

$$n_c^{1/3} a_H \cong 0.4, \quad (2.11)$$

where  $n_c$  is the electron density. Remarkably, this estimate of the Mott criterion agrees very well with the estimate from the Mott-Hubbard model (equation 2.11, with the electron density instead of the doping density).

**Quasi-Fermi levels** While the doping-induced Mott transition happens in thermodynamic equilibrium, photoexcitation creates a non-equilibrium state of matter. If the carriers have thermal distribution, two quasi-Fermi levels can be introduced for the electrons in the CB and the holes in the VB [Kli12]. The quasi-Fermi level of the electrons in the CB does not coincide with the equilibrium Fermi level normally. Upon increasing the charge carrier density in the CB, the position of the quasi-Fermi level should shift to higher energy (Burstein-Moss shift). Thus a metal-like state is formed that would have different transport properties than an equilibrium metal, see the introduction to this thesis. However, band structure changes (see the succeeding section 2.3.5) can shift the position of the CB, and thus also the position of the quasi-Fermi level on the absolute energy scale.

**Experimental observation of the ultrafast exciton Mott transition** The exciton Mott transition is frequently studied with optical spectroscopy. Upon strong photoexcitation, a broad photoluminescence feature below the fundamental gap emerges<sup>7</sup>, which is attributed to emission from an electron-hole plasma. Furthermore, optical gain is ob-

---

<sup>7</sup>It appears below the fundamental gap due to band gap renormalization

served above a certain threshold fluence, indicating population inversion in the CB and VB [Kli12]. At the same time, in reflectivity/absorption spectroscopy, the exciton resonance below the fundamental becomes broadened and its amplitude is reduced. This is nicely demonstrated in strongly photoexcited monolayers and bilayers of the transition metal dichalcogenide  $\text{WS}_2$  [Che15]. In these ultrathin semiconductor layers, the Coulomb interaction between electron and holes is screened less efficiently than in bulk semiconductors, giving rise to large exciton binding energies. The change of screening via photoexcitation has gigantic effects on the band positions and leads to strong changes of the amplitude and width of the exciton resonance. At elevated photoexcitation densities, the resonance disappears completely and only optical gain at lower photon energies remains.

In general, the screening-induced changes to the optical spectra is overlaid with the photoinduced absorption changes due to photoexcited electrons in the bands and excitonic states, thereby blocking initial/final states (Pauli blocking) and inducing optical gain [Che15, Ric20], with possible ambiguities in the data interpretation [Ric20]. One way to overcome this issue is to use THz spectroscopy, where the probe photon energy is on the order of few meV, so that excitons can be probed by intra-excitonic transitions. The optical response is then contrasted to the Drude response of an electron-hole plasma. Already in early studies using THz spectroscopy of GaAs upon ultrafast photoexcitation above the Mott density [Hub01] it was shown that photoexcited electrons form an electron-hole plasma with a collective plasmon oscillation on a time scale of 100 fs. Recently, Sekiguchi et al. [Sek17] used THz spectroscopy to investigate the crossover between excitons and an electron-hole plasma in GaAs using photoexcitation resonant with the 1s exciton state at different fluences. The 1s to 2p-transition in the THz spectra vanishes in favor of a broad response that can be described with the Drude model of free carriers. The authors reported that the effective mass of the free carriers increases with increasing charge carrier density, and so does the scattering rate, contrary to predictions from Fermi-liquid theory. The increase of the effective mass is also in contrast to the expectation from tight-binding theory, such as the Mott-Hubbard model and the phase has hence been termed an anomalous metal phase by Sekiguchi et al.

THz spectroscopy cannot resolve the absolute position of the electronic energies, i.e. band positions and quasi-Fermi level with respect to the equilibrium Fermi level. For this, trARPES can be used. The exciton Mott transition has been addressed very recently in a  $\text{WSe}_2$  bulk crystals using soft-x-ray probe photons and a strong pump photon energy tuned to the exciton resonance. The experimental setup allows the simultaneous measurement of the photoinduced changes of the core-level photoemission spectra together with the population dynamics in the conduction band with femtosecond time resolution [Den20]. Based on a model to describe the core-level line shape, the contributions of excitons and electrons of the excited state population in the CB were disentangled. The authors con-

clude that resonant photoexcitation populates excitons nearly instantaneously, and within about 100 fs, an electron-hole plasma is formed in a continuous transition.

**Mahan excitons** Even above the Mott limit, weakly bound excitonic states may exist due to non-local many-body interactions (so-called Mahan excitons) [Mah67, Sch11]. Experimentally, this has been tested using optical pump-probe spectroscopy, where the pump creates a large density of photoexcited carriers, and the probe monitors how the optical response changes. A spectral feature attributed to excitonic enhancement was indeed detected above the (calculated) Mott density for different systems recently, including ZnO [Ric20, Pal20].

**Open questions** Experiments agree in that excitons undergo a transition to a metal-like phase on a femtosecond timescale. The properties of this photoinduced phase are, however, still far from completely understood as exemplified with the finding of the anomalous metal phase in GaAs by Sekiguchi et al. In the particular case of ZnO, because of the observation of an exciton resonance in optical spectroscopy even well above the Mott density, Richter et al. [Ric20] even doubted that an electron-hole plasma would be generated at all in ZnO.

In this thesis I identify a Mott transition in ZnO. It occurs between defect excitons in ZnO as mentioned in the preceding section. The Mott transition is addressed by fluence-dependent trARPES measurements in section 6.1.3, which unveil the evolution of localized electronic states into a metallic band at a threshold photoexcitation density. This shows that an electron-hole plasma is indeed formed in ZnO. As detailed in section 6.1.5 it is generated on a time scale of 20 fs and decays within few hundred ps. Remarkably, despite the fast time scale the quasi-Fermi level of the metallic phase equals the equilibrium Fermi energy. A quasi-Fermi level equal to the equilibrium Fermi level requires a photoinduced band structure change of the electronic band structure in addition to the exciton Mott transition. Possible band structure changes in conventional semiconductors are band gap renormalization and surface photovoltage effects, as described in the next section.

### 2.3.5 Photoinduced changes of the electronic band structure

The dynamics of photoexcited charge carriers cannot be analyzed with respect to a rigid electronic band structure, as the latter itself can be changed. In semiconductors such as ZnO, band gap renormalization or and photovoltage effects are considered [Ric20, Spe13]. The situation becomes more complex in strongly correlated materials. Changes of the equilibrium band structure are required to generate a real photoinduced SMT with density of states at the equilibrium Fermi energy as opposed to a metal-like state, as outlined in the introduction to this thesis.

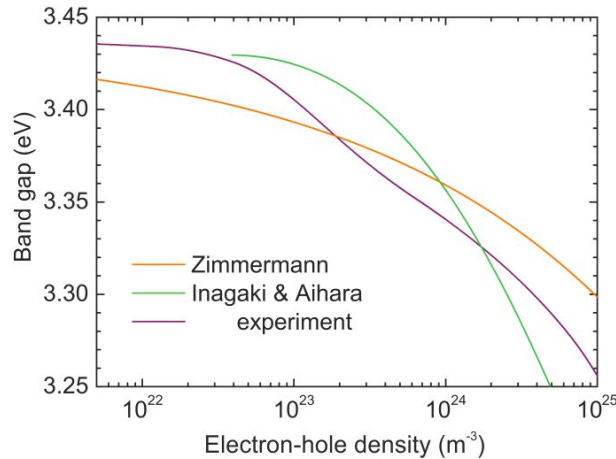


**Figure 2.13:** Band gap renormalization of ZnO, derived from photoluminescence data and compared to theoretical results. From [Ver12].

**Band gap renormalization** The non-equilibrium occupation of electronic states can reduce the fundamental gap of a semiconductor, shifting the VB and CB toward each other. Band gap renormalization has been observed directly using trARPES in different semiconductors [Liu19, Mor17, Pup17]. Inferring band gap renormalization from optical data is challenging, because band gap renormalization lowers the optical transition energy of the exciton while screening of the electron-hole interaction increases it. Moreover, band filling shifts the absorption onset to higher energies (the above mentioned Burstein-Moss shift), which also counteracts the effect of band gap renormalization [Kli12]. For ZnO, Figure 2.13 shows experimental data obtained inferred from photoluminescence data, compared to theoretical results [Ver12]. According to Figure 2.13, band gap renormalization becomes appreciable at high electron-hole densities above the Mott density, which is expected to be in the range of  $10^{23}$  to  $10^{25} \text{ m}^{-3}$  according to different theoretical and experimental studies [Kli12].

An interesting question is, if band gap renormalization can be used to create a transient metal as opposed to a metal-like semiconductor in the manner defined in the introduction to this thesis. In GaAs the band gap completely collapses upon strong photoexcitation at several 10's of  $\text{mJ}/\text{cm}^2$  fluence [Hua98]. This then means that there *must be* density of states at the equilibrium Fermi level. However, the required photoexcitation fluence is close to or above the damage threshold of the material [Hua98]. To my knowledge, this is the only photoinduced *ultrafast* SMT in conventional semiconductors, which are not strongly correlated.

**Surface photovoltage effects** Section 2.2.3 introduced band bending at semiconductor surfaces in the context of surface metallization. In this case, downward band bending is

caused by shallow donors which build a layer of positive charges at the surface. Even on a clean semiconductor surface, surface states can exist as the lattice is abruptly truncated [Zha12]. Surface states at semiconductor surfaces can generally cause upward or downward band bending, depending on whether they are positively charged or negatively charged [Zha12, Stä16]. If such band bending exists, the generation of electrons and holes in the CB and VB upon cross band gap photoexcitation leads to a rigid band shift by diminishing the band bending. This is the so-called surface photovoltage (SPV) effect. The inverse effect is also known: By direct photoexcitation of surface states, surface charges can be generated and the band bending can be enhanced. This is called photovoltage inversion [Kro99].

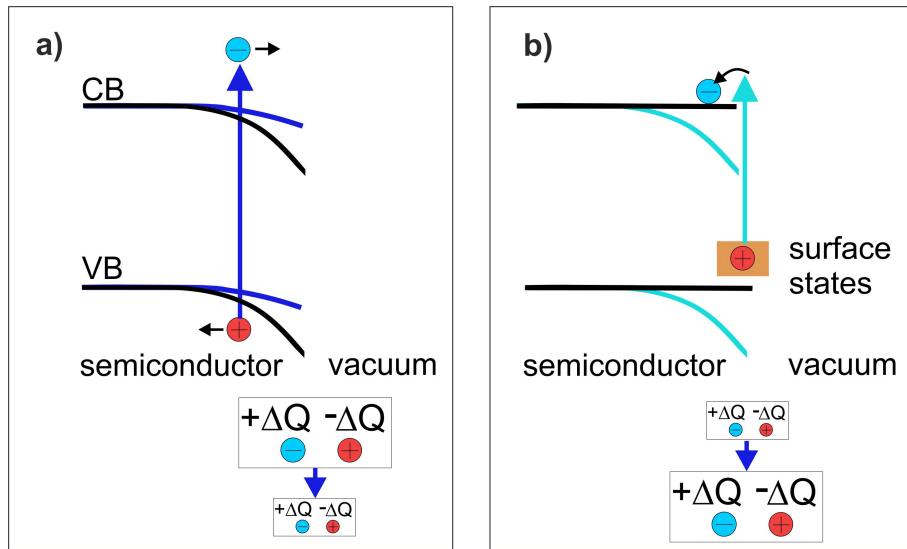


**Figure 2.14:** Surface photovoltage and photovoltage inversion. a) Surface photovoltage: If band bending in equilibrium exists due to charge transfer between surface and bulk (here displayed: downward band bending), photoexcited carriers are spatially separated. This diminishes the pre-existing charge transfer and hence the band bending. b) Photovoltage inversion: If surface states are photoexcited directly, the band bending can be enhanced. Displayed is the case, where photoexcitation depletes occupied in-gap states and the electron is excited into the CB. Provided that electron and hole are separated spatially, this generates (or enhances pre-existing) downward band bending.

Figure 2.14 illustrates these two cases. In Figure 2.14 a) it is assumed that downward band bending in equilibrium exists due to charge transfer from surface states into the bulk. Upon photoexcitation across the band gap, the photoexcited holes in the VB are driven into the bulk, and the electrons in the CB are driven to the surface. Thus, the surface is charged negatively with respect to the equilibrium and the pre-existing charge transfer is diminished. For strong enough photoexcitation, the initial positive surface charge would be compensated completely, yielding flat bands.

Figure 2.14 b) shows how band bending can be generated by photoexcitation. The

photodepletion of surface states charges the surface positively with respect to the equilibrium, thereby causing downward band bending. Also upward band bending could be reached by populating previously unoccupied surface states. For this case, no band bending in equilibrium is required. Assuming that these surface states lie within the band gap, this process also works with below band gap photoexcitation.

Both effects have been used for the characterization of semiconductor surface and interfaces: Analyzing the SPV as a function of doping density, temperature, photon energy or other parameters yields information of the equilibrium band bending, the energetic position of doping- or adsorbate induced electronic states, the band gap itself and other properties like carrier diffusion length [Kro01].

It should be noted that the band shifts induced by SPV also happens very fast: Yang et al. [Yan14] reported an upward shift of the CB and VB in GaAs due to surface photovoltage using time-resolved photoelectron spectroscopy. The bands shifted upward within a time scale faster than the time resolution of the experiment (160 fs). Rettig et al. [Ret12] employed time-resolved photoelectron spectroscopy to measure the dynamics of an occupied in-gap state induced by a metal overlayer at the Si surface. Below a certain photoexcitation fluence, SPV occurs and diminishes pre-existing band bending until flat bands are reached. In flat band conditions, an ultrafast downward shift and relaxation of the in-gap state was observed. Since the in-gap state is derived from Si states and its position relative to the band edge was assumed as fixed, the downward shift was interpreted as a result of the photoinduced creation of downward band bending by the photodepletion of the in-gap state.

**Strongly correlated materials** Apart from conventional semiconductors, much research has been carried out in the field of so-called strongly correlated materials. The term strongly correlated is used for materials, in which electrons cannot be regarded as free (such as in ideal metals), but the interaction between electrons and other quasiparticles is considerable. This can lead to isolating behaviour instead of conducting behaviour. For example, in some metal oxides such as NiO, an insulating state results due electron-electron repulsion of the electrons in the highest occupied atomic orbitals. The electronic wave functions are strongly localized and thus, the Mott-Hubbard model predicts that two bands are formed (the lower and the upper Hubbard band), one of which is fully occupied. This is as for the doping-induced SMT introduced in section 2.2.2. In such a system, the band structure can be changed by photoexcitation, via heating the lattice or by other changes of the system parameters, e.g. the number of free carriers. If such a system is at the verge of a phase transition in equilibrium, it is an appealing idea that photoexcitation could trigger a photoinduced phase transition (PIPT) [Bas11].

Indeed, such PIPTs, including SMTs can be induced in many inorganic and organic

materials. A canonical example is the photoinduced SMT in  $\text{VO}_2$ . A SMT in  $\text{VO}_2$  can be induced by changing the temperature of the system, and the transition temperature is only slightly above room temperature. By photoexcitation, time-resolved photoelectron spectroscopy has revealed the rise of density of states at the equilibrium energy within less than 50 fs. This has been attributed to a band gap collapse induced by the screening of photogenerated carriers [Weg14b, Weg15]. Because the phase transition requires high laser fluence on the order of few  $\text{mJ}/\text{cm}^2$ , the lattice becomes heated up considerably and the transient metallic phase stabilizes for a time scale on the order of nanoseconds [Wen13]. Notably, PIPs typically require such strong laser fluence in inorganic materials, for a review see [Bas11, Gia16].

**Open questions** Changes of the electronic band structure can be photoinduced in conventional (not strongly-correlated semiconductors) via band gap renormalization and surface photovoltage effects. At which fluence would the photoexcitation be effective and which of both effects would prevail in ZnO? I will show in section 6.2.3 that, for vacuum-annealed ZnO, the photoexcitation of deep defects localized at the ZnO surface leads photovoltage inversion and that this band structure change is very large: It exceeds band gap renormalization by far and, at a fluence of few  $\mu\text{J}$  only, the CB at the ZnO surface is bent below the equilibrium Fermi energy. Combined with the low threshold density to undergo a Mott transition, a low-fluence SMT at the ZnO surface results.

### 2.3.6 Summary

In summary, the conceptual description of excitons as extended hydrogen atoms is alike to that of shallow donor dopants. Consequently, like shallow donor dopants, excitons are expected to undergo a transition into a metal-like state which is referred to as exciton-Mott transition. The Mott transition between free excitons is however, different from chemical doping by two aspects: Firstly quasi-Fermi levels are formed in the photoexcited state that do not normally coincide with the equilibrium Fermi energy. Secondly, free excitons are mobile. This also means that metallization confined to the surface of a bulk crystal would be impossible. Defect excitons form the most direct analogy to chemical doping. They are supposedly at the origin of persistent photoconductivity, which occurs amongst other semiconductors in ZnO and a Mott SMT using persistent photoconductivity has been demonstrated, yet not on the ultrafast time scale.

After having established this basis, the next chapter will introduce the experimental tools, i.e. trARPES, the UHV environment and the data acquisition schemes. Chapter 4 then present a newly developed mathematical framework that is needed to understand how long-lived states could be recognized in experiments with pulsed laser excitation and

what their contribution in pump-probe experiments would be. This is necessary, because a long-lived electron population will be revealed in chapter 5. This long-lived state is likely intimately related to persistent photoconductivity in ZnO, and shows indeed similarity to a shallow donor state. Finally in chapter 6, the ultrafast photoresponse of ZnO above the Mott threshold will be investigated.

## 3 Experimental techniques and setup

### 3.1 Photoelectron spectroscopy

ARPES is a well-established tool to investigate the electronic band structure of crystalline solids based on the photoelectric effect.

#### 3.1.1 Concept

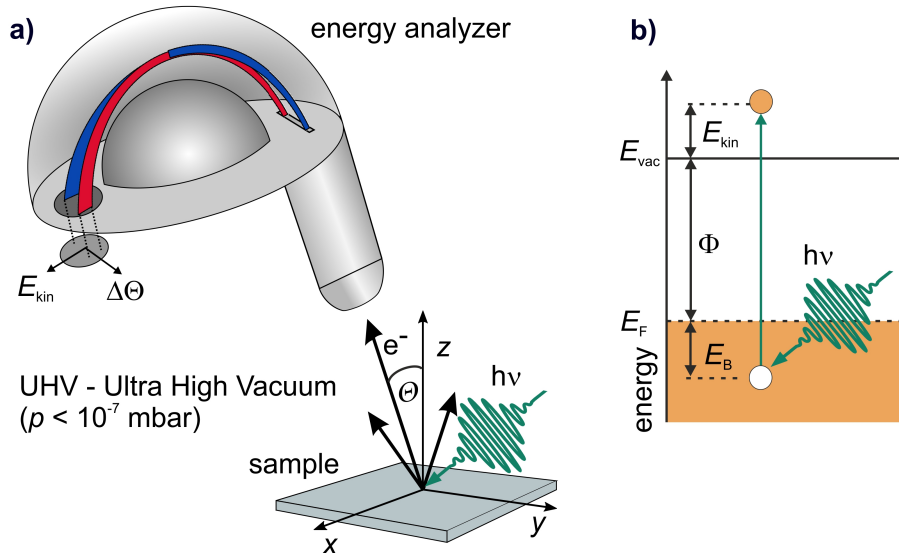


**Figure 3.1:** The concept of ARPES. a) Photoemission of electrons and detection with a hemispherical analyzer. b) Basic energy level diagram. The Fermi energy  $E_F$  separates occupied electronic (yellow filled box) from unoccupied states. When electrons from states with a certain binding energy  $E_B$  are photoexcited above the vacuum level  $E_{vac}$  they can leave the sample. The difference between  $E_{vac}$  and  $E_F$  is the work function  $\Phi$ . The excess energy of excited electrons with respect to  $E_{vac}$  is the kinetic energy  $E_{kin}$ .

The concept of ARPES is shown in Figure 3.1. An incoming photon emits electrons from the sample, if the photon energy  $h\nu$  is larger than the work function  $\Phi$ . These photoelectrons are analyzed with respect to their kinetic energy  $E_{kin}$  (referenced to the vacuum level  $E_{vac}$ ) and emission angle with a spectrometer. Displayed here is a hemispherical energy analyser such as used for the present thesis. The energy of the photon determines if electrons are removed from core levels (X-ray photoelectron spectroscopy) or from energy levels close to the Fermi energy  $E_F$ , i.e. from the valence and conduction bands. An intuitive description of the photoemission process is given by the three-step-model [H95, Rot10, Dam04]:

1. In the **first step** electrons in occupied states  $|\Psi_{ini}\rangle$  (Bloch states with energy  $E$  and wavevector  $\mathbf{k}$ ) close to the surface are excited by photons with energy  $h\nu$  into

an unoccupied final state  $|\Psi_{\text{fin}}\rangle$ . The transition probability is within perturbation theory given by Fermis golden rule [Dam04]:

$$s = |\langle \Psi_{\text{fin}} | \mathbf{A}(\mathbf{r}) \cdot \mathbf{p} | \Psi_{\text{i}} \rangle|^2 \delta(E_{\text{fin}} - E_{\text{ini}} - h\nu) \quad (3.12)$$

Final and initial states are coupled through the product of vector potential  $\mathbf{A}$  of the photon and the impulse operator  $\mathbf{p}$  of the electron. The delta function ensures the energy conservation in this step. Since the impulse of a photon is small in comparison to the Brillouin zone this is a direct transition (in the reduced zone scheme), i.e.

$$\mathbf{k}_{\text{fin}} \approx \mathbf{k}_{\text{ini}}$$

2. In the **second step** the propagation of the electron through the crystal to the surface is considered. Here, electrons can be absorbed or be (in-)elastically scattered, which leads to a tail of so called secondary electrons, which have lost the information of the initial state. Besides forming a background signal accumulating at low kinetic energies, which needs to be dealt with when looking at spectroscopic signatures, these electrons can be used to determine the work function of the system, as will be shown later. Note that the mean free path of electrons is short. Depending on their kinetic energy it amounts to few nanometers, which makes ARPES a surface sensitive technique [Dam04, Dei16].

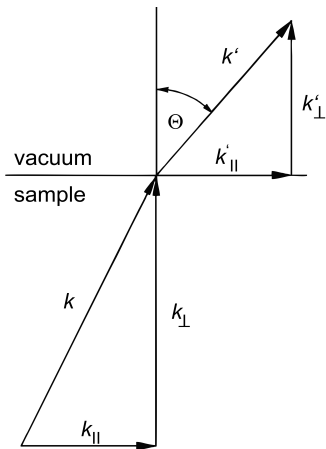


**Figure 3.2:** Transmission of the electron through the surface.

3. In the **third step** the transmission through the surface is described, which leads to a change in the component of the  $\mathbf{k}$  vector perpendicular to the surface,  $k_{\perp}$ . The components parallel to the surface,  $k_{\parallel}$ , are conserved because no breaking of the translational symmetry occurs. Simple trigonometry (Fig. 3.2) with the dispersion relation for free electrons  $E_{\text{kin}} = \frac{\hbar^2 k'^2}{2m_e}$  yields:

$$k_{\parallel} = \frac{1}{\hbar} \sqrt{2m_e E_{\text{kin}}} \sin \Theta \quad (3.13)$$

where the angle  $\Theta$  is defined as in Fig. 3.1.

For the whole process we have (see Fig. 3.1 b):

$$E_{\text{B}} = h\nu - E_{\text{kin}} - \Phi \quad (3.14)$$

where  $E_{\text{B}} > 0$  is the binding energy with respect to the Fermi energy  $E_{\text{F}}$ . For certain cases, e.g. for surface states or in two-dimensional systems, the electron dispersion does not have a  $k_{\perp}$

dispersion[Dam04]. For those cases, it is sufficient to know about  $E_B(k_{\parallel})$ . Otherwise, for a full determination of the bandstructure the component  $k_{\perp}$  has to be determined. One approach is to assume free electron states for the final state  $|\Psi_{\text{fin}}\rangle$  inside the crystal, since the potential of the crystal ions should be only a minor perturbation for high energies. Then the kinetic energy  $E_{\text{kin,int}}$  inside the crystal can be written down:

$$E_{\text{kin,int}} = \frac{\hbar^2(k_{\parallel}^2 + k_{\perp}^2)}{2m_e} - E_0$$

where  $E_0$  is an unknown offset. The kinetic energy outside the crystal  $E_{\text{kin}}$  is related via the work function

$$E_{\text{kin,int}} = E_{\text{kin}} + \Phi$$

$$\Rightarrow k_{\perp} = \sqrt{\frac{2m_e}{\hbar^2}(E_{\text{kin}} + V_0) - k_{\parallel}^2}$$

with the so called 'inner potential'  $V_0 = E_0 + \Phi$ , which can be determined by measuring at normal emission (i.e.  $k_{\parallel} = 0$ ) and varying the photon energy  $h\nu$  (thus varying  $E_{\text{kin}}$  and, in turn,  $k_{\perp}$ ). From the periodicity upon traversing one (or several) full Brillouin zone(s) in  $k_{\perp}$  direction, one can determine  $k_{\perp}$ . Such measurements can be carried out using synchrotron radiation. An exemplary measurement of a metal surface (Al(001)) is presented in Figure 3.3. The binding energy of the observed valence band oscillates periodically as a function of photon energy due to the momentum conservation rule (step 1). A non-dispersive (in  $k_{\perp}$ ) surface state is also observed.

For the measurements done in this thesis a table top laser source was used, yielding a photon energy of maximally 6.3 eV (described in detail in chapter 3.2.1). For such low photon energies the free electron final state assumption is questionable, and rather, so called 'inverse-LEED' states should be consid-

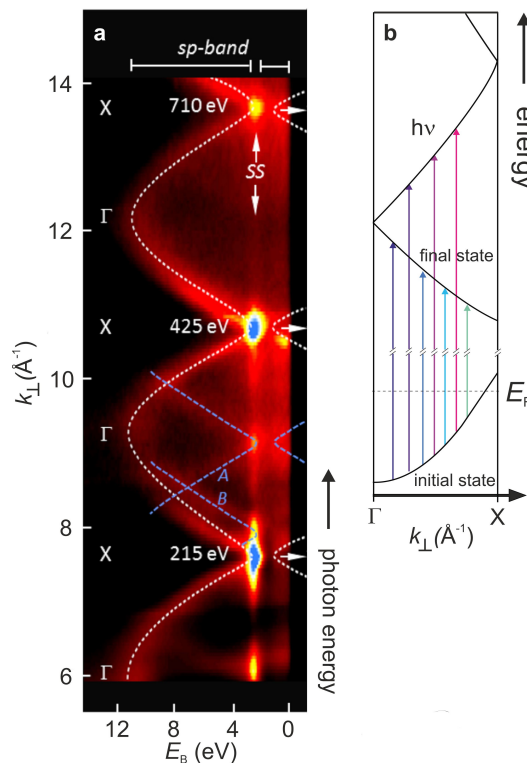


**Figure 3.3:** a) Exemplary measurement of the  $k_{\perp}$  dispersion via a photon energy dependence of Al(001). From [Hof02]. b) Sketch of the momentum conservation rule in the reduced zone scheme, when one free electron final state is available.

ered, which are free electron-like states in the vacuum, decaying into the crystal (and coupling to the intrinsic electronic structure). This concept refers to the '1-step-model' of photoemission, treating the photoemission as a single coherent step [H95, Weg14a]. In ref. [Sch08], low photon energy band structure data is compared to high photon energy data giving satisfactory results.

Using low photon energies one cannot easily measure how  $E_B(k_{\parallel}, k_{\perp})$  varies as a function of  $k_{\perp}$ . In fact, the momentum conservation with respect to  $k_{\perp}$  in step 1 is relaxed in the photoemission process, such that one measures the dispersion  $E_B(k_{\parallel}, k_{\perp})$  integrated over several  $k_{\perp}$  at a single photon energy. Firstly, due to the surface sensitivity of photoemission through the short electron mean free path, final states that contribute to the photoemission process (step 1) are spatially confined. This leads to an intrinsic broadening in  $k_{\perp}$  of the final state by the uncertainty principle [Str03, Ros01, Mil01]. Thus, for an initial state which is dispersive in  $k_{\perp}$  direction, several transitions are possible for a given  $k_{\parallel}$ , which in turn leads to an broadening of the kinetic energy distribution. Initial states with no  $k_{\perp}$  dispersion (i.e. 2D states, surface states) do not exhibit 'final state broadening' and are usually much sharper [Mil01]. Secondly, such broadening also occurs when several final states are available, or when final state and initial state disperse in parallel with respect to  $k_{\perp}$  [Rot10].

Note that, according to equation 3.13, the range of the  $k_{\parallel}$ -Brillouin zone that can be accessed depends on the photon energy. If the analyzer detects a certain cone of photoemitted electrons, the range of momenta contained within the cone becomes smaller as the kinetic energy of photoelectrons is lowered.

### 3.1.2 Measurement of the workfunction

Photoelectron spectroscopy can be used to determine the work function, which an electron has to overcome in order to leave the sample. This energy barrier is governed by the surface dipole due to the 'spill out' of electron density upon truncation of the bulk forming the surface. Additionally, an electron feels the attractive image potential arising from a charge in front of a polarizable surface [Stä16, Zhu04, Wan97]. The energy barrier is short ranged, on the order of nanometers [Chu99]. The work function is an important quantity, which governs the onset of electron emission at free surfaces, and is used to predict and understand the energetics of interfaces [Koc07].

The measurement of the work function is performed via the low-energy cutoff of the photoemission spectrum. Figure 3.4 sketches a photoemission spectrum from a semiconducting sample. Assuming that the transition probability (equation 3.12) is the same for all accessed occupied states and that a broad continuum of final states is available, the photoemission intensity resembles the density of states of the occupied electrons. The photoemission is possible up to a certain binding energy only, as indicated by the dashed

line in the valence states. Photoelectrons arising from a state with this binding energy have initially zero  $E_{\text{kin}}$  (cf. equation 3.14).

As indicated in the sketched photoemission spectrum, one usually observes an increasing intensity towards the low-energy cutoff, which does not relate to the density of states within the sample. This is because a large part of the photoelectrons with low  $E_{\text{kin}}$  is not constituted by **primary** electrons, but inelastically scattered **secondary** electrons, which have lost energy during the travel to the surface. This is why the low-energy cutoff is named secondary edge (or secondary tail) [Cah03]. From Figure 3.4 one can infer that the width  $b$  of the spectrum, consisting of the fastest electrons arising from the Fermi energy  $E_F$ , and the secondary edge is equal to  $b = h\nu - \Phi$ . Therefore, the width can be used to infer  $\Phi$  if  $h\nu$  is known. To determine  $b$ , for a semiconducting sample,  $E_F$  normally needs to be determined from a metal in electrical contact with the sample, e.g. the sample holder. Once  $E_F$  is known (and the sample does not get charged with respect to the metal reference), a change of the position of the secondary edge relates to a change of the work function. This type of measurement, i.e. taking photoelectron spectra under different conditions that change the work function, is performed in several instances in this thesis. It should be noted that photoelectrons with initially zero  $E_{\text{kin}}$  can also be measured, because the measured kinetic energy is not equal to the initial kinetic after photoemission. Instead, it depends on the electric fields that exist between sample and analyzer, as will be reviewed in the next section.

For samples with a homogeneous surface, the work function introduces a sharp cut in the photoelectron spectra, which can be viewed as a step function in energy [Stä16]. The resulting low-energy cutoff or secondary edge is then broadened solely due to the finite resolution of the electron analyzer, and the width can therefore be used to determine the latter. In the present experiment the so-determined energy resolution of the analyzer is 30-50 meV.<sup>8</sup>

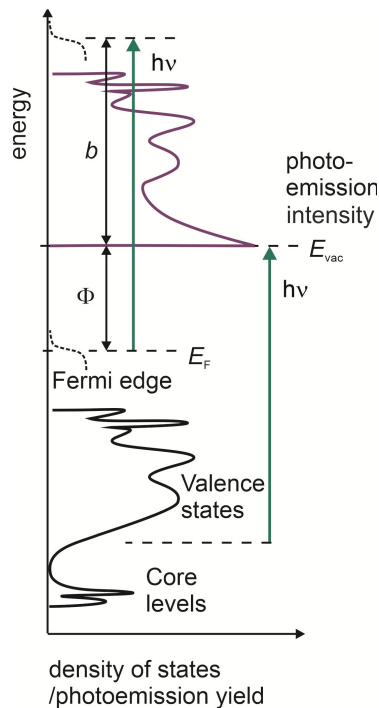


**Figure 3.4:** Photoemission from a semiconducting sample. Electrons are photoemitted when they are excited above  $E_{\text{vac}}$ . Adopted from [Cah03].

<sup>8</sup>This results from fitting a Gaussian function convoluted with a step function to the secondary edge. The given value corresponds to the full width half maximum of the Gaussian function. Note that the light source also contributes to energy broadening of any feature *beside* the secondary edge, cf. section 3.2.2.

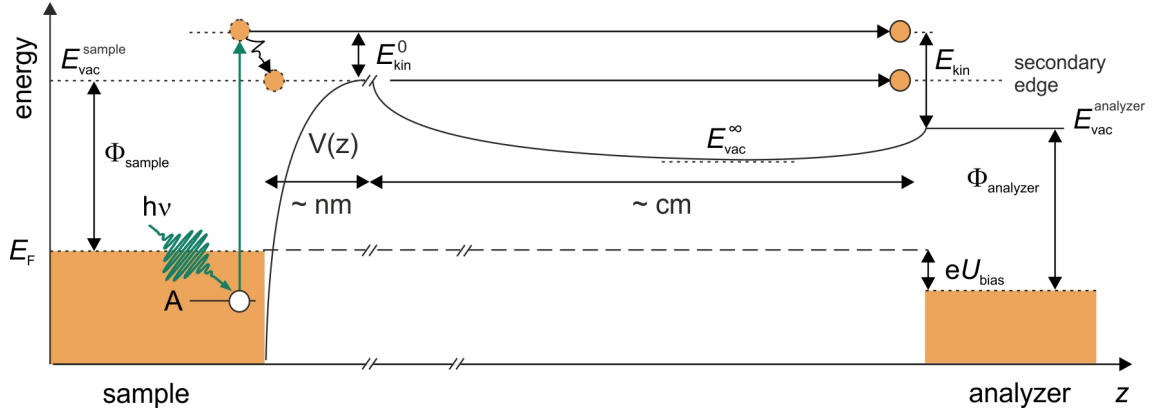


**Figure 3.5:** Energy level diagram of a metal surface and the electron analyzer illustrating the electrostatics involved in the detection of photoemitted electrons.  $V(z)$  denotes the potential energy due to image potential and surface dipole. The Fermi level is the same across the system, unless a bias  $U_{\text{bias}}$  is applied. Note that, to simplify the sketch, the potential as a function of  $z$  due to the bias is not drawn. Primary electrons (from an occupied state A) and secondary electrons with initially  $E_{\text{kin},0} = 0$  are emitted from the sample. The measured kinetic energy of the secondary electrons (the secondary edge) is not zero anymore. Adopted from [Cah03].

### 3.1.3 Fields between sample and analyzer - part 1

This section is devoted to the electrostatics between sample and analyzer, which influence the measured kinetic energy of the photoelectrons. As will be detailed in a second part on this topic, section 3.1.5, photoexcitation can change this electrostatic field landscape with consequences for static as well as pump-probe spectroscopy. The following is the basis to understand these effects, which are also observed in the present thesis. The section is based on a review by Cahen and Kahn [Cah03].

Figure 3.5 shows an energy level diagram of a metal surface and the electron analyzer, where the bottom axis is the position along the surface normal. The analyzer-sample distance is typically on the order of cm, while the energy barrier due to the surface dipole and the image potential, denoted as  $V(z)$ , is on the order of nm, as mentioned in the last section. Upon overcoming this barrier, photoelectrons are emitted from the sample and have a kinetic energy of  $E_{\text{kin}}^0$  determined from the energy conservation (equation 3.14), but they are not measured at this point. Instead, they have to propagate to the analyzer, where they experience acceleration or deceleration according to the electrical fields in between sample and analyzer. At first, the photoemitted electrons experience an accelerating field due to the already mentioned surface dipole: The surface dipole is oriented such that the negative charge points outwards and pushes the electrons away. The length scale of the decay is on the order of the sample size (i.e. usually mm to cm), as can be estimated by approximating the sample by a disk with the radius  $R$  with uniform point dipole density  $D$ [Zhu04]. For the case of the electron on the center axis and at a distance  $z$  from the

surface, the potential energy is:

$$V_D(z) = -\frac{eD}{2\epsilon_0} \left(1 - \frac{z}{\sqrt{R^2 + z^2}}\right) \quad (3.15)$$

The potential energy reaches zero as  $z \gg R$ . Then the electrons (hypothetically) reach the field-free regime, i.e. the vacuum level at infinity  $E_{\text{vac}}^\infty$ . The analyzer itself also has a surface dipole and an associated vacuum level  $E_{\text{vac}} = E_{\text{vac}}^{\text{analyzer}}$ . Upon approaching the analyzer, the electrons have to overcome this field. Eventually, the kinetic energy of the photoelectron is given by the electron energy with respect to the analyzer vacuum level  $E_{\text{vac}}^{\text{analyzer}}$ . The kinetic energy of the photoelectrons after propagation to the analyzer is

$$E_{\text{kin}} = \underbrace{h\nu - \Phi_{\text{Sample}} - E_{\text{B}}}_{E_{\text{kin}}^0 \text{ from equation 3.14}} + \underbrace{(\Phi_{\text{Sample}} - \Phi_{\text{Analyzer}}) + eU_{\text{bias}}}_{\text{kinetic energy change after propagation}} \quad (3.16)$$

Here,  $eU_{\text{bias}}$  is the kinetic energy change from an additional applied bias. This shifts the Fermi energy by  $eU_{\text{bias}}$ , and thus the vacuum level, as indicated in Figure 3.5. From the above energy consideration it follows that the kinetic energy of the measured photoelectrons is determined by the analyzer work function. The sample work function  $\Phi_{\text{sample}}$  cancels out in equation 3.16. With respect to the determination of binding energies by the photoemission setup, it should be noted that electrons constituting the Fermi edge undergo the same kinetic energy change as all other electrons. As all spectral features are shifted rigidly on the energy axis, the determination of peak positions *with respect to* the Fermi edge still contains the information on the binding energy of the primary electrons. Thus, for determination of the binding energy, one has just to determine the position of the Fermi edge in the spectrum. For a metal sample, the Fermi edge can often be distinguished directly from the spectrum. In case of a semiconducting sample with vanishing density of states at  $E_{\text{F}}$ , the Fermi edge needs to be determined from a metal that is in electrical contact with the sample surface, e.g. the sample holder.

Note that, according to equation 3.16 the kinetic energy change  $E_{\text{kin}} - E_{\text{kin}}^0$  after propagation is net negative if the analyzer work function is higher than the sample and  $eU_{\text{bias}}=0$ . Therefore, slow electrons, especially those with  $E_{\text{kin}}^0 = 0$  would not arrive at the detector. Amongst other low-energy features that might get lost in the spectrum, the low-energy cutoff in the measured spectrum would not yield information on the sample work function. To circumvent this, a bias has to be applied, which creates an additional potential accelerating the photoelectrons. It should be noted that at high bias values the angular dependence of the photoelectrons is distorted [Dei11], and thus, low bias values (maximally 1.5 V) are generally used throughout this work, unless otherwise specified.

As will be explained in section 3.1.5, the spectral positions of both, primary and secondary electrons can change in a non-trivial way, when the electrostatic fields are changed

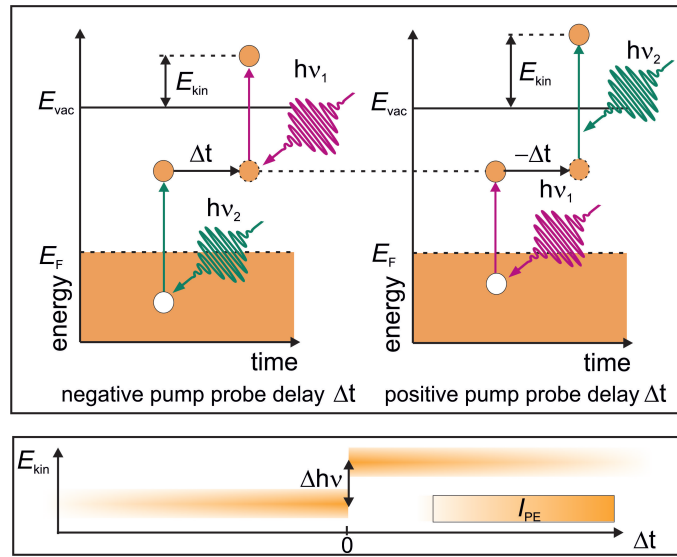


**Figure 3.6:** Concept of time-resolved 2PPE. a) Time-resolved 2PPE exploits the pump-probe principle. Two laser pulses are time-delayed to each other by  $\Delta t$ . The first pulse populates the intermediate state, the second excites the electron above  $E_{vac}$ . By scanning the pump-probe delay the lifetime of the electron population in the intermediate state can be measured. Dynamics towards both, positive delays and negative delays arises if both laser pulses can populate and monitor the intermediate state, as in the given example. The photoemission intensity as a function of pump-probe delay is shown in the bottom in false colors.

upon photoexcitation.

### 3.1.4 Time- and angle-resolved photoelectron spectroscopy

ARPES can be performed with a single laser beam, but a great advancement in the capabilities of the technique is to perform it in a time-resolved pump-probe fashion. This gives direct access to the dynamics of excited electronic states with a time resolution down to few femtoseconds limited essentially by the pulse duration of the laser pulses, as described below.

Figure 3.6 illustrates the concept of time-resolved photoelectron spectroscopy. Two laser beams ( $h\nu_1$ ,  $h\nu_2$ ) are time-delayed to each other. The time delay is set by a delay stage that is used to vary the optical path of one of the laser beams. At positive delays, the pump laser pulse  $h\nu_{Pump} = h\nu_1$  arrives first. Upon incidence it populates a normally unoccupied state above  $E_F$ . After the pump-probe delay  $\Delta t$ , the probe laser pulse  $h\nu_{Probe} = h\nu_2$  excites the electron population above  $E_{vac}$ . At negative delay, the probe laser pulse  $h\nu_2$  arrives first. In the example given in Figure 3.6, both photons can populate the intermediate state and have enough energy to excite the electron population of the intermediate state above  $E_{vac}$ . Consequently, if one plots the photoemission intensity versus pump-probe delay in a false color plot, such as done in the bottom of Figure 3.6, two peaks arise. The intensity

decay of the peak can be associated with the population decay of the intermediate state.

When a probe with a photon energy  $h\nu_{\text{Probe}}$  larger than the work function  $\Phi$  is used, one gets access to the time-resolved changes of the occupied band structure. Usually the term trARPES is used for this technique, while for  $h\nu_{\text{Probe}}$  smaller than the work function  $\Phi$  the term time-resolved two-photon photoemission (tr2PPE) is common. Time-resolved photoemission has been used, for example, to monitor electron dynamics in metals [Fan92, Lis04], and, more recently, to observe how the occupied band structure changes during a photoinduced phase transition [Per06, Sch08, Weg14b, Nic18].

While it seems generally favorable to work with  $h\nu_2 > \Phi_{\text{sample}}$  and get simultaneous access to both, the normally unoccupied and occupied states, measurements with  $h\nu_2 < \Phi_{\text{sample}}$  offer the advantage to be free of one-photon photoemission. One-photon photoemission emission can form a disturbing background, when one wants to examine a tiny excited state population, e.g. excited states in molecules adsorbed at metal surfaces. In both cases, the angular distribution of the photoemitted electrons can be analyzed to gain additional information from the sample. Recent developments in table-top laser sources have made it possible to measure the occupied and excited electronic states in the entire Brillouin zone [Pup19]. In tr2PPE, where the photon energy is low, only a fraction of the Brillouin zone can be accessed. The angular dependency can nevertheless be insightful, for example to distinguish between localized and delocalized states, see e.g. refs. [Bov03, Kin19].

Note that, for a single delay not only one photoemission event is recorded, but the measurement is an integration over many pump-probe events that occur with the laser repetition rate. Because the photoemission technique is essentially an electron counting method, it is generally favorable to work with high repetition rates, provided that the system decays back to the equilibrium within two subsequent pump-probe events. Otherwise, a *photostationary* equilibrium results with potential complications for the measurement as described in chapter 4.

**Time resolution** The time delay between pump and probe laser pulses can be adjusted within high precision via motorized delay stages with sub-femtosecond precision. However, the time resolution is limited by the pulse duration of the laser pulses (in the present experiments on the order of 50-100 femtoseconds) and, consequently the precise knowledge of the temporal envelopes of the laser pulses at the sample. The intensity envelope of pump- and probe laser pulses is usually determined *in situ* by non-resonant photoemission from occupied metal surfaces [Her96, Pet98]. In this case the intermediate state is a virtual state with vanishing lifetime, such that the photoemission signal as a function of delay  $\Delta t$  is given by a convolution between the temporal profile of the individual laser pulses  $I_1(t)$ ,

$I_2(t)$

$$I_{\text{PE}}(\Delta t) = \int I_1(t)I_2(t - \Delta t)dt = XC(\Delta t). \quad (3.17)$$

An exemplary measurement will be presented in section 3.2.2. This so-called pump-probe cross-correlation can then be used to extract lifetimes of intermediate states. Throughout this work, simple exponential functions of the form

$$\begin{aligned} R(\Delta t) &= A e^{-\Delta t/\tau} && \text{exponential decay} \\ R(\Delta t) &= A(1 - e^{-\Delta/\tau}) && \text{exponential rise} \end{aligned} \quad (3.18)$$

are employed to describe the photoresponse at a certain energy (for  $\Delta t > 0$ , i.e. after the arrival of the pump pulse). An exponential decay results from classical rate equations upon decay of the intermediate state into the ground state or into a state at lower energy [Bog15]. An exponential rise results upon population of a state at lower energy via a single intermediate state at higher energy, see also section 4.2.2 for an exemplary system of differential equation describing this. The photoemission intensity from the intermediate state is given by a convolution between the intermediate state response function and the cross-correlation [Her96]:

$$I_{\text{PE}}(\Delta t) = \int XC(t - \Delta t)R(t)dt. \quad (3.19)$$

More precisely, the two-photon photoemission (2PPE) process consisting of two sequential steps (initial to intermediate state, intermediate to final state) is described by optical Bloch equations, which include coherence effects but require knowledge of the dephasing times. The temporal evolution of electronic populations can be described with classical rate equations, under the assumption that all coherences are lost [Her96, Fog15]. A precise knowledge of  $XC(\Delta t)$  allows to extract lifetimes shorter than the pulse duration, with a precision given ultimately by the knowledge of time zero and the dephasing times [Her96].

### 3.1.5 Fields between sample and analyzer - part 2

Section 3.1.3 introduced the electrostatic fields that exist between sample and analyzer due to the work function difference and the bias, and how they affect the kinetic energy of the measured photoelectrons. In this section, photoinduced changes to these electrostatic fields are considered.

How could such changes occur? The idea was developed in studies using pump-probe photoelectron spectroscopy. Widdra et al. [Wid03] performed pump-probe photoelectron using an x-ray pulse from a synchrotron facility as probe laser pulse. The authors observed shifts of the core level spectra at an oxidized Si surface upon photoexcitation with a pump photon energy larger than the band gap. Figure 3.7 a) shows that, at positive delays,

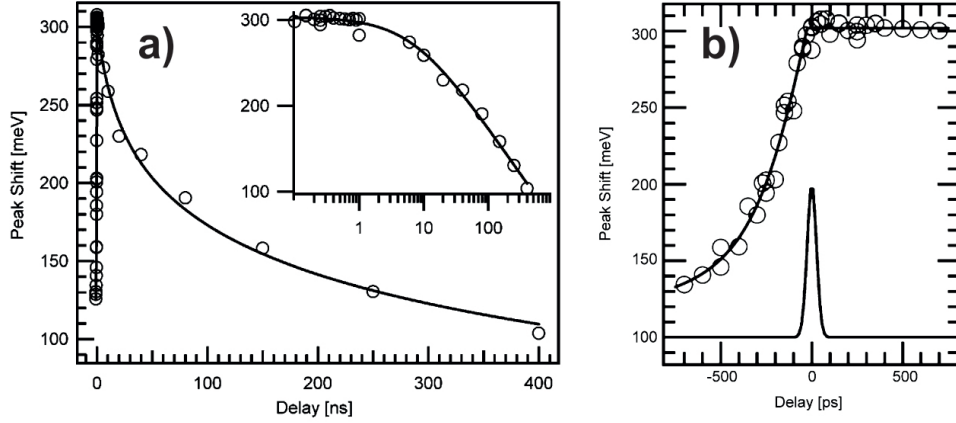


**Figure 3.7:** Shift of the Si 2p core level at a Si/SiO<sub>2</sub> interface detected by the probe at a) positive pump-probe delays and b) negative pump-probe delays. The inset in a) shows that the position of the Si 2p core level approaches the equilibrium (unpumped) position within several hundred nanoseconds. Adopted from [Wid03].

the pump induces a shift that appears instantaneously and decays within hundreds of nanoseconds. This is attributed to the surface photovoltage effect, which creates a transient surface dipole (see chapter 2.3.5). However, also at negative pump-probe delays, a shift of the core level signal occurs, depending on the pump-probe timing. This is shown in Figure 3.7 b): The largest shift is observed at time zero, and the shift becomes smaller towards larger negative pump-probe delays. At negative pump-probe delays, no change of the occupied electronic states emitted by the pump is expected, because the pump arrives *after* the probe. The observed shift is explained as the result of the influence of pump-induced field in the sample that affect the electron propagation to the detector. Further experimental reports of such negative delay shifts followed [Ret12, Yan14, Uls15], as well as a theoretical investigation by Tanaka [Tan12]. The following summarizes the basic physics.

A pump-induced field extending from the sample into the vacuum results, when the pump charges the sample surface, or rather, changes the surface dipole. The potential energy as a function of distance from the surface is approximately the form given by equation 3.15, i.e.

$$\Delta V_D(z) = -\frac{e\Delta D}{2\epsilon_0} \left(1 - \frac{z}{\sqrt{R_{\text{pump}}^2 + z^2}}\right), \quad (3.20)$$

where  $\Delta D$  denotes the photoinduced change to the surface dipole, and  $R_{\text{pump}}$  the spot radius of the pump beam. This function approaches zero within  $R_{\text{pump}}$ , which is typically on the order of tens of  $\mu\text{m}$ , much smaller than the sample. Hence this dipolar field decays much faster than the that of the rest of the sample.

Figure 3.8 presents an overview of the resulting electrostatic fields that exist in between

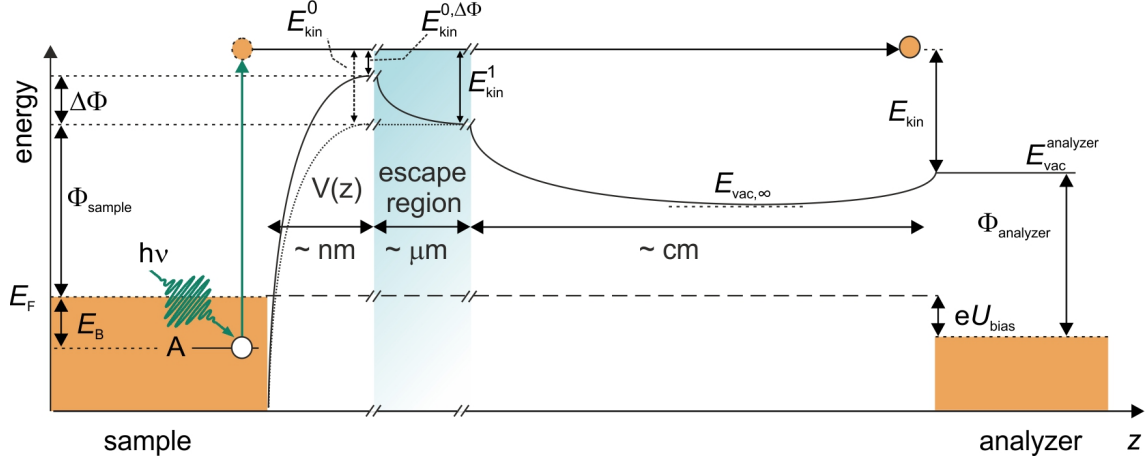


**Figure 3.8:** A photo-induced change of the surface potential also modifies the electrostatic potential between sample and analyzer. Displayed is an increase of the surface dipole by  $\Delta\Phi$ ; due to the change, a short ranged accelerating field (on the order of the spotsize) exists in front of the surface. The kinetic energy of a photoelectron emitted from a state A can be affected, depending on the lifetime of the pump induced field, the kinetic energy of the photoelectron, and the timing with respect to the photo-induced change (in a pump-probe experiment).

sample and analyzer when photoexcitation changes the surface dipole. Drawn is the case of a photoinduced increase of the surface dipole, i.e. an increase of the work function by  $\Delta\Phi = \frac{e\Delta D}{2\epsilon_0}$ . Note that in the case of a metal surface (as given here in the overview figure) a photoinduced surface dipole change does not occur due to surface photovoltage, but might occur, e.g. upon photoinduced dynamics in adsorbed molecules [Szy05]. A photoinduced change of the surface dipole has the following consequences for the kinetic energies of photoemitted electrons (cf. Figure 3.8):

1. The vacuum level shifts up on the absolute energy scale by  $\Delta\Phi$ . For electrons arising from a state A with a certain binding energy, it means that the initial kinetic energy after photoemission is smaller than without the photoinduced change of the surface dipole:  $E_{\text{kin}}^{0,\Delta\Phi} = E_{\text{kin}}^0 - \Delta\Phi$ .
2. Upon traversing the photoinduced surface dipole field with a range of tens of  $\mu\text{m}$ , kinetic energy is gained, such that  $E_{\text{kin}}^1 = E_{\text{kin}}^0$ .
3. After this, the photoelectrons undergo the acceleration/deceleration due to the work function difference of analyzer and sample, as well as due to the bias (see section 3.1.3). Because  $E_{\text{kin}}^1 = E_{\text{kin}}^0$ , no net kinetic energy change is measured for primary electrons. But the secondary edge should shift up, reflecting the pump-induced work function increase.

In a pump-probe experiment, one has to consider that the photoemission can take place *before* and *after* the work function change  $\Delta\Phi$  occurs. If the pump pulse creates  $\Delta\Phi$  and

the probe pulse photoemits the electrons, this corresponds to negative and positive pump-probe delays, respectively. For the measured kinetic energy of primary photoelectrons this means

- Positive pump-probe delays:** The energy balance is maintained, as described above, so that no shift of the kinetic energy at the analyzer occurs. This, however, only holds true if the pump-induced field is sufficiently long lived, such that the photoemitted electrons can traverse it fully before it decays. If it decays faster, then  $E_{\text{kin}}^1 < E_{\text{kin}}^0$ , because the electrons do not undergo the full acceleration. As indicated with the blue shaded box in Figure 3.8, an 'escape region' can be defined. If photoelectrons cross this region before the pump-induced surface dipole decays the effects of  $\Delta\Phi$  on the kinetic energy cancel out. Only then, the pump-induced effects of interest (e.g. pump-induced shifts of peak A) can be measured correctly. One can define a corresponding 'escape time', which depends on the initial kinetic energy of the photoelectrons. For slow photoelectrons (especially secondary electrons for which  $E_{\text{kin}}^0 = 0$ ), the escape time is longer, yielding a greater risk that the pump-induced field decays during the electrons traverse the escape region. Hence, for surface photovoltage measurements one should use a large probe photon energy [Tan12].
- Negative pump-probe delays:** When the probe pulse arrives before the pump pulse, the initial kinetic energy  $E_{\text{kin}}^0$  is not lowered, because photoemission takes place *before*  $\Delta\Phi$  was induced. Upon arrival of the pump, an accelerating field is created, such that  $E_{\text{kin}}^1 > E_{\text{kin}}^0$ . This gain of kinetic energy will persist until the electrons arrive at the analyzer, meaning that the electrons are shifted up in energy. This upward shift is stronger for small negative pump-probe delays and vanishes for large negative pump-probe delays as observed by Widdra et al. (cf. Figure 3.7 b)). The reason for this delay dependency is illustrated in Figure 3.9: For small negative delay (close to time zero) the photoelectrons emitted by the probe are very close to the sample surface, i.e. at the beginning of the escape region (Figure 3.9 a)). Upon propagating to the analyzer, they traverse the entire escape region, during which they are accelerated by the pump-induced field. If the negative pump-probe delay is larger, the probe arrives later with respect to the pump, meaning that the probe electrons already had time to travel towards the analyzer (Figure 3.9 a)). The kinetic energy shift induced by the pump becomes smaller and vanishes when the negative pump-probe delay is such that the position of the probe electron is beyond the escape region when the pump pulse arrives.

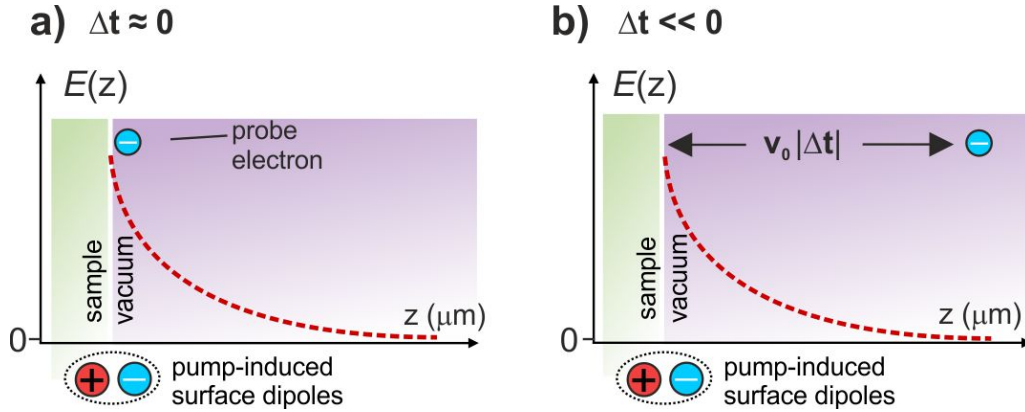


**Figure 3.9:** Origin of the delay dependency of the pump-induced shift at negative delays. The pump induces an accelerating field due to a change of the surface dipole that affects the propagation of the probe electron to the detector. For small negative delays  $\Delta t \approx 0$  (a)), the probe electron has not propagated and is close to the sample surface. In contrast, for large negative delays (b)), the electron has traveled a distance of approximately  $v_0 |\Delta t|$  ( $v_0$ : speed of the probe electron) and is out of the reach of the pump-induced field by the time the pump arrives at the sample to create it. Hence probe electrons are only affected by the pump-induced field at small negative delays.

**Preview to the results** In the present work, photoexcitation of ZnO depletes deep defects at the ZnO surface. The resulting defect excitons lead to a surface dipole *reduction*, because the photoholes are localized at the surface and the electrons are spatially separated upon injection into the conduction band. As a result, photoexcitation leads to downward band bending and a work function reduction, as has been observed for doping of oxide surfaces with shallow donors. The photoinduced defect exciton population has a short-lived component decaying within few hundred picoseconds and a component that partially survives the inverse repetition rate of the laser system (i.e. a photostationary contribution). This has the following consequences for the energetics in the photoemission and photoelectron detection process:

- **Influence of the photostationary surface dipole reduction on the measured secondary edge:** The photostationary defect exciton population leads to a change of the secondary edge position in static (i.e. not time-resolved) ARPES. The effect on the secondary edge is not trivial. Above, a work function *increase* has been considered, corresponding with the theoretical work of Tanaka [Tan12]. The situation becomes somewhat different for a photoinduced work function *decrease*. First of all, a decrease of the energy barrier on the nm scale results (negative  $\Delta\Phi$ , cf. Figure 3.8), such that the width  $b$  of the photoelectron spectrum is wider than without the photoinduced surface dipole change directly after photoemission. Subsequently, the photoelectrons traverse a decelerating surface dipole field extending into the vacuum on the order of the spot size. Since it is *decelerating*, the slowest electrons cannot

overcome it. In fact, the kinetic energy loss during traversing the decelerating field is as large as the kinetic energy gain from the decrease of the energy barrier on the nm scale; hence the width of the photoelectron spectrum  $b$  after the propagation *is the same as without*  $\Delta\Phi$ . The secondary edge therefore stays at the same position in the measured photoelectron spectrum and  $\Delta\Phi$  cannot be observed, *unless* an additional accelerating field is present that compensates the surface dipole field. Such a field can be the bias between sample and analyzer. Considerations of this kind and measurements that confirm this view will be presented in section 5.9. From tuning the bias, an effective description of the spatial extension of the pump-induced potential energy is obtained.

- **Pump-induced shifts at negative pump-probe delays:** In pump-probe spectroscopy, the pump-induces a reduction of surface dipoles that partially decays faster than the inverse repetition rate leads to a dynamic downward shift of the probe spectra at negative delays on a timescale of 100 ps, similar to the observations of Widdra et al. These results are presented in section 6.2.4. They are an important corroboration of the proposed mechanism responsible for the photoinduced SMT at the ZnO surface. The decay of the shift towards negative delays directly maps the spatial extension of the pump-induced field. Comparing the result from this approach to the bias series mentioned above finds them to be in excellent agreement.
- **Influence of photoinduced surface dipoles on the measured secondary edge in trARPES:** Although photoexcitation with the pump laser pulse induces surface dipoles, in pump-probe scans on the picosecond time scale a shift of the secondary edge cannot be observed, neither at negative, nor when going from negative to positive pump-probe delays. It will be shown by numerical simulations in section 6.2.5 that the secondary electrons are simply too slow. However, a transient work function reduction would be reflected in a change of the intensity of the secondary edge and this is also observed experimentally. These simulations go beyond Tanaka's work [Tan12], who explicitly excluded very low energy electrons.

## 3.2 Experimental Setup

After having established the theoretical background to understand the time- and angle-resolved photoemission measurements presented within this thesis, this section gives an overview of the experimental setup. The setup consists of two essential components: A femtosecond laser system and a UHV chamber for sample preparation and photoemission spectroscopy.

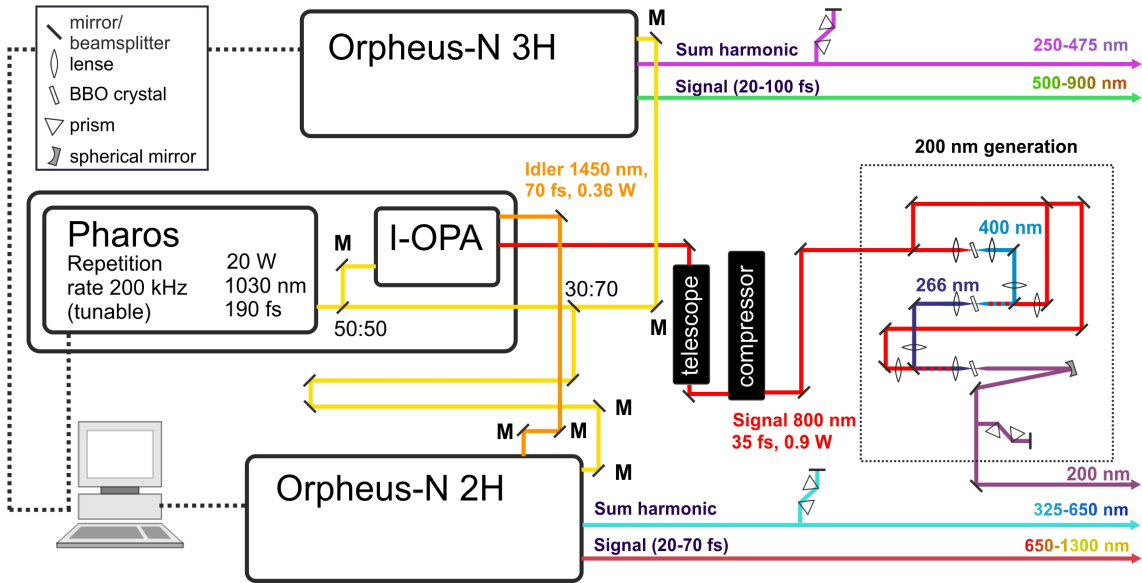


**Figure 3.10:** Schematic overview of the Light Conversion laser system. The Pharos delivers strong femtosecond pulses at 1030 nm, which are frequency converted via several optical parametric amplifiers: IOPA, Orpheus-N-2H and Orpheus-N-3H. The IOPA serves to create a strong 800 nm output that is frequency converted into a 200 nm beam and its idler at 1450 nm serves to seed the white light generation in the N-2H. The two Orpheus units provide ultrashort laser pulses in the broad spectral range of 250-1300 nm. Shifting the output wavelength is simplified by motorized, computer controlled translation and rotation stages. The mirrors marked with **M** are used for optimization of the output power by the user.

### 3.2.1 The femtosecond laser system

To induce the non-equilibrium states that are the subject of this thesis and monitor their temporal evolution in the time domain with photoemission spectroscopy, a powerful and versatile laser system is needed. During the time this work was carried out, a new femtosecond laser system, manufactured by *Light Conversion* was installed. The new laser system differs from the laser system previously used in the group, as described in [Weg14a], by higher output powers, an extended tuning range of photon energies (200 nm to 1300 nm, or 6.2 eV to 0.9 eV) and motorized components that facilitate an easier day-to-day operation.

**The Light Conversion laser** Figure 3.10 presents a schematic of the laser system. The fundament of the laser system is the Pharos. The laser is a Ytterbium-based solid state regenerative amplifier system and provides 190 fs-short laser pulses at a base repetition rate of  $R_{\text{base}}=200$  kHz. An integrated, computer-controlled pulse picker allows to reduce the repetition rate to any value  $R_{\text{base}}/Dev.$ , where the divider  $Dev.$  is an integer, while maintaining the same energy per pulse. At 200 kHz the output is 20 W. The fundamental is centered at 1030 nm and is normally not used directly in the experiment. Several non-collinear optical parametric amplifier (NOPA) units are used to generate light at ultraviolet

(UV) to infrared (IR) wavelengths:

50% of the output of the Pharos is used to pump an internal optical parametric amplifier (IOPA). The term 'internal' stems from its compact design, which allows to arrange it with the Pharos into one box, as indicated by the black frame around both units in Figure 3.10. The IOPA provides laser pulses at 800 nm and at 1450 nm pulses (IOPA signal and idler). Both outputs are further frequency converted. The IOPA signal is directed into a telescope and a compressor to optimize divergence and pulse duration, respectively. After the compressor, the pulse duration is 35 fs. This beam is further frequency converted to 200 nm for photoemission experiments, see further below. In turn, the IOPA idler is used for white light generation in the Orpheus-N-2H NOPA, which is pumped by the Pharos as well, as described in the following.

The other 50 % of the output of the Pharos is split 70:30 to pump two NOPAs, the Orpheus-N-3H and the Orpheus-N-2H, respectively. These NOPAs have both a computer-controlled output tunable in the visible to IR range; the range of photon energies accessed by the N-2H extends more to the IR (650-1300 nm) than the N-3H (500-900 nm). Both NOPAs also feature the option to use a built-in second harmonic generation unit: By frequency doubling the photon energy range is then extended to 250-475 nm in case of the N-3H and to 325-650 nm in case of the N-2H. The shifted output spectra of the two NOPAs stems from using different photon energies as seed for the white light generation. In the N-3H the white light is generated by the Pharos fundamental at 1030 nm, while in the N-2H the idler of the IOPA at 1450 nm is used (see the beam path from the IOPA into the N-2H in Figure 3.10). In the core of their spectral range, the NOPAs deliver pulses with a pulse duration down to 20 fs; the pulse duration gets longer towards the infrared for both NOPAs (up to 70 fs for the N-2H, and up to 100 fs for the N-3H). All in all, by the combination of both NOPAs the spectral range of 250-1200 nm is accessed with pulse durations between 20 to 35 fs. The power conversion efficiency is very good, especially for the N-2H signal. Over a broad spectral range about 10% of the pump (3 W) are converted. For the signal of the N-3H the converted part of the pump power (7 W) is about an order of magnitude lower, but still decent. Note that the N-3H has to be purged constantly with Nitrogen (1.5-2 liter/min.) in order to avoid damaging of the mirrors by Ozon created by strong UV irradiation in the NOPA.

Optimization of the system on a day to week basis by the user is normally performed via the alignment mirrors into the Orpheus units marked with **M** in Figure 3.10 and by using the computer-controlled motorized stages. The alignment mirrors are: A pair of mirrors for the incoupling of the Pharos fundamental into the N-2H and the N-3H, respectively, and a pair of mirrors for the incoupling of the IOPA idler into the N-2H. The incoupling mirror of the Pharos fundamental into the IOPA needs to be optimized on a weekly to monthly basis. The computer-controlled motorized stages Orpheus units can be

used to shift the output to any wavelength of the spectral range given above; the IOPA output is not tunable.

**Forth harmonic generation of the IOPA signal** The output of the NOPAs can be used to excite a large range of optical transitions. For trARPES experiments, the employed photon energy has to be larger than the work function  $\Phi$  of the investigated sample surface. Because work functions are typically on the order of 4-5 eV this requirement is only marginally fulfilled for the most UV part of the Orpheus-3H at 250 nm (4.96 eV). In order to reach even higher photon energies, one option is frequency doubling of the second harmonic output of the NOPAs (option not shown in the schematic in Figure 3.10). Sum harmonic generation in the commonly used nonlinear  $\beta$ -barium borate (BBO) crystals can be carried out for fundamental energies up to 3.02 eV [Weg14a]. A slightly higher photon energy can be reached by consecutive frequency doubling of the IOPA signal at 800 nm. This approach is applied here in order to get the forth harmonic at 200 nm (6.2 eV).

The forth harmonic generation setup is custom built and consists of three frequency conversion steps. The principle of the setup is shown in Figure 3.10; delay stages are omitted for simplicity. The incoming IOPA signal at 800 nm (1.55 eV) is split into three arms. In the first arm, 400 nm is generated by sum harmonic generation. The 400 nm beam (3.1 eV) is overlapped in space and time collinearly with the second arm of the IOPA signal for sum frequency generation to yield 266 nm (4.65 eV). Finally, the 4.65 eV beam is overlapped collinearly with the third arm to yield 200 nm (6.2 eV). About 0.4 mW of 200 nm are typically generated. To direct the beam towards the sample special dielectric-overcoated Aluminum mirrors are used (*DUVA-PM-1025-UV*, *CVI Laser Optics*) with high reflectivity at 200 nm at variable reflectance angles.

**Prism compressors** The time resolution in pump-probe experiments is determined by the laser pulse duration. Propagation through air and dispersive optics such as lenses causes pulse broadening by inducing chirp. Pairs of prism can be used for pulse compression [For84] and are employed in the beam paths of the sum harmonic output of Orpheus-N-2H and Orpheus-N-3H, respectively, and for the 200 nm beam as indicated in Figure 3.10. For the signal of the N-2H and the N-3H, a prism compressor is already contained within the NOPAs. The determination of the laser pulse duration is described in the next subsection.

### 3.2.2 Characterization of the laser pulses

The analysis of trARPES data requires knowledge of photon energy, spot size, power, and pulse duration of the pump and probe laser pulses at the sample. Their determination is described in this subsection.

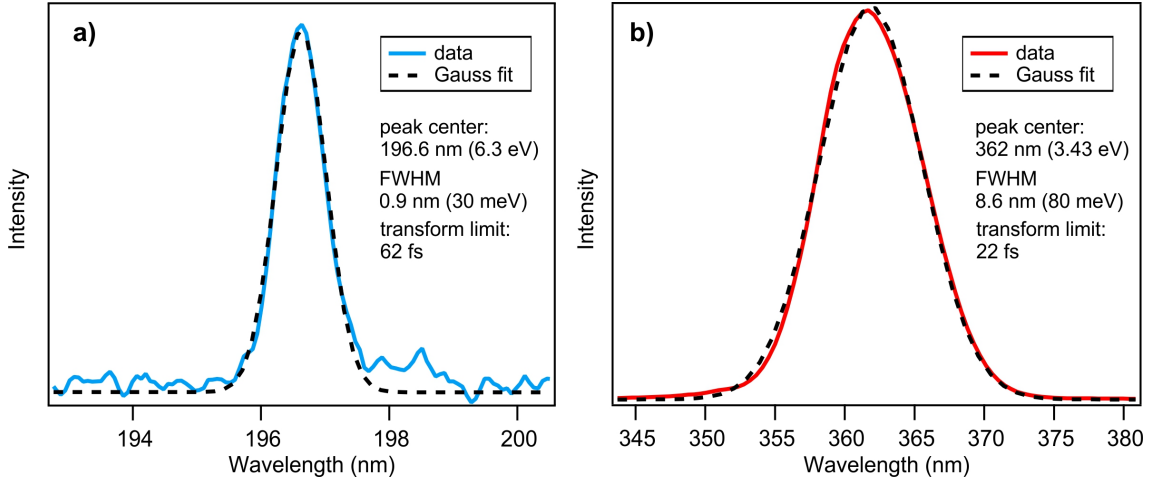


**Figure 3.11:** Exemplary laser spectra of a) the fourth harmonic of the I-OPA output and b) of the Orpheus-2H tuned resonant to the ZnO band gap of 3.4 eV. Dashed lines: Fits with a Gaussian function.

**Determination of the photon energy** The photon energies of both, pump and probe pulses have to be determined for interpretation of the photoemission data. For the probe pulse, the photon energy enters in the energy conservation relation, equation 3.14, i.e. it determines up to which energy with respect to  $E_{\text{vac}}$  electrons can be photoemitted. For the pump pulse, it is important to know which optical transitions are addressed. The photon energy is determined with a spectrometer (*Maya2000Pro*, *Ocean Optics*). An exemplary laser spectrum of the fourth harmonic of the IOPA signal and of the output of the Orpheus-2H tuned to 3.4 eV is shown in Figure 3.11 a) and b), respectively. The dashed lines are Fits with a Gaussian function that yield the central photon energy and bandwidth of the laser beams. The fourth harmonic of the IOPA is centered at 6.3 eV and is used as probe pulse for the major part of the results of this work. The Orpheus-2H output is centered at 3.43 eV, i.e. resonant to the ZnO band gap, and is used as pump pulse to drive the ultrafast SMT in chapter 6. Both laser beams have a bandwidth of several ten meV. The transform-limited pulse duration evaluated via the time bandwidth product

$$\Delta\nu\Delta t = 0.441$$

gives the lower limit for the attainable pulse duration [Weg14a], which is 62 fs for the fourth harmonic of the IOPA output and 22 fs for the Orpheus-N-2H at this energy. The actual pulse duration at the sample is directly determined from pump-probe photoemission spectroscopy as described below. Note that the bandwidth of the probe pulse also contributes

to the energy resolution, which is determined by [SPE]

$$\Delta E = \sqrt{\Delta E_S^2 + (h\Delta\nu)^2},$$

where  $\Delta E_S$  is the energy resolution of the electron analyzer, determined via the low-energy cutoff, cf. section 3.1.2.

**Spot size and laser power** Spot size  $A$  and laser power  $P$  of the laser pulses are needed to calculate the energy per pulse and unit area (i.e. the laser fluence) via

$$F = \frac{P}{R A}.$$

Here,  $R$  is the repetition rate. The laser power is measured with a power meter (*Newport*) just before the beam is coupled into the UHV chamber and hits the sample. The spot size is measured with a beam profiler (*SP620U*, *Spiricon*) placed outside the UHV chamber at a position to which the light travels the same distance as to the sample. Typically the spot sizes are around 80-150  $\mu\text{m}$  for the pump pulse, and around 40-80  $\mu\text{m}$  for the probe pulse to ensure a homogeneous pump-induced non-equilibrium state over the probed area.

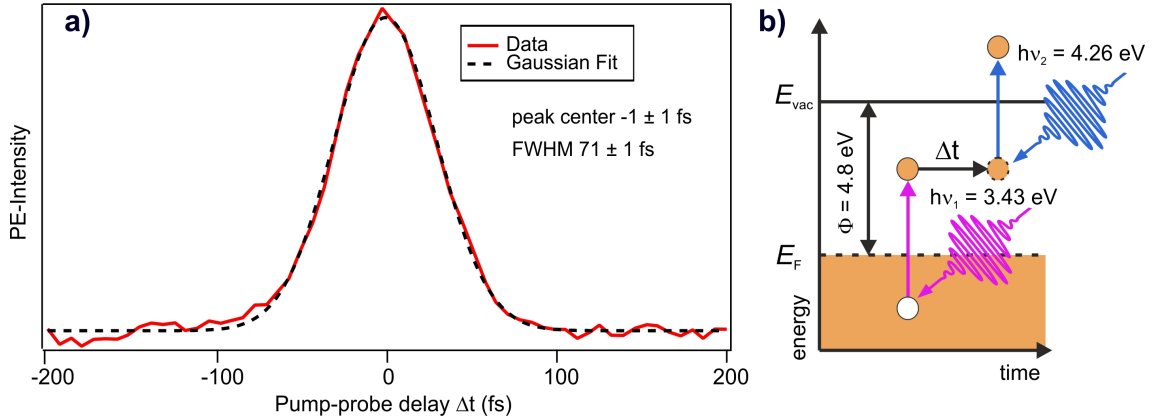


**Figure 3.12:** Exemplary measurement of the pump-probe cross-correlation function by tr2PPE from the tantalum (Ta) sample mount. a) Energy and angle-integrated intensity trace resulting from photoemission with  $h\nu_1=4.26$  eV and  $h\nu_2=3.43$  eV, which are both below the work function of  $\Phi=4.8$  eV of the Ta surface. b) Energy level diagram.

**Determination of the pump-probe cross-correlation** Exact knowledge of the pump-probe cross-correlation, i.e. the convolution of the temporal envelopes of pump and probe pulses, is crucial for the time resolution of the experiment (see section 3.1.4). It is usually measured *in situ* via time-resolved 2PPE from occupied states via (virtual) intermediate states with very short lifetime [Pet98]. Such short-lived states are found at transition

metal surfaces, which are part of the sample holder. An exemplary dataset and energy sketch is shown in Figure 3.12 a) and b), respectively. Figure 3.12 a) represents the photoemission intensity from occupied states of the Ta sample mount versus pump-probe delay. An energy level diagram that illustrates how the photoelectron intensity arises is shown in Figure 3.12 b). The used photon energies are  $h\nu_1=4.26$  eV and  $h\nu_2=3.43$  eV, which are both below the workfunction of this surface. The intensity trace in Figure 3.12 a) can be fitted with a Gaussian function, representing the pump-probe cross-correlation. From this fit, the cross-correlation width and time-zero can be determined with high precision, resulting in a full width at half maximum (FWHM) of  $71 \pm 1$  fs and an error bar of only one fs for the determination of time zero<sup>9</sup>. It should be noted, though, that an error bar for time zero on the order of 5 fs is typically assumed, resulting from the positioning the sample in front of the analyzer after such a pulse determination measurement. This might change the spatial overlap between pump and probe and hence also the temporal overlap slightly.

When using the forth harmonic of the I-OPA at 6.2 eV as probe, the photon energy is above the work function of the transition metal surfaces of the sample mount. In that case, a large background signal arises due to one-photon photoemission (1PPE) from the occupied states and no correlated signal can be detected on top of this signal. It is still possible to determine the pump-probe cross-correlation *in-situ* via the time-resolved photoemission from the ZnO surface<sup>10</sup>. ZnO CB electrons exhibit very short intermediate state lifetimes that depend on their excess energy with respect to the band edge, see section 2.3.2. The pump-probe cross-correlation is extracted by a global fit to several intensity traces corresponding to the signal of different intermediate states (and hence lifetimes) at once. Details of the procedure are given in section 6.1.5 in context with the evaluation of the data. The extracted pump-probe cross-correlation is typically on the order of 100-120 fs (FWHM). Note that the prism compressor distances always need to be iteratively optimized in order to yield the shortest pump-probe cross-correlation width.

### 3.2.3 The ultrahigh vacuum chamber

The UHV system is needed to enable contamination-free, well-defined sample surfaces and to perform photoemission measurements. Figure 3.13 gives an overview of the chamber. Briefly, it consists of two levels which are stacked vertically, and separated by a gate valve. In both levels, the base pressure is in the  $10^{-10}$  to  $10^{-11}$  mbar range and is monitored by

---

<sup>9</sup>The Gaussian function used to fit the pump-probe cross-correlation results from the convolution of the temporal envelopes of pump and probe laser pulses (equation 3.17). When both pulses are Gaussian functions, the convolution is again a Gaussian function, and assuming that both pulses are equally short, the duration of the individual pump and probe can be deconvoluted giving a pulse duration (FWHM) of  $71 \text{ fs}/\sqrt{2} \approx 50$  fs in this case

<sup>10</sup>Although the probe photon energy is above the work function also in case of ZnO, the 1PPE signal is small, due to a low density of states at the Fermi energy.

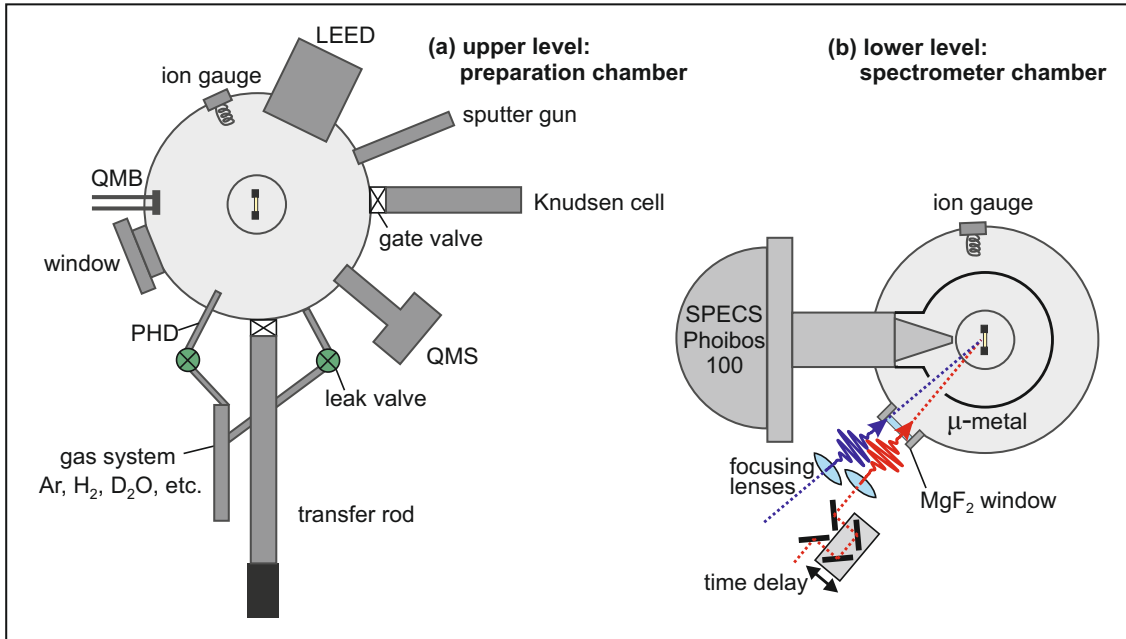


**Figure 3.13:** Schematic of the UHV chamber. The chamber consists of two levels. a) Upper level, used for cleaning the ZnO surface with sputtering and annealing cycles, for LEED measurements and for adlayer preparation. b) Lower level, used for photoemission spectroscopy. It is equipped with an incoupling window for pump and probe laser pulses as well as the hemispherical electron analyzer. From [Bog15]

ion gauges. The vacuum is established by turbomolecular pumps in the upper level and an ion getter pump in the lower level. The upper level is used for sample preparation before photoemission measurements, and the lower level contains the electron analyzer and an incoupling window for pump and probe laser pulses. In the following, the capabilities of the upper and lower level are summarized. The chamber has been described in detail before [Bog15, Dei11].

The upper level (cf. Figure 3.13 a)) is connected via a gate valve to a transfer system ('transfer rod'), in which samples can be introduced from outside. Once transferred into the UHV, the sample is attached to a flow cryostat, which is mounted to a motorized manipulator that can be moved in all three spatial directions and rotated around the vertical axis. The sample mount and the sample holder is described in the Appendix. Cooling of the sample is routinely done with liquid nitrogen which allows sample temperatures as low as 100 K, and heating is possible via the Ta wires at the sample mount (cf. Appendix and section 3.2.6). Besides the temperature control and guaranteeing a contamination-free environment, the upper level provides the capabilities for

- **Sputtering:** For sputtering of sample surfaces, the sputter gun and the gas system are used. The gas system is filled with pure Argon, which is brought into the chamber

up to the required partial pressure with a leak valve.

- **Characterization of the surface reconstruction:** The low-energy electron diffraction (LEED) allows to judge the surface ordering via Bragg reflection from the top-most layers of the sample.
- **Adlayer preparation:** With the Knudsen cell, adlayers can be produced by thermal evaporation. The growth of adlayers is monitored by the quartz microbalance (QMB) by the change of the resonance frequency upon increasing coverage. Furthermore, adlayers can be prepared by introducing any desired gas from the gas system via the leak valve or the so-called pinhole doser (PHD), with which very small quantities of gases can be directly brought onto the sample surface [Dei16].
- **Adlayer characterization:** A quadrupole mass spectrometer is employed for thermal desorption spectroscopy, but such data is not part of this thesis. The QMS is used for residual gas analysis in order to check for contaminants.

After sample preparation, the sample is moved down to the lower level (cf. Figure 3.13 b)), which is equipped with a hemispherical electron analyzer (*Phoibos 100, SPECS*) and has an incoupling window for pump and probe laser pulses. For photoemission spectroscopy, the alignment of the sample as well as the laser beams on the sample is ensured with CCD cameras mounted to optical viewports.

### 3.2.4 Setup for trARPES measurements

In ARPES, photoemitted electrons are counted as a function of their kinetic energy and emission angle. This is achieved with the hemispherical electron analyser, which separates electrons with different kinetic energy and emission angle spatially due to different trajectories (cf. section 3.1, Figure 3.1). After this, the electrons are multiplied using a micro-channel plate, and finally hit a phosphorescing screen. The electron distribution on the screen is then recorded using a CCD camera. The overall setup is described in more detail in ref. [Dei11]. It should be noted that each spectrum is an integrated measurement over several thousand shots of ultrafast laser pulses. This is because the repetition rate of the laser system is in the kHz range, while the detection system integrates over several milliseconds, because the camera exposure time can be set equal or higher than 30 ms.

### 3.2.5 Data acquisition and analysis

The raw data collected by the detection system described above contains the electron intensity as a function of electron kinetic energy and emission angle. Two actions have to be taken in order to be able to interpret the spectra:

- Calibration of the energy axis: The kinetic energy depends on the analyzer work function as described in section 3.1.3 and has to be calibrated in order to give information about the binding energy of electrons within the sample. This is done, as already mentioned in section 3.1.3, by determining the kinetic energy that corresponds to electrons arising from the Fermi energy  $E_F$ .
- Conversion of emission angle into  $k_{\parallel}$ : The as-measured kinetic energy enters in equation 3.13 to convert the emission angle into  $k_{\parallel}$ .

Now photoemission spectra give information about the electronic band structure  $E(k_{\parallel})$ . ARPES spectra can be recorded using a single laser beam under variation of parameters such as laser repetition rate or laser fluence. For trARPES, photoelectron spectra are recorded with two laser beams (pump and probe) as a function of pump-probe delay  $\Delta t$ . At each delay, typically several camera images are taken, with an exposure time of 30-100 ms each. Afterwards the delay is changed and a new ARPES spectrum is recorded. Figure 3.14 a) shows an exemplary set of ARPES spectra recorded as a function of pump-probe delay for ZnO(10-10). The photon energy used as probe is the fourth harmonic of the I-OPA at 6.3 eV and the pump photon energy is 3.43 eV, i.e. resonant to the ZnO band gap. For each pump-probe delay a three-dimensional data set, i.e. photoelectron intensity versus energy and  $k_{\parallel}$  is obtained. The displayed spectra show the pump-induced rise of photoelectron intensity below  $E_F$ . In principle, there are different ways to visualize and analyze the data:

- One option is to inspect energy-resolved photoelectron intensity as a function of pump-probe delay by integrating over a certain  $k_{\parallel}$  interval (green box in Figure 3.14 a). The resulting spectra are shown in Figure 3.14 b) and yield energy-resolved changes of the photoelectron intensity as a function of pump probe delay that can be analyzed, for example to resolve transient shifts of spectral features.
- One can also inspect the temporal evolution of the photoelectron intensity in a certain interval of emission angles and energies directly (Figure 3.14 c, integration window indicated with the purple box in Figure 3.14 a)). The energy-integrated intensity traces can be fitted to extract time constants of the rise and decay of pump-induced electron populations as described in section 3.1.4<sup>11</sup>.
- To analyze how electron populations evolve for different  $k_{\parallel}$  one can adjust the integration windows, i.e. the  $k_{\parallel}$  interval in the boxes in Figure 3.14. One can also take a number of cuts for different  $k_{\parallel}$  for a fixed delay to extract the apparent dispersion

<sup>11</sup>Provided that no transient shifts occurs, because the integrated intensity in a certain spectral range can of course also change when a feature shifts into or out of the integration box.

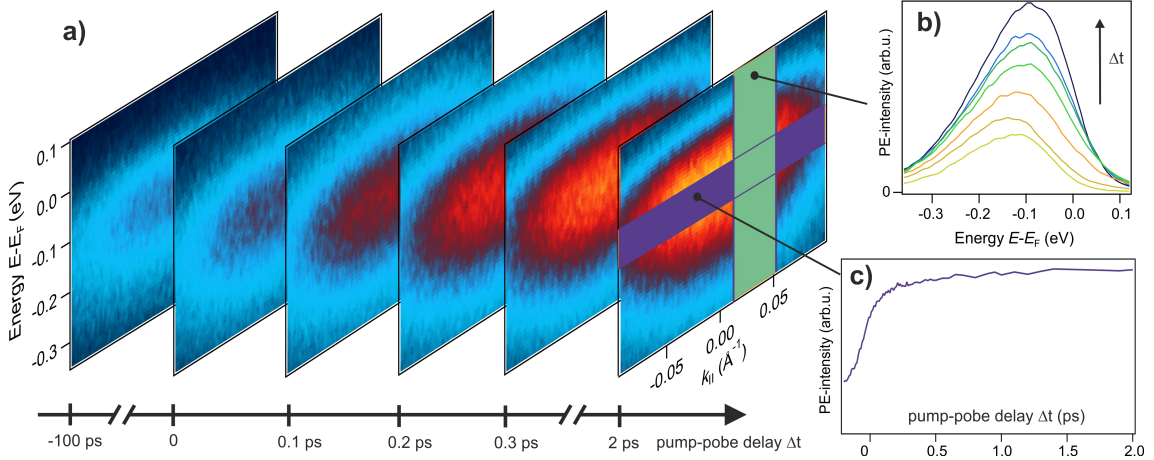


**Figure 3.14:** trARPES data acquisition and representation. a) The trARPES data consists of a stack of ARPES measurements that are recorded at different pump-probe delays one after another. b) and c) show angle-integrated photoemission spectra for different pump-probe delays and an exemplary energy- and angle-integrated intensity trace as a function of pump-probe delay, respectively.

of transiently occupied electronic states as a function of pump-probe delay, see e.g. ref. [Kin19].

An analysis and interpretation of the measurement shown in Figure 3.14 will be given in section 6. In general, for data analysis, fitting and simulations, in this work IGOR Pro by *WaveMetrics* is used.

### 3.2.6 Sample preparation

The ZnO(10-10) sample is purchased at *Mateck GmbH*. The hydrothermally grown single crystal is of the size 7 mm x 7 mm x 1 mm with a polished surface and oriented with a precision of  $< 0.5^\circ$ . The sample is transparent, with a yellowish color and is mounted via a sample 'ship' to the sample holder attached to the manipulator cryostat. The sample holder and the ship are described in the Appendix, see Figure 7.1. For the direct mount of the sample two different designs are used. The first consists of a Molybdenum (Mo) frame to which a Ta sheet is screwed down holding the sample in place. The second consists of a Ta foil wrapped around the crystal back and partly around the crystal front. Both designs have the same functionality of holding the sample in place, ensuring a good thermal contact for cooling and providing temperature control via resistive heating, reached by Ta wires in the back of the sample. The advantage of the first design is that the sample can be exchanged easily, but the Mo frame forms an additional thermal mass, which makes

efficient cooling a challenge, as discussed in the Appendix. To read the sample temperature a thermocouple (TC) is attached to the sample mount. In the first design it is clamped to the front while in the second it is spot-welded to the Ta pocket at the back of the sample. A photograph of the mounted sample can be found in the Appendix, Figure 7.2. The electric contact through the Ta sheet to the sample front ensures that the sample surface is not charged upon photoemission and is needed to apply a bias voltage to the sample surface in the photoemission experiments.

**Preparation of clean ZnO surfaces by sputtering and annealing** Once inserted in the UHV chamber, the ZnO surface is cleaned by repeated cycles of sputtering with Argon ions (0.75 keV, 10 min.,  $T_{\text{Sample}}=300$  K,  $p_{\text{Ar}}=2 \times 10^{-6}$  mbar) and annealing at elevated temperature ( $T_{\text{Sample}}=700-950$  K, 30 min.). Heating rates of 30-40 K/min. are used. Typically, on the order of 15 cycles are needed to produce a clean surface. The quality of the so-prepared ZnO surface is checked by recording LEED images and by determining the VB maximum and the work function with photoemission measurements. An exemplary LEED is shown in Figure 3.15, which shows sharp spots at a rectangular pattern in agreement with literature [Dul02], indicating a well-ordered sample surface. The VB maximum and the work function measured with photoelectron spectroscopy (PES) are also found to be in agreement with literature, as described in subsection 5.1. No difference between using the different sample mounts mentioned above was found. The annealing temperature was tuned such that an optimal LEED was obtained.

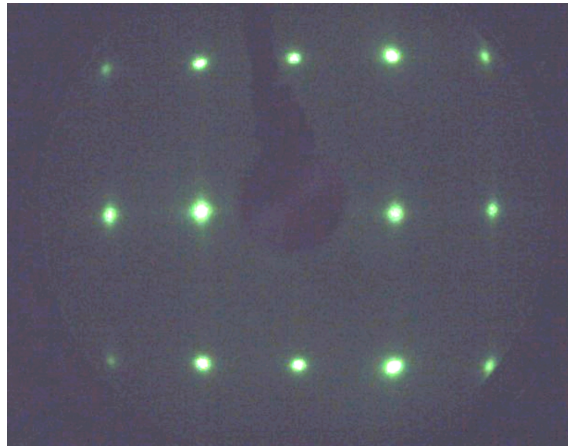


**Figure 3.15:** Exemplary LEED of the ZnO(10-10) sample after repeated sputtering and annealing cycles. The LEED is recorded at a sample temperature of  $T_{\text{Sample}}=100$  K and using an electron energy of 65 eV.

**Point defects and impurities at vacuum-annealed ZnO(10-10)** Scanning tunneling microscopy (STM) measurements of the ZnO(10-10) surface after sputtering and

annealing cycles carried out by Diebold et al. [Dul02, Die04] show flat terraces with few point defects or impurities. The authors reported, though, that magnesium or calcium impurities might segregate to the surface and that desorption of lattice atoms occurs at increasingly efficient at elevated annealing temperatures [Die04]. Using mass spectroscopy, desorption from lattice oxygen was detected at annealing temperatures of 700 K, becoming more effective at higher temperatures [Göp80]. Zinc desorption is detected at temperatures above 900 K [Göp77]. In the present work, annealing temperatures in the range of 700 K to 950 K are used implying the potential existence of lattice vacancies at the surface. Thus, point defects such as lattice vacancies at the ZnO surface can be expected at the surface. The density of oxygen vacancies is expected to increase upon UV illumination as will be discussed in section 2.3.3 and 5. The effects of the annealing on the observed photoinduced physics will be analyzed in section 6.2.7.

**Preparation of H terminated ZnO** The main part of this work is performed on the as-prepared ZnO surface. A few comparison measurements are presented in chapter 6 with a H-terminated ZnO surface. H termination of the as-prepared ZnO surface is reached following an established procedure [Dei16, Oza10]: A leak valve (LV) is used to fill the chamber with clean H<sub>2</sub> gas and the sample is located within a distance of about 15 cm to the tungsten filament of the Bayard-Alpert pressure gauge, which breaks some H<sub>2</sub> into H. The adsorption of H<sub>2</sub> can be neglected due to the vanishing sticking coefficient [Dei16]. During the dosing the sample temperature is 100 K. Due to the unknown sticking coefficient and cracking efficiency the actual H coverage of the surface is unknown [Dei16]. The coverage is given in units of Langmuir (L), which corresponds to an exposure of 1 second at a pressure of  $1.33 \cdot 10^{-6}$  mbar [Dei16].

---

## 4 Mathematical framework to deal with photostationary states in pump-probe spectroscopy

In experiments with pulsed lasers, long-lived electron populations can be photoexcited, which do not decay completely in the time between two subsequent pulses  $\Delta T = 1/R$  ( $R$ : Repetition rate). As sketched in Figure 4.1, a part of the population remains for subsequent laser pulses and after many excitation events a photostationary state  $n_\infty$  is reached where the population does not change anymore from pulse to pulse. Obviously, the higher the repetition rate, the more likely it is that an excited state exists that survives  $\Delta T$ . Although the strength of pump-probe spectroscopy with ultrafast laser pulses clearly lies in the analysis of ultrashort dynamics, it is important to understand how such states could interfere with the usual interpretation of data, which is based on the assumption that the pump excites a sample that is in equilibrium. These considerations become increasingly important with regard to recent developments in trARPES. To probe pump-induced dynamics with decent statistics and without space charge effects over a wide range of momenta and energies, XUV light sources with high repetition rates (several 100 kHz to MHz) are developed [Cor18]. The temporal distance between two pulses is then in the  $\mu\text{s}$  to ns range - a time span that is easily surpassed for example by excitons in molecules or semiconductor surfaces, such as ZnO [Fog19]. Consequently, photostationary states are quite ubiquitously reported in literature, see e.g. refs [Spe13, Wei04, Nep16].

Further, the analysis of such states offers means to determine lifetimes that exceed the delay range covered by delay stages. The determination of such lifetimes requires fast electronics (e.g. for time-tagging approaches [Nep16, Mäh16]), or, alternatively, a laser system with variable repetition rate: Qualitatively it is clear that a decrease of the repetition rate provides more time to the state to relax and leads to a decrease of the photostationary state population (cf. Figure 4.1). The detected signal must depend on the lifetime of the state, but the exact functional form is not known. To determine the lifetime from such measurements and to treat photostationary state contributions to pump-probe spectroscopy, an appropriate model is developed in this chapter.

I first review the lifetime determination of photostationary states that live long enough to be tackled with the detection electronics of the present experiment. For lifetimes that are too short to be determined with this technique, a new model is developed that establishes a relation between the lifetime of a photostationary states and the population upon variation the repetition rate. This relation will be used to determine the lifetime of a long-lived exciton at the ZnO surface in chapter 5. Finally, an extension of the model for pump-probe experiments with two different beams delayed with respect to other, which may or may not influence the photostationary state, is developed. An example dataset is analyzed to show that photostationary states can lead to counterintuitive ultrafast dynamics in pump-probe

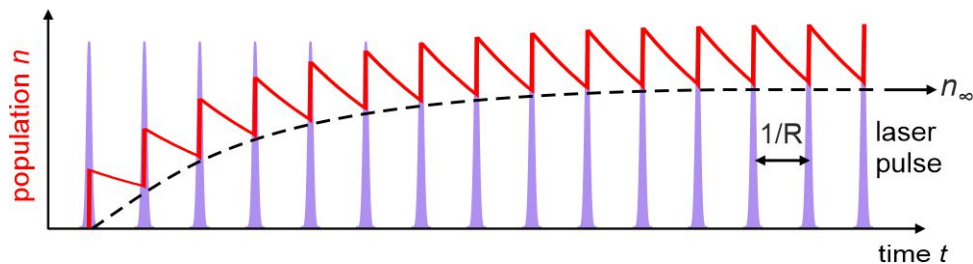


**Figure 4.1:** Build-up of a photostationary state. The temporal distance between two pulses is given by the inverse repetition rate  $\Delta T = 1/R$ . A photoexcited state that survives  $\Delta T$  forms a quasi-stationary background  $n_\infty$  in pulsed laser experiments.

scans.

## 4.1 Lifetime determination

### 4.1.1 Very long lifetimes

For lifetimes larger than  $\Delta T$  and large enough to be tackled with the detection electronics, the lifetime can be determined rather easily and a model already exists. For example, in typical photoemission setups such as the one used in the present work, snapshots of the photostationary state population can be taken in time intervals as short as the camera exposure time ( $>30$  milliseconds (ms)) as the laser is switched on. This experimental configuration is used in the present work and it has been used to analyze the lifetime of extremely long lived electron population in ice layers on metal surfaces (lifetime on the order of seconds) [Gah04, Sta07, Bov09, Weg14a, Kin17]. Because the time constant of the photostationary state is much larger than the inverse repetition rate, the laser can be regarded as quasi-continuous light source, which allows to model the population  $n$  with infinitesimal time steps [Gah04]:

$$\frac{dn}{dt} = \tilde{\alpha}(N - n) - \tilde{\beta} n - \frac{1}{\tau} n \quad (4.21)$$

Here,  $\tilde{\alpha}$  and  $\tilde{\beta}$  are the rate coefficients due to optical population and depopulation of the state, respectively.  $N$  is the maximum number of states that can be photoexcited and  $\tau$  is the intrinsic lifetime of the state. The rate coefficients are both proportional to the photoexcitation cross section and the number of photons per time interval of the quasi-continuous light source. The latter is determined by the laser power density, i.e. laser fluence  $F$  and repetition rate  $R$ . One can therefore write

$$\tilde{\alpha} = a F R ; \tilde{\beta} = b F R \quad (4.22)$$

Here,  $a$  and  $b$  are the photoexcitation cross sections for optical population and depopulation of the state, respectively. The solution of the differential equation 4.21 is

$$n(t) = n_0 e^{-(\tilde{\alpha} + \tilde{\beta} + 1/\tau)t} + (1 - e^{-(\tilde{\alpha} + \tilde{\beta} + 1/\tau)t}) \frac{\tilde{\alpha}N}{\tilde{\alpha} + \tilde{\beta} + 1/\tau}, \quad (4.23)$$

where  $n_0$  is the population present before illuminating the sample (0 if the sample is in equilibrium). In the limit  $t \rightarrow \infty$  the photostationary equilibrium is approached:

$$n_\infty = \frac{\tilde{\alpha}N}{\tilde{\alpha} + \tilde{\beta} + 1/\tau} \quad (4.24)$$

According to equation 4.23 the buildup of the photostationary equilibrium for  $n_0 = 0$  (cf. dashed line in Figure 4.1) is described by an exponential rise with the rise time constant

$$\tau_{\text{rise}} = \tilde{\alpha} + \tilde{\beta} + 1/\tau.$$

For low fluences ( $\tilde{\alpha}(F) \rightarrow 0$ ,  $\tilde{\beta}(F) \rightarrow 0$ ), the lifetime determines the time constant of the exponential rise of the photostationary state signal. As the laser fluence is enhanced, the time constant increases linearly with the laser fluence. This has been experimentally observed for the solvated electron population in ice layers on metal surfaces [Gah04]. From such measurements, one could in principle determine the lifetime  $\tau$  by extrapolation of the measured rise time constants to  $F = 0$ . Yet, the most straightforward way of probing the lifetime is to do 'pump-wait-probe' experiments. Here, the pump is used to create the photostationary state population ('pump' phase), then the pump is switched off ('wait' phase) and then a probe is used to detect the remaining population ('probe' phase)[Gah04, Weg14a, Kin17].

#### 4.1.2 Less long lifetimes

If the photoexcited population is too short-lived to be tackled with the detection electronics, the above-described 'pump-wait-probe' approach to determine  $\tau$  cannot be used. The decay of the state would appear instantaneously by virtue of the slow detection electronics. Moreover, the population of the state would rise very fast (cf. the discussion above regarding equation 4.23). As a consequence of its immediate rise/decay the photostationary state might easily be misinterpreted as static (i.e. photoexcitation independent) signal. In order to identify the photostationary state and determine its lifetime in this case, the repetition rate  $R$  can be tuned. A variation of  $R$  would change the photostationary state population in a way that is intimately connected to its lifetime. As already mentioned in the introduction to this chapter, decreasing the repetition rate provides more time to the excited state population to relax, hence the photostationary population should decrease.

The expression for  $n_\infty$  developed with the continuous wave model in the last section (equation 4.24) features a repetition rate dependency via the rate coefficients  $\tilde{\alpha}(F, R)$  and  $\tilde{\beta}(F, R)$ . Without inspecting the expression more closely, it is clear that the continuous wave model is not expected to describe the change of  $n_\infty$  with  $R$  correctly: Only states with a lifetime on the order of the inverse repetition rate  $\Delta T = 1/R$  should show a significant population change upon variation of the laser repetition rate. In this case the basic requirement of the model, namely lifetimes much larger than  $\Delta T$ , breaks down. As the population evolves faster than the temporal distance between two laser pulses the pulsed laser cannot be approximated as continuous wave laser. In order to tackle this situation, the present section develops a model that explicitly takes into account the pulsed laser excitation.

I consider a single color experiment, i.e. only photons of one laser beam are incident on the sample. The laser pulses are assumed as delta functions in time, and the optical population of the state is assumed to be fast compared to  $\Delta T$ , but not instantaneous.<sup>12</sup> The idea of the pulsed laser populating and depopulating the long-lived electronic population is summarized in Figure 4.2. The process of population is summarized with an excitation probability:

$$\alpha = aF, \quad (4.25)$$

where  $F$  is the fluence and  $a$  is the photoexcitation cross section. The so-created population of the state is depopulated with the subsequent laser pulse, i.e. after  $\Delta T$ . The process of depopulation is summarized the excitation probability

$$\beta = bF. \quad (4.26)$$

Further, the laser pulse then again populates the state (with probability  $\alpha$ ). Within the time between two subsequent laser pulses, the population of the state decays exponentially, i.e.

$$n(\Delta T) = n(0) e^{-\frac{\Delta T}{\tau}} \quad (4.27)$$

Here,  $n(0)$  is the population just after the depopulation and subsequent population by the first laser pulse. In the following I call the population just after the population with the first laser pulse  $n_1^0$  and equivalently just after the depopulation and population with subsequent laser pulses  $n_2^0, n_3^0, \dots, n_k^0$ . Equivalently, the population that the  $k$ -th laser pulse encounters is termed  $n_{k-1}^{\Delta T}$ . This population is related to  $n_{k-1}^0$ , i.e. the population just after the preceding excitation event by the exponential decay (equation 4.27):

$$n_{k-1}^{\Delta T} = n_{k-1}^0 e^{-\frac{\Delta T}{\tau}} \quad (4.28)$$

---

<sup>12</sup>This means that the excited state population cannot be populated and detected with the same laser pulse (e.g. in a 2PPE-process), but only with the subsequent laser pulse of the repetitive laser excitation.

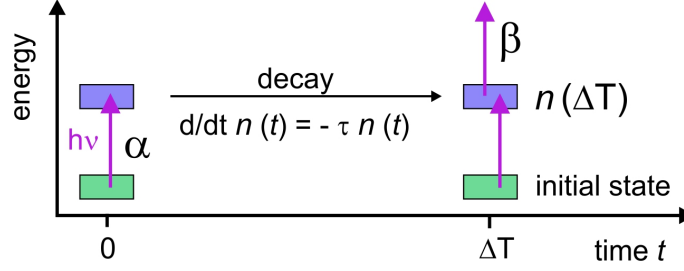


**Figure 4.2:** Model for probing long lived states within a single color experiment. The first laser pulse *populates* the state with the probability  $\alpha$ . The second laser pulse *depopulates* and thereby monitors it (e.g. by a photoemission measurement). Furthermore, the second laser pulse populates the state with the probability  $\alpha$ . The sequence is repeated for subsequent laser pulses.

To model the photostationary state population, I consider the full history of photoexcitation events: The laser pulses arrive on the sample in equilibrium and then build up the photostationary population successively starting from zero (cf. Figure 4.1). The population *change* upon each excitation event is

$$\Delta n_k = \alpha(N - n_{k-1}^{\Delta T}) - \beta n_{k-1}^{\Delta T}, \quad (4.29)$$

i.e. it consists of a population term and a depopulation term. Both terms depend on the number of already populated states  $n_{k-1}^{\Delta T}$  that remain from the preceding excitation event. This is clear for the depopulation term, as only populated states can be depopulated. For the population term this dependency enters by introducing a maximum number  $N$  of states that *can be* populated. Hence, the population is proportional to  $(N - n_{k-1})$ .

The population just after each laser excitation event is given by

$$n_k^0 = n_{k-1}^{\Delta T} + \Delta n_k \quad (4.30)$$

Now I can write down a series, which describes the buildup of the population of the long-lived state with repetitive laser pulses:

$k$	$n_k^0$
0	0 (sample is in equilibrium)
1	$n_1^0 = 0 + \Delta n_k = \alpha(N - 0) - \beta \cdot 0 = \alpha N$
2	$n_2^0 = n_1^{\Delta T} + \alpha(N - n_1^{\Delta T}) - \beta n_1^{\Delta T} = \alpha N(1 + (1 - (\alpha + \beta))e^{-\frac{\Delta T}{\tau}})$
3	$n_3^0 = \dots$

And so on for  $n_3^0, n_4^0, \dots$ . By expanding a higher order term I identify the *geometric series*

$$n_k^0 = \alpha N \sum_{j=0}^{k-1} (1 - (\alpha + \beta))^j (e^{-\Delta T/\tau})^j = \alpha N \sum_{j=0}^{k-1} q^j \quad (4.31)$$

with a constant ratio  $q$  between successive terms. It converges if the modulus of  $q$  is

smaller than one. In the present case

$$q = (1 - (\alpha + \beta))e^{-\Delta T/\tau} \quad (4.32)$$

For  $\alpha$  and  $\beta$  smaller than one (defined as excitation probabilities) the modulus of  $q$  is always smaller than one and the series therefore converges. In the limit  $k \rightarrow \infty$  the geometric series approaches

$$n_{\infty}^0 = \frac{1}{1 - q} \quad (4.33)$$

By inserting the expression for  $q$  this gives the photostationary population just after a laser excitation event

$$n_{\infty}^0 = \frac{\alpha N}{1 + (\alpha + \beta - 1)e^{-\Delta T/\tau}} \quad (4.34)$$

The photostationary state population monitored experimentally is given by multiplication with another  $e^{-\frac{\Delta T}{\tau}}$  (equation 4.28 and see Figure 4.2):

$$n_{\infty} \equiv n_{\infty}^{\Delta T} = n_{\infty}^0 e^{-\frac{\Delta T}{\tau}} = \frac{\alpha N}{e^{\Delta T/\tau} + \alpha + \beta - 1} \quad (4.35)$$

This expression is explicitly dependent on  $\Delta T$  and is valid for all lifetimes  $\tau$ , in contrast to the continuous wave model described in section 4.1.1. In the following three paragraphs, I will discuss how the model can be used to extract lifetimes of photoexcited states that are on the order of  $\Delta T$ . Furthermore I will discuss what to expect for the buildup time of a photostationary state according to the model. Finally, I will show that the expression for  $n_{\infty}$  converges with the result from the continuous wave model when the lifetime is much larger than the  $\Delta T$ . In this limiting case both models are equivalent.

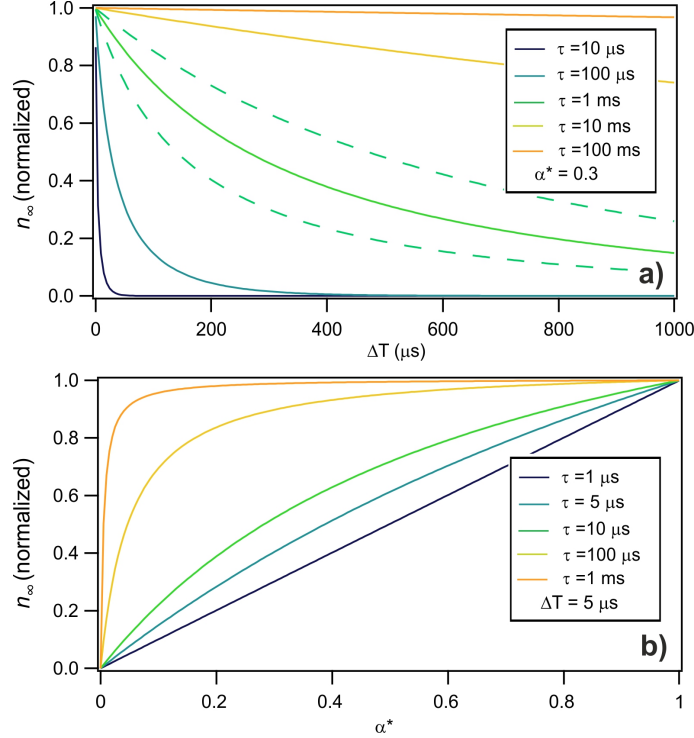


**Figure 4.3:** Numerical evaluation of the photostationary equilibrium resulting from the pulsed laser model. a) Repetition rate dependency:  $n_\infty$  as a function of  $\Delta T = 1/R$ . All solid lines are calculated with  $\alpha^* \equiv \alpha + \beta = 0.3$  and different lifetimes  $\tau$  as indicated in the legend. The two dashed lines are calculated with  $\alpha^* = 0.15$  (lower trace) and  $\alpha^* = 0.6$  (upper trace), respectively, with the same lifetime  $\tau = 1 \text{ ms}$ . b) Fluence dependency:  $n_\infty$  as a function of  $\alpha^*(F)$  for different lifetimes  $\tau$ . Experimentally, repetition rate and fluence dependency can be used to determine the lifetime of a photostationary state, when  $\tau$  is on the order of  $\Delta T$  (see text).

**Lifetime determination via tuning of laser repetition rate and laser fluence** In Figure 4.3 a) plots of  $n_\infty$  (equation 4.35) as a function of the inverse repetition rate  $\Delta T$  are shown for different values of  $\tau$ . Inverse repetition rate  $\Delta T$  and lifetime  $\tau$  are chosen to be in the  $\mu\text{s}$  range;  $\Delta T$  is between 1 and 1000  $\mu\text{s}$ . Note that  $n_\infty$  is fluence-dependent via the excitation probabilities  $\alpha(F)$  and  $\beta(F)$ . For the solid lines in Figure 4.35,  $\alpha^* \equiv \alpha + \beta = 0.3$  is chosen. Figure 4.3 a) shows that, for all traces, the photostationary state population decreases as  $\Delta T$  increases. If  $\tau$  is 10  $\mu\text{s}$ ,  $n_\infty$  decays rapidly to 0, but as  $\tau$  becomes larger, the variation of  $n_\infty$  with  $\Delta T$  becomes smaller. If  $\tau$  exceeds the  $\mu\text{s}$  range (e.g.  $\tau = 100 \text{ ms}$ ), almost no variation with  $\Delta T$  is observed. **This is qualitatively as expected and shows that measuring the population of a long-lived state as a function of  $\Delta T$  can be used to determine its lifetime, if  $\tau$  is in the range of  $\Delta T$  accessed by tuning the laser repetition rate.**

It should be noted, though, that the dependency of  $n_\infty$  on  $\Delta T$  is also strongly dependent on laser fluence, i.e.  $\alpha^*$ . In Figure 4.3 a), in addition to the solid lines, for  $\tau = 1 \text{ ms}$

two dashed lines are shown, which correspond to  $\alpha^* = 0.15$  and  $\alpha^* = 0.6$ , respectively. Clearly, although  $\tau$  is the same, the dependence of  $n_\infty$  on  $\Delta T$  is very different. The traces are still unique for a given  $\tau$ , i.e. one cannot find a combination of  $\alpha^*$  and  $\tau$  that yields the *exact* same result: A fit with equation 4.35 of any of the traces calculated above gives the correct  $\tau$ , upon leaving  $\alpha^*$  as free parameter. Yet, by try and error I find that  $\tau = 550 \mu s$ ,  $\alpha^* = 0.3$  comes very close to  $\tau = 1 ms$ ,  $\alpha^* = 0.15$  (within less than 3% deviation for all  $\Delta T$ , not shown). Hence, **determining the lifetime of the photostationary state with a repetition rate dependency requires ideally very high quality data. Alternatively, the additional knowledge of the proportionality factor between laser fluence and the population/depopulation parameters  $\alpha$  and  $\beta$  gives access to the lifetime.** This strategy is pursued in this thesis: In chapter 5, section 5.3 I will apply the model to determine the lifetime of a photostationary electron population at the ZnO(10-10) surface.  $\alpha$  can be estimated to be much lower than  $\beta$  and  $\beta$  can be determined with the help of pump-probe measurements.

$n_\infty$  also has a non-trivial fluence dependence which can be used as additional measure of the lifetime. 4.3 b) shows what to expect from a variation of  $\alpha^*(F)$  for a *given* laser repetition rate  $R = 200 kHz$  ( $\cong \Delta T = 5 \mu s$ ). For  $\tau = 1 \mu s$ ,  $n_\infty$  increases almost linearly upon increasing  $\alpha^*$  from 0 to 1. For larger  $\tau$ ,  $n_\infty$  rises faster at low fluence and saturates towards higher fluences (see the traces for  $\tau = 100 \mu s$  and  $\tau = 1000 \mu s$ ). The fluence dependence is characteristic for the photostationary state lifetime. Also in this case it is important to know the proportionality factor between laser fluence and the population/depopulation coefficient for the scaling of the x-axis. Note that, a trivial case is, when  $\tau \rightarrow \infty$ . Then the population becomes independent of fluence like a truly static occupied (photoexcitation independent) state.

**Rise of the photostationary population.** For experiments on a sample that is in a photostationary state, it is important to know at which timescale the photostationary equilibrium is assumed. It is possible to model the rise of the photostationary state population, the dashed line in Figure 4.1, by calculating the partial sum for a finite number of pulses. The partial sum is for a geometric series with ratio  $q$  between successive terms:

$$n_k^0 = \alpha N \frac{1 - q^k}{1 - q} \quad (4.36)$$

With  $q$  from equation 4.32 and  $n_\infty$  from equation 4.35, the population monitored by the  $k + 1$ -th pulse can be written as

$$n_{k+1}^{\Delta T} = (1 - (1 - (\alpha + \beta))^k e^{-k\Delta T/\tau}) n_\infty. \quad (4.37)$$

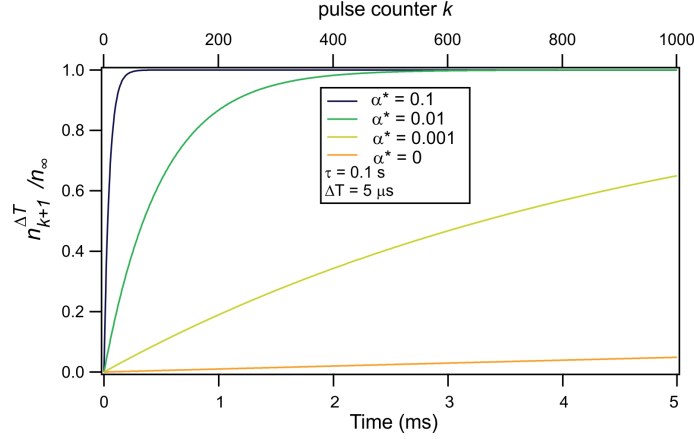


**Figure 4.4:** Numerical evaluation of the rise of the photostationary equilibrium for different laser fluences, i.e.  $\alpha^* \equiv \alpha + \beta$  as indicated in the legend. Plotted is the partial sum, equation 4.37, normalized by photostationary equilibrium  $n_{\infty}$  which is eventually approached. The top axis is the pulse counter  $k$  and the bottom axis is the time passed, calculated from the pulse counter and the temporal distance between two pulses  $\Delta T$ , which is taken as  $5 \mu\text{s}$ . The lifetime is assumed as  $0.1 \text{ s}$ .

Figure 4.4 shows a numerical evaluation of the buildup of the photostationary population for different laser fluences, i.e.  $\alpha^* \equiv \alpha + \beta$ . Plotted is the partial sum, equation 4.37, normalized by photostationary equilibrium  $n_{\infty}$  which is eventually approached. The top axis is the pulse counter  $k$  and the bottom axis is the time passed calculated via  $t = k \Delta T$ .  $\Delta T$  is taken as  $5 \mu\text{s}$ , corresponding with most experiments presented in this thesis.<sup>13</sup> The lifetime is assumed to be  $0.1 \text{ s}$ . For low fluences  $\alpha^* \approx 0$ , the rise is slow, on timescales that correspond with the lifetime of the state. Indeed, for  $\alpha(F) \approx 0$  and  $\beta(F) \approx 0$  the exponential function in equation 4.37 is dominant and hence the photostationary population builds up exponentially with  $e^{-\frac{k\Delta T}{\tau}} = e^{-\frac{t}{\tau}}$ . The rise time is identical to  $\tau$ . For finite  $\alpha$  and  $\beta$ , the convergence of the geometric series is quicker, which leads to a faster buildup of the photostationary state. As can be seen from Figure 4.4, for  $\alpha^* = 0.1$  the rise lasts only about  $300 \mu\text{s}$ . This value of  $\alpha^*$  is a realistic value for the experiments on the photostationary state at the ZnO(10-10) presented within this thesis: At the end of this chapter I will show that  $\beta$  alone must be on the order of  $0.1$ . For such high values of  $\alpha$  and  $\beta$  the exponential term containing  $\tau$  in equation 4.37 becomes irrelevant, and the photostationary equilibrium is approached on a  $\mu\text{s}$  timescale, even if the state had a lifetime of minutes or hours.

Note that if at the start the sample is not in equilibrium, but some population  $n_0$  is

<sup>13</sup>The base repetition rate of the laser system is  $200 \text{ kHz}$ , which corresponds to  $\Delta T = 5 \mu\text{s}$ . The repetition rate can be lowered as described in section 3.2.1

present already before the first laser pulse excites the sample, the partial sum becomes

$$n_k^0 = \alpha N \frac{1 - q^k}{1 - q} + n_0 q^k. \quad (4.38)$$

The contribution of the initial population approaches zero with the same pace as the new population rises, which is in analogy to the continuous wave model, cf. equation 4.23. Also the above-discussed result that the buildup time is equal to  $\tau$  and becomes faster with increasing fluence (hence increasing  $\alpha$  and  $\beta$ ) is analogous to the continuous wave model in section 4.1.1. In the next paragraph I show that both models yield the identical expression for  $n_\infty$ , when the lifetime of the long-lived state is much longer than the pulse-to-pulse distance  $\Delta T$ .

**Limiting case  $\tau \gg \Delta T$ : Convergence of pulsed laser and continuous wave model.** The basic assumption made to model the photostationary state population with infinitesimal time steps was to assume that the photostationary population does not evolve substantially within the gap between subsequent laser pulses, i.e.  $\Delta T$ , see section 4.1.1 and ref. [Gah04]. In this case, the pulsed laser can be considered as quasi-continuous light source. Here I show that the expression for  $n_\infty$  developed with the pulsed laser model in this section approaches the result of the continuous wave model of section 4.1.1 when  $\tau \gg \Delta T$ .

The two expressions are:

$$n_\infty = \frac{\tilde{\alpha} N}{\tilde{\alpha} + \tilde{\beta} + 1/\tau} \text{ eq. 4.24}; n_\infty = \frac{\alpha N}{e^{\Delta T/\tau} + \alpha + \beta - 1} \text{ eq. 4.35} \quad (4.39)$$

They have a very similar structure. In the pulsed laser result the repetition rate (or  $\Delta T$ ) dependency is explicitly contained in the exponential  $e^{\Delta T/\tau}$ . In the continuous wave result the repetition rate enters via the rate coefficients. Their definition is (equation 4.22)

$$\tilde{\alpha} = a F R ; \tilde{\beta} = b F R. \quad (4.40)$$

In contrast, the excitation probabilities  $\alpha$  and  $\beta$  in the pulsed laser model are defined as

$$\alpha = aF ; \beta = bF. \quad (4.41)$$

In both cases,  $a$  and  $b$  are defined as the photoexcitation cross section for optical population/depopulation and  $F$  is the laser fluence. Clearly, both definitions are just different by the repetition rate  $R = 1/\Delta T$  and one can write

$$\tilde{\alpha} = \frac{\alpha}{\Delta T} ; \tilde{\beta} = \frac{\beta}{\Delta T} \quad (4.42)$$

With this, the expression for  $n_\infty$  resulting from the pulsed laser model (eq. 4.35) can be written as:

$$n_\infty = \frac{\alpha N}{e^{\Delta T/\tau} + \alpha + \beta - 1} = \frac{\tilde{\alpha} N}{\frac{1}{\Delta T} e^{\Delta T/\tau} + \tilde{\alpha} + \tilde{\beta} - \frac{1}{\Delta T}} \quad (4.43)$$

Expanding the exponential function in the denominator as series

$$n_\infty = \frac{\tilde{\alpha} N}{\frac{1}{\Delta T} (1 + \frac{\Delta T}{\tau} + \frac{\Delta T^2}{2\tau^2} + \dots) + \tilde{\alpha} + \tilde{\beta} - \frac{1}{\Delta T}} \quad (4.44)$$

one can finally introduce the approximation  $\tau \gg \Delta T$  and  $n_\infty$  from the pulsed laser model becomes

$$n_\infty \approx \frac{\tilde{\alpha} N}{\frac{1}{\Delta T} (1 + \frac{\Delta T}{\tau}) + \tilde{\alpha} + \tilde{\beta} - \frac{1}{\Delta T}} = \frac{\tilde{\alpha} N}{\tilde{\alpha} + \tilde{\beta} + \frac{1}{\tau}}. \quad (4.45)$$

Hence, notably, in this approximation the pulsed laser model gives the identical result as the continuous wave model (equation 4.24). Note that when  $\tau$  is on the order of  $\Delta T$  the higher order terms in the series  $1 + \frac{\Delta T}{\tau} + \frac{\Delta T^2}{2\tau^2} + \dots$  dominate the  $\Delta T$  dependency. For such lifetimes the pulsed laser model is the appropriate model to use.

In summary of this section, a pulsed laser model for describing photostationary state populations based on optical population and depopulation was developed. It represents the extension of the continuous wave model (section 4.1.1) to small lifetimes on the order of the inverse laser repetition rate  $\Delta T$ . The model describes the change of a photostationary population upon variation of the laser fluence and repetition rate and can be used to extract the lifetime of such states.

## 4.2 Pump-probe spectroscopy with photostationary states

In the preceding section a model was developed to describe the population of photoexcited states that survive the inverse laser repetition rate, which explicitly takes into account excitation with repetitive laser pulse. Assuming that each laser pulse populates and depopulates the electronic population, an expression was derived for the buildup of a photostationary population, which does not change anymore from pulse to pulse. The model will be used in the subsequent chapter 5 for lifetime determination of a photostationary electron population at the ZnO(10-10) surface, measured with photoelectron spectroscopy. The fact that the sample is in a photostationary state is in conflict with the usual assumption for pump-probe spectroscopy that the pump laser pulse encounters a sample in equilibrium. As photostationary states are not only observed for the system investigated within this thesis, but are quite ubiquitously reported in literature (see the introduction to this chapter), it is important to understand how photostationary populations can contribute to the signals measured in pump-probe spectroscopy. The present

section develops the extension of the population-depopulation model for the case of two laser beams delayed to each other that can both influence the photostationary state. It is demonstrated with exemplary time-resolved photoelectron spectroscopy measurements of ZnO(10-10) that this leads to counterintuitive delay-dependent signals. As a motivation for carrying out the calculations, an outline of the experimental data and the idea to explain the observed counterintuitive ultrafast dynamics is given in the following.

### 4.2.1 Motivation

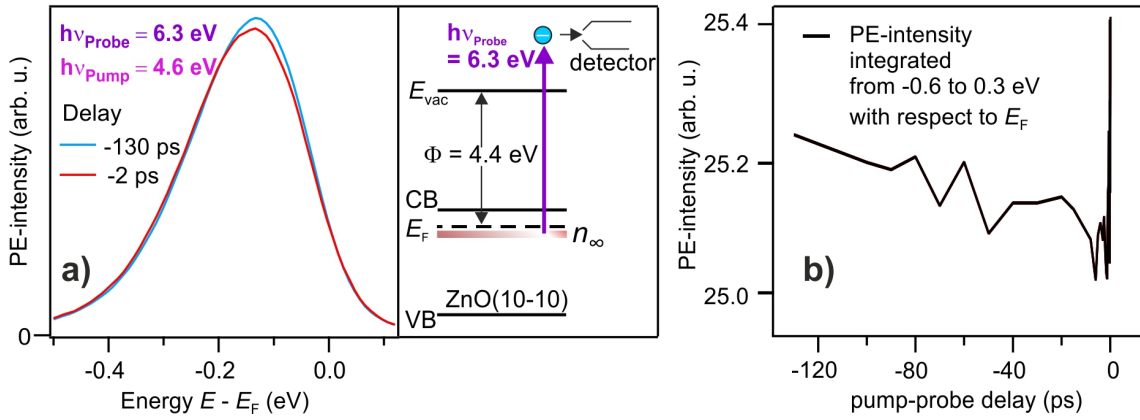


**Figure 4.5:** Counterintuitive ultrafast dynamics in pump-probe scans at ZnO(10-10). a) Photoemission (PE)-intensity upon photoemission with  $h\nu_{\text{Probe}}=6.3$  eV from ZnO(10-10) displayed versus initial state energy  $E - E_F$ . A pump laser pulse  $h\nu_{\text{Probe}}=4.6$  eV is applied at negative pump-probe delays, -2 ps and -130 ps). The photoelectrons arise from a photostationary state  $n_\infty$  just below  $E_F$  as indicated in the energy level diagram. Vacuum level  $E_{\text{vac}}$ , work function  $\Phi$ , CB and VB of ZnO are also indicated; as the sample is n-type doped the Fermi level is just below the CB. b) Integrated intensity of the probed electrons below  $E_F$  for negative delays between 0 and -130 ps.

The basic observation that the model aims to describe is shown in Figure 4.5. The photostationary electron population at the ZnO(10-10) surface is, on the absolute energy scale, located below the equilibrium Fermi energy. Figure 4.5 a) shows photoelectron spectra of this energy range that reveal a broad peak of several hundred meV at about 0.1 eV below the Fermi energy  $E_F$ . The electrons are photoemitted from the sample with  $h\nu_{\text{Probe}}=6.3$  eV in a one-photon photoemission (1PPE) process as the photon energy is above the work function of the sample ( $\Phi=4.4$  eV), cf. the energy level diagram in Figure 4.5 a). In addition to the probe laser pulses, time-delayed pump laser pulses with a photon energy of  $h\nu_{\text{Pump}}=4.6$  eV arrive at the sample. Figure 4.5 a) shows that the intensity of the photostationary state probed with  $h\nu_{\text{Probe}}=6.3$  eV changes upon setting different *negative* pump-probe delays: For  $\Delta t=-130$  ps the photoelectron intensity is higher than at  $\Delta t=-2$  ps. The effect is small but systematic: Figure 4.5 b) shows the integrated

photoelectron intensity due to the photostationary electron population as a function of negative pump-probe delays from 0 ps to -130 ps. From small negative to large negative there is a monotonous rise of the signal.

The observed dynamics toward negative delays cannot be explained within the usual framework of pump-probe spectroscopy: From the pump-probe scheme to monitor ultrafast population dynamics, only at *positive* pump-probe delays a change of the photoelectron intensity detected by the probe laser beam would be expected, cf. section 3.1.4. At positive delays, the pump laser pulse arrives at the sample before the probe laser pulse and creates a non-equilibrium electronic population which is then monitored by the probe laser pulse. At negative pump-probe delays, ultrafast dynamics launched by the pump pulse in the sample cannot be observed with the probe laser pulse, because the pump pulse arrives after the probe pulse. It should be noted that pump-induced fields that extend from the sample into the vacuum can lead to *shifts* of the probe photoelectron spectra at negative pump-probe delays. As explained in section 3.1.5, these shifts result from the acceleration or deceleration of the probe electrons by the pump-induced field during their propagation to the detector. However, this leaves the overall amount of detected photoelectrons emitted by the probe laser pulses unaffected. Hence, the observed delay dependency of the photoelectron *intensity* emitted by the probe laser pulses in Figure 4.5 also cannot be explained by this effect.

Instead, it seems likely that the negative delay dynamics is related to that the state survives longer than the inverse laser repetition rate: Negative pump-probe delays mean, on the one hand, that the pump laser pulse arrives after the probe laser pulse (delayed by  $\Delta t$ ). On the other hand, because the laser excitation is repetitive, negative pump-probe delays also mean that there is a pump laser pulse that arrives *before* the probe laser pulse by about the inverse laser repetition rate (5  $\mu\text{s}$  in the present experiment), cf. Figure 4.6 a). As the photoexcited population by the pump survives longer than the inverse repetition rate, this leads to a finite pump-induced signal at negative pump-probe delays. This explains why *in general* an effect of the pump is expected at negative delays, but the question remains why the timing on a *picosecond* timescale matters for the population detected after *microseconds*.

In order to understand this it is important to recapitulate how pump-probe measurements are carried out in the present experimental setup. As described in section 3.2.5, trARPES measurements are performed by setting a certain delay between pump and probe pulses and then staying at this delay for a certain integration time. The integration time has to be at least as long as the smallest camera exposure time, which is 30 ms. Over this time span thousands (30 ms/5  $\mu\text{s}$ =6000) of laser pulses arrive at the sample - long enough to establish a photostationary state. This was shown in the last section by modeling the

rise of the photostationary state with the pulsed laser model.<sup>14</sup> The basic idea to explain the dependency of the photostationary signal on the negative pump-probe timing is that both, pump *and* probe pulses, modify the photostationary state population via optical population and depopulation. A different photostationary equilibrium results due to the interplay of these two pulses on the ultrafast time scale.

This idea is detailed in Figure 4.6. Figure 4.6 a) sketches the build-up of the photostationary population upon repetitive excitation with laser pulses from two laser beams that are delayed with respect to each other. The sample is initially in equilibrium, but because the photoexcited state does not decay in between to subsequent laser pulses, a photostationary population builds up. The photoexcited electron population is then encountered by both, the first and second laser pulse in the sequence of pulse pairs. For negative pump-probe delays, the probe is the first pulse in the sequence, and the pump is the second. In order to realize a different photostationary population  $n_\infty$  depending on the negative pump-probe timing the population scheme displayed in Figure 4.6 b) is proposed, first for the probe laser beam only: Upon arrival of the probe laser pulse, the long-lived state  $n$  is populated indirectly via an intermediate state. The intermediate state populates  $n$  with the time constant  $\kappa$ , which is on the picosecond time scale.  $n$  then survives the inverse laser repetition rate and is depopulated with the coefficient  $\beta$  and populated again via the intermediate state with the next laser pulse. In Figure 4.6 c) and d) the scheme is extended to two laser beams, delayed by  $\Delta t$ . The second laser beam (the pump laser beam) is also capable of depopulating  $n$  with the coefficient  $\beta_+$ . In addition it depopulates the intermediate state with the coefficient  $\gamma_+$  and after a time scale corresponding with  $\kappa$  a certain  $n$  is established. A dependence of  $n$  on the negative pump-probe timing  $\Delta t$  arises when the coefficients  $\gamma_+$  and  $\beta_+$  are not equal: At small negative pump-probe delays (Figure 4.6 c)), the pump laser pulse encounters a larger intermediate state population (and smaller  $n$ ) than at large pump-probe delays (Figure 4.6 d)). If, say,  $\gamma_+$  is larger than  $\beta_+$ , at small pump-probe delays more states are depopulated than at large pump-probe delays. Consequently, a smaller population of  $n$  results after the pulse pair. Upon repetitive excitation a smaller *photostationary* population  $n_\infty$  is established at small negative pump-probe delays compared to large negative pump-probe delays.

The probe and pump laser pulses  $h\nu_{\text{Probe}}=6.3$  eV and  $h\nu_{\text{Pump}}=4.6$  eV of the experiment presented above indeed both influence the  $n_\infty$  population likewise by depopulation and subsequent population via an intermediate state as will be shown in section 4.2.3. Hence, the above outlined idea explains qualitatively why a dynamic rise of the probed photoelectron intensity of the photostationary population is observed from small to large

---

<sup>14</sup>The fast rise time is experimentally verified by blocking and unblocking the pump laser beam at negative pump-probe delays. Because the pump laser beam populates the long-lived state, it induces an increase of the photoemission intensity detected with the probe laser beam. The signal increase is observed promptly, i.e. from one to another frame taken with the camera.

negative delays. The time scale at which the dynamic change occurs must be related to the characteristic time constant the intermediate state decays into the long-lived state  $n$ , i.e to  $\kappa$ . The functional form to describe this relationship will be derived with the model in the next section.

Note that the transition from the intermediate state to  $n$  does not necessarily have to be a transition between different electronic levels, but it could be also, for example, a strong dynamic modification of  $n$  e.g. via electron-phonon interaction. This could change the matrix elements in Fermis golden rule, equation 3.12, i.e. the transition probability from  $n$  to the final state and hence modify the depopulation probability.

In the subsequent section, I will elaborate the mathematical framework to substantiate the above-introduced explanation. The model is then compared to the experimental data in section 4.2.3.

#### 4 Mathematical framework to deal with photostationary states in pump-probe spectroscopy

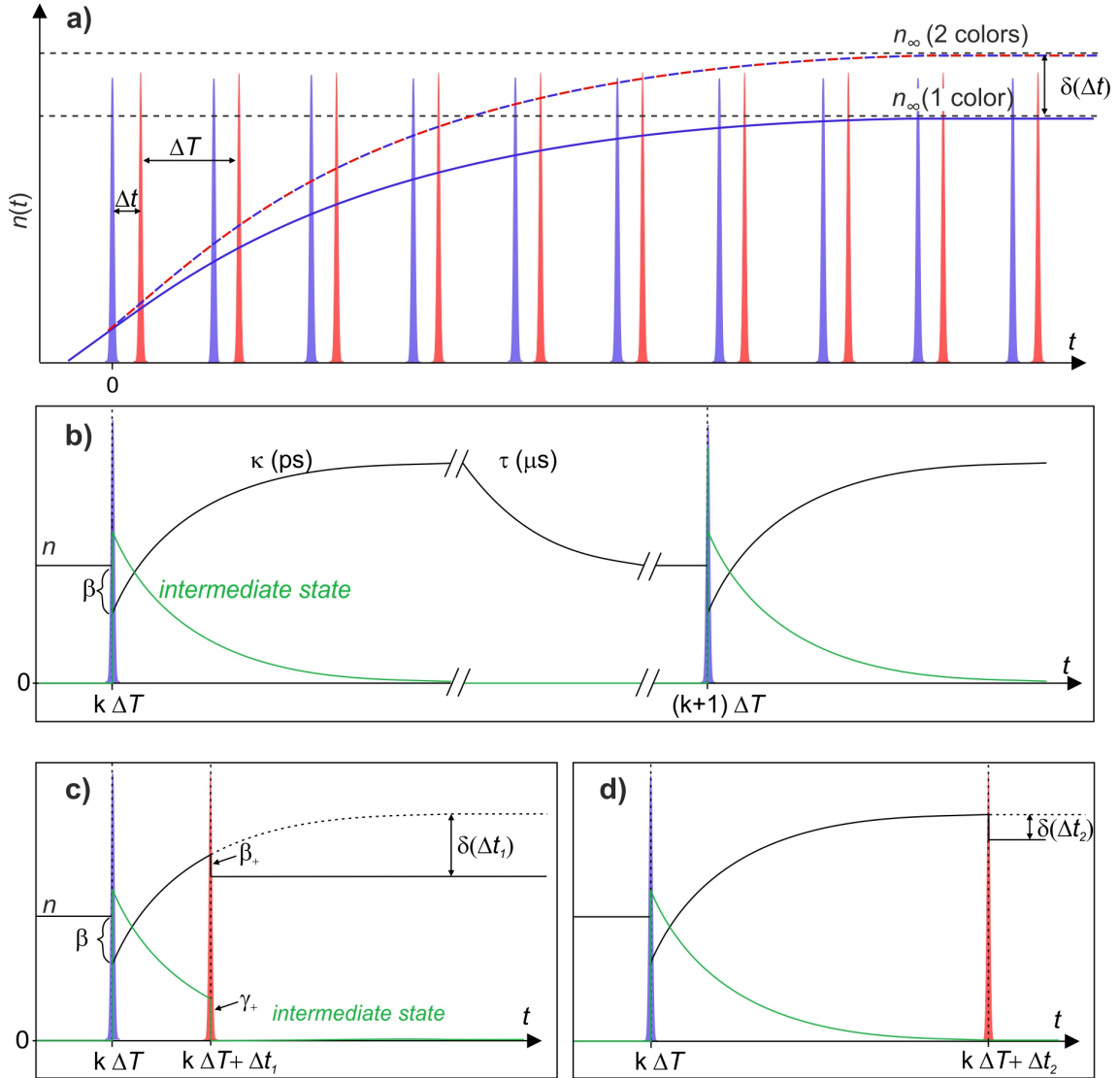


**Figure 4.6:** a) Pump-probe spectroscopy with photostationary states: Two pulses are delayed with respect to each other by  $\Delta t$ . If the first laser pulse is defined as 'pump' and the second as 'probe' laser pulse, the configuration corresponds to negative delays. The stationary state population  $n_\infty$  of a long-lived photoexcited state may depend on the timing between first and second laser pulse. b)-d) Schematics to explain the delay dependency of  $n_\infty$ . b) Simple population model for  $n$  on ultrafast ( $\Delta t \ll \Delta T$ ) time scale (case of single laser beam).  $n$  is populated indirectly via an intermediate state, exponentially with the time constant  $\kappa$ . c) d) Extension to two laser beams. The first laser pulse populates the intermediate state and depopulates  $n$ . The second laser pulse arrives within a time on the order of  $\kappa$ . It depopulates  $n$  with  $\beta_+$  and the intermediate state with  $\gamma_+$ . In the case that the intermediate state is depopulated more efficiently than  $n$ , at a small time delay (c) overall more depopulation takes place than at a large delay (d)), where all intermediate states have decayed into  $n$ . The population of  $n$  after the pulse pair is hence delay-dependent, with  $\delta(\Delta t_1) > \delta(\Delta t_2)$ ,  $\Delta t_1 < \Delta t_2$ . The model in section 4.2.2 shows that this delay-dependency is then manifested in  $n_\infty$  as well. It corresponds with the filling of  $n$  via the intermediate state, i.e. is an exponential rise with time constant  $\kappa$ . Note that, for simplicity, in c) and d), the coefficient for *populating* the intermediate state with the second laser pulse is set to 0. This does not influence the argument that a larger  $n$  is reached for larger pump-probe delays, because the efficiency to populate the intermediate state is equal for small and large delays.

### 4.2.2 Model for pump-probe spectroscopy

In this section, I extend the geometric series model to two pulses in order to tackle pump-probe measurements involving photostationary states. I treat the case, where both, pump *and* probe populate and depopulate the long-lived state  $n$  (the cases, where either of them does not occur are contained as limiting cases). The simple model introduced in the preceding section for the population of the photostationary state on ultrafast timescales is assumed. I introduce it first for a single laser beam. Each laser pulse populates an intermediate state which then subsequently populates  $n$  with the time constant  $\kappa$ , which is much smaller than  $\Delta T$  (cf. Figure 4.6 b)). This process is mathematically described with

$$\begin{aligned}\frac{d}{dt}n_{\text{is}} &= -1/\kappa n_{\text{is}}(t) \\ \frac{d}{dt}n &= 1/\kappa n_{\text{is}}(t).\end{aligned}\tag{4.46}$$

Here  $n_{\text{is}}$  is the population of the intermediate state. The process of population of the intermediate state is, as in the single color model developed in section 4.1.2, described with an excitation probability  $\alpha$  that is proportional to the laser fluence. The number of excited states is given by multiplication of  $\alpha$  with the maximum number of states that can be populated,  $N$ :

$$n_{\text{is}}(t=0) = \alpha N,\tag{4.47}$$

The solution of the coupled rate equations (equation 4.46) is

$$\begin{aligned}n_{\text{is}}(t) &= \alpha N e^{-t/\kappa} \\ n(t) &= \alpha N (1 - e^{-t/\kappa}) + n_0\end{aligned}\tag{4.48}$$

where  $n_0$  is a constant offset. Furthermore,  $n$  decays exponentially with the intrinsic lifetime  $\tau$ , which is on the order of  $\Delta T$  and hence occurs at a vastly different time scale than the ultrafast population via the intermediate state. Hence, it is not included in the rate equation system, equation 4.46. At time scales where the exponential decay with  $\tau$  comes into play, the population via the intermediate state is by far completed. The evolution of  $n(t)$  for time scales much longer than  $\kappa$  is therefore

$$n(t) = (\alpha N + n_0)e^{-\frac{t}{\Delta T}}\tag{4.49}$$

Each laser pulse encounters a population remaining from preceding excitation events, termed  $n_R$ . The offset  $n_0$  is related to this via the depopulation coefficient  $\beta$  (cf. Figure 4.6 b))

$$n_0 = (1 - \beta)n_R\tag{4.50}$$

With this, equation 4.49 becomes

$$n(t) = (\alpha N + (1 - \beta)n_R)e^{-\frac{t}{\Delta T}}. \quad (4.51)$$

Now a second laser beam, delayed by  $\Delta t$  is introduced.  $\Delta t$  is restricted to values much smaller than the inverse laser repetition rate  $\Delta T$ . In the following, the second laser beam is referred to as 'probe' and the first laser beam is referred to as 'pump', corresponding to positive pump-probe delays. For the probe, the population and depopulation probabilities  $\alpha_+$  and  $\beta_+$  are defined. The depopulation of the intermediate state by the probe laser pulse is neglected for now and will be included later in this section.

As in case of the single color model in section 4.1.2, I start again with the sample in equilibrium, i.e.  $n_R = 0$  and then calculate the population of the long-lived state  $n$ . The pulse counter  $k$  now stands for a pulse pair.

$k=1$ : The first pump laser pulse arrives at the time  $t_1$  and the first probe laser pulse follows at  $t_2$ . The population of  $n$  at the time the probe laser pulse arrives can be described with equation 4.48:

$$n(t_2) = \alpha N(1 - e^{-(t_2-t_1)/\kappa}). \quad (4.52)$$

The probe laser pulse populates the intermediate state  $n_{is}$ , which subsequently enhances the population of  $n$  according to equation 4.48. In addition, it depopulates the existing  $n$ , i.e.  $n(t_2)$ . After the arrival of the probe laser pulse and for time scales of  $\Delta T$  or  $\tau$  (i.e. much larger than  $\kappa$ ),  $n$  is described with :

$$n(t - t_2) = [\alpha_+ N + (1 - \beta_+)n(t_2) + \alpha N e^{-\Delta t/\kappa}]e^{-(t-t_2)/\tau} \quad (4.53)$$

The term  $[\alpha_+ N + (1 - \beta_+)n(t_2)]e^{-(t-t_2)/\tau}$  corresponds to equation 4.51, with  $n_R = n(t_2)$ . The term

$$e^{-\Delta t/\kappa}(1 - e^{-(t-t_2)/\kappa}) \quad (4.54)$$

is the part of the intermediate state population that fills up  $n$  after the arrival of the probe pulse.<sup>15</sup> It therefore is not depleted by the probe pulse (no  $(1 - \beta_+)$  prefactor for this term).

---

<sup>15</sup>This term is not contained in 4.51, because for a sequence of repetitive laser pulses with only one laser beam, no intermediate state population is left at the time a pulse arrives (because the temporal distance  $\Delta T$  between subsequent laser pulses is large compared to  $\kappa$ ).

$k=2$ : The next pump laser pulse arrives at  $t = t_1 + \Delta T$  and encounters the population

$$n(t_1 + \Delta T) = [\alpha_+ N + (1 - \beta_+)n(t_2) + \alpha N e^{-\Delta t/\kappa}] e^{-(t_1 + \Delta T - t_2)/\tau}. \quad (4.55)$$

Because  $\Delta t = t_2 - t_1 \ll \Delta T$  one can approximate the argument  $e^{-(t_1 + \Delta T - t_2)/\tau}$  of the exponential function:

$$n(t_1 + \Delta T) = [\alpha_+ N + (1 - \beta_+)n(t_2) + \alpha N e^{-\Delta t/\kappa}] e^{-\Delta T/\tau}. \quad (4.56)$$

At this point it is useful to define the following abbreviations:

$$A(\Delta t) = ((1 - \beta_+)\alpha N + \beta_+ \alpha N e^{-\Delta t/\kappa}) e^{-\Delta T/\tau} \quad (4.57)$$

$$B = \alpha_+ N e^{-\Delta T/\tau} \quad (4.58)$$

With these abbreviations the population encountered by the pump pulse of the second pulse pair, equation 4.56, can be abbreviated after some algebra as

$$n(t_1 + \Delta T) = A(\Delta t) + B \quad (4.59)$$

Now, again the pump laser pulse populates the intermediate state  $n_{is}$ , which subsequently enhances the population of  $n$  according to equation 4.48. In addition, it depopulates the existing  $n$ . After  $\Delta t$ , the probe laser pulse of the second pulse pair thus encounters the population (note again: the decay of the population with  $\tau$  happens on a much longer time scale than  $\Delta t$ ):

$$n(t_1 + \Delta T + \Delta t) = (1 - \beta)(A(\Delta t) + B) + \alpha N(1 - e^{-\Delta t/\kappa}). \quad (4.60)$$

Now, again the probe laser pulse populates  $n$  via the intermediate state, and depopulates the population  $n(t_1 + \Delta T + \Delta t)$  it encounters. For time scales of  $\Delta T$  or  $\tau$  (i.e. much larger than  $\kappa$ ) after the arrival of the probe laser pulse,  $n$  decays exponentially. The equation to describe the temporal evolution after the arrival of the probe laser pulse is analogous to equation 4.53 is not explicitly written down here again.

$k=3$ : The population the pump laser pulse of the third pulse pair encounters is

$$\begin{aligned} n(t_1 + 2\Delta T) &= [\alpha_+ N + (1 - \beta_+)((1 - \beta)(A(\Delta t) + B) + \alpha N(1 - e^{-\Delta t/\kappa})) \\ &\quad + \alpha N e^{-\Delta t/\kappa}] e^{-\Delta T/\tau} \\ &= (1 - \beta_+)(1 - \beta)(A(\Delta t) + B)e^{-\Delta T/\tau} + A(\Delta t) + B \end{aligned} \quad (4.61)$$

The population the probe laser pulse of the third pulse pair encounters is

$$n(t_1 + 2\Delta T + \Delta t) = (1 - \beta)(1 - \beta_+)(1 - \beta)(A(\Delta t) + B)e^{-\Delta T/\tau} + (1 - \beta)(A(\Delta t) + B) + \alpha N(1 - e^{-\Delta t/\kappa}) \quad (4.62)$$

The same structure repeats in the following pulse pairs. For the  $k$ -th pulse pair, the population the pump and probe laser pulses encounter is

$$n_{k,\text{pump}} = (A(\Delta t) + B) \sum_{j=0}^{k-2} (1 - \beta_+)^j (1 - \beta)^j (e^{-\frac{\Delta T}{\tau}})^j \quad (4.63)$$

$$n_{k,\text{probe}} = \alpha N(1 - e^{-\Delta t/\kappa}) + (1 - \beta)n_{k,\text{pump}}$$

This is, as in the single color model, a geometric series. In the limit  $k \rightarrow \infty$  the photostationary equilibrium is reached:

$$n_{\infty,\text{pump}} = \frac{A(\Delta t) + B}{1 - (1 - \beta_+)(1 - \beta) e^{-\frac{\Delta T}{\tau}}} \quad (4.64)$$

$$n_{\infty,\text{probe}} = \alpha N(1 - e^{-\Delta t/\kappa}) + (1 - \beta)n_{\infty,\text{pump}}$$

with

$$A(\Delta t) = ((1 - \beta_+)\alpha N + \beta_+\alpha N e^{-\Delta t/\kappa}) e^{-\Delta T/\tau}$$

$$B = \alpha_+ N e^{-\Delta T/\tau} \quad (4.65)$$

Note that the definition of the first laser pulse as the 'pump' and the second laser pulse as the 'probe' with the delay  $\Delta t > 0$  and much smaller than  $\Delta T$  corresponds to positive pump-probe delays. It is also possible to define the first laser pulse as the 'probe' and the second laser pulse as the 'pump'. This corresponds to negative pump-probe delays. In this case, in the model still  $\Delta t > 0$  has to be assumed, and this delay is the modulus of the negative pump-probe delay. In general, the model above is the result for two laser pulses delayed by  $\Delta t > 0$  and much smaller than  $\Delta T$ . For the general case (positive *or* negative pump-probe delays), it makes sense to label the photostationary population the laser pulses encounter, equation 4.64, as:

$$n_{\infty,1} = \frac{A(\Delta t) + B}{1 - (1 - \beta_+)(1 - \beta) e^{-\frac{\Delta T}{\tau}}} \quad (4.66)$$

$$n_{\infty,2} = \alpha N(1 - e^{-\Delta t/\kappa}) + (1 - \beta)n_{\infty,\text{pump}}$$

**The above is a remarkable result because it shows that the photostationary state population depends on the modulus of the pump-probe timing  $\Delta t$  through**

**the term**  $A(\Delta t)$ . The delay dependency is found for both, the population encountered by the first and the second laser pulse in the sequence of pulse pairs, respectively. In the framework of pump-probe spectroscopy this is unusual: In configuration of *positive delays* only the probe laser pulse is expected to be able to monitor ultrafast dynamics (always assuming  $\Delta t \ll \Delta T$ ). The model shows that, due to the interplay between population and depopulation of pump and probe pulses, combined with the lifetime of the so-modulated state larger than  $\Delta T$ , also the population the pump pulse encounters depends on  $\Delta t$ . This is although it arrives the large time span  $\Delta T - \Delta t \approx \Delta T$  after the preceding probe excitation event. If the pump laser pulse is suitable to *monitor* the population  $n$ , in a pump-probe experiment one would see dynamics toward positive delays detected by the *pump* laser pulse. The other way around is also possible: If one defines the second laser pulse in the above model as 'pump' and the first laser pulse as 'probe', the configuration corresponds to *negative delays*. The model predicts then that one sees dynamics toward negative delays detected by the *probe* laser pulse.

Note that the so-calculated delay-dependency of the photostationary state corresponds with the transition of the short-lived intermediate state into the long-lived state. In the above model, I assumed that this happens exponentially, i.e. with  $e^{-\Delta t/\kappa}$ . Thus, the delay-dependency of the photostationary state is not some kind of artifact arising in pump-probe spectroscopy, but contains information of a real population process happening on the ultrafast time scale.

In the model, the delay dependency in  $A(\Delta t)$  arises due to the capability of the first laser pulse to populate the intermediate state and hence  $n$ , and the second laser pulse to depopulate  $n$  (prefactor  $\beta_+\alpha$  in front of the term  $e^{-\Delta t/\kappa}$ ). Because both parameters  $\beta_+$  and  $\alpha$  are positive, an exponential *decay* upon increasing  $\Delta t$  is expected. Qualitatively, the decay arises because at a large  $\Delta t$  the second laser pulse encounters a larger population  $n$  and hence depletes more states than at a small  $\Delta t$ , cf. Figure 4.6 c) and d).

The depopulation of the intermediate state population drawn in Figure 4.6 c) and d) is so far completely neglected. In order to include this in the model, I simply modify equation 4.54 in the derivation above. This term

$$e^{-\Delta t/\kappa}(1 - e^{-(t-t_2)/\kappa}) \quad (4.67)$$

is the part of the intermediate state population that fills up  $n$  *after* the arrival of the second laser pulse. If it is depleted by the second laser pulse with the probability  $\gamma_+$ , only the fraction

$$(1 - \gamma_+)e^{-\Delta t/\kappa}(1 - e^{-(t-t_2)/\kappa}) \quad (4.68)$$

remains to fill up  $n$ .  $A(\Delta t)$  then becomes:

$$A(\Delta t) = ((1 - \beta_+) \alpha N + (\beta_+ - \gamma_+) \alpha N e^{-\Delta t/\kappa}) e^{-\Delta T/\tau} \quad (4.69)$$

and the rest of the derivation above stays identical. Now the delay dependent term  $A(\Delta t)$  and hence the photostationary population detected by the first laser pulse,  $n_{\infty,1}$ , describes an exponential *decay* if  $\beta_+$  is larger than  $\gamma_+$  and an exponential *rise* if  $\beta_+$  is smaller than  $\gamma_+$ . The delay dependent term of the photostationary state population only vanishes if  $\beta_+$  and  $\gamma_+$  are identical. Note that, if the photoexcited state  $n$  does not survive the inverse laser repetition rate,  $A(\Delta t) \rightarrow 0$ , because for  $\tau \ll \Delta T$ ,  $e^{-\Delta T/\tau} \rightarrow 0$ . In fact, the probe laser pulse would not encounter any photoexcited population at negative pump-probe delays as  $n_{\infty,1} \rightarrow 0$ . At positive pump-probe delays, it would still encounter the photoexcited population created by the preceding pump laser pulse as the term

$$\alpha N (1 - e^{-\Delta t/\kappa})$$

in the equation for  $n_{\infty,2}$  does not have the prefactor  $e^{-\Delta T/\tau}$ . Similarly, any other ultrafast population dynamics launched by the pump pulse can be observed by the probe pulse on top of dynamics related to photostationary states.

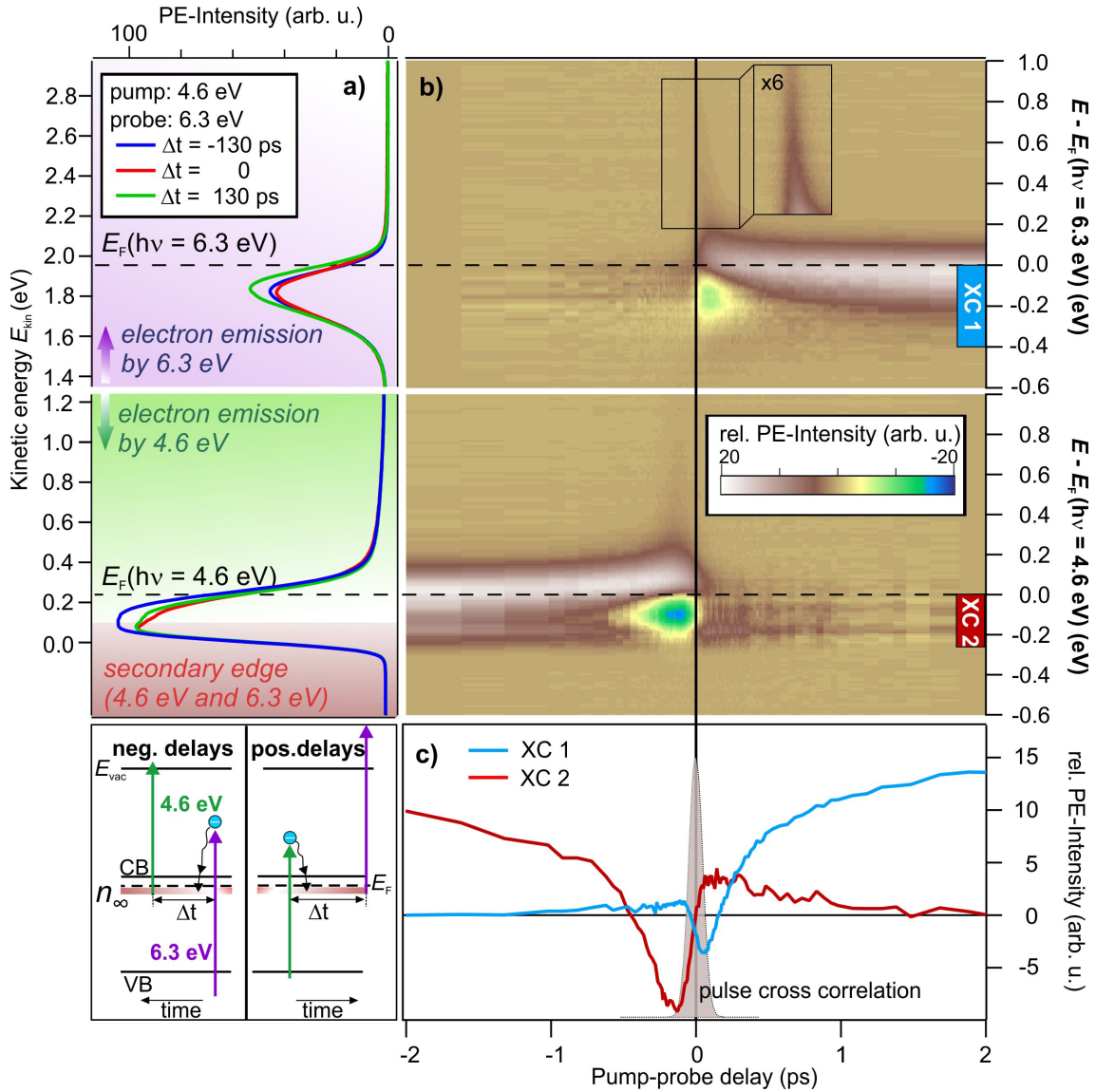


**Figure 4.7:** a) Photoelectron spectrum of ZnO upon overlapping 4.6 eV and 6.3 eV pulses at different delays  $\Delta t$ . Bottom: Schematic to illustrate how the pump-probe delay is defined: For positive pump-probe delays, 4.6 eV comes first and 6.3 eV follows. For negative pump-probe delays, 6.3 eV comes first and 4.6 eV follows. The photon energy of both colors is high enough to photoemit electrons from a photostationary electron population, indicated with  $n_{\infty}$  in the bottom of a). b) False color representation of a pump-probe scan in a window of 2 ps around time zero. The photoemission signal at a negative (positive) delay of 2 ps for the upper (lower) panel has been subtracted in order to show the pump-induced ultrafast dynamics. The energy axis is the energy with respect to  $E_F$  calculated for 6.3 eV (4.6 eV) photoemission in the upper (lower) panel. c) Integrated intensity traces (XC 1, 2 as indicated in b)) show the instantaneous depopulation and subsequent ps filling of electronic states spectrally located just below  $E_F$ , i.e. at the energy of  $n_{\infty}$ , monitored with the 6.3 eV and 4.6 eV, respectively. The population dynamics launched with 4.6 eV or 6.3 eV laser pulses are identical: The traces XC 1, 2 are mirrored with respect to time zero.

### 4.2.3 Exemplary dataset

In this section the dataset introduced in section 4.2.1 is compared to the model developed in the preceding section. I first present the experimental data in detail and then proceed with the evaluation. At the end of this section, I use the experiment and the model to extract the depopulation parameter  $\beta$  that will be needed for the lifetime determination of the photostationary state at the ZnO(10-10) surface in section 5.3.

**Description of the pump-probe experiment** Figure 4.7 a) shows photoelectron spectra of the ZnO(10-10) surface, prepared by sputtering and annealing cycles (cf. section 3.2.6), upon photoexcitation with 4.6 eV and 6.3 eV at different delays between the two laser beams; no background was subtracted. They are plotted versus kinetic energy  $E_{\text{kin}}$  (left axis) of the photoelectrons, which is determined with the hemispheric electron analyzer. The kinetic energy is zero for the low energy cut-off or the secondary edge.<sup>16</sup> Pump-probe delays are defined as illustrated in the bottom of Figure 4.7 a): For positive pump-probe delays, 4.6 eV comes first and 6.3 eV follows and for negative pump-probe delays, 6.3 eV comes first and 4.6 eV follows, delayed by  $\Delta t$ .

In the photoelectron spectra in Figure 4.7 a), two peaks are identified. Both change in intensity upon setting the pump-probe delay to 0, -130 and 130 ps. These intensity variations are related to the population and depopulation of a photostationary state population  $n_{\infty}$  as discussed below. On a binding energy scale the photostationary state population is located just below  $E_{\text{F}}$ , as indicated in the bottom of Figure 4.7 a). Because two different photon energies are used, which both can photoemit from below  $E_{\text{F}}$ , two peaks arise in the photoelectron spectra in Figure 4.7 a). The peak at low kinetic energy in the spectra is due to the electron population below  $E_{\text{F}}$  monitored with photoemission by the 4.6 eV laser pulses. In addition, there is a contribution from secondary electrons caused by 4.6 eV and 6.3 eV laser pulses, as this energy region is very close to the low energy cut-off at  $E_{\text{kin}}=0$ . Upon photoemission by 6.3 eV laser pulse the electron population below  $E_{\text{F}}$  is better resolved: Because the photon energy is higher by 1.7 eV, the photoelectrons emitted by 6.3 eV from the photostationary electron population have a higher kinetic energy and, hence, are well separated from the low energy cut-off. The peak center appears at  $E_{\text{kin}}=1.8$  eV and, in contrast to photoemission with 4.6 eV an almost symmetric Gaussian peak shape is observed. The peak width is several hundred meV. A detailed discussion regarding the origin of the photostationary population below  $E_{\text{F}}$  beyond what follows will be presented in chapter 5. In the following I focus on the ultrafast population changes related to the photostationary state.

---

<sup>16</sup>Note that, this kinetic energy axis denotes the kinetic energy of electrons that are just photoemitted from the sample (i.e.  $E_{\text{kin}}^0$  in the notation of section 3.1.3). This axis is derived from the raw data by setting the energy of the low energy cut-off to 0, since these electrons must arise from electrons with initially zero kinetic energy.

At first, it is demonstrated that both 4.6 eV and 6.3 eV laser pulses have exactly the same effect on the electron population below  $E_F$ ; they both populate and depopulate the electronic states detected in this energy region. This is evidenced by the ultrafast dynamics very close to time zero, visualized in a false color plot in a delay window of 2 ps around  $\Delta t = 0$  in Figure 4.7 b). The photoemission intensity is shown versus pump-probe delay (bottom axis) and initial state energy  $E - E_F$  (right axis) calculated for 6.3 eV and 4.6 eV photoemission. To show the ultrafast changes induced by the respective excitation pulse, the signal at negative delays (upper panel, photoemission by 6.3 eV) or positive delays (lower panel, photoemission by 4.6 eV) has been subtracted. For both, upper and lower panel, the photoelectron intensity below  $E_F$  is reduced immediately at  $\Delta t = 0$  and is subsequently enhanced within few hundred fs. Integration of the photoemission intensity below  $E_F$  (Figure 4.7 c)) gives a more detailed view of the temporal evolution. The depopulation happens within the pulse cross correlation (FWHM 130 fs). The successive rise of the signal happens on a few ps time scale.<sup>17</sup> **The traces are mirrored with respect to time zero. This shows that 4.6 eV and 6.3 eV laser pulses launch the same ultrafast depopulation and population dynamics.**

The interpretation of the dynamics within few ps around time zero is analogous to time-resolved photoemission measurements of mildly Hydrogen doped ZnO surfaces [Dei16, Dei14], which are reviewed in chapter 2.3.2. Upon arrival, the first laser pulse depopulates the state below  $E_F$  and populates the conduction band with electrons. The hot electron population created with 4.6 eV and monitored with 6.3 eV can be seen in Figure 4.7 b). Because the photoemission intensity of this signal is small, it is magnified in the inset of the upper panel. The hot electron population is broad and extends to high energies of at least 0.8 eV above  $E_F$ . Towards  $E_F$  the signal gets more intense and extends to larger delays, i.e. the lifetime of the electron population increases. This is qualitatively as observed in ref. [Dei16, Dei14] and is attributed to the scattering of the electrons to the bottom of the ZnO CB. The hot electron lifetimes as a function of excess energy above the CB bottom are identical (analysis not shown). Subsequently, the hot electrons funnel into an excitonic state, which leads to the signal increase below  $E_F$ . Beyond the interpretation of Deinert et al., a central finding of the present thesis is that the population below  $E_F$  originates partially from defect excitons for as-prepared ZnO. This causes 'ultrafast photodoping' of the ZnO surface, as will be described in chapter 5 and 6. A fraction of the photoexcited state population survives the inverse laser repetition rate.

Next I present the ultrashort dynamics for large positive and negative delays. As out-

<sup>17</sup>For both traces, also an increase of signal before the dip due to the optical depopulation of  $n_\infty$  is observed, occurring at negative delays for XC1 and positive delays for XC2, respectively. For negative delays, the signal in XC1 is attributed to electrons that are excited to high energies above  $E_F$  (hot electrons, discussed below) with the 6.3 eV pulses and monitored with time-delayed 4.6 eV pulses. The signal in XC2 at positive delays is tentatively attributed to a change of the secondary electron intensity, which falls also in this energy region as mentioned above.

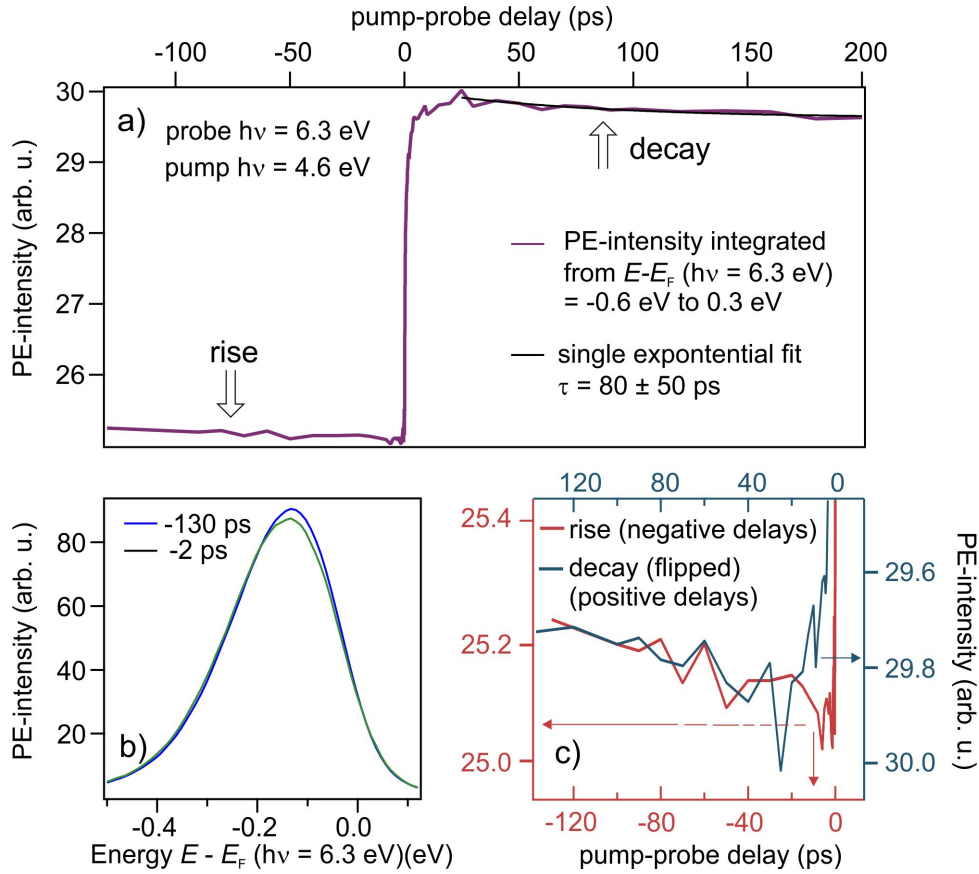


**Figure 4.8:** Negative delay dynamics decipher the rise time of the photostationary state: a) Integrated intensity across the spectral signature of the photostationary state detected by photoemission with 6.3 eV for positive and negative delays. For both directions, dynamic changes of the intensity are observed. b) The photostationary state signal rises towards negative delays. c) Overlaying the decay at positive delays (flipped) and the rise at negative delays shows that both changes occur with the same time constant. The amplitude of the decay towards positive delays and the rise towards negative delays are also approximately identical (cf. the respective photoemission intensities given on the right and left axis, respectively).

lined in section 4.2.1, dynamics towards negative delays probed with 6.3 eV are observed, which are counterintuitive in the framework of pump-probe spectroscopy. It is these dynamics that solely occur because the state below  $E_F$  probed by the 6.3 eV laser pulses at negative pump-probe delays is a photostationary state as will be analyzed with the model further below.<sup>18</sup> Figure 4.8 a) shows the evolution of the photoelectron signal detected by 6.3 eV as a function of pump-probe delay from -130 ps to 200 ps. The photoelectron signal is integrated from -0.6 to 0.3 eV with respect to  $E_F$  (initial state energy axis with respect

<sup>18</sup>Ref. [Dei16, Dei14] focused on the dynamics within few ps around time zero. Large negative delays were not measured. It was also not identified that the state below  $E_F$  is a photostationary state. The signal below  $E_F$  at negative delays was attributed exclusively to be a Hydrogen adsorption induced state that is static (i.e. not photoinduced).

to photoemission with 6.3 eV), i.e. covering the photostationary state situated below  $E_F$ . For positive delays, after the initial rise, the signal decays by a few percent within the first 200 ps (a single exponential fit gives a time constant of  $\kappa = 80 \pm 50$  ps). The signal also changes towards negative delays: It rises monotonously within the accessed delay window from 0 to -130 ps. Figure 4.8 b) shows two selected spectra at negative delays, one at -130 ps and one at -2 ps. These spectra show that the signal increase spectrally occurs at the energy of the photostationary state. Interestingly, the intensity increase towards negative occurs with the exact same time constant as the intensity decrease at positive delays and is of about the same magnitude. This is shown in Figure 4.8 c), where the signal decrease at positive delays is flipped and overlaid on the signal increase at negative delays.

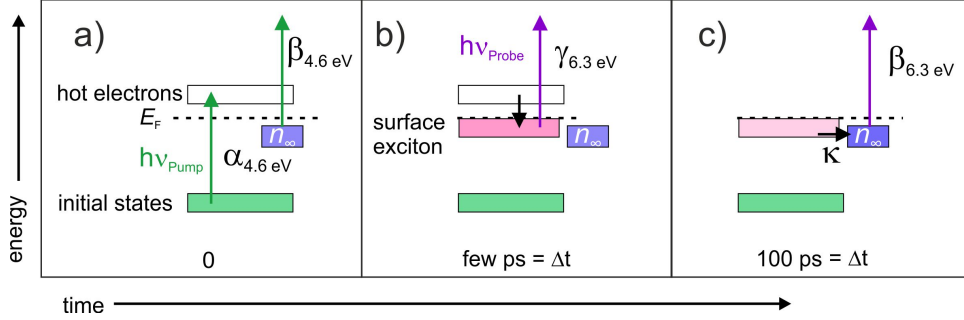


**Figure 4.9:** Population/depopulation scheme of the photostationary state (please see text).

### Analysis of the observed dynamics with regard to the photostationary state

In the following I apply the two-pulse model developed in section 4.2.2 to explain the above observed dynamics monitored with the 6.3 eV probe on a timescales of few hundred ps toward positive and negative delays. The negative delay dynamics is explained by assuming different depopulation coefficients for an intermediate state decaying into a long-lived state surviving  $\Delta T$  and the long-lived state itself, respectively, as outlined in section 4.2.1. I will show that from the model also the observed decay toward positive delays with the same time constant and amplitude as the rise towards negative delays is expected. The mirrored dynamic results because in the present experiment, both pump and probe laser pulses have the same effect on the sample and the intermediate state and the long-lived state are spectrally overlapping.

I start with the expected dynamics towards positive pump-probe delays. A population scheme is drawn in Figure 4.9. For positive pump-probe delays, the 4.6 eV pump pulse depopulates the photostationary state  $n_\infty$  with  $\beta_{4.6}$  eV and creates hot electrons in the ZnO CB with  $\alpha_{4.6}$  eV (Figure 4.9 a)). Subsequently, on a few ps timescale, the hot electrons relax to the band bottom and the excitonic state below  $E_F$  forms. For simplicity, I assume that

every CB electron eventually forms an exciton by Coulomb interaction with a photohole, i.e. no extra proportionality constant is introduced and the pump-induced increase of the exciton population below  $E_F$  is simply described with the coefficient  $\alpha_{4.6 \text{ eV}}$ . The 6.3 eV probe arrives afterwards, delayed by  $\Delta t$  and depopulates the excitonic state with the efficiency  $\gamma_{6.3 \text{ eV}}$  (Figure 4.9 b)). The excitonic state, called surface exciton in the following, spectrally overlaps with  $n_\infty$ . It forms  $n_\infty$  within the time constant  $\kappa$ . The probe depopulates  $n_\infty$  with the efficiency  $\beta_{6.3 \text{ eV}}$  that is different from the depopulation efficiency of the surface exciton  $\gamma_{6.3 \text{ eV}}$  (Figure 4.9 c)). It also excites hot electrons with  $\alpha_{6.3 \text{ eV}}$ , hence subsequently the surface exciton and the long-lived state, but this process is not explicitly drawn in Figure 4.9. In view of the population/depopulation scheme of the two-pulse model developed in section 4.2.2, the surface exciton is the intermediate state for the generation of  $n_\infty$ .

The 6.3 eV probe laser pulse interferes with the population process of  $n_\infty$ . At an early timing (Figure 4.9 b)) the probe encounters a higher intermediate state population and a lower  $n_\infty$  population than at later time delays (Figure 4.9 c)). If the two depopulation parameters,  $\beta_{6.3 \text{ eV}}$  and  $\gamma_{6.3 \text{ eV}}$  are different, the photostationary state population depends on the pump-probe timing, as discussed in the previous section. The number of photostationary states  $n_\infty$  detected by the 6.3 eV laser pulse at small positive delays is given by  $n_{\infty,1}$  (equation 4.66), with the definition of  $A(\Delta t)$  including the depopulation of the intermediate state (equation 4.69):

$$\begin{aligned}
 n_{6.3\text{eV}, \text{ positive delays}} &= [n_{\infty,2}(\Delta t)]_{\alpha=\alpha_{4.6\text{eV}}, \beta=\beta_{4.6\text{eV}}, \alpha_+=\alpha_{6.3\text{eV}}, \beta_+=\beta_{6.3\text{eV}}, \gamma_+=\gamma_{6.3\text{eV}}} \\
 &= (1 - \beta_{4.6 \text{ eV}}) \frac{(1 - \beta_{6.3 \text{ eV}}) \alpha_{4.6 \text{ eV}} N e^{-\Delta T/\tau} + \alpha_{6.3 \text{ eV}} N e^{-\Delta T/\tau}}{D} \\
 &\quad (1 - \beta_{4.6 \text{ eV}}) \frac{(\beta_{6.3 \text{ eV}} - \gamma_{6.3 \text{ eV}}) \alpha N e^{-\Delta t/\kappa} e^{-\Delta T/\tau}}{D} \\
 &\quad + \alpha_{4.6 \text{ eV}} N (1 - e^{-\Delta t/\kappa}) \\
 &\quad \text{with } D = 1 - (1 - \beta_{6.3 \text{ eV}})(1 - \beta_{4.6 \text{ eV}}) e^{-\frac{\Delta T}{\tau}}
 \end{aligned} \tag{4.70}$$

Regarding the delay-dependent terms, the probe encounters the fresh population

$$\alpha_{4.6 \text{ eV}} N (1 - e^{-\Delta t/\kappa}),$$

which would be detected also without the population surviving  $\Delta T$ . In addition, a delay-dependent term arises from the photostationary population:

$$(1 - \beta_{4.6 \text{ eV}}) \frac{(\beta_{6.3 \text{ eV}} - \gamma_{6.3 \text{ eV}}) \alpha N e^{-\Delta t/\kappa} e^{-\Delta T/\tau}}{D}.$$

This term appears solely because the population survives  $\Delta T$  (if  $\tau \ll \Delta T$ ,  $e^{-\Delta T/\tau} \rightarrow 0$ ).

In this particular measurement, because the surface exciton (i.e. the intermediate state) and  $n_\infty$  are spectrally overlapping, they cannot be separated in the photoelectron spectra. To simulate the photoemission intensity, the photoelectron signal in the energy region corresponding with the two states is assumed to be proportional to the depopulation parameters for the intermediate state and  $n_\infty$ , respectively. This means that optical depopulation leads to photoemission from the state by promoting the electrons above the vacuum level  $E_{\text{vac}}$ , cf. the bottom panel of Figure 4.7 a). With this the photoemission signal detected by 6.3 eV below  $E_F$  at positive pump-probe delays becomes

$$\begin{aligned}
 I_{6.3 \text{ eV, pos. delays}} &= \underbrace{\beta_{6.3 \text{ eV}}}_{n_\infty \text{ population}} \underbrace{n_{6.3 \text{ eV, positive delays}}}_{n_\infty \text{ population}} + \gamma_{6.3 \text{ eV}} \underbrace{\alpha_{4.6 \text{ eV}} N(e^{-\Delta t/\kappa})}_{\text{intermediate state population}} \\
 &= \beta_{6.3 \text{ eV}}(1 - \beta_{4.6 \text{ eV}}) \frac{(\beta_{6.3 \text{ eV}} - \gamma_{6.3 \text{ eV}}) \alpha_{4.6 \text{ eV}} N e^{-\Delta t/\kappa} e^{-\Delta T/\tau}}{D} \\
 &\quad + (\gamma_{6.3 \text{ eV}} - \beta_{6.3 \text{ eV}}) \alpha_{4.6 \text{ eV}} N e^{-\Delta t/\kappa} \\
 &\quad + \text{delay independent terms} \\
 &= \left[ 1 - \frac{\beta_{6.3 \text{ eV}}(1 - \beta_{4.6 \text{ eV}}) e^{-\Delta T/\tau}}{D} \right] (\gamma_{6.3 \text{ eV}} - \beta_{6.3 \text{ eV}}) \alpha_{4.6 \text{ eV}} N e^{-\Delta t/\kappa} \\
 &\quad + \text{delay independent terms}
 \end{aligned} \tag{4.71}$$

The delay-dependency of the photostationary state is contained in the term

$$\frac{\beta_{6.3 \text{ eV}}(1 - \beta_{4.6 \text{ eV}}) e^{-\Delta T/\tau}}{D}.$$

This term appears solely because the population survives  $\Delta T$  (because, again, if  $\tau \ll \Delta T$ ,  $e^{-\Delta T/\tau} \rightarrow 0$ ). If it is a significant contribution to the delay-dependent photoemission intensity depends on the population/depopulation parameters. At the end of this subsection I determine  $\beta_{4.6 \text{ eV}}(6.3 \text{ eV}) = 0.085(0.17)$ , assuming that the cross sections for both photon energies are the same and taking into account that the fluence of the 6.3 eV laser beam is double as high as the fluence of the 4.6 eV laser beam. Furthermore, with the lifetime determined in subsection 5 I get  $e^{-\Delta T/\tau} \approx 1$ . This yields

$$\frac{\beta_{6.3 \text{ eV}}(1 - \beta_{4.6 \text{ eV}}) e^{-\Delta T/\tau}}{D} \approx 0.5.$$

Thus, the term is by no means small, but amounts to half of the delay-dependent part photoemission intensity! Overall, equation 4.71 describes an exponential decay with  $\Delta t$  of the photoemission intensity if  $\gamma_{6.3 \text{ eV}} > \beta_{6.3 \text{ eV}}$ . An exponential decay of the photoelectron

signal probed by 6.3 eV towards positive delay is what is observed experimentally (Figure 4.8). I thus conclude that the decay of the photoemission intensity is correctly described by the two-pulse model developed in the preceding section by assuming  $\gamma_{6.3 \text{ eV}} > \beta_{6.3 \text{ eV}}$ . Note that an alternative explanation of the signal decrease at positive delays would be simply a population decrease of the pump-induced electron population below  $E_F$ , e.g. by recombination with the photoholes, even if the depopulation parameters  $\beta_{6.3 \text{ eV}}$  and  $\gamma_{6.3 \text{ eV}}$  are the same.

To distinguish both scenarios and to unveil the contribution of the photostationary state population to the time-resolved data I now turn to negative pump-probe delays, i.e. where the 6.3 eV laser pulse comes first and the 4.6 eV laser pulse arrives after. The same population scheme as for positive pump-probe delays is assumed, i.e. the 6.3 eV probe laser pulse depopulates the photostationary state and populates the intermediate state with  $\beta_{6.3 \text{ eV}}$  and  $\alpha_{6.3 \text{ eV}}$ , respectively. The time-delayed 4.6 eV pump laser pulse depopulates the intermediate state and the long-lived state population with  $\beta_{4.6 \text{ eV}}$  and  $\gamma_{4.6 \text{ eV}}$ , respectively. According to the model the photostationary population detected by the 6.3 eV probe laser pulses at negative pump-probe delays is (equation 4.66 with equation 4.69):

$$\begin{aligned} n_{6.3\text{eV, negative delays}} &= [n_{\infty,1}]_{\alpha=\alpha_{6.3\text{eV}},\beta=\beta_{6.3\text{eV}},\alpha_+=\alpha_{4.6\text{eV}},\beta_+=\beta_{4.6\text{eV}},\gamma_+=\gamma_{4.6\text{eV}}} \\ &= \frac{e^{-\Delta T/\tau}}{D}(\beta_{4.6 \text{ eV}} - \gamma_{4.6 \text{ eV}})\alpha_{6.3 \text{ eV}}N e^{-\Delta t/\kappa} + \text{delay-independent terms} \end{aligned} \quad (4.72)$$

The photoemission intensity is

$$\begin{aligned} I_{6.3 \text{ eV, neg. delays}} & \\ &= \frac{\beta_{6.3 \text{ eV}} e^{-\Delta T/\tau}}{D}(\beta_{4.6 \text{ eV}} - \gamma_{4.6 \text{ eV}})\alpha_{6.3 \text{ eV}}N e^{-\Delta t/\kappa} + \text{delay-independent terms} \end{aligned} \quad (4.73)$$

For the photostationary state signal probed by 6.3 eV toward negative delays the depopulation efficiencies  $\gamma_{4.6 \text{ eV}}$  and  $\beta_{4.6 \text{ eV}}$  of the 4.6 eV beam are relevant. If  $\gamma_{4.6 \text{ eV}} > \beta_{4.6 \text{ eV}}$ , an exponential rise towards negative delays is expected, happening with the time constant  $\kappa$ , i.e. the formation time constant of the photostationary state from the intermediate state. The observed mirrored ultrafast dynamics in Figure 4.7 suggests that both pulses are equivalent, i.e. if towards positive delays an exponential decay with  $\kappa$  due to  $\gamma_{6.3 \text{ eV}} > \beta_{6.3 \text{ eV}}$  is observed, an exponential rise with  $\kappa$  due to  $\gamma_{4.6 \text{ eV}} > \beta_{4.6 \text{ eV}}$  towards negative delays is expected. The model even allows to quantitatively predict the intensity change towards negative delays. With  $\alpha_{6.3 \text{ eV}} = 2 \alpha_{4.6 \text{ eV}}$ ,  $\gamma_{6.3 \text{ eV}} = 2 \gamma_{4.6 \text{ eV}}$  and the values for  $\beta_{4.6 \text{ eV}}(6.3 \text{ eV})$ ,  $e^{-\Delta T/\tau}$  and  $D$  mentioned above I calculate for the ratio of the

*delay-dependent* part of the photoemission intensity for positive and negative delays:

$$\frac{I_{6.3 \text{ eV, neg. delays}}}{I_{6.3 \text{ eV, pos. delays}}} = \frac{[\beta_{6.3 \text{ eV}} e^{-\Delta T/\tau}/D] (\beta_{4.6 \text{ eV}} - \gamma_{4.6 \text{ eV}}) \alpha_{6.3 \text{ eV}} N e^{-\Delta t/\kappa}}{[\beta_{6.3 \text{ eV}} (1 - \beta_{4.6 \text{ eV}}) e^{-\Delta T/\tau}/D - 1] (\beta_{6.3 \text{ eV}} - \gamma_{6.3 \text{ eV}}) \alpha_{4.6 \text{ eV}} N e^{-\Delta t/\kappa}} \approx 1 \quad (4.74)$$

**Thus, from the model I expect that the photoemission intensity rises towards negative delays with the same amplitude and time constant as it decays towards positive delays.** Remarkably, this is precisely what is observed in the experiment: By comparing the signal detected by photoemission with 6.3 eV at positive and negative delays, it is found that both have the same temporal evolution (Figure 4.8 c)). In addition the change of the signal as a function of delay is about of the same magnitude.

I thus conclude that the population/depopulation model with different depopulation parameters for intermediate state and  $n_\infty$ , respectively, describes the observed dynamics for positive as well as negative delays. I attribute the time constant  $\kappa = 80 \pm 50$  ps to the formation of the photostationary state from the intermediate state and exclude a simple population decay as the origin of the dynamics observed at positive delays. Physically, the formation of  $n_\infty$  from the initial surface exciton population could be, for example, a stabilization by local lattice deformations. Indeed, it is the lattice deformation that is supposed to lead to an exceedingly long lifetime of defect excitons in ZnO (see ref [Lan05] and section 2.3.3), which form part of the surface exciton signal as mentioned above.

The above shows that photostationary states can contribute to pump-probe signals in a way that is counterintuitive and by no means neglectable. On the one hand this might lead to unwanted complications of the data interpretation, but on the other hand an in-depth analysis as presented here can also reveal otherwise obscured informations.

**Addendum 1: Pump-induced signal increase at negative delays (delay independent)** Overall, the signal of the long-lived state detected by the probe at negative delays can be enhanced or decreased when the pump is applied, depending on the population and depopulation parameters of the pump laser beam. For delays  $\Delta t \gg \kappa$ , i.e. far away from ultrafast formation dynamics, the term  $A(\Delta t)$  (equation 4.69) becomes delay-independent:

$$A = ((1 - \beta_+) \alpha N) e^{-\Delta T/\tau} \quad (4.75)$$

The number of photostationary states seen by the probe laser beam at negative delays is then given by

$$\begin{aligned}
 n_{\text{probe, negative delays}} &= [n_{\infty,1}]_{\alpha=\alpha_{\text{Probe}},\beta=\beta_{\text{Probe}},\alpha_+=\alpha_{\text{Pump}},\beta_+=\beta_{\text{Pump}},\gamma_+=\gamma_{\text{Pump}}} \\
 &= \frac{((1 - \beta_{\text{Pump}})\alpha_{\text{Probe}}N + \alpha_{\text{Pump}}N) e^{-\Delta T/\tau}}{1 - (1 - \beta)(1 - \beta_+) e^{-\Delta T/\tau}} \quad (4.76)
 \end{aligned}$$

$n_{\text{probe, negative delays}}$  increases if the depopulation with  $\beta_{\text{Pump}}$  is inefficient compared to the population with  $\alpha_{\text{Pump}}$  (i.e. if  $|\beta_{\text{Pump}} \alpha_{\text{Probe}}| < |\alpha_{\text{Pump}}|$ ), but can in principle also decrease and become a complicated function of pump fluence. If  $\tau \ll \Delta T$ ,  $e^{-\Delta T/\tau} \rightarrow 0$  the pump-induced signal vanishes. Thus checking for correlated signal at negative delays is another proof for the presence of a photostationary state, besides performing a repetition rate dependency. The above-derived formula will be compared to the experimental data recorded on ZnO in section 5.8.

**Addendum 2: Determination of the depopulation parameter  $\beta$**  In the integrated intensity traces below  $E_F$  a dip at time zero for both, photoemission with 4.6 eV and 6.3 eV is detected (Figure 4.7 c)). The depopulation parameter  $\beta_{4.6\text{eV}(6.3\text{eV})}$  can be determined from the dip of the measured traces. For photoemission with 6.3 eV probe, the signal change at time zero relative to large negative delays is determined from the data (not shown):

$$\frac{I_{6.3\text{eV}}(\Delta t = 0) - I_{6.3\text{eV}}(\Delta t = -200\text{ps})}{I_{6.3\text{eV}}(\Delta t = -200\text{ps})} = 0.08 = Y \quad (4.77)$$

Naively one would simply attribute this to the depopulation parameter  $\beta_{4.6\text{eV}}$  of the 4.6 eV pump, but the photostationary population  $n_{\infty}$  is actually a function of  $\Delta t$ . The dip  $Y$  has to be calculated with the help of the two-pulse model. According to the model,  $Y$  is:

$$Y = \frac{n_{\text{probe, negative delays}} - n_{\text{probe, } \Delta t=0}}{n_{\text{probe, negative delays}}} = \frac{\alpha_{4.6\text{eV}} - (1 - \beta_{4.6\text{eV}})(1 - \beta_{6.3\text{eV}})\alpha_{4.6\text{eV}}}{(1 - \beta_{4.6\text{eV}})\alpha_{6.3\text{eV}} + \alpha_{4.6\text{eV}}} \quad (4.78)$$

here I used equation 4.76 and  $n_{\text{probe, } \Delta t=0} = (1 - \beta_{4.6\text{eV}}) n_{\infty,1}(\Delta t = 0)$ , with  $n_{\infty,1}$  from equation 4.66.  $\beta_{4.6\text{ eV}(6.3\text{ eV})}$  and  $\alpha_{4.6\text{ eV}(6.3\text{ eV})}$  are, as before, the depopulation/population parameters for 4.6 eV (6.3 eV).

The theoretical expression for the dip  $Y$  and the experimentally determined value of the dip must be equal. However, there are too many parameters to determine  $\beta_{4.6\text{ eV}(6.3\text{ eV})}$  directly from this. Hence, I assume that the cross subsections for depopulation and population are the same for both photon energies, which seems reasonable because both laser beams launch the same ultrafast dynamics (cf. Figure 4.7). The fluence of the 6.3 eV laser

pulse is twice that of the 4.6 eV laser pulse, ergo:

$$\beta_{6.3 \text{ eV}} = 2 \beta_{4.6 \text{ eV}}, \text{ and } \alpha_{6.3 \text{ eV}} = 2 \alpha_{4.6 \text{ eV}} \quad (4.79)$$

Now all population cross sections  $a = \alpha/F$  are cancelled out in equation 4.78 and I can determine  $\beta_{6.3 \text{ eV}}$  from equation 4.78 and the experimentally measured value of the dip  $Y$  to:

$$\beta_{6.3 \text{ eV}} = 0.17 \quad (4.80)$$

With this  $\beta_{4.6 \text{ eV}} = 0.085$ , i.e. almost coinciding with the naively expected value (equation 4.77). The depopulation cross section is (with  $F_{6.3 \text{ eV}} = 5 \mu\text{J}/\text{cm}^2$ ):

$$b = 0.034 \text{ cm}^2/\mu\text{J} \quad (4.81)$$

### 4.3 Summary

In summary, a model for photostationary states taking into account pulsed laser excitation was developed. It establishes relations between the lifetime of the photostationary state and the population upon varying laser excitation parameters such as repetition rate and fluence. The extension to two subsequent pulses predicts counterintuitive ultrashort dynamics in pump-probe experiments. While for usual pump-probe experiments the signal at negative delays detected by the probe is expected to be delay-independent, this model suggests that - in the presence of photostationary states - the signal may well be delay-dependent because of the formation efficiency of the photostationary state that depends on the pump-probe timing. I presented an exemplary datasets with dynamics at negative delays that are attributed to the predicted effect. The dynamics at negative delays are directly related to the formation dynamics of the photostationary state. This example shows that, beyond the need to understand the contribution of photostationary states to pump-probe scans in order to avoid erroneous data interpretation, the correct treatment of photostationary state effects can be used to decipher otherwise obscured processes.

## 5 Metastable photodoping of the ZnO surface

Despite its promising properties mentioned in the introduction, a major drawback of using ZnO in devices is the disability to control the doping of this material [Kli10b, Ell16]: ZnO is unintentionally n-type doped, the origin of which is not entirely clear yet. Recently, this has been attributed to Zn-interstitials or H impurities, after it had been attributed to oxygen vacancies for a long time [Kin11]. p-doping in ZnO is rarely reported and remains a challenge [Ell16]. Unintentional n-doping can compensate intentional p-doping. In this context, it is often disregarded [Ell16] that the degree of n-doping of ZnO depends strongly on its exposure to UV light [Hör18]. The 'photodoping' effect is known to affect the electrical properties of semiconductor heterojunctions involving ZnO [Hör18, Lak10]. Exposure to UV light can happen during storage (day light) or in an optoelectronic application of ZnO. Also, many characterization techniques can not avoid photoexcitation of ZnO, such as photoluminescence or photoelectron spectroscopy. Understanding photodoping is therefore an indispensable step to understand ZnO.

The reason why oxygen vacancies are excluded as cause of the intrinsic n-doping is that they form deep donors, in contrast to Zn-interstitials or H impurities [Jan09]. However, several theoretical works hypothesize that the conductivity in ZnO crystals stems from the *photoexcitation* of the deep donor states due to oxygen vacancies [Jan09, Lan07, Lan05]. Lany and Zunger [Lan05, Lan07] predict that photoexcitation of the oxygen vacancy creates a state equivalent to a shallow donor dopant: The electron is excited to the CB and is bound to the photohole in a hydrogen-like state, in other words, forming a defect exciton. This kind of photodoping is strongly related to the observation of PPC in ZnO [Lan07]: Charging of the oxygen vacancy leads to a strong lattice distortion creating a thermal barrier that increases the lifetime of the excited state, making it a doping effect that persists on a timescale of hours to days, cf. section 2.3.3.

Experimentally, the rise of PPC occurs on a minutes to hours time scale upon UV illumination and can be quenched by the exposure to Oxygen [Col58, Bao11]. X-Ray photoelectron spectroscopy unveils the formation of Zn-rich surface on this time scale [Gur14]. These experiments suggest a relation between the photodoping and the UV illumination-induced *creation* of oxygen vacancies in the sample. Furthermore, it was found that PPC can be triggered with photoexcitation below the fundamental gap [Col58, Liu09], which suggests that it is the *photoexcitation* of these oxygen vacancies that leads to PPC, as proposed by theory. Yet, PPC is often discussed in a band bending picture and is attributed to the band-flattening of the CB that is upwards bent towards the surface prior to photoexcitation [Spe13, Gur14]. This is in strong contrast to the theoretical prediction of photodoping being an equivalent to doping with shallow donors [Lan05, Lan07]. Shallow donors at the surface are expected to lead to the formation of an accumulation layer, i.e.

---

downward surface band bending instead of upwards band bending, in analogy to what is observed after H surface doping of ZnO [Oza10, Dei15].

Here, I use the capabilities of trARPES and a controlled UHV environment to study the photoexcited metastable properties of ZnO. I identify a photostationary electron population that is assigned to a long-lived defect exciton: It is bound to a positive charge that is localized at the surface and laterally confined. It will be demonstrated that the defect exciton is a direct analog to H doping of the surface: Both, photoexcitation and H doping induce localized electronic states at the same energy, at 150 meV below the Fermi energy (or 350 meV below the bulk CB) and lead to a work function reduction due to the electric dipole arising from a hole localized at the surface. An excitation photon energy dependence of the defect exciton formation shows that the neutral defect state is energetically situated deeply in the ZnO band gap, not higher than 400 meV above the VB maximum. The energetic position of the defects as well as the rise of the state upon UV illumination on a time scale of minutes/hours are in agreement with PPC studies. This directly establishes a relation between UV illumination-induced metallicity and the photoexcitation of oxygen vacancies and unveils the analogy of photoexcitation to chemical doping of the ZnO surface with shallow donors.

The chapter is organized as follows: First the electronic structure of the ZnO(10-10) surface under photostationary conditions is determined (section 5.1). The photostationary state is identified (section 5.2), and it is thoroughly analyzed with respect to its lifetime, localization and dependence on surface conditions (UV exposure time) (section 5.2 to section 5.5). Then, I use pump-probe spectroscopy to unveil the photon energy dependent-formation of the defect excitons in the ultrafast time domain (section 5.6). As the defect exciton forms a shallow donor-like state, for high defect exciton densities the sample should become metallic. Such high defect densities can be reached upon UV exposure of several hours (section 5.7). The characterization of the photostationary state is finalized by showing that for rather low defect densities, even at the highest pump excitation fluence, the photoexcited electron population stays localized. This is attributed not to a saturation of the number of defect excitons that can be excited, but to a balance between population and depopulation of the state (section 5.8). This detail is important with regard to the next chapter 6, where I show that the sample undergoes a transition from a photodoped semiconductor to a metal, as individual photodopants delocalize in a transient phase that is limited to the ultrafast time domain. Finally, I report some technical insights about work function measurements in photoemission, when the sample work function is not uniformly lowered, but only in a small spot on the sample, in this case by photoexcitation (section 5.9).

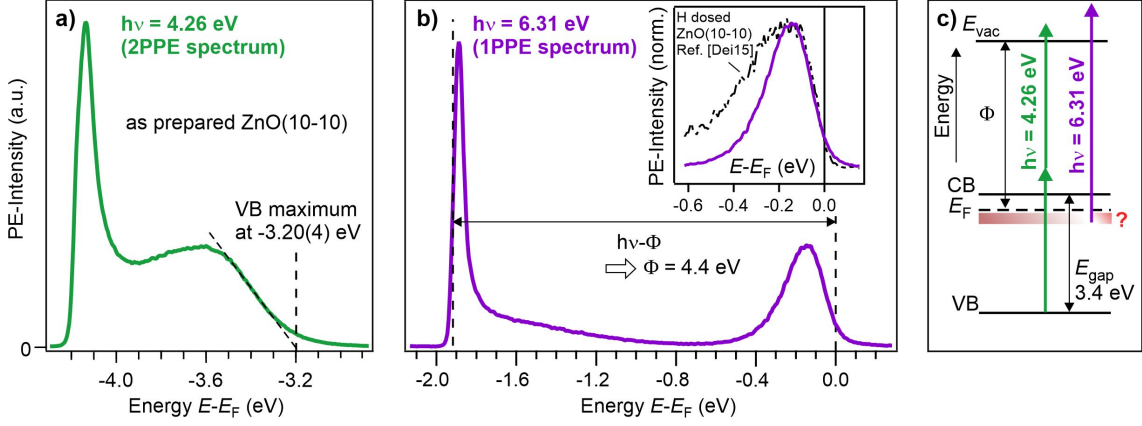


**Figure 5.1:** PE signal of the as-prepared ZnO(10-10) surface: a) 2PPE with  $h\nu = 4.26$  eV from the ZnO VB. The lower energy feature is the secondary edge. The VB maximum is determined to  $-3.20(4)$  eV below the Fermi level  $E_F$  by linear extrapolation. b) Direct photoemission with  $h\nu = 6.31$ , which is higher than the work function  $\Phi = 4.4$  eV. Just below  $E_F$  a feature of unknown origin is probed. The inset shows that it is spectrally almost coinciding with the PE signal induced by H termination of the ZnO(10-10) surface. The shown spectrum is taken from ref. [Dei16] and corresponds to a low dose of 10 L. c) Energy level diagram.

## 5.1 Electronic structure of the ZnO surface in the photostationary state

All measurements are performed on a ZnO(10-10) single crystal prepared under UHV conditions as described in chapter 3.2.6 and carried out at 100 K unless specified otherwise. The sample preparation enables reproducibility and a surface with few impurities.

Figure 5.1 presents photoelectron spectra of the freshly prepared ZnO(10-10) surface, using the photon energies  $h\nu = 4.26$  eV (Figure 5.1 a)) and  $h\nu = 6.3$  eV (Figure 5.1 b)), respectively. The PE-intensity is plotted versus binding energy  $E - E_F$ , where  $E_F$  is the Fermi level, which is determined from the gold sample holder that is in electrical contact with the sample surface.

For Figure 5.1 a), the photon energy  $h\nu = 4.26$  eV is smaller than the work function  $\Phi$  (see below) and the electrons are therefore emitted in a 2PPE process. The photon energy is effectively  $h\nu = 2 \times 4.26$  eV = 8.52 eV, which is sufficient to reach the ZnO valence band (see energy level diagram in Figure 5.1 c)). The spectrum consists of the low energy cutoff (secondary edge) at  $-4.2$  eV, and one peak centered at about  $-3.65$  eV, assigned to the ZnO VB. The position of the VB maximum is determined using the conventional method of linear extrapolation of the edge, which yields a value of  $E_{\text{VBM}} = -3.20(4)$  eV.  $E_{\text{VBM}}$  as well as the maximum intensity of the VB at  $-3.65$  eV are in agreement with synchrotron-based photoemission data [Oza03, Oza05]. Considering the electronic band gap of 3.4 eV [Kli10b], the CB minimum should lie at 0.2 eV above  $E_F$ , as expected for

nominally undoped, but intrinsically n-doped ZnO [Jac84].

Figure 5.1 b) shows the PE-intensity upon direct photoemission (1PPE) with  $h\nu = 6.3$  eV  $> \Phi$ , which is the highest photon energy available from the laser source. The spectrum consists of the secondary edge at -1.9 eV, and one peak just below  $E_F$  of yet unknown origin. From the position of the secondary edge with respect to  $E_F$ , the work function  $\Phi$  can be conveniently read:  $\Phi$  limits the accessible range of occupied electronic states, i.e. the width of the spectrum to  $b = h\nu - \Phi$  (Figure 5.1 b)). For the present case  $\Phi = 4.4$  eV, which is close to the work function of  $\Phi_{\text{lit}} = 4.5$  eV of ZnO(10-10) surfaces prepared under UHV conditions reported in [Dei16, Dei15, Oza11].

In the inset of Figure 5.1 b) I compare the peak detected on as-prepared ZnO(10-10) to the feature that is induced by adsorbing a small amount of H (10 L<sup>19</sup>). The spectrum is taken from ref [Dei16]. Comparing both spectra unveils a close resemblance: The high energy tail is identical, as well as the peak position, the H-induced feature just extends about 100 meV more to lower energies. H forms a ubiquitous contaminant in UHV systems, so the state below  $E_F$  may simply be due to H adsorption at the ZnO surface.

However, in contrary to a static signal that would result from surface contamination, I will reveal in the following that the peak depends strongly on photoexcitation: It is a photostationary state, i.e. a photoexcited electron population that survives the inverse laser repetition rate.

## 5.2 Uncovering the photostationary state and its analogy to surface doping with hydrogen

To reveal the photostationary state I vary the repetition rate  $R$  of the laser from normally 200 kHz down to few kHz. Note that the PE signal results from integrating many photoemission events, because the camera exposure time is in the ms regime and the time between pulses  $1/R$  is in the  $\mu\text{s}$  regime. Therefore, the PE-intensity from an occupied electronic state  $n$  is proportional to  $R$ , simply because more photoemission events take place. Furthermore, the PE-intensity is proportional to the laser fluence for 1PPE (cf. section 3.1.4) and the camera exposure time  $t_{\text{exp}}$ , i.e.

$$I_{\text{PE}} \propto F R t_{\text{exp}} n \quad (5.82)$$

The camera exposure time (50 ms) stays fixed for all experiments shown in this section. From the above consideration it follows, that if the fluence  $F$  is kept constant,  $I_{\text{PE}}/R$  should be *independent* of  $R$ , if  $n$  is *independent* of the photoexcitation. In contrast, for a photostationary state, the PE-intensity should depend on the photoexcitation conditions

---

<sup>19</sup>1 L corresponds to a H exposure of 1 second at a partial pressure of  $1.33 \times 10^{-6}$  mbar. The amount of H that is adsorbed at the surface is unknown, cf. ref. [Dei16] and section 3.2.6.

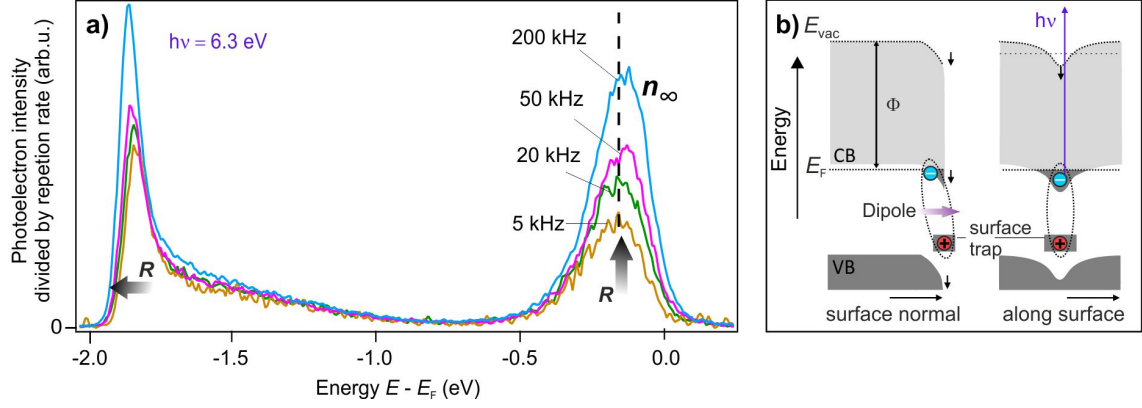


**Figure 5.2:** Uncovering the photostationary state  $n_\infty$ : a) Repetition rate  $R$  dependency of the PE-intensity using  $h\nu = 6.3$  eV. The spectra are normalized to  $R$ . Upon lowering  $R$ , the state below  $E_F$  is lowered, and the secondary edge shifts upwards. The dashed line indicates the peak maximum of the PE-intensity at 5 kHz, which is at a slightly lower energy than at 200 kHz. b) Interpretation of the observation:  $n_\infty$  is a long-lived electron population bound to a positive charge at the ZnO surface, such as a positively charged defect. The lateral confinement (right panel in b)) is evidenced by ARPES in subsection 5.4.

(fluence  $F$ , repetition rate  $R$ ) in a more complicated way. A photostationary state is reached, when a photoexcited electron population has a lifetime exceeding the inverse laser repetition rate (cf. the introduction to photostationary states in chapter 4). In this case,  $n$  is the limit of an electronic population that builds up over many laser pulses, i.e.  $n = n_\infty(F, R)$  and depends on the laser fluence and repetition rate. Generally the PE signal  $I_{PE}/R$  from a photostationary state should be lowered as  $R$  is lowered, because the time between excitation events increases and the photoexcited electron population has more time to relax.

In Figure 5.2 a)  $I_{PE}/R$  recorded with  $h\nu = 6.3$  eV is plotted versus binding energy  $E - E_F$  for repetition rates between 200 kHz and 5 kHz and the same fluence  $F$ . There are clear changes as a function of  $R$ : Firstly, the peak just below  $E_F$  is reduced to about half of its intensity upon decreasing the repetition rate from 200 kHz to 5 kHz. Secondly, the secondary edge shifts upwards as  $R$  is reduced, meaning that the work function increases<sup>20</sup>. This observations reveals that the peak just below  $E_F$  is a photostationary state with a lifetime on the order of  $\mu\text{s}$ . Furthermore, the increase of the work function upon lowering  $R$  shows that the photostationary *electron* population is bound to a *positive* charge at

<sup>20</sup>The approach was crosschecked on a gold surface at the sample holder, that does not show long-lived states. On gold, indeed no work function shift was measured. A slight intensity variation of the PE-intensity ( $<10\%$  from 5 kHz to 200 kHz) was detected and attributed to a systematic error in adjusting the fluence at the sample. Such error could be the uncertainty in measuring the power or due to thermal effects, e.g. by different heating of the mirrors, as the same fluence does lead to a higher power at a higher repetition rate. In the evaluation of the repetition rate dependence (Figure 5.3), the peak amplitude of the photostationary state has been corrected for this systematic error.

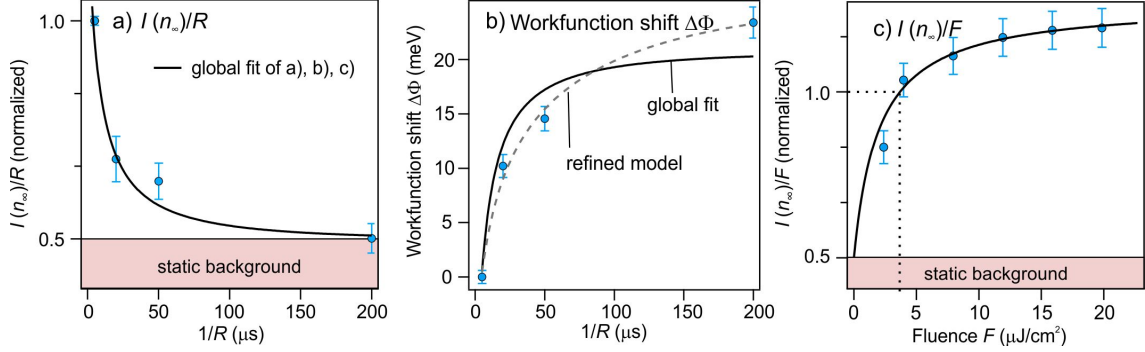


**Figure 5.3:** a) PE-intensity of the photostationary state population  $n_\infty$ ,  $I(n_\infty)$ , divided by the repetition rate  $R$ . The black line is a global fit of a), b) and c), according to the rate equation model described in subsection 4.1.2. b) Work function shift as a function of repetition rate. The global fit (black line) is refined by taking into account technical details of the work function measurement (dashed gray line, see subsection 5.9). c)  $I(n_\infty)$  as a function of excitation fluence (at  $R = 200$  kHz), divided by the fluence  $F$ . The dashed line marks the value of  $F$ , at which the  $R$  dependency was measured. The PE-intensity is set to 1 for both, a) and b), at this excitation condition.

the ZnO surface. The resulting dipole pointing outwards the surface normal pulls down the surface potential and reduces the work function, which is a surface property (see the sketch in Figure 5.2 b)). The work function reduction happens analogously to H surface doping [Dei15]. Together with the spectral overlap of the photostationary state with the H-induced electron pocket shown in the previous subsection, I conclude that photoexcitation acts like doping of the surface. The state that leads to the electronic population just below  $E_F$  is referred to as DX in the following, whereas the photostationary population of the state is termed  $n_\infty$ . The photoemission amplitude due to  $n_\infty$  is termed  $I(n_\infty)$ .

### 5.3 Lifetime of the photostationary state

Figure 5.3 a) and b) show, respectively, the amplitude of the peak below  $E_F$ , i.e.  $I(n_\infty)$ , divided by  $R$  and the work function shift as a function of the time between successive laser pulses  $1/R$ . The peak amplitude was extracted from the raw data by fitting an asymmetric Gaussian peak to the PE-intensity around  $E_F$  in Figure 5.2 and the work function shift by fitting a step function convoluted with the experimental energy resolution to the secondary edge (analysis not shown). The error bars are statistical error bars from repeating the experiment three times (the fit errors are neglectable). The work function shift is plotted with respect to the laser excitation with  $R = 200$  kHz ( $1/R = 5 \mu\text{s}$ ).

Qualitatively,  $I(n_\infty)/R$  decays as  $1/R$  is increased on a  $\mu\text{s}$  timescale and is half at 5 kHz with respect to 200 kHz. In a complementary trend, the work function rises with  $1/R$ . The decay of  $I(n_\infty)/R$  suggests that the electronic population has a lifetime in the  $\mu\text{s}$  range and, furthermore that there is a background with a lifetime exceeding the  $\mu\text{s}$

range that can not be discerned from a photoexcitation-independent, static signal. Note that the quasi-static background is also at a slightly higher binding energy (cf. Figure 5.2 a)). The quasi-static background is most likely a long-lived fraction of the DX state, as will be discussed in section 5.5.

The rest of this section is dedicated to extract the lifetime of the  $\mu\text{s}$  component of the DX state. To extract the DX lifetime from the data I apply the mathematical model developed in chapter 4.1.2. I assume that every pulse creates a number of DX, and eliminates some DX by removing an electron due to photoemission. The population and depopulation probabilities are named  $\alpha$  and  $\beta$ , which are assumed to be proportional to fluence. Within this model the photostationary population  $n_\infty$  of DX can be written down (cf. equation 4.35):

$$n_\infty = \frac{\alpha N}{e^{\frac{\Delta T}{\tau}} + \alpha + \beta - 1} \quad (5.83)$$

The detected PE-intensity is:

$$I_{\text{PE}} = d R t_{\text{exp}} \beta n_\infty \quad (5.84)$$

Here,  $d$  is the electron detection probability and  $\beta$  is, as defined above, the depopulation/photoemission probability. Unfortunately, fitting the  $1/R$  dependency of the amplitude of  $n_\infty$  with equation 5.84 does not allow to extract  $\tau$  directly, because the fit function is over-parametrized: The  $1/R$  dependency of equation 5.83 depends also on the values of  $\alpha$  and  $\beta$  through their weighting in nominator and denominator. These parameters vary as a function of fluence. In order to get an estimate on  $\tau$ , I determine  $\beta$  from the population depletion detected in ultrafast pump-probe spectroscopy, see chapter 4.2.2. This yields  $\beta = 0.034 \text{ cm}^2/\mu\text{J } F$ . Further, I introduce the approximation

$$\alpha \ll \beta,$$

which is equivalent to assuming that  $n_\infty$  never comes close to the maximum number  $N$  of DX states that can be populated<sup>21</sup>. With this, equation 5.83 becomes

$$n_\infty \approx \frac{a F N}{e^{\frac{\Delta T}{\tau}} + 0.034 \text{ cm}^2/\mu\text{J } F - 1}, \text{ where } a = \alpha/F \quad (5.85)$$

---

<sup>21</sup>Introducing this approximation leads to  $\alpha(N - n_{i-1}(\Delta T)) \approx \alpha N$  in equation 4.29, i.e. it is assumed that for all  $i$  the electronic population is much smaller than  $N$ . It therefore does not saturate due a lack of states that can be photoexcited, but only due to the balance between population and depopulation with  $\beta$ . This assumption is justified later using fluence dependent pump-probe spectroscopy in subsection 5.6 and subsection 5.8.

and the fit function for the PE-intensity of  $n_\infty$  becomes

$$\frac{I_{\text{PE}}(1/R = \Delta T, F)}{F R} = A \frac{F}{e^{\frac{\Delta T}{\tau}} + 0.034 \text{ cm}^2/\mu\text{J} F - 1} + I_0 \quad (5.86)$$

with the scaling parameter

$$A = d b a N t_{\text{exp}}, \text{ with } , b = \beta/F = 0.034 \text{ cm}^2/\mu\text{J} \quad (5.87)$$

and the offset  $I_0$  is to account for the quasi-static background. The work function shift is assumed to be proportional to  $n_\infty$  as well:

$$\Delta\Phi = D_\Phi n_\infty \quad (5.88)$$

Equation 5.86 and 5.88 can now be fitted to the PE-intensity  $I(n_\infty)/R$  and work function shift, respectively. The solid black lines in Figure 5.3 a), b)) represent a global fit, i.e. varying  $\tau$  simultaneously for both data sets. The data is described well by the fit. The time constant is determined to  $\tau = 46(19)\mu\text{s}$ . Note, that for the work function, the match is less satisfying than for the intensity change. A perfect agreement can be achieved when taking into account that the *measured* work function is not actually proportional to the work function shift induced by  $n_\infty$ , but is a more complicated function involving the electrostatics in front of the sample surface. This is detailed in subsection 5.9 and results in the 'refined model' fit, the dashed line in Figure 5.3 b).

$I_{\text{PE}}(\Delta T, F)$  (equation 5.86) also predicts a peculiar fluence dependence of the PE signal of  $n_\infty$ . Thus, in order to crosscheck the fit model, the fluence dependence can be examined. Figure 5.3 c) shows  $I(n_\infty)/F$  as a function of fluence for constant  $R$ . Qualitatively, a rise with increasing fluence is observed, tending towards saturation. Note that a small work function reduction of about 10 meV was found upon increasing the excitation fluence, too, consistent with  $n_\infty$  inducing a work function decrease (not shown). In order to compare the predicted fluence dependence to the measurement,  $I_{\text{PE}}(\Delta T, F)/(F R)$  (equation 5.86) is fitted to the fluence dependent data  $I(n_\infty)/F$  *using and holding*  $A$  and  $\tau$  from the fit of the repetition rate dependency  $I(n_\infty)/R$ , which results in the solid black line in Figure 5.3 c)<sup>22</sup>. As seen in Figure 5.3 c), the fit describes the fluence dependent data  $I(n_\infty)/F$  very well. Notably, the only free fit parameter is the quasi-static background  $I_0$ . To fit the fluence dependent data it has to be adjusted by only 14% with respect to the repetition rate dependent data. Thus the model predicts the fluence dependence precisely. This

<sup>22</sup>Both data sets,  $I(n_\infty)/R$  and  $I(n_\infty)/F$ , are normalized to  $I(n_\infty)(R = 200\text{kHz}, F = F_0)$  ( $F_0$ : fluence used for recording the repetition rate dependency). One can therefore fit both,  $I(n_\infty)/R$  and  $I(n_\infty)/F$  with the fit function  $I_{\text{PE}}(\Delta T, F)/(F R)$  using the same parameter  $A$  ( $R$  and  $F$  just enter as constants in the fluence and repetition rate dependency, respectively, and this constant is cancelled out upon normalizing the datasets).

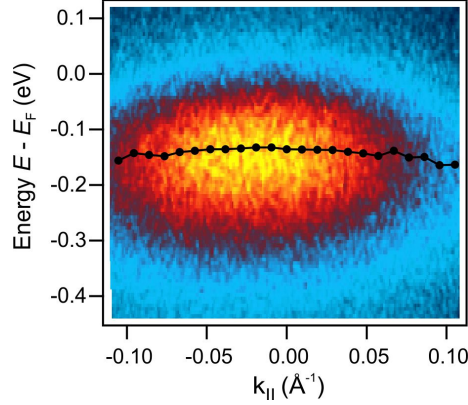


**Figure 5.4:** Angle-resolved PE-intensity probed with  $h\nu = 6.2$  eV in false colors. On top in black: peak maxima evaluated for different  $k_{\parallel}$ .

supports the above used approach to extract the time constant  $\tau$ .

Having ascertained this consistency, I use a global fit of  $I(n_{\infty})/R$ ,  $I(n_{\infty})/F$  and  $\Delta\Phi(R)$ , where  $\tau$ ,  $I_0$ , and  $A$  are varied simultaneously to get a more precise number for  $\tau$ . This approach yields  $\tau = 55(8)\mu s$ . The fit curves can practically not be distinguished from the solid black lines in Figure 5.3 a)-c). Note that the error in  $\tau$  is the fit error assuming a fixed value of  $\beta$ . The determination of  $\beta$  from time-resolved experiments may itself be erroneous due to the assumptions that are made (see chapter 4.2.2). Assuming a conservative error bar of 50% for  $\beta$ , the DX lifetime becomes  $\tau = 77(45)\mu s$ .

## 5.4 Lateral localization of the photostationary state

Beside the surface localization, which is evidenced by the work function change associated with the DX population, I analyze the lateral localization of the DX state with ARPES. The angular distribution of the PE-intensity contains qualitative information of the lateral localization of electronic states: Delocalized states (due to free-electron like electron bands) have a parabolic dispersion close to the  $\Gamma$  point of the Brillouin-zone, while laterally localized states confined to few nanometer (nm) exhibit a flat dispersion [Bov03]. As a rule of thumb, the angular spread of the PE-intensity of localized electrons is inversely proportional to their lateral extent, but an exact determination of the latter is not possible if the final state is not known [And05].

Figure 5.4 presents an angle-resolved PE spectrum of the DX state recorded with  $h\nu = 6.3$  eV. The PE-intensity is plotted in false colors versus binding energy (left) and  $k_{\parallel}$  (bottom). The PE-intensity decays rapidly with  $k_{\parallel}$  and shows apparently no dispersion. On top of the data, the positions of the maximum of the PE-intensity is plotted as a function of  $k_{\parallel}$ , which are evaluated by an asymmetric Gaussian fit to the data (not shown).

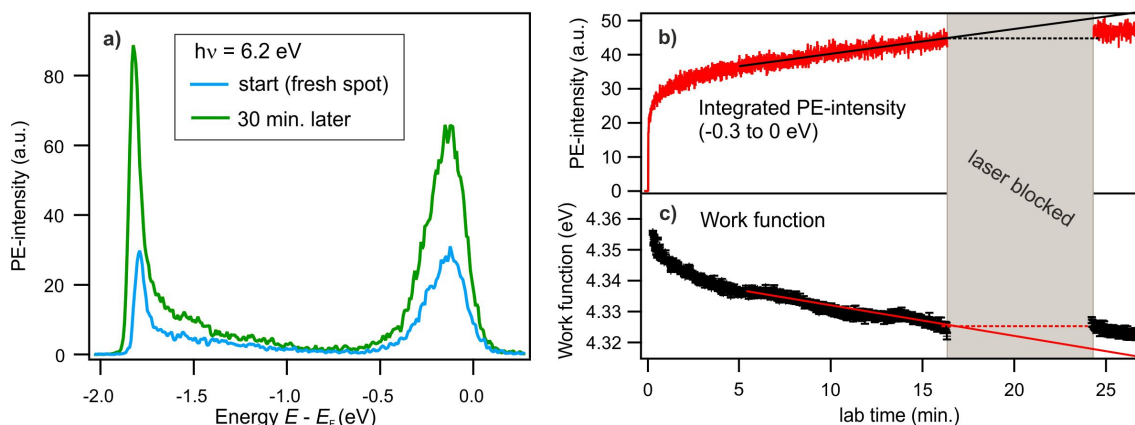


**Figure 5.5:** a) PE signal with  $h\nu = 6.2$  eV of the as-prepared ZnO surface at a virgin (previously not illuminated) spot at two different times: Upon first incidence of the laser (start), and after 30 minutes of illumination. b) Integrated PE-intensity (from -0.3 to 0 eV) and c) work function shift. PE-intensity increase and work function downward shift occur concomitantly. After 17 minutes, the laser is blocked for few minutes and then unblocked again. Solid and dashed lines in b) and c) are linear extrapolations of the changes during the dark time (linearly increasing or constant, respectively) (see text).

The peak positions suggest that the angular distribution is not exactly flat, but exhibits a slight negative dispersion. From this one might infer that the state is delocalized. However, a negative dispersion has been observed before in the context of localized states: The angle-resolved spectrum is reminiscent of the photoemission signature of solvated electrons in ultrathin ice layers deposited on copper surfaces. The negative dispersion of the solvated electrons was attributed to the simultaneous sampling of several solvation sites with different degree of localization [Bov03, And05]. An *apparent* negative dispersion results because stronger localized electrons have a higher binding energy and a larger angular spread of PE-intensity. Thus at high angles the PE-intensity gets a weight at lower energies. In the present case of the DX, electron traps might be distributed in the surface and subsurface region yielding different degree of lateral localization. The negative dispersion might also result from sampling the  $\mu$ s long-lived state and the quasi-static background, which is located at a slightly higher binding energy (subsection 5.2). As a further criterion of lateral localization, the momentum spread of the PE-intensity of the DX state is comparable to the solvated electron [And05]. The observed angular dependence of the DX state is thus consistent with a localized state confined to few nm.

## 5.5 Lab time change of the photostationary state

The above showed that the DX state is localized to a positive charge at the surface and is confined laterally. Because the DX state (and the associated positive charge) is localized, a long lived *free* exciton can be excluded: Although the photoemission signal of such states

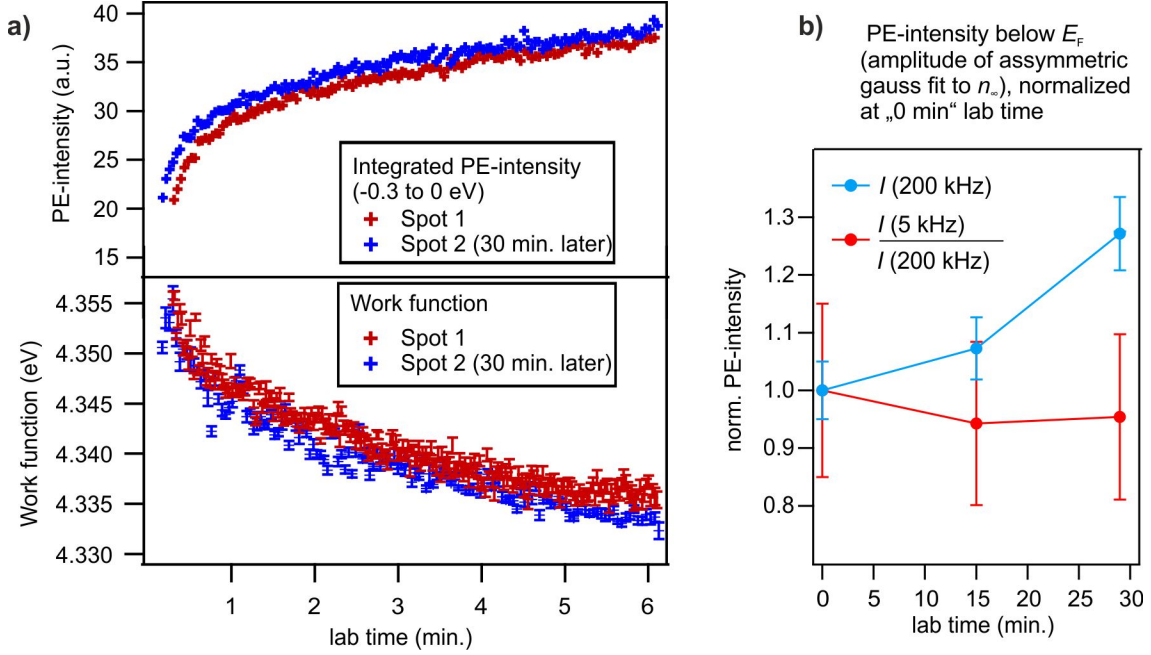
can be non-dispersive [Cui14, Tan19, Chr19] (and hence the latter section can not exclude free excitons), the localization *at the surface* is inconsistent with electron hole pairs that can move freely in the solid. The positive charge at the surface could be due a (valence band) hole polaron, which are known to have a long lifetime [Sez15], or alternatively due to a charged defect. Defect excitons in ZnO also exhibit lifetimes in the  $\mu s$  range [Fog19]. In this subsection the lab time change of the DX state is analyzed to address the question whether it is an intrinsic feature of the ZnO surface or whether its formation depends on the sample conditions, which are changed e.g. by residual gas adsorption or due to UV-illumination.

Figure 5.5 a) presents two photomission spectra recorded with  $h\nu = 6.2$  eV at different times: Upon first incidence of the laser on a fresh (previously not illuminated) spot on ZnO(10-10), and after 30 minutes of illumination. Significant changes are observed at the secondary edge as well as at the energy of the DX state: The secondary edge rises in intensity and shifts to lower energies, and the DX photoemission signal  $I(n_\infty)$  rises by a factor of two. This change continues for at least 3 hours (not shown). In Figure 5.5 b) and c), the increase of  $I(n_\infty)$  and the work function downward shift are displayed as a function of time in minutes, respectively. The work function change is evaluated from the secondary edge position by an error function fit<sup>23</sup> (analysis not shown).  $I(n_\infty)$  is extracted by spectrally integrating across -0.3 to 0 eV. As indicated by Figure 5.5 b) and c),  $I(n_\infty)$  and work function show a mirrored behaviour, starting with a non-linear rise (decay) in the first 1-2 minutes and followed by a linear rise (decay). This mirrored behaviour of the increase of DX population and the work function decrease is entirely consistent with the results of subsection 5.2, which showed that the DX state is connected to a positive surface charge.

Thus, clearly, the DX population depends on the sample conditions that change with time. Therefore, the DX state must be related to the creation of defects or other sample modifications and can not be an intrinsic feature of ZnO. To investigate the lab time changes to the sample in more detail, I tested whether the change is induced by laser illumination or whether it occurs also in the dark, e.g. due to residual gas absorption. To this end, the laser is blocked after about 17 minutes from the start of the measurement and switched on again after few minutes (see Fig. 5.5 b)). Clearly,  $I(n_\infty)$  has increased slightly in the dark but did not continue with the same rate as during illumination. This becomes evident by the linear extrapolations during the dark time, either assuming a slope as during illumination (solid line in Figure 5.5 b)) or assuming no change (dashed line in Figure ref 5.5 b)). By the same kind of analysis I find no change of the work function in the dark within error bars (solid line in Figure ref 5.5 c)). This suggests that the change

---

<sup>23</sup>The error function results from a convolution of a step function with a Gaussian peak to account for the energy resolution of the experiment.



**Figure 5.6:** a) Integrated PE-intensity (from -0.3 to 0 eV) and work function shift at two fresh (previously not illuminated) spots. The second spot is addressed 30 minutes after the first spot. Both data sets almost coincide, consistent with a sample change caused by UV illumination. b) PE-intensity at  $R=200$  kHz compared to the ratio between the  $\mu\text{s}$  long-lived state and the quasi-static background ( $I(5 \text{ kHz})/I(200 \text{ kHz})$ ). This suggests that both,  $\mu\text{s}$  long-lived state and the quasi-static background, rise on the same time scale and thus have a common microscopic origin.

is mainly induced by laser illumination.

This is corroborated by addressing a fresh spot (spot 2) *just after* the above described experiment on spot 1. Figure 5.6 a) shows that  $I(n_\infty)$  as well as work function are nearly identical for both spots:  $I(n_\infty)$  is only slightly higher, and the work function slightly lower at spot 2. This is although spot 2 was addressed about 30 min. later (after measuring on spot 1). Thus, there are minor changes that occur independent of UV illumination, simply by waiting in the dark, but the major modification occurs during laser illumination.

Thus, residual gas adsorption, such as H or CO, can be excluded as microscopic origin, because this process would be illumination-independent. Instead, UV illumination likely increases the defect density of the sample. Notably, the observed time scale of the increase of the DX population agrees well with the rise of persistent photoconductivity (PPC) in ZnO. Both the non-linear rise and the linear rise on a minutes [Col58, Hei55] to hours [Bao11, Gur14] time scale have been observed. Most groups reported the decay of the photoconductivity on the order of hours and days [Bao11, Gur14], but a fast decay component (faster than seconds) was also observed, also at liquid nitrogen temperatures [Hei55]. This is in agreement with the two components of the DX state ( $\mu\text{s}$  long-lived and quasi-static) that were unveiled in subsection 5.3. The DX state is energetically situated

just below the Fermi level  $E_F$ , isoenergetic with the states induced by H adsorption. The latter is known to lead to metallic surfaces [Dei15]. Therefore it is reasonable to assume that the DX population can contribute to conductivity. As mentioned in the introduction, the rise of PPC is related to the creation of oxygen vacancies by UV exposure.

One possible mechanism that can lead to the formation of oxygen vacancies is surface photolysis, i.e. the UV illumination-induced desorption of lattice oxygen. The desorption of oxygen atoms from ZnO(10-10) upon UV illumination ( $h\nu = 3.4$  eV) was directly observed with mass spectroscopy [Göp80]. However, it should be noted that the oxygen desorption rate increases exponentially with temperature [Göp80], i.e. the effect may be small at low temperatures (all spectra shown here are recorded at a sample temperature of 100 K). An alternative mechanism leading to an increased oxygen vacancy concentration at the surface was proposed by Jacobi et al. [Jac84]. The authors reported a work function decrease and a concomitant downward shift of the VB of ZnO single crystals prepared under UHV conditions by sputtering and annealing cycles. They noted that the process is faster with UV illumination but happens also in the dark. To explain these observations, they proposed a diffusion-based process, in which surface oxygen atoms diffuse into the sub-surface to heal oxygen vacancies that are produced during the annealing process<sup>24</sup>. The UV illumination simply accelerates this diffusion-limited oxygen vacancy healing mechanism due to heating [Jac84]. This mechanism would explain both, the surface condition change in the dark as well as upon UV illumination.

Regardless of the exact mechanism, the creation of surface oxygen vacancies is most likely the source of the increase of the DX population with lab time. Oxygen vacancies as the microscopic origin of the DX state can also explain that, when extrapolated to '0 min' labtime,  $I(n_\infty)$  does not go to zero but approaches a finite offset (cf. Figures 5.5 and 5.6). Even without UV illumination, surface oxygen vacancies are expected to be present after annealing in UHV [Göp80]. Thus, the DX state, i.e. the photostationary electron population that is bound to a positive surface charge, is attributed to a defect exciton with the hole at an oxygen vacancy at the surface.

As mentioned before, the photoemission signal at the energy of DX has contributions from a  $\mu\text{s}$  long-lived state and a quasi-static background located at a slightly higher binding energy. Figure 5.6 b) shows that the ratio of the PE-intensity at  $R = 5$  kHz ( $I(5$  kHz), essentially only quasi-static background) and the PE-intensity  $R = 200$  kHz ( $I(200$  kHz),

---

<sup>24</sup>Jacobi et al. state: 'During annealing the diffusion in the bulk and to the surface is greatly increased. Oxygen diffuses to the surface and the number of oxygen vacancies in the bulk near the surface increases too. If one then cools, the diffusion is slowed down by several orders of magnitude. Only at the surface is there enough chemical gradient to allow some back diffusion of oxygen into near-surface vacancies. The basic argument is the following: at the elevated temperature the disorder in the bulk, including oxygen vacancies, certainly increases. At lower temperatures there is the tendency to order again. In the region near the surface the oxygen atoms in the surface layer are able to fill vacancies in the bulk. One simple argument is that the surface oxygen is bound more weakly than the bulk oxygen. Thus, after several hundred minutes the defect concentrations in the bulk and at the surface have reached a new equilibrium.' [Jac84]

containing both components), stays constant over 30 min., while at the same time the photoemission signal at the energy of DX (i.e.  $I(200 \text{ kHz})$ ) rises by 30%. Also, the peak position of the DX state does not shift within this time (not shown). This suggests both, the  $\mu\text{s}$  long-lived state and the quasi-static background rise with the same rate and they likely originate both from the same microscopic origin. These two states could be due to one- and two-fold charged oxygen vacancies predicted unanimously by theory [Jan09, Lan05]. Thus, the quasi-static background is likely also a photostationary state, but with a lifetime that exceeds the  $\mu\text{s}$  window accessed in the repetition rate dependency. A state with  $\tau \gg \Delta T$  would appear as fluence- and repetition rate-independent background in the photoemission data (cf. equation 5.83).

## 5.6 Photon energy dependent excitation of the photostationary state

Several groups have reported that sub-band gap illumination with  $h\nu > \approx 3.1 \text{ eV}$  is sufficient to lead to PPC [Col58, Liu09, Spe13]. This is consistent with theory calculations of oxygen vacancies in ZnO that show that the vacancy forms a deep donor level in the ZnO band gap [Ell16]. Advanced hybrid-DFT results, which yield the correct band gap energy of bulk ZnO, predict a value of 3.0 eV below the CB minimum [Pat06]. The observed onset of PPC also agrees with other experimental work, where oxygen vacancies are induced to ZnO nanostructures by purpose to lower the absorption edge into the visible range for photocatalysis applications [Wan12].

In order to determine if also the DX state can be populated with sub-band gap illumination, I use pump-probe spectroscopy, keeping the probe higher than the work function to detect the DX state and tuning the pump photon energy below the band gap.

Figure 5.7 a) presents a pump-probe experiment using a pump photon energy of 3.2 eV (FWHM 0.1 eV), which is below the fundamental band gap of 3.4 eV, and 6.2 eV as probe (see the inset for an energy level diagram). The PE-intensity is plotted in a false color plot versus pump-probe delay (bottom) and binding energy (left). The intensity at negative delays consisting of the photostationary state was subtracted to show the photoinduced ultrafast change. As can be seen Figure 5.7 a), the ultrafast pump-induced change is characterized by a fast electron population increase below  $E_F$ . Within the pump-probe cross correlation of about 200 fs FWHM<sup>25</sup>, the electron population rise instantly. The signal shows a small downward shift within the first picoseconds (ps) and then does not visually change in intensity or peak position within the first 10 ps. Figure 5.7 b) compares the pump-induced signal at  $\Delta t = 215 \text{ ps}$  to the photostationary DX state (the spectra

<sup>25</sup>Determination from integrating the pump-probe data shown in Figure 5.7 a) at electron energies above  $E_F$ , where a short-lived electronic population is observed, likely due to hot electrons in the ZnO CB [Dei14] (not shown).

are normalized). The pump-induced 'fresh population' is partially spectrally overlapping, but is shifted to higher energies by approximately 0.1 eV. I attribute this to a further energetic stabilization that takes place on a timescale of ns or  $\mu$ s. After  $\Delta T$  the pump-induced population increase is isoenergetic with the photostationary state, as shown by the pump-induced signal increase detected by the probe at negative delays in Figure 5.7 c). The latter measurement is the proof that the pump-induced population partially survives  $\Delta T$  and adds to the photostationary state population (cf. chapter 4).

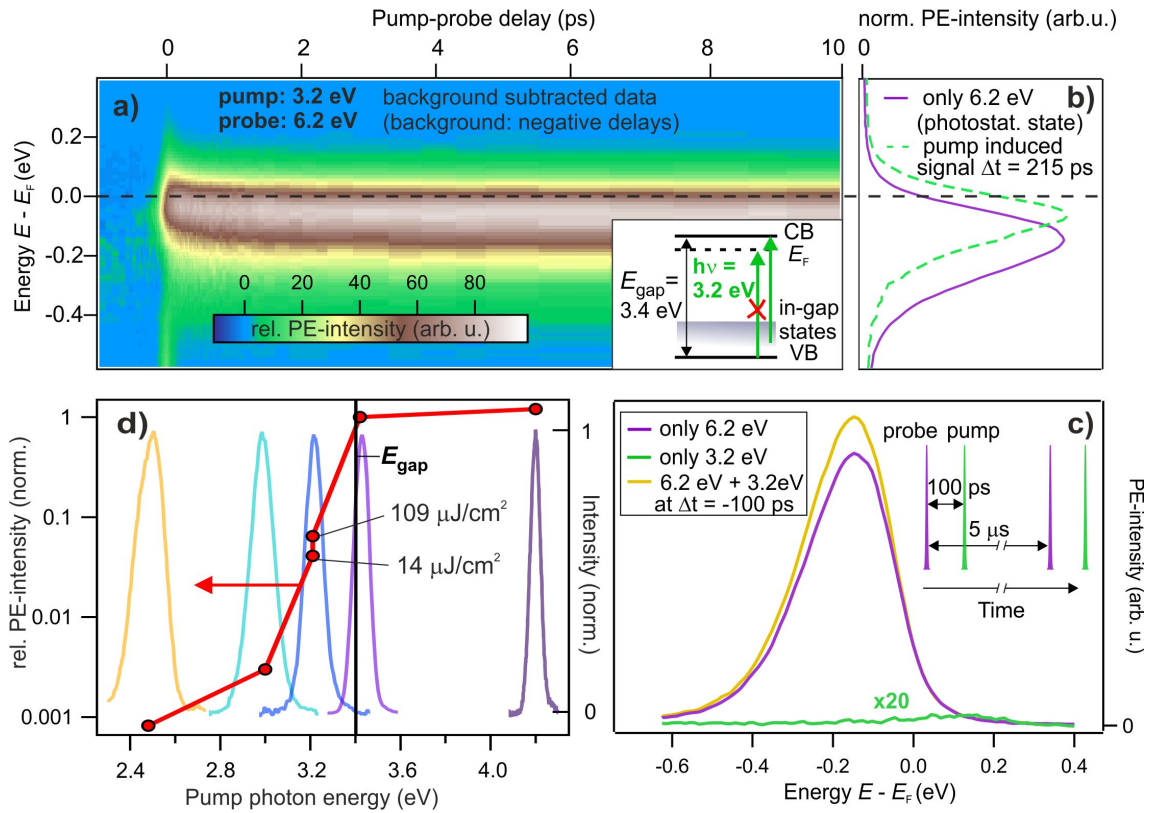


**Figure 5.7:** Pump-probe experiment with sub-bandgap excitation: a) False color plot of the pump-induced PE-intensity (pump: 3.2 eV, probe: 6.2 eV) on a timescale of few ps. The background at negative delays was subtracted. Inset: Energy level diagram. The pump is below the fundamental gap of 3.4 eV, thus exclusively accessing in-gap states. b) Comparison of energetic position of the pump-induced signal at 215 ps and the photostationary state population. c) Pump-induced signal increase detected by the probe at a negative time delay of  $-100$  ps, showing that the pump-induced population survives the inverse repetition rate (5  $\mu$ s). Inset: Sketch of the timing of pump and probe pulses. d) Pump-induced signal increase below  $E_F$  at 1 ps with respect to  $-1$  ps normalized by pump fluence (cf. equation 5.89). The laser spectra are also displayed to indicate the energy range that is accessed with the pump. The action spectrum shows that the electrons are photoexcited from in-gap states close to the VB maximum.

I therefore conclude that the DX (or at least its precursor state, see also the discussion in chapter 4.2.3) is formed within 200 fs and with sub-bandgap illumination of 3.2 eV. The

fast timescale is consistent with exciton formation that was identified in previous trARPES experiments on ZnO(10-10) using above band gap excitation [Dei14]. Because the photon energy is not high enough to excite electrons across the band gap and is also not high enough to form free excitons resonantly (the free exciton series starts at 3.33 eV at room temperature; band gap and exciton peak shift to higher energies at lower temperatures [Kli10a]), the photoholes can not be formed in the VB, but must be formed in in-gap states.

In order to determine the energetic position of the in-gap states I tune the pump photon energy over a wide range, from 2.5 eV to 4.2 eV. Figure 5.7 d) displays the pump-induced signal increase at 1 ps with respect to a negative delay of -1 ps on a logarithmic scale versus pump-photon energy. The signal increase is calculated as

$$\frac{I(\Delta t = 1ps) - I(\Delta t = -1ps)}{I(\Delta t = -1ps)} / F_{\text{pump}} \quad (5.89)$$

where  $F_{\text{pump}}$  is the pump fluence. This shows that the exciton signal can be induced by pump excitation below the fundamental gap but that the efficiency rapidly decays. At 3.2 eV the efficiency is already an order of magnitude lower than at 3.4 eV. For pump energies lower than 3.0 eV the signal increase vanishes. Remarkably this absorption curve compares very well to the photon energy dependence of PPC [Col58, Liu09]. This strongly supports that the in-gap states are due to oxygen vacancies and hence that the photostationary electron population is due to long-lived defect excitons, where the hole is at an oxygen vacancy at the surface.

**Addendum: Fluence dependence** To exclude two-photon pumping across the band gap I varied the pump fluence across one order of magnitude for pump excitation with 3.2 eV. The pump-induced signal increase at positive delays with respect to negative delays according to equation 5.89 is plotted Figure 5.7 d) for two pump fluences, 14  $\mu\text{J}/\text{cm}^2$  and 109  $\mu\text{J}/\text{cm}^2$ . Both data points nearly coincide, i.e. the excitation efficiency in the ultrafast time domain varies linearly upon varying the pump fluence. The linear fluence dependence shows that the population of the state below  $E_F$  indeed takes place from in-gap states and not via excitation across the band gap in a two-photon process. Furthermore it clearly suggests that the number of states that can be photoexcited (termed  $N$  in section 5.3) is large enough not to induce saturation effects. An extended fluence dependence of the pump-induced population increase at positive delays will be presented in the next chapter (subsection 6.1.5) using a pump photon energy of 3.4 eV. Also there an almost linear fluence dependence is observed.

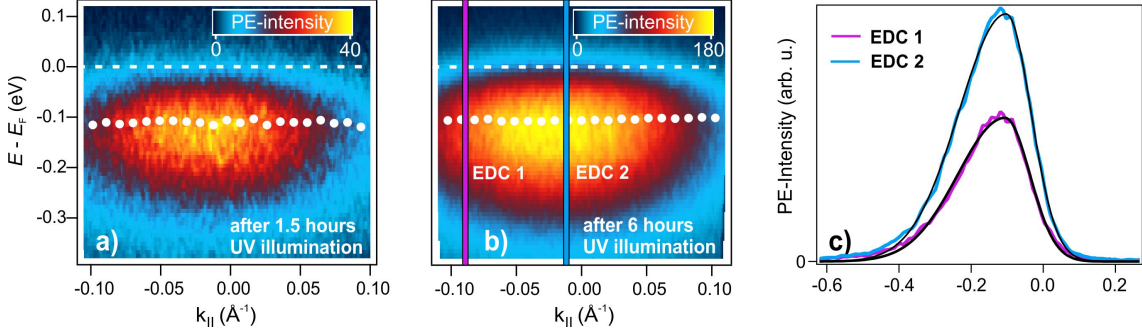


**Figure 5.8:** Angle-resolved PE-intensity at two different UV illumination times: a) After 1.5 hours, the angular distribution is practically identical to Figure 5.4, exhibiting a feature with slight negative dispersion. b) After 6 hours of UV illumination, the angular distribution does not exhibit a negative dispersion anymore. Instead, a slight positive dispersion may be discerned. White markers: Peak maxima of the intensity distribution evaluated by asymmetric Gaussian fits. c) Exemplary angle-integrated cuts for the spectrum shown in b) (EDC 1, EDC 2, integration window as indicated in b)) and Fits with an asymmetric Gaussian function.

## 5.7 Angular distribution of the photostationary state after long UV exposure - the onset of delocalization

The photostationary defect exciton population revealed in the last sections leads to a similar spectroscopic signatures as the surface 'doping' of ZnO via adsorption of H. From the analogy to chemical doping, individual 'photodopants' are expected to form a collective metallic phase above a critical density inducing a Mott (or Mott-Anderson) SMT. A SMT induced by long-lived defect excitons was reported previously using transport measurements by Katsumoto et al. [Kat87], cf. section 2.3.3. UV illumination leads to a constantly increasing long-lived photodoping density due to an increase of the density of deep defects at the surface (cf. subsection 5.5). Thus, a photostationary SMT might occur after long UV exposures.

Figure 5.8 shows the angle-resolved PE-intensity of the DX for two different UV illumination times at the same spot. After 1.5 hours of UV illumination the spectrum is alike to the one presented before, cf. Figure 5.4 in section 5.4. The photoemission intensity is slightly separated from the Fermi energy  $E_F$ , decays rapidly towards higher  $k_{||}$  and has apparently no dispersion. An evaluation of the maximum of the photoemission intensity with an asymmetric gaussian fit to the data (not shown) confirms this impression: The peak maxima (white dots in Figure 5.8 a)) exhibit a flat or slightly negative apparent dispersion. After 6 hours of UV illumination, however, the angle-resolved PE-intensity changes. Within this time span, the PE-intensity from the photostationary state increased by a factor of about 4, indicating that much more photostationary defect excitons are present. The PE-intensity after 6 hours of UV illumination is shown in Figure 5.8 b). In contrast to the spectrum after 1.5 hours of UV illumination, in this case the PE intensity is di-

rectly adjacent to  $E_F$ , appears broadened and asymmetric, i.e. it has apparently a more pronounced curvature at lower energies and seems to be cut by  $E_F$ . It seems more like a partially filled band than a localized state. To evaluate the dispersion of the maximum of the photoemission intensity, again asymmetric Gaussian fits are performed. Two exemplary cuts at constant angle at close to the Brillouin zone center ( $k_{\parallel}=0$ ) and at large  $k_{\parallel}$  are shown in Figure 5.8 c)) together with asymmetric Gaussian fits (EDC 1, EDC 2 and black lines). To the eye the spectra are at the same energetic position. Indeed, even after normalization, a difference is hard to detect by eye (not shown). However, the dispersion of the peak maxima extracted from the asymmetric Gaussian Fits is now slightly different than for the spectrum after 1.5 hours of UV illumination. This becomes apparent by comparing the peak maxima of both cases (white dots in Figure 5.8 a) and b)), which exhibit a slight tendency to a negative curvature in case of Figure 5.8 a) and a slight tendency to a positive curvature in case of Figure 5.8 b).

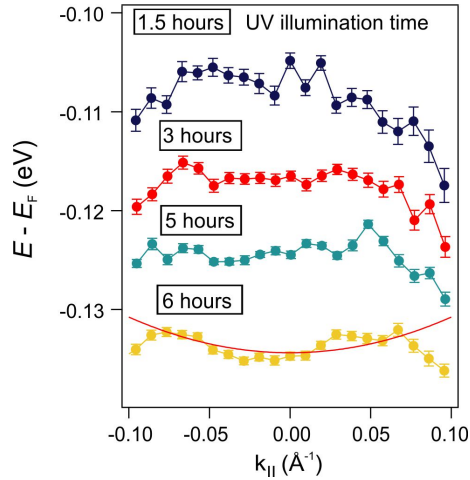


**Figure 5.9:** Peak maxima extracted from asymmetric Gaussian fits (such as shown in Figure 5.8 c)) for four different UV illumination times, 1.5 hours, 3 hours, 5 hours and 6 hours. The peak maxima are vertically offset for clarity. The red line is the plot of a free electron-like parabola (see text).

Figure 5.9 directly compares the peak maxima extracted from the fits for four different UV illumination times, 1.5 hours, 3 hours, 5 hours and 6 hours. For all cases the same fitting procedure with asymmetric Gaussian functions was used (cf. Figure 5.8 c)). After 1.5 hours and 3 hours, the angular dispersion is negative. After 5 hours, the negative dispersion is not as clear anymore. Finally, after 6 hours, close to the center of the Brillouin zone, a small positive dispersion can be detected. The variation of the peak positions with  $k_{\parallel}$  is very small, only on the order of few meV, but a clear tendency can be discerned. The red line in Figure 5.9 is the plot of a free electron-like parabola,

$$E(k) = \frac{\hbar^2 k^2}{2m_{\text{eff}}}, \quad (5.90)$$

with a heavy effective electron mass of  $m_{\text{eff}} = 10 m_e$ , where  $m_e$  is the free electron mass. The apparent dispersion of the peak maxima close to the center of the Brillouin zone can be well described by this parabola. There is a deviation at higher  $k_{\parallel}$ , that may be attributed to a remaining localized electron population, or the overlap of spectral signatures with different angular spread, which is also the supposed origin of the apparent negative dispersion observed at shorter UV illumination times (cf. section 5.4). The observed change of the apparent dispersion indicates that the electrons are no longer localized after 6 hours of UV exposure but form a free electron-like band with a large effective mass. Indeed, close to the Mott density, a heavily correlated electron liquid should arise with a large effective mass, see section 2.2.2.

In conclusion, the observed change of the angular spectrum for long UV illumination times indicates a photostationary SMT. After 6 hours the electrons are at the verge of delocalization. Even longer UV illumination should enhance this tendency as observed by Katsumoto et al. [Kat87]. It can be noted that in case of Katsumoto et al., the interpretation of UV illumination-induced SMT was based on the increasing number of defect excitons at a *fixed* defect density upon increasing illumination time while in the present case, every UV exposure time corresponds to a *different* defect density, for which a population of defect excitons is established straightaway. This is a result of the pulsed laser excitation at high repetition rate and relatively high fluence as discussed in section 4.1.2. Katsumoto et al., in contrast, use a continuous wave light source; a fluence is not indicated, but it is probably relatively low. In this case, the rise of the photostationary population can be very slow, because it is dominated by the lifetime of the photoexcited population, cf. section 4.1.1, equation 4.24.

In the next chapter I will show that, for a given defect density at the surface, the defect exciton density is increased significantly with respect to the photostationary population within few hundred picoseconds after excitation of a strong pump laser pulse. Upon controlling the defect exciton density in the ultrafast time domain, a transient SMT occurs, and a clear evolution of the effective mass can be discerned (section 6.2.2).

## 5.8 Angular distribution of the photostationary state at high photoexcitation fluences and short UV exposure times

For the discussion of the ultrafast metallization dynamics in the next chapter, it is important to make sure that the initial state of the sample is semiconducting. As seen in the last section this condition can only be fulfilled for a spot that was not exposed to UV for too long. This is because the density of deep defects induced by UV illumination becomes larger and larger the longer a spot is illuminated, eventually causing photostationary metallization of the ZnO surface. In this subsection I investigate the angle-resolved

## 5.8 Angular distribution of the photostationary state at high photoexcitation fluences and short UV exposure times

photoemission intensity of the photostationary state in the case of comparably short UV exposure times, i.e. low defect densities. The photostationary state preserves the flat dispersion characteristic for a localized state for all excitation conditions. This is attributed to a balance of depopulation and population, limiting the photostationary photodopant density.

**Angular dependency at the highest  $h\nu_{\text{Probe}}=6.3$  eV fluence** Using  $h\nu_{\text{Probe}}=6.3$  eV to excite and probe the photostationary state was shown lead to a rapid saturation of the photostationary state population upon increasing the photoexcitation fluence, see subsection 5.3. The dependency of the photostationary state population on the fluence was described using a model based on population and depopulation probabilities, named  $\alpha$  and  $\beta$ , respectively.  $\alpha$  and  $\beta$  were assumed to increase linearly with fluence. According to the model, the saturation results because of the depopulation probability  $\beta$  shows up in the denominator of equation 5.85. At the highest 6.3 eV fluence used  $F=20 \mu\text{J}/\text{cm}^2$ , the angular dispersion is flat; the angular-resolved PE-intensity is identical to Figure 5.4.

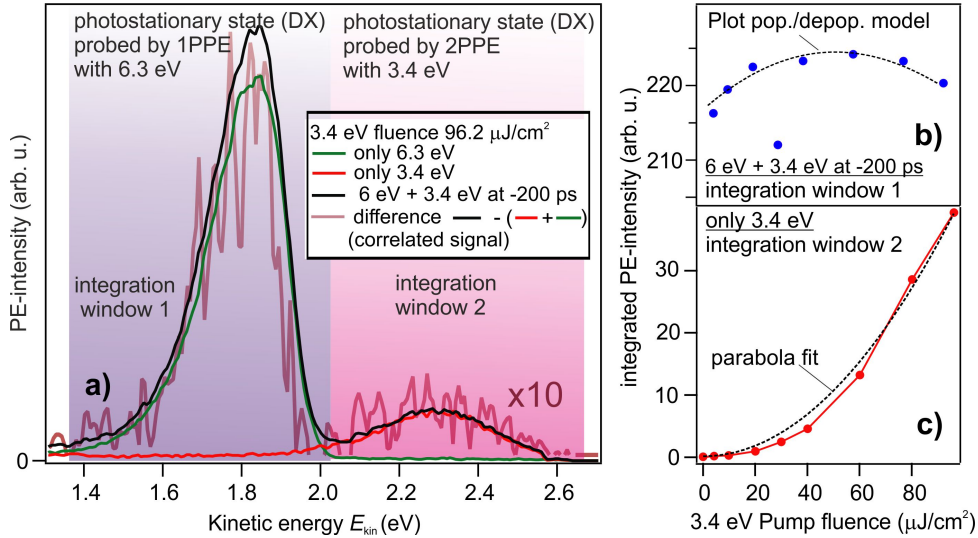


**Figure 5.10:** PE from the DX upon overlapping pump  $h\nu_{\text{Pump}}=3.4$  eV and probe  $h\nu_{\text{Probe}}=6.3$  eV at a pump-probe delay of -200 ps. a) The PE spectrum consists of two parts, which are due to PE with  $h\nu_{\text{Probe}}=6.3$  eV (purple box, integration window 1) and  $h\nu_{\text{Probe}}=3.4$  eV (pink box, integration window 2) from the DX, respectively. Upon overlapping the two beams the DX signal is enhanced. The correlated signal overlaps after scaling with a factor of 10 with the DX detected by pump  $h\nu_{\text{Pump}}=3.4$  eV and probe  $h\nu_{\text{Probe}}=6.3$  eV, respectively. b) PE-intensity detected by the probe  $h\nu_{\text{Probe}}=6.3$  eV for different pump fluences. The dashed line is a plot of equation 5.91 (see text) c) PE-intensity detected by the pump  $h\nu_{\text{Pump}}=3.4$  eV alone for different pump fluence. The trend can be fitted with a parabola.

**Population of the photostationary state using an additional pump  $h\nu_{\text{Pump}}=3.4$  eV**

Applying an additional pump beam enhances the photodoping density at positive as well as negative delays as shown in section 5.6. When using  $h\nu_{\text{Pump}}=3.4$  eV as pump, the action spectrum shows a large enhancement of the surface electron signal at positive delays with respect to negative delays. However, the major part of this electronic population decays faster than the inverse repetition rate, as will be shown in the next chapter. It thus does not contribute to the photostationary state. Only the part of the pump-induced population that survives the inverse repetition rate enhances the photostationary state population, and this enhancement is detected by the probe detected at negative delays, as discussed in section 5.6.

Figure 5.10 a) shows the PE-intensity emitted by  $h\nu=3.4$  eV only (2PPE),  $h\nu=6.3$  eV only (1PPE), and when both laser beams are incident at a negative delay of -200 ps. Two peaks in the energy windows indicated with the purple and pink boxes, can be discerned. They are energetically separated by about 0.5 eV, corresponding to the difference between the photon energies of the two laser beams. The two peaks are attributed to photoemission from the photostationary state, the DX. When both beams are incident at -200 ps, the signal emitted by the 6.3 eV laser beam is enhanced; the signal emitted by 3.4 eV seemingly stays constant. However, when taking the difference between the spectrum with both beams incident and the sum of the single color spectra (correlated signal, purple curve in Figure 5.10 a)), it becomes clear that the emitted PE-intensity is enhanced for both beams at the energy of the DX state. This shows that the combination of both beams enhances the photostationary DX population.

The DX population probed with 6.3 eV at -200 ps is plotted as a function of 3.4 eV fluence in Figure 5.10 b). The data points show some scatter but seem to first increase and then decrease with increasing fluence. Figure 5.11 shows that the angular distribution of the PE-intensity stays flat even at the highest pump fluence, meaning that a photostationary SMT does not occur.

The fact that the DX population is not increased further even by strong photoexcitation by the pump can have two different reasons. Firstly, the maximum number of states that can be populated is reached, which is unlikely because the pump-induced population increase at positive delays at the energy of DX does not saturate as a function of pump fluence (cf. section 5.6 and section 6.1.5 in the next chapter). Secondly, the effect could be due to a balance of population and depopulation of the DX due to the pump beam, similar to the probe only. This seems indeed the most likely explanation as will be shown in the following using the mathematical model developed in section 4.2.2. Within this model I showed that the signal increase at negative delays induced by the pump beam can have any dependence on the pump fluence, depending on how efficiently the photostationary state is populated and depopulated. The DX population detected by the probe at negative

delays is given by equation 4.76, which is reproduced here:

$$n_{\text{probe, negative delays}} = \frac{((1 - \beta_{\text{Pump}})\alpha_{\text{Probe}}N + \alpha_{\text{Pump}}N) e^{-\Delta T/\tau}}{1 - (1 - \beta_{\text{Pump}})(1 - \beta_{\text{Probe}}) e^{-\Delta T/\tau}} \quad (5.91)$$

where  $\alpha_{\text{Pump}}$ ,  $\alpha_{\text{Probe}}$ , and  $\beta_{\text{Pump}}$ ,  $\beta_{\text{Probe}}$  are the population and depopulation probabilities of pump and probe, respectively. A simple case is if the depopulation  $\beta_{\text{Pump}}$  by the pump can be neglected, and the population probability  $\alpha_{\text{Pump}}$  increases proportionately with pump fluence. Then,  $n_{\text{probe, negative delays}}$  would increase linearly with pump fluence, in all other cases it becomes more complicated.

In the present case  $\beta_{\text{Pump}}$  can not be neglected: There is clearly photoemission from the DX due to pump, which means that the state *must be* depopulated by the pump. Moreover, the PE increases superlinearly: As shown in Figure 5.10 c), the PE signal emitted by  $h\nu=3.4$  eV only from the DX state has a parabolic fluence dependence, consistent with a 2PPE process. Thus,  $\beta_{\text{Pump}} = b_{\text{Pump}}F^2$ , where  $b_{\text{Pump}}$  is a proportionality constant. If one assumes that the population probability by the pump  $\alpha_{\text{Pump}}$  increases linearly, which is reasonable considering that excitation from in-gap states to the CB does not require two photons, then the depopulation by the pump becomes more and more crucial as the fluence increases. This qualitatively explains the experimentally observed dependence of  $n_{\text{probe, negative delays}}$  on the pump fluence, which first increases and then decreases. To confirm that the observed fluence dependence can be described by the population/depopulation model, I compare equation 5.91 to the experimental data. The dashed line in Figure 5.10 b) is a plot of equation 5.91, using known values for  $\tau$ ,  $\beta_{\text{Probe}}$  (cf. subsection 5.3) and  $\Delta T = 5 \mu\text{s}$ .  $\alpha_{\text{Probe}}$  and  $b_{\text{Pump}}$  enter as free parameters. Data and model coincide, showing that the dependence of  $n_{\text{probe, negative delays}}$  can be explained by the balance between population and depopulation by the pump.

The above two paragraphs showed that the photostationary state is localized at all photoexcitation fluences. The balance between population and depopulation prevents the photostationary population to increase with increasing photoexcitation fluence. This evidently impedes a photostationary SMT, as long as the density of deep defects is low, i.e. at comparably short UV exposure times. For the ultrafast metallization dynamics presented in the next chapter, all shown data is derived from experiments performed within 4-5 hours after surface preparation with sputtering and annealing. A localized photostationary population is always assured. Hence the initial state for the pump-induced metallization is that of semiconductor, photodoped below the Mott density.

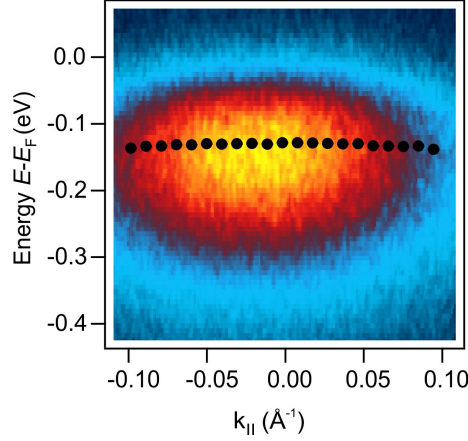


**Figure 5.11:** Angle-resolved spectrum of the photostationary state at highest pump excitation fluence probed by  $h\nu_{\text{probe}}=6.3$  eV at a pump-probe delay of -200 ps. Black dots represent the peak maximum of the PE-intensity.

## 5.9 Uncovering the true photoinduced work function change

In subsections 5.2 and 5.3 it was shown that photoexcitation of the ZnO surface populates a photostationary state which induces a surface dipole change. This was evidenced by a shift of the secondary edge to lower energies, which is linked to the population increase upon changing the excitation conditions, i.e. fluence or repetition rate. In the following it will be analyzed in detail how the *measured* work function decrease is related to the applied bias, which changes the electrostatics in front of the sample surface. Building on that, the relation between the work function change induced by the photostationary state population and the measured work function change has to be reconsidered. The practical outcome is that the photoinduced work function decrease of a small photoexcited area is in reality higher than what is measured directly under typical bias values. The true work function change of the photoexcited area is measured only at high bias values. Tuning the bias turns out to be a practical tool to determine *if* a photoinduced work function decrease occurs and to estimate its value.

**Dependence of the measured work function on the applied bias** Within the approximation that the laser excitation creates a homogeneous, circular disk of photoinduced dipoles, the potential energy of an electron on the center axis and at a distance  $z$  from the surface, is described by [Tan12] (cf. chapter 3.1.2, equation 3.15):

$$V_D(z) = -\frac{eD}{2\epsilon_0} \left(1 - \frac{z}{\sqrt{R^2 + z^2}}\right) \quad (5.92)$$

Here,  $D$  is the dipole density, and  $R$  is the radius of the circular disk. On the other hand there is a potential due to the sample and the analyzer, which are charged against each

other with the bias voltage  $U_{\text{bias}}$ . The distance between sample and analyzer is  $d = 4$  mm, and the potential energy is approximated by a plate capacitor, i.e.

$$V_C(z) = -\frac{eU_{\text{bias}}}{d}z. \quad (5.93)$$

Strictly speaking there would be a term due to difference in the work function of sample and analyzer, but in the case considered here,  $\Phi_{\text{ZnO}} \approx 4.4$  eV and  $\Phi_{\text{Analyzer}} \approx 4.35$  eV, i.e. they are considered identical.

In Figure 5.12 a) the potential energy  $V(z) = V_D(z) + V_C(z)$  is plotted for  $\frac{eD}{2\epsilon_0} = 0.5$  and  $R=50$   $\mu\text{m}$  (a typical laser spot size in the present experiments) for different values of  $U_{\text{bias}}$ . For photoelectrons escaping the sample, the energy barrier that results from the short ranged surface dipole on the order of nm (cf. section 3.1.2, Figure 3.5 and 3.8) is reduced by 0.5 eV due to the additional dipole at the surface. However, until the photoelectrons reach the analyzer, they have to overcome an additional potential energy barrier on a lengthscale of  $R$ , resulting from  $V(z)$  (cf. Figure 5.12 a)). If no bias is applied, the energy gain from reducing the barrier just in front of the surface is exactly cancelled. Therefore, the measured work function (i.e. the lowest kinetic energy detected by the analyzer) is expected to be unaffected. Yet, an *increase* of  $U_{\text{bias}}$  lowers the potential well and thus the measured work function is expected to *decrease*.

In Figure 5.12 b) the secondary edge measured for different bias values on ZnO is plotted versus versus final state energy, which is calculated as

$$E_{\text{final}} - E_{\text{F}} \equiv E_{\text{B}} + h\nu = E_{\text{kin, measured}}(U_{\text{bias}}) - E_{\text{F}}(U_{\text{bias}}) + h\nu \quad (5.94)$$

In this representation the energy of the fastest electrons with zero binding energy  $E_{\text{B}} = 0$  equals the energy of the photon energy  $h\nu = 6.2$  eV, and the secondary edge equals the work function.  $E_{\text{kin, measured}}(U_{\text{bias}})$  and  $E_{\text{F}}(U_{\text{bias}})$  refer to the measured kinetic energy of the photoelectrons at an arbitrary energy and from zero binding energy electrons, respectively.  $E_{\text{F}}(U_{\text{bias}})$  is measured at the gold sample holder. Both increase proportionately with  $U_{\text{bias}}$  and by taking the bias in both terms into account it cancels out. Thus, the position of the secondary edges or any spectral signature can be compared.

In Figure 5.12 b) it is seen that the secondary edge shifts systematically to lower energies as the bias is increased, i.e. the measured work function decreases. Upon increasing the bias from 1 V to 4 V the measured work function decreases by several tens of meV and it seems to saturate at even higher  $U_{\text{bias}}$ . The inset shows the photostationary state. It does not shift as a function of  $U_{\text{bias}}$ , as expected, since for a normal spectroscopic signature, the bias cancel out in the calculation of the final state energy (equation 5.94). The bias dependent work function decrease would be consistent with the picture shown in Figure 5.12 a).

As a cross check, a bias series was also taken at the gold sample holder. At the gold surface, no photoinduced work function decrease is expected to occur and thus no  $\mu\text{m}$  ranged potential in front of the surface should exist which could be influenced by  $U_{\text{bias}}$ . Yet, also at gold a minor downward shift is detected, which amounts to less than 10 meV upon increasing the bias from 0.5 V to 3.5 V (Figure 5.12 d)). Besides systematic errors such as the energy calibration of the analyzer, in theory the surface potential on a nm range might be lowered as well. This effect is known in literature as Schottky effect in the context of thermal electron emission [Pat10] and the concept is closely related to the bias-dependent tuning of  $V(z)$  that is presented within this chapter. In any case, the observed effect on gold is an order of magnitude lower than on ZnO, and thus an influence of systematic errors or the Schottky effect is minimal in the case of ZnO.

In the following, a quantitative evaluation is presented to support the interpretation of the secondary edge shift on ZnO due to a bias dependent tuning of the energy barrier (Figure 5.12 a)). In Figure 5.12 c) the positions of the secondary edge are plotted versus  $U_{\text{bias}}$ . They are referenced to the value with a bias of 1 V<sup>26</sup>. In order to compare the measurement to the model in Figure 5.12 a), the derivative of the potential energy  $V(z)$  was calculated which yields the maximum of the potential energy as a function of the distance from the sample surface  $z$ . The maximum  $z_{\text{max}}$  is

$$z_{\text{max}} = \sqrt{\left(\frac{dR^2 |\Delta\Phi|}{U_{\text{bias}}}\right)^{2/3} - R^2}. \quad (5.95)$$

It is a function of  $U_{\text{bias}}$  and the photoinduced work function change in front of the sample,  $\Delta\Phi \equiv -\frac{eD}{2\epsilon_0}$ . The measured work function change is given by the value of the potential  $V(z)$  at  $z_{\text{max}}$ . This value is calculated for different  $U_{\text{bias}}$  and referenced with respect to the work function  $U_{\text{bias}} = 1 \text{ V}$ :

$$\Delta = V(z_{\text{max}}(U_{\text{bias}})) - V(z_{\text{max}}(1\text{V})) \quad (5.96)$$

This equation is fitted to the data points in Figure 5.12 c), with the spot size  $R$  and the work function shift  $\Delta\Phi$  entered as fitting parameters. The fit matches the data precisely, resulting in  $\Delta\Phi = -195(1) \text{ meV}$  and an disk radius of  $76(1) \mu\text{m}$  (diameter  $152(2) \mu\text{m}$ ). This shows that the secondary edge shift observed experimentally can be explained by a bias dependent tuning of the energy barrier (Figure 5.12 a)). The disk diameter used in the model is reasonable considering the beam diameter of the laser beam, which is  $171 \mu\text{m}$

---

<sup>26</sup>The values of the secondary edge have been corrected for the lab time change that occurs due to UV illumination, cf. section 5.5. The spectra were recorded at uniform time intervals and a spectrum with the same bias was recorded before and after the series. By this, the lab time shift could be discerned and it was subtracted from all spectra in the series assuming a linear change (decrease), which is what is observed experimentally, see section 5.5.

(FWHM)<sup>27</sup>. Note that for this measurement, a  $h\nu = 3.4$  eV pump beam was applied in addition to the  $h\nu = 6.2$  eV probe beam, at a negative delay of -100 ps. The 3.4 eV beam lowers the work function by increasing the photostationary state population (not shown), i.e. the disk size of photoinduced dipoles should be of the size of the 3.4 eV beam. Clearly,  $R$  should be regarded as effective value for the disk radius of photoinduced dipoles, since the photoinduced dipole density is not homogeneous in reality. The effective radius  $R$  used in equation 5.92 is 0.9 times the beam radius of the exciting laser beam creating the photoinduced dipole density.

I conclude that, if the work function is reduced due to photoexcitation within a small spot of the sample surface, the measured work function in photoemission depends strongly on the bias between sample and analyzer. The work function reduction leads to a decelerating field reaching from the sample surface into the vacuum and by tuning the bias it is possible to tune the energy barrier that photoelectrons have to overcome. The extension of the field into the vacuum is on the order of the beam radius. Modelling the electrostatics and fitting them to bias dependent data revealed for the present case a work function reduction of  $\Delta\Phi = -195(1)$  meV within the photoexcited area. Typical measurements are carried out at low bias. At a bias of 1.5 V (such as used throughout this work) the measured work function reduction would be only  $-59$  meV, i.e. more than a factor of three lower than the 'true' work function reduction. The here made considerations are thus vital to extract quantitative work function shifts caused by photoexcitation.

---

<sup>27</sup>This value results from averaging the long and short axis of the elliptical spot via  $\sqrt{174\mu m \cdot 112\mu m \cdot 1/\cos(45^\circ)}$ , which are determined with a beam profiler, cf. section 3.2.2. The factor  $1/\cos(45^\circ)$  accounts for the projection onto the sample surface under  $45^\circ$  grazing incidence.

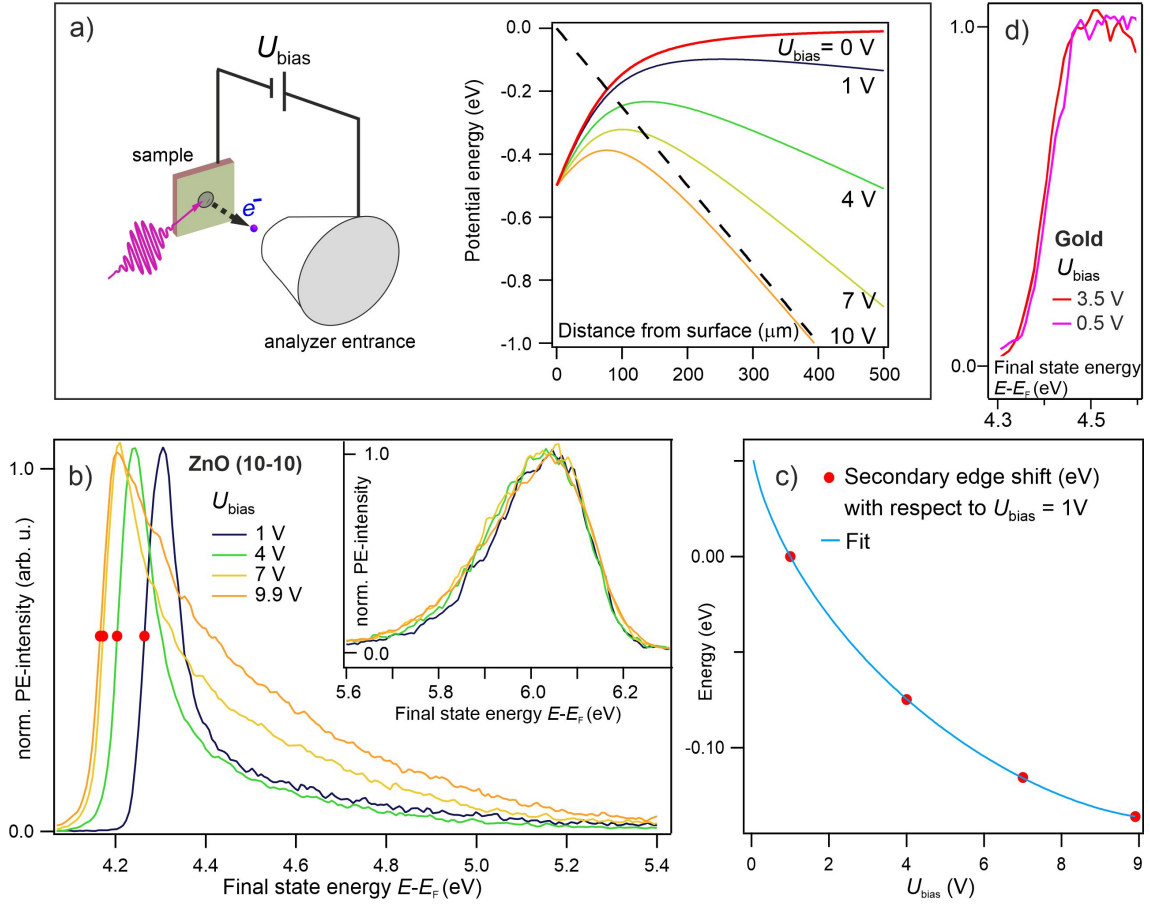


**Figure 5.12:** a) Left: Sketch of the geometry of the experimental setup. An incoming laser pulse excites a small area on the sample and photoemits an electron. A bias  $U_{\text{bias}}$  between sample and analyzer is applied. Right: the electric potential felt by an electron is determined by the accelerating field due to  $U_{\text{bias}}$  and a deceleration field on the order of the spot size if the laser leads to a work function change within the spot (here:  $\Delta\Phi = -0.5$ ). An energy barrier exists in front of the sample, which is tuned by the bias, and affects the low energy cutoff measured in photoemission. b) Bias dependence of the ZnO secondary edge position. The photostationary DX state probed by  $h\nu = 6.3$  eV is shown in the inset. c) Secondary edge position as a function of bias together with a fit according to the model in a) (see text). d) Control bias series on the Gold sample holder, where no photoinduced work function change is expected.

**Relation between the magnitude of the photoinduced work function change and the measured value in photoemission** Based on the above insights into the effect of the electrostatics on the measured work function in photoemission, the relation between the measured work function and the photostationary state population  $n_\infty$  (equation 5.88) has to be reconsidered. The dependence between lowering the work function  $\Delta\Phi$  within the photoexcited spot and the measured workfunction  $\Delta\Phi$  (measured) is not linear, as can be seen directly from plotting  $V(z)$  for the same  $U_{\text{bias}}$  but different  $\Delta\Phi$ , see Figure 5.13. Accordingly, equation 5.88 should be modified by:

$$\Delta\Phi(n_\infty) \longrightarrow V(z_{\text{max}}(\Delta\Phi(n_\infty))) \quad (5.97)$$

Thus, the global fits of the work function change and the change of  $n_\infty$  as a function of repetition rate have to be recalculated taking into account the applied bias (1.5 V) and the spot radius of the 6.3 eV probe beam in this measurement (25  $\mu\text{m}$ ). Both determine the electrostatics in front of the sample and thus the measured work function as discussed above.

As shown in Figure 5.3 b) the global fit using the relation 5.97 describes the measured work function shift as a function of repetition rate well, and it actually leads to a better accuracy than simply assuming proportionality between  $n_\infty$  and the work function shift, cf. equation 5.88. The work function reduction in the photoexcited area that is induced by the photostationary state with  $\mu\text{s}$  lifetime, that is, the difference between the work function at 200 kHz and 5 kHz, is revealed by this analysis to  $\Delta\Phi(n_\infty) = -70$  meV. The measured work function change was only -20 meV. There is a discrepancy between the photoinduced work function reduction unveiled here ( $\Delta\Phi(n_\infty) = -70$  meV) and in the bias dependence above ( $\Delta\Phi = -195$  meV). This may be, on the one hand, due to the different excitation conditions in both experiments, since during the bias dependence a 3.4 eV pump beam was applied that was absent during the repetition rate dependency. On the other hand, in the repetition rate dependency only the work function change due to the component of  $n_\infty$  with  $\mu\text{s}$  lifetime is measured, while in the bias dependency the total photoinduced work function is measured, i.e. the work function shift includes a possible contribution of the quasi-static component of  $n_\infty$ . Additional measurements with the same excitation conditions for both, the repetition rate dependency and bias dependency would need to be performed in order to quantify the contribution of the quasi-static component of  $n_\infty$  to the work function reduction.

Note that, so far, I have only considered photoinduced surface dipoles that are photostationary. However, fast decaying surface dipoles (i.e. not photostationary) are also created at the ZnO surface. The associated fields on a  $\mu\text{m}$  lengthscale should lead to delay dependent shifts on the photoelectrons emitted in trARPES, as described in chapter 3.1.5. Such effects are indeed observed and will be described in chapter 6.2.4. It will also

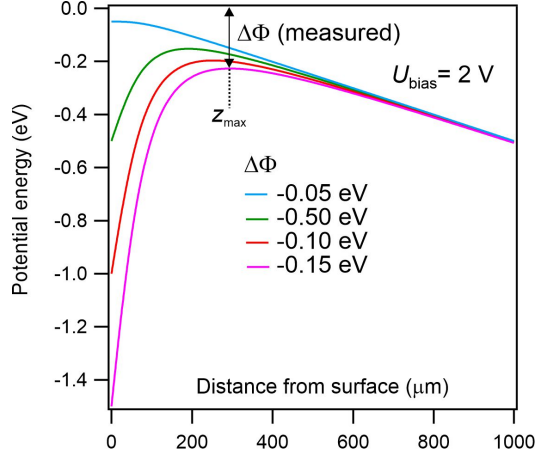


**Figure 5.13:** Dependence of the electrostatic potential in front of the sample surface for different photoinduced work function changes  $\Delta\Phi$ .

be demonstrated that detecting photoinduced work function changes has an even more complex (temporal) component.

## 5.10 Summary and conclusions

In summary, I have unveiled a long-lived defect exciton at the ZnO(10-10) surface. The hole is localized at a surface defect leading to an electrical dipole pointing outward the surface normal which reduces the work function (cf. subsection 5.2) and leads to a decelerating field within a distance from the sample that corresponds to the spot size (cf. subsection 5.9). Photon energy dependent measurements show that the associated defect level is located less than 400 meV above the VB maximum, consistent with oxygen vacancies that form deep donor levels (cf. subsection 5.6). The electron population is detected 150 meV below the Fermi energy, i.e. 350 meV below the bulk CB minimum (cf. subsection 5.1) and is localized laterally (cf. subsection 5.4 and 5.7).

The defect exciton lifetime has two components: Half of the population decays with  $\tau = 77 \pm 45 \mu\text{s}$ . The other half is invariant under varying the inverse repetition rate in the  $\mu\text{s}$  regime as well as the fluence, indicating a static or very long-lived contribution. Both the  $\mu\text{s}$ -long lived state as well as the static contribution rise with the same rate on a minutes to hours time scale as a function of UV illumination. This suggests that both contributions rise due to same microscopic origin (cf. subsection 5.5), i.e. the creation of oxygen vacancies. It seems likely that these two states are due to one- and two- fold charged oxygen vacancies predicted unanimously by theory [Jan09, Lan05, Pat06].

The long-lived electron population is isoenergetic with the occupied electronic state induced by surface doping with H. The latter is also accompanied by a work function reduction. Thus, photoexcitation acts analogously to chemical doping of the surface with H and

increases the n-doping at the surface. By this I show that PPC is a surface phenomenon, as has been suggested by the sensitivity to oxygen gas exposure in the earliest experiments on PPC in ZnO [Col58]. Furthermore, it clarifies that PPC can not be explained by band-flattening due to upwards band bending towards the surface [Spe13, Gur14]. Instead, this study unveils that PPC is due to switching of the oxygen-vacancy induced donor state from a strongly bound deep donor to a hydrogenic shallow donor, in agreement with the theoretical predictions of Lany and Zunger [Lan05, Lan07].

The photodoping density rapidly saturates as a function of photoexcitation fluence because the long-lived defect exciton can be populated *and* depopulated by the laser excitation (cf. subsection 5.3 and subsection 5.8). However, when the density of deep defects at the surface is large enough due to sustained UV illumination of a spot, the photostationary state exhibits the signature of delocalized electrons as opposed to localized electrons (cf. subsection 5.7). This indicates that a SMT in ZnO occurs due to an increased number of defect excitons that act like shallow donor dopants.

Given a defect density at which the photostationary electron population is localized, I will show in the succeeding chapter that the density of defect excitons can be enhanced within few hundred picoseconds after excitation with a strong pump pulse. This leads to delocalization and generation of a *transient* SMT at the ZnO surface. The metal decays faster than the inverse repetition rate, namely on a time scale of few hundred ps as the defect exciton population decreases again below the critical limit.

## 6 Ultrafast generation and decay of a surface metal

Ultrafast PIPTs are extreme examples for the optical control of material properties such as the electrical conductivity. They occur in a range of inorganic and organic materials for instance due to carrier-lattice or carrier-carrier interactions that change the screening of the Coulomb interaction (see chapter 2.3.5). A canonical example is the ultrafast photoinduced SMT in Vanadium dioxide ( $\text{VO}_2$ ) that fascinates researchers to date from a fundamental [Wal18] and applied point of view [Cha, Ryc13]. However, similar to photoinduced SMT in other inorganic compounds [Sch08, De 13], the generation of the metallic phase in  $\text{VO}_2$  requires strong photon fluxes on the order of few  $\text{mJ}/\text{cm}^2$ . Moreover, due to the high energy uptake, the photoinduced phase becomes thermally stabilized, and the backswitching to the semiconducting phase is limited by thermal diffusion processes of nanosecond duration [Wen13]. Both, high laser power requirements as well as a limited recovery rate are drawbacks for ultrafast high-frequency switching applications.

In the last chapter I showed that, in case of  $\text{ZnO}$ , photoexcitation acts similar to chemical surface doping with H by creating defect excitons localized at the surface. The defect excitons survive longer than the inverse repetition rate forming a photostationary state. The photostationary population rapidly saturates with increasing photoexcitation fluence, and the electron population is localized.<sup>28</sup> In this chapter the focus is on the ultrafast time domain, where the defect exciton population can be transiently enhanced for a time span much shorter than the inverse repetition rate. Restricted to a timescale of few hundred ps, sufficiently strong photoexcitation results in a non-equilibrium state that shows all footprints of a metal: (1) density of states around the equilibrium Fermi level  $E_F$  resulting from a partially filled dispersive band and (2) an electron distribution following Fermi-Dirac statistics that thermalizes with the lattice within 200 fs. This transient metallisation of the  $\text{ZnO}$  surface can be understood by photodoping via the photoexcitation of defects at the  $\text{ZnO}$  surface: The photohole at a surface defect site leads to downward band bending (DBB) towards the surface in analogy with chemical doping of oxide surfaces. As the CB is bent below the Fermi level it becomes partially filled and the surface is metallized above a critical electron density. Unlike metal-like states resulting from an exciton Mott transition without photoinduced changes of the electronic band structure (see the introduction to this thesis), the quasi Fermi level of the transient metal phase equals the equilibrium Fermi level for all photoexcitation fluences, showing that a PIPT takes place.

Relevant for technological applications as an ultrafast photoconductive switch, the here demonstrated SMT can be realized at an extraordinarily low threshold fluence on the order of  $\mu\text{J}/\text{cm}^2$ , three to four orders of magnitude below the laser fluence needed to

---

<sup>28</sup>In case of low densities of deep defects at the surface. As discussed in section 5.7 the defect density can be increased by sustained UV illumination such that a photostationary SMT occurs. In this chapter, the defect density is below this threshold for all shown measurements.

---

induce the SMT in bulk VO<sub>2</sub> and other inorganic semiconductors. Moreover, in contrast to e.g. VO<sub>2</sub>, generation *and* decay occur on a sub-ns time scale, within 20(20) fs and few hundred ps, respectively. Finally, the discovered ultrafast photodoping mechanism is not ZnO specific and can most likely be applied to realize photoinduced SMTs at many semiconductor surfaces at interfaces. The only prerequisite is a sufficient amount of deep donor defects.

This chapter is organized in two parts: In section 6.1 the photoinduced SMT is demonstrated and the associated time constants are determined. I investigate the temperature dependence and show that the SMT can be realized up to close to room temperature, at least up to 256 K. The SMT must be confined to the surface, exhibiting a striking similarity with the 2DEG induced by chemical doping with hydrogen at the ZnO(10-10) surface. Section 6.2 is then devoted to the mechanism, which is unveiled in great detail. I show that the effective mass of the photoinduced metallic band shows the same critical behaviour at the localization threshold as upon inducing a SMT by chemical doping with shallow donors. Furthermore, the VB shifts transiently downward, evidencing DBB along with the generation of the surface metal phase. I demonstrate that the cause of the DBB is the photohole created in a defect state in lying in the band gap of ZnO, and accordingly can be induced with photoexcitation slightly below the fundamental band gap, analogously to the excitation of the photostationary 'metastable photodopant' (cf. subsection 5.6). As a confirmation of this statement I employ trARPES to map the electrostatic potential in front of the sample surface, which unambiguously demonstrates that the surface is positively charged by photoexcitation. Because the surface is positively charged upon photoexcitation the work function should shift down, however, the naively expected shift of the secondary edge does not occur in the ultrafast time domain. This is explained by simulations of the trajectories of slow electrons. Finally, I show that the surface metal occupation and the transient DBB becomes stronger on a time scale of minutes/hours due to the creation of deep defects by UV illumination; this happens analogously to the growth of the photostationary state population (cf. subsection 5.5), showing that the microscopic origins of the ultrafast surface metal generation and the photostationary state must be one and the same. Beside UV illumination, the surface preparation with sputtering and annealing also enhances the defect density at the surface. The findings suggests that the surface metal is generated by the photoexcitation of surface oxygen vacancies.

A part of this chapter is published in Gierster et al., *Ultrafast generation and decay of a surface metal*, Nature Communications (accepted), <https://arxiv.org/abs/2005.13424>.

## 6.1 Unveiling the ultrafast semiconductor-to-metal transition

In this subsection, I demonstrate the photoinduced SMT at the ZnO(10-10) surface using trARPES and determine the rise and decay of the metal phase. I further investigate how changing the sample temperature affects the PIPT. Finally I compare the photoinduced metal phase to the 2DEG induced by chemical doping with H at the ZnO(10-10) surface and investigate how the adsorption of H affects the ability to transiently metallize the surface by photoexcitation.

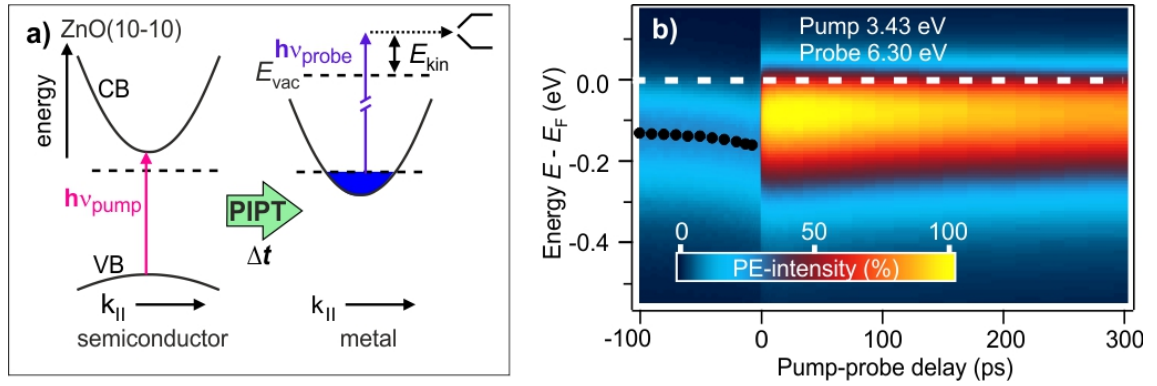


**Figure 6.1:** a) Energy level diagram and illustration of the discussed photoinduced phase transition. b) Angle-integrated PE-intensity in false colors as a function of pump-probe delay  $\Delta t$  and energy. Probe: 6.3 eV, pump: 3.43 eV ( $27 \mu\text{J}/\text{cm}^2$ ). The pump pulse induces an abrupt increase of the electron density below  $E_F$ . It also induces a shift at negative delays that is discussed in section 6.2.4.

### 6.1.1 A photoinduced free electron-like band

Metallic conduction occurs without thermal activation (i.e. down to 0 K) through an electronic state delocalized over the whole specimen. The electronic band must be partially filled, i.e. the Fermi level  $E_F$  must be within the band, to allow the directional movement of charge carriers at an applied voltage. Close to the center of the Brillouin zone, the band is in the simplest case free-electron like, meaning that the energy-momentum relation can be described by a parabola of the form

$$E(k) = \frac{\hbar^2 k^2}{2m_{\text{eff}}} \quad (6.98)$$

where  $m_{\text{eff}}$  is the effective mass. Thus, the question whether ZnO is metallic or not can be addressed by ARPES, which gives direct access to the band structure. Here trARPES is used to see if strong photoexcitation induces an ultrafast SMT in ZnO (cf. the sketch in Figure 6.1 a)).

For the pump-probe experiment, a probe photon energy of 6.3 eV is used, photoemitting electrons around  $E_F$ ; the sample is excited using a time-delayed pump pulse with a photon energy of 3.43 eV, i.e. resonant to the ZnO band gap (see Figure 6.1 a)). Already in subsection 5.6 it was shown that the photodoping density can be increased very efficiently with this pump photon energy. At the same time the photoexcitation with 3.43 eV is well below the work function and thus does not contribute to the PE intensity even at elevated fluences but only modifies the sample properties measured with the probe.

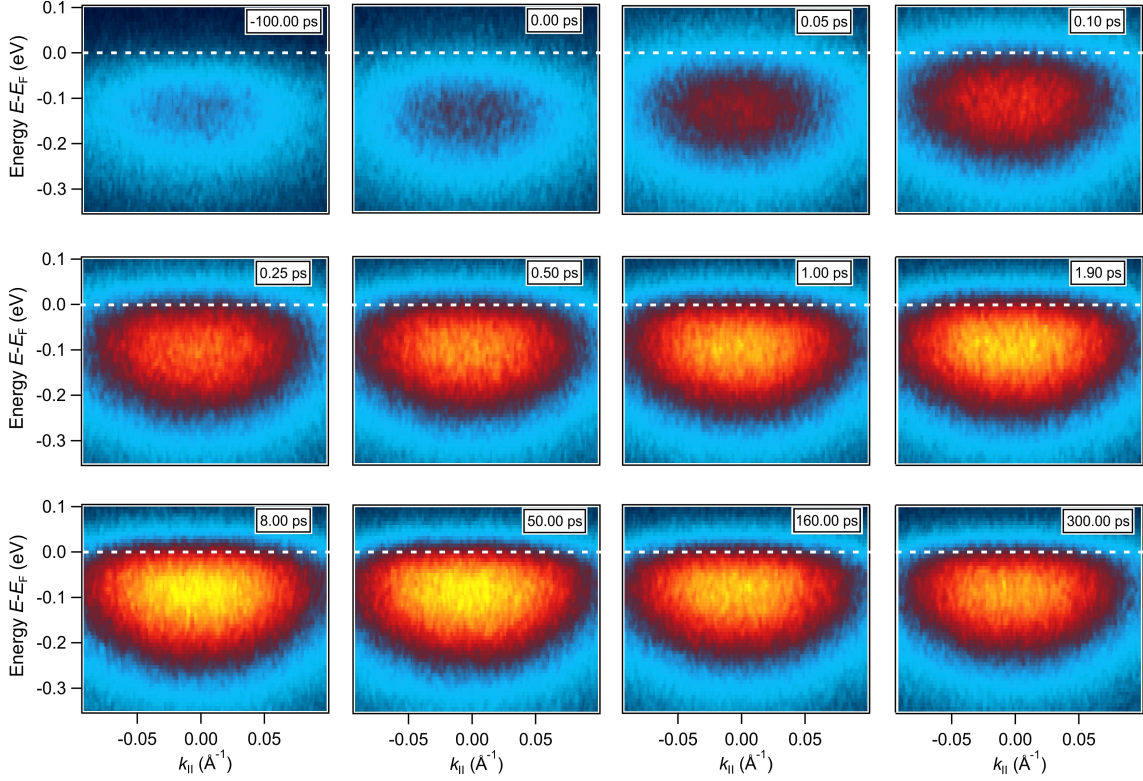
Figure 6.1 b) represents a pump-probe scan using a pump fluence above the PIPT threshold. The PE intensity is plotted versus pump-probe delay (bottom axis) and energy (left axis). All photoelectrons are emitted by the 6.3 eV probe. At negative delays a small signal below  $E_F$  is observed due to the photostationary state discussed in detail in chapter 5. The signal shows a shift on a hundred ps time scale, as indicated by the black markers in the figure. This shift will be analyzed in detail in subsection 6.2.4. In this subsection I focus on the positive delays: Upon incidence of the pump a large PE signal is induced that is apparently cut by the equilibrium Fermi level  $E_F$  and persists over the here presented delay window, i.e. for several hundred ps.

Figure 6.2 gives a more detailed impression of the photoresponse by showing the angular distribution of the PE intensity at different pump probe delays. Starting with the localized photostationary state at negative delays, the signal below  $E_F$  rapidly increases after time zero (first row). On a timescale of hundreds of fs it evolves into a feature of few 100 meV width, which is cut by  $E_F$  and shows a positive curvature, to the eye most apparent at low energies (cf. the last image in the first row and the first image in the second row). The PE intensity then increases further on a timescale of few ps (second row) and eventually decays on a timescale of hundreds of ps (third row). The apparent curvature as well as the formation of a clear Fermi-cutoff indicate the formation of a metallic band after arrival of the pump.

To confirm the finding of the pump-induced formation of a metallic band with positive curvature, I evaluate the distribution at an exemplary pump-probe delay few ps after time zero. Figure 6.3 a) shows the angular distribution of the PE intensity averaged from 4 to 8 ps. I extract the curvature by fitting PE spectra at fixed angles with a Gaussian peak multiplied by a Fermi-Dirac distribution, convolved with another Gaussian peak to account for the energy resolution ( $res=30$  meV)<sup>29</sup>. Explicitely written down the fit function is:

$$f(E) = A e^{-(E'-E_0)^2/w^2} \frac{1}{1 + e^{\frac{E'-E_F}{k_b T}}} \otimes e^{-(E')^2/res^2} \quad (6.99)$$

<sup>29</sup>Energy broadening occurs due to the electron analyzer and from the finite spectral width of the probe laser beam. The energy resolution of the electron analyzer is determined from the sharpest feature in the PE spectrum, the secondary edge. The width of the probe laser beam is determined with a spectrometer, cf. section 3.2.2.



**Figure 6.2:** Snapshots of the ultrafast generation and decay of a surface metal: Angular distribution of the photoresponse upon resonant photoexcitation, pump: 3.43 eV ( $27 \mu\text{J}/\text{cm}^2$ ), probe: 6.3 eV, at different pump-probe delays. First row: -100 ps (photostationary state), to +100 fs, generation within a screening time scale. Second row: Strengthening within few ps. Third row: Decay within hundreds of ps.

The Fermi level is fixed to the equilibrium  $E_F$  and the width  $w$  as well as the 'electronic temperature'  $T$  are globally optimized for all spectra. Free fit parameters are the Gaussian peak positions  $E_0$  and the amplitude  $A$ . Exemplary spectra and the fits with equation 6.99 are shown in Figure 6.3 b). The resulting Gaussian peak positions are plotted on top of the angular distribution in Figure 6.3 a). They can be described by a free electron-like parabola (equation 6.98, black lines in Figure 6.3 a)), with an effective mass of  $m_{\text{eff}} = 1.2(1) m_e$ , where  $m_e$  is the free electron mass. To exclude any errors from this specific analysis I also evaluated the curvature by two complementary methods: I tracked the position of the maximum of the intensity distribution, as well as the position of the half maximum (at the lower energy side) numerically<sup>30</sup>, cf. Figure 6.3 b). The resulting positions are also displayed in Figure 6.3 a) and they likewise describe a free electron-like parabola. The effective masses are  $m_{\text{eff}} = 1.7(5)m_e$  and  $m_{\text{eff}} = 1.8(3)m_e$ , respectively. Thus, independent of the specific analysis method, a free electron-like band is found with an occupation that

<sup>30</sup>By evaluating the maximum or half maximum position in the PE spectra; to increase the accuracy the data was interpolated.

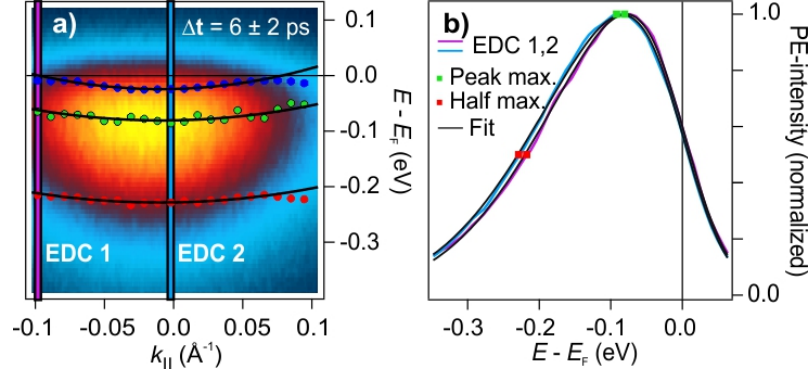


**Figure 6.3:** Angular distribution of the photoresponse and different evaluation of the apparent dispersion. a) Angular distribution, averaged between a delay of 4 to 8 ps after resonant photoexcitation with a fluence of  $27 \mu\text{J}/\text{cm}^2$ . Blue: Peak positions from fitting energy distribution curves at different  $k_{\parallel}$  (e.g. EDC 1, EDC 2 as indicated with the blue/purple boxes) with equation 6.99. Green: Peak maximum of the EDC, red: position of the low energy edge half maximum. The black lines are fits with a free electron parabola (equation 6.98). b) Exemplary energy distribution curves EDC 1, EDC 2. Black curves: Fits with equation 6.99. Green squares: Position of the low energy edge half maximum. Red squares: Peak maximum of the EDC (numerically determined).

is governed by the *equilibrium* Fermi-Dirac distribution. This is in strong contrast to the photostationary state population at negative delays, which consists of *localized* electronic states at the Fermi level with a flat or slightly negative dispersion (cf. subsection 5.4 and subsection 5.8). I conclude that the pump induces a free electron-like band, indicative of a photoinduced SMT.

### 6.1.2 Thermalization and cooling of the electron system

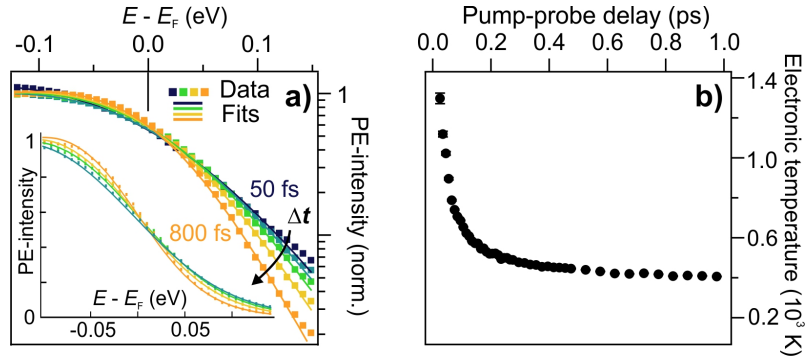


**Figure 6.4:** Cooling of a thermalized electron system. a) Normalized angle-integrated PE-intensity for different delays (50 to 800 fs) with Fermi-Dirac distribution fits (solid lines). The fluence of the 3.43 eV pump beam is  $96.2 \mu\text{J}/\text{cm}^2$ . Inset: Data on a non-log scale. b) Electronic temperature as a function of  $\Delta t$  extracted from the fits.

If the pump indeed would cause a SMT with delocalized electrons around at the Fermi

level, the electron system (consisting of many delocalized electrons) would form an ensemble and an electronic temperature could be defined. Shortly after photoexcitation with ultrashort laser pulses, metals typically exhibit an increased electronic temperature, which subsequently cools down on a time scale of few hundred femtoseconds (fs) due to equilibration with the phonon bath (hot electron gas cooling) [Lis04, Fan92]. The electronic temperature is encoded in the broadening of the Fermi-Dirac distribution that can be tracked by trARPES [Lis04, Fan92].

To see if an electronic temperature can be defined in the case of photoexcited ZnO and if hot electron gas cooling takes place, it is insightful to inspect the angle-integrated PE-intensity for different delays in the first ps after incidence of the pump. The corresponding spectra (normalized to maximum intensity) are displayed in Figure 6.4 a) on a logarithmic scale. Between spectra at early time delays (50 fs) and late time delays (800 fs) the signal above  $E_F$  systematically decreases. From a non-logarithmic representation in the inset of Figure 6.4 a) it can be seen that the signal is also concomitantly increased below  $E_F$ . The solid lines in Figure 6.4 a) represent Fermi-Dirac fits with equation 6.99. The Gaussian width  $w$  and peak position  $E_0$  were set to a global optimum for pump-probe delays larger than 100 fs and the only fit parameters are the electronic temperature  $T$  and the amplitude  $A$ . Before this delay, the spectra undergo substantial changes that cannot be accounted for by just varying the latter two parameters and  $w$  and  $E_0$  enter as free parameters. These fits match the data perfectly, showing that the intensity change can be well described by a Fermi-Dirac function with a delay-dependent temperature. The electronic temperatures resulting from the fit are displayed in Figure 6.4 b) and show a clear trend. Initially (at  $\Delta t=25$  fs), the electronic temperature is 1300 K and it subsequently cools down on a timescale of few hundred fs. In this plot I included the datapoints below 100 fs although the fit is more uncertain (the fit error bars are still small, though). The timescale of the cooling of the hot electron system is comparable to what is observed for photoexcited metals [Fan92].

The above shows that an electronic temperature can be indeed defined in the case of photoexcited ZnO. The material shows a thermalized electron system after few tens of fs after optical excitation that is initially hot and cools down subsequently. Thus, ZnO behaves like a metal after photoexcitation, strongly affirming the above statement that a photoinduced SMT takes place. The observed thermalization time is very fast. Photoexcited metals can show a significant contribution of non-thermalized electrons with a sizeable excess energy above  $E_F$  up to hundred's of fs after optical excitation [Lis04]. In the case of ZnO the fast thermalization time may be related to the efficient coupling of electrons to optical phonons which also leads to hot electron relaxation times on the order of tens of femtoseconds at high excess energies above  $E_F$  [Dei14]. Furthermore, electron-phonon interaction is likely responsible for the energy loss of the electron system,

expressed by the decay of the temperature on a timescale of few hundred fs, in analogy to metals. An equivalently short electron thermalization time of 50 fs was recently revealed in graphite by trARPES [Roh18], followed by a cooling phase on a longer timescale. Also there, the fast thermalization was attributed to strong coupling between electrons and optical phonons that assist in the initial momentum relaxation. During the cooling phase the phonons take up energy from the electron bath.

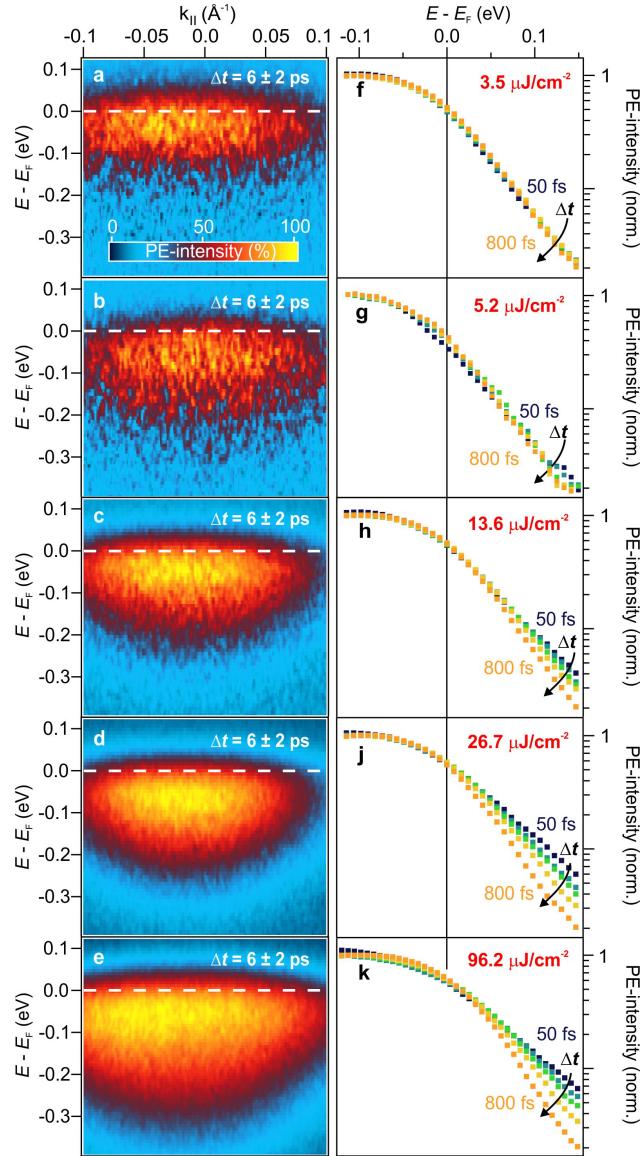


**Figure 6.5:** a)-e), Angular distribution of the pump-induced signal, averaged between 4 to 8 ps, below and above the PIPT threshold  $F_C$  of  $13.6 \mu\text{J}/\text{cm}^2$ . The photostationary signal is subtracted to show the low fluence response. Below  $F_C$ , the pump induces a non-dispersive state below  $E_F$ . Above  $F_C$ , a dispersive band evolves, with increasing bandwidth and curvature. f)-k), Corresponding angle-integrated PE-spectra (log. scale, normalized) for different pump-probe delays (50 fs to 800 fs). Below  $F_C$ , all spectra are identical. Above  $F_C$  the high energy tail shows hot electron gas cooling as characteristic for photoexcited metals, cf. Figure 6.4.

### 6.1.3 Determination of the threshold fluence

Typically, PIPT require a minimum threshold photoexcitation fluence below which the impact of the laser pulse is not enough to induce the phase transition. To see whether the metallic phase in photoexcited ZnO shows such a threshold behavior I varied the photoexcitation fluence of the 3.4 eV pump beam over a wide range, from few  $\mu\text{J}/\text{cm}^2$  to tens of  $\mu\text{J}/\text{cm}^2$ .

Figure 6.5 a)-e) presents the angular distribution of the PE intensity around  $E_F$  as a function of fluence, averaged between 4 to 8 ps. The angular distribution of the PE intensity shows a systematic change upon increasing the fluence. For low fluences ( $3.5 \mu\text{J}/\text{cm}^2$ ,  $5.2 \mu\text{J}/\text{cm}^2$ ), the intensity is characterized by one feature that appears constant as a function of emission angle. Peak position and width of the feature appear almost identical for both fluences. In stark contrast to this, starting with a fluence of  $13.6 \mu\text{J}/\text{cm}^2$ , the PE intensity gains spectral weight at lower energies. The lower edge exhibits an apparent parabolic dispersion. Gradually, width and apparent dispersion increase with fluence. At the high energy side, notably, the PE intensity is always cut-off at  $E_F$ , the equilibrium Fermi level, indicative for the formation of a metallic band with an occupation governed by the Fermi-Dirac distribution. Note that the photoelectron intensity at positive delays with respect to negative delays is smaller or equal to the photostationary state intensity at negative delays until about  $F=13.6 \mu\text{J}/\text{cm}^2$ . It becomes comparably large at high fluences. Therefore, to show the pump-induced change in the low fluence regime the photostationary background measured at -100 ps was subtracted in the measurement series Figure 6.5 a)-e). The photostationary state itself can vary as a function of  $\Delta t$  as discussed in chapter 4, but I assumed that the change is small and that the photostationary signal measured at a negative delay of -100 ps represents a good reference for all  $\Delta t$ . The resulting series of background-subtracted PE spectra suggests that a metallic phase, characterized by a free electron-like band, is formed at a threshold fluence of  $F_C=13.6 \mu\text{J}/\text{cm}^2$ .

To confirm the above finding I also analyzed the thermalization and cooling of the electron system for different fluences. As described in the previous paragraph 6.1.2, this is a further marker for the metallic phase besides the angular distribution of the PE intensity. Figure 6.5 f)-k) presents the angle-integrated PE-intensity for different  $\Delta t$  between 50 fs and 800 fs normalized to maximum intensity on a logarithmic scale. Clearly, for low fluences ( $3.5 \mu\text{J}/\text{cm}^2$ ,  $5.2 \mu\text{J}/\text{cm}^2$ ), the spectra lie on top of each other. In contrast to this, starting with a fluence of  $13.6 \mu\text{J}/\text{cm}^2$ , the spectra show the characteristic change of the high energy tail around  $E_F$  that can be well described with a delay-dependent Fermi-Dirac distribution as described in the previous paragraph 6.1.2. Thus, this measurement shows that the metallic phase forms at  $F_C=13.6 \mu\text{J}/\text{cm}^2$ , in exact agreement with the evolution of the angular distribution of the PE intensity. Note that, for this series of measurements, I did not subtract any background. This is physically more meaningful

since the whole system of photoexcited electrons (photostationary electrons as well as pump-induced short-lived electrons) should be considered to test if they form a collective metallic phase. Subtracting the photostationary background gives actually the same result (not shown). In the angular distribution of the PE intensity, as already mentioned, the background needed to be subtracted to unveil the qualitative change of the spectra. I will discuss the background subtraction in more detail in subsection 6.2.2.

In conclusion, the characteristics of the metallic phase, i.e. a free-electron like band and the electron thermalization only occur above a threshold fluence  $F_C$ . At low fluences, the photoinduced signal is independent of emission angle and the electron thermalization is absent. The latter indicates that an interaction between the photoexcited electron does not take place - a collective phase is not formed. It is noteworthy that the threshold fluence  $F_C$  can be translated into a threshold bulk excitation density using optical absorption constants from literature [Gor10], which yields  $F_{exc.,C} = 2.7 \cdot 10^{18} \text{ cm}^{-3}$ . This threshold excitation density agrees well with literature values for the exciton Mott density in ZnO determined using optical spectroscopy [Ver11, Hen07]. I acknowledge that this may be a coincidence due to two reasons: Firstly, because the determination of the exciton Mott density has a large error bar in different experimental setups (cf. ref. [Fog19]) and secondly, because in this particular case the excitation density is strongly dependent on the defect concentration at the surface which is a function of UV exposure, as will be shown in subsection 6.2.6.

Nevertheless, I tentatively assign the low fluence phase to an excitonic phase. The flat angular distribution at low fluences is in agreement with the photostationary defect excitons analyzed in the previous chapter 5 (cf. subsection 5.4), although peak position, width and angular spread are clearly different for both states. This is not surprising considering that the photostationary defect excitons might have undergone energetic stabilization due to formation of the exciton ground state or interaction with the lattice. In addition, there might be a contribution of free excitons, or defect-bound excitons, cf. the work of Deinert et al., who found a similar pump-induced increase of PE intensity below  $E_F$  using low pump fluences and attributed it to excitons bound to H adsorption sites at the ZnO surface (section 2.3.2). Note that, above the critical fluence, the photoemission signal cannot be due to excitons anymore, alone from the fact that their binding energy should decrease, while the majority of surface electrons become more strongly bound with respect to  $E_F$  (see the evolution of the surface metal as a function of fluence, Figure 6.5)<sup>31</sup>.

Subsections 6.1.1 to 6.1.3 showed that ZnO(10-10) undergoes a SMT upon sufficiently strong photoexcitation resonant to the band gap. While, in the low fluence regime, the

---

<sup>31</sup>This arguments includes the Mahan excitons proposed by refs. [Sch11, Ric20, Pal20] and cf. section 2.3.4. A number of electrons around the Fermi energy might still be bound in such excitonic states, but not the gros of electrons detected well below  $E_F$ .

photoresponse is attributed to excitons, above the threshold fluence of  $F_C=13.6 \mu\text{J}/\text{cm}^2$  a transient metal forms. The metal phase is characterized by a dispersive free electron-like band cut by  $E_F$  and shows hot electron gas cooling alike to photoexcited metals.  $F_C$  is extraordinarily low compared to laser fluences in the  $\text{mJ}/\text{cm}^2$  regime that are needed to induce a SMT in other inorganic materials [Wal18, Sch08, De 13].

#### 6.1.4 Rise and decay of the metal phase

For ultrafast switching applications of the photoinduced SMT presented in the last subsection, it is essential to know the time constants of the rise and decay of the metal phase.

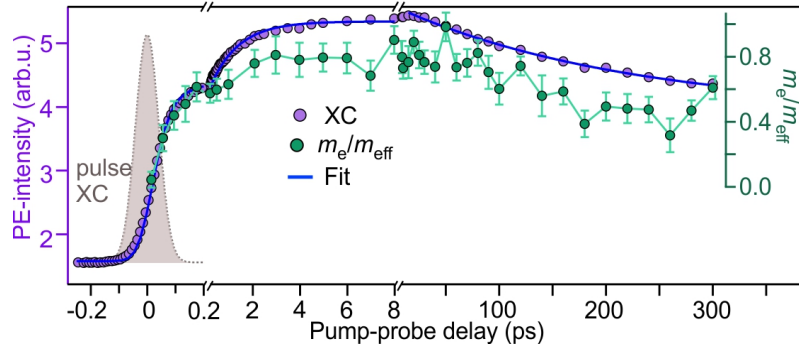


**Figure 6.6:** Dynamics of the ultrafast surface metallization of ZnO(10-10). a) Purple: PE intensity below  $E_F$  (proportional to the surface electron density in the metallic band), obtained by integrating the PE intensity shown in Fig. 6.1 from -0.63 to 0.12 eV. Green: Curvature of the metallic band (determination see Fig. 6.3; method: Fermi-Dirac Gauss Fit). Error bars represent standard deviations. The blue line is a fit with a double exponential rise and a single exponential decay (see subsection 6.1.5). The grey area indicates the instrument response function (pump-probe cross correlation).

Simple integration of the PE signal yields information of the occupied density of states around the equilibrium Fermi level and can be evaluated as a function of pump-probe delay easily, but does not tell if the states are localized or delocalized, i.e. whether they constitute a metallic band or not. The latter requires an analysis of the angle-resolved spectra at each pump-probe delay. A flat angular distribution is characteristic for localized states, while a dispersive band with a finite effective mass is characteristic for the metallic phase (cf. subsection 6.1.3). The effective mass of the metallic band is expected to depend strongly on the renormalization of the band structure due to, for example electron-electron or electron-phonon interaction and/or spatial confinement of the electrons, see ref. [Bas11]. At the verge of electron localization e.g. upon polaron formation [Kin19] or upon a Mott transition (see section 2.3) the effective mass is expected to increase (diverge) continuously. The curvature of the dispersive band is therefore as a measure of the 'degree' of electron localization.

Figure 6.6 displays the PE-intensity integrated around -0.63 to 0.12 eV with respect

to  $E_F$  as a function of pump-probe delay (purple markers) upon resonant photoexcitation above the threshold fluence  $F_C$  ( $F = 26.7 \mu\text{J}/\text{cm}^2$ ). The energy-resolved data for this trace is presented in section 6.1, Figure 6.1. The integrated intensity trace shows a rise with two components, one within the pump-probe pulse cross correlation (grey area, FWHM 115 fs) and one that occurs on a significantly slower timescale of few ps. Subsequently, the signal decays partially on timescale of hundred's of ps. The solid blue line in Figure 6.6 represents a fit with a two-exponential rise and a single exponential decay. A detailed description of the fit function and an analysis of the time constants for this and other pump excitation fluences is presented in the next subsection 6.1.5.

In the same graph, I also show the inverse effective mass  $1/m_{\text{eff}}$  determined by Fermi-Dirac Gauss Fits of the angle-resolved spectra as a function of pump-probe delay (green markers, cf. Figure 6.3 for the analysis). A finite  $1/m_{\text{eff}}$  is observed starting at  $\Delta t = 0$ , but not before. Negative delays correspond to the photostationary state, which exhibits a flat angular distribution (cf. section 5.4). Overall,  $1/m_{\text{eff}}$  exhibits the same two-step rise as the integrated PE intensity. The effective mass reaches  $1.2 m_e$  at a pump-probe delay of 8 ps. Subsequently, it decays within hundred's of ps as the electron density reduces. After 300 ps, the effective mass has reached about  $2 m_e$  when the carrier density has decayed by 30 %. Thus, the delocalized metallic band is formed within the cross correlation (115 fs). As the electron density is reduced, the electrons localize. The observed dynamics suggest that the insulating/semiconducting state is recovered on a timescale of few hundred's of ps.

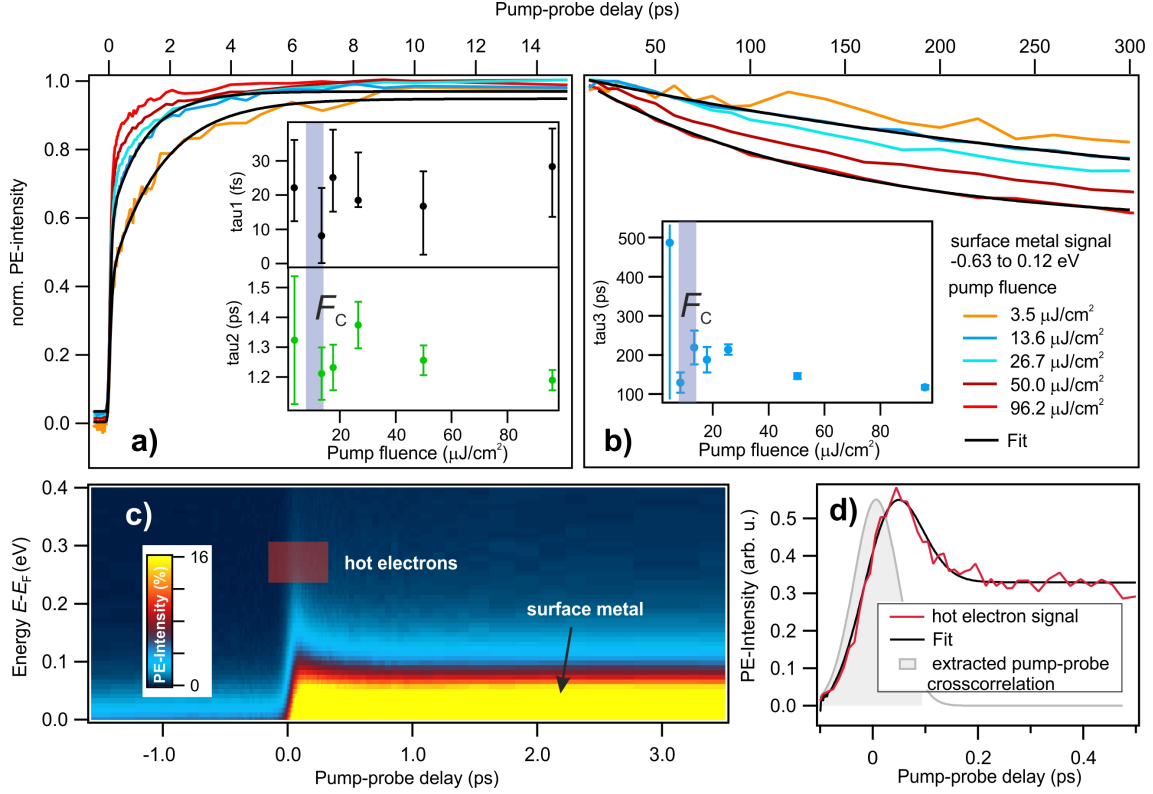


**Figure 6.7:** Evaluation of the photoinduced ultrafast dynamics as a function of pump fluence. a) Integrated PE intensity (-0.63 to 0.12 eV with respect to  $E_F$ ) for different excitation fluences (pump  $h\nu=3.4$  eV), normalized to their maximum intensity at 15 ps. Black solid lines: Exemplary fits with a double-exponential rise (equation 6.100). Inset: Rise time constants  $\tau_1$ ,  $\tau_2$  as a function of pump fluence. b) Extended pump-probe delay window showing the decay of the signal up to 300 ps. Black solid lines: Exemplary single exponential decay fits. Inset: Decay time constant  $\tau_3$  as a function of fluence. c) and d): Extraction of the pump-probe cross correlation from short-lived hot electrons above  $E_F$ . c) Zoom-in of the PE intensity above  $E_F$  as a function of pump-probe delay. The signal of the surface metal below  $E_F$  is also indicated. d) Hot electron intensity transient to determine the pump-probe cross correlation. The trace is obtained by energy integration of the PE signal as indicated with the red box in c). The black solid line is a fit with equation 6.101.

### 6.1.5 Determination of the time constants

In this subsection the PE intensity integrated around  $E_F$  is analyzed to extract the time constants of the surface metal generation and its decay. Fluences below and above  $F_C$  are compared to see if the dynamics are specific for the metal phase.

The intensity transients for different fluences are plotted in Figure 6.7 a) as a function of pump-probe delays up to 15 ps. The background at negative delays was subtracted for each spectrum and they are normalized to maximum intensity for comparison. All transients show the same two-step rise. For increasing fluence the ratio between the first and second rise becomes less pronounced. The black lines are exemplary fits with

$$(A_1 (1 - e^{-(\Delta t' - \Delta t_0)/\tau_1}) + A_2 (1 - e^{-(\Delta t' - \Delta t_0)/\tau_2})) \otimes e^{-(\Delta t')^2/ccw^2}, \quad (6.100)$$

i.e. a double exponential rise convolved with a Gaussian representing the pump-probe cross correlation.

An exact knowledge of the rise time constants requires an independent information on the pump-probe cross correlation, i.e. the cross correlation width  $ccw$  and time zero  $\Delta t_0$  in equation 6.100. These parameters are determined from a short-lived PE signal above  $E_F$ , shown in 6.7 c) and d): Figure 6.7 c) reproduces the PE intensity from Figure 6.1 on a strongly enhanced false color contrast and only for energies above  $E_F$ . Close to  $E_F$  the signal of the metallic phase prevails but a tiny signal can be discerned up to several hundred meV above  $E_F$  around  $\Delta t=0$ . This signal is attributed to non-thermalized hot electrons, as observed upon cross band gap excitation of ZnO(10-10) (see ref. [Dei14] and cf. Figure 4.7 in chapter 4.2.2). Possibly, these electrons arise from the ZnO bulk whereas the metal phase is a surface feature. Figure 6.7 d) displays the PE intensity integrated over the box indicated in Figure 6.7 c) together with a fit with the function

$$\left. \begin{array}{l} A (e^{-(\Delta t' - \Delta t_0)/\tau}) + \text{const.}, \text{ if } \Delta t' > \Delta t_0 \\ 0, \text{ else} \end{array} \right\} \otimes e^{-(\Delta t')^2/ccw^2}. \quad (6.101)$$

In the fit  $ccw$  as well as  $\Delta t_0$  enter as free parameters. In order to be sure about the values and to get realistic error bars, I manually moved  $\Delta t_0$  until no good fit to the data was obtained any more, resulting in an error bar of  $\pm 20 fs$  for  $\Delta t_0$  as well as for the  $ccw$ .

The so extracted pump-probe cross correlation can now be used for fitting the surface metal signal, i.e. PE intensity around  $E_F$  in Figure 6.7 a) with equation 6.100. The resulting values of  $\tau_1$  and  $\tau_2$  are plotted in the inset of Figure 6.7 a). The error bars result from fixing and holding the pump-probe cross correlation at the different  $\Delta t_0$  and  $ccw$  values that still match the hot electron signal. Overall, there is no apparent difference in  $\tau_1$  and  $\tau_2$  for the fluences below and above  $F_C$  although the data points scatter. Using this

analysis procedure I conclude that the signal below  $E_F$  forms within  $\tau_1=20(20)$  fs, where 20 fs is the average over the different fluences and the error bar of 20 fs is conservative. The second time constant is  $\tau_2=1.3(2)$  ps, again with a conservative error bar.

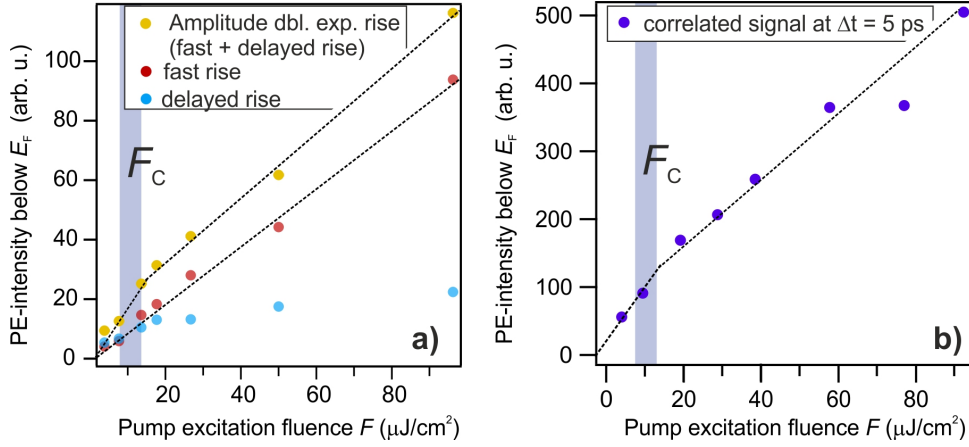


**Figure 6.8:** a) Fit amplitude of the two-step rise of the signal around  $E_F$  (cf. Figure 6.7 a). b) The general trend of the overall intensity below  $E_F$  is corroborated by measuring the difference between the PE signal around  $E_F$  probed by 6.3 eV with the pump on and off, respectively (correlated signal), and varying the pump fluence in short time intervals to avoid an influence of the change of the sample with lab time. Dashed lines are guides to the eye.

Figure 6.8 a) shows the amplitudes of the two-step ('fast' and 'delayed') rise extracted from the fits. The amplitude of the first rise follows a simple linear trend as a function of pump-probe fluence, indicating no change with  $F_C$ , as observed for  $\tau_1$  and  $\tau_2$ . The amplitude of the second rise, however, exhibits an apparent slope change at about  $F_C$ . As a result, at higher fluences the second rise becomes less pronounced, as also obvious from inspecting the normalized intensity transients in Figure 6.7 a). The sum of both amplitudes, equal to the total PE signal after few ps, shows a kink at  $F_C$  due to the slope change of the second rise. As a corroboration of the trend of the PE signal below  $E_F$  I also recorded the pump-induced signal as a function of fluence, where the fluence was varied in short time intervals to avoid a possible influence of the versus lab time change of the sample<sup>32</sup>. This measurement is shown in Figure 6.7 b) and exhibits exactly the same trend. Thus, while the process associated with  $\tau_1$  is independent of  $F$ , the process associated with  $\tau_2$  is sensitive to the character of the electron population, i.e. if it forms a metal or not.

Turning to the decay, the PE signal accessed within the delay window of 300 ps is shown in Figure 6.7 b) as a function of fluence. The decay becomes more pronounced with

<sup>32</sup>For the evaluation of the time constants, the different data points were taken at substantially different lab times and partially on different days, because pump-probe scans take at least 30-60 minutes

increasing fluence. The solid black lines are exemplary fits with a single exponential decay

$$A e^{-(\Delta t - \Delta t_0)/\tau_3} + y_0. \quad (6.102)$$

The fit results for  $\tau_3$  are shown in the inset of Figure 6.7 b). At low fluences below  $F_C$  the error bar is large, because the amplitude of the decay is low. The amplitude  $A$  increases approximately linearly with fluence (not shown).  $F = 26.7 \mu\text{J}/\text{cm}^2$  corresponds to the measurement described in the previous paragraph (Figure 6.6); for this fluence  $\tau_3 = 214(13)$  ps, which can be assigned directly to the electron localization by the simultaneous increase of  $m_{\text{eff}}$  (decrease of  $1/m_{\text{eff}}$ ). The decay becomes faster and reaches  $\tau_3 = 117(5)$  ps for the highest fluence. It should be noted that the ultrafast population decay occurs within approximately the same time constant as the variation of the photostationary background with  $\Delta t$  (cf. chapter 4.2.2). At elevated fluences, I exclude an influence of the latter to the observed decay alone by the fact that the photostationary background is small compared to the pump-induced signal, but it likely plays a role at small fluences.

In connection with the dynamic electron delocalization and subsequent localization described in the last paragraph, I conclude that the metal phase rises within  $\tau_1=20(20)$  fs, i.e. at the timescale of electronic screening [Hub01, Cui14] and decays within  $\tau_3 = 214(13)$  ps (at  $F = 26.7 \mu\text{J}/\text{cm}^2$ ). The fast rise timescale suggests that the SMT arise due to pure electronic processes, without involving movement of the lattice at this stage. In addition there is a second rise  $\tau_2=1.3(2)$  ps, which could well involve carrier-lattice interactions. From the above analysis it follows that the process associated to  $\tau_1$  does not vary below and above  $F_C$ . This indicates that, independent of fluence, the PE signal is of the same physical origin and that its just the character of the photoinduced electrons (localized or delocalized) that changes with  $F_C$ . A discussion of the rise and decay time constants will be given in subsection 6.2.8 after a presentation of all related experimental data.

In summary of subsections 6.1.4 and 6.1.5 I showed that the metal phase rises within a time scale of 20(20) fs and decays within 214(13) ps (at  $F = 26.7 \mu\text{J}/\text{cm}^2$ ). The degree of electron delocalization and the electron density in the metallic band are intimately connected; the correlation between them will be analyzed in detail in subsection 6.2.2.

### 6.1.6 Temperature dependence

For device applications of the photoinduced SMT in ZnO it would be advantageous if the effect was operative at room temperature or at least close to it. While all experimental data shown so far was recorded at 100 K, this subsection examines the temperature dependence of the discovered PIPT.

Figure 6.9 a)-c) and d)-f) show, respectively, the angle-resolved PE intensity averaged between  $\Delta t=3$  ps to  $\Delta t=10$  ps and the angle-integrated PE intensity within the

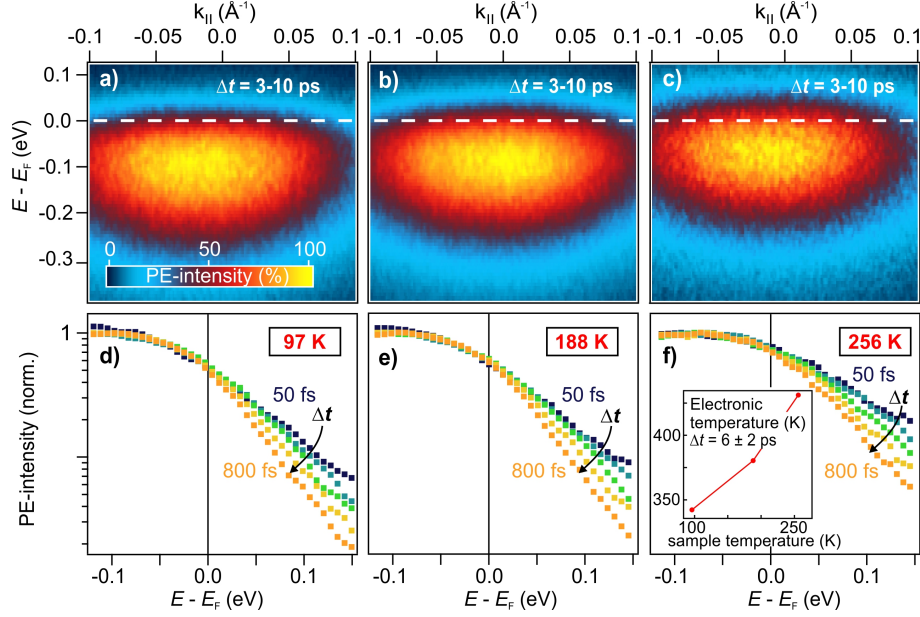


**Figure 6.9:** Temperature dependence of the photoresponse. a)-c), Angle-resolved PE spectra at 97, 188 and 256 K, respectively, averaged across pump-probe delays between 3 and 10 ps. All show a free electron-like band. d)-f), Corresponding angle-integrated spectra showing the cooling of a hot system of thermalized electrons. The inset of f) shows that, after equilibration with the lattice at a late delay of  $6 \pm 2$  ps, the electron (lattice) temperature also increases with the sample temperature.

first ps after pump excitation for sample temperatures of 97 K, 188 K and 256 K. The pump excitation fluence is  $39 \mu\text{J}/\text{cm}^2$ , which is well above  $F_C$ . At all temperatures, the two characteristics of a delocalized metallic electron system are observed, namely a free electron-like band with a positive curvature cut by  $E_F$  and the cooling of a hot system of thermalized electrons. The electronic temperature extracted at a delay of 6 ps (see subsection 6.1 for the evaluation), i.e. well after the equilibration of the electron system with the lattice, is shown in the inset of Figure 6.9 f). It increases with the sample temperature, as expected.

This measurement series shows that the photoinduced SMT is feasible at least up to 256 K, i.e. close to room temperature.

### 6.1.7 A transient 2DEG? Comparison of resonant photoexcitation to surface doping with hydrogen

As shown in chapter 5, photoexcitation leads to the formation of metastable defect excitons at the ZnO surface that show similar changes to the electronic structure as upon H adsorption. I motivated in the introduction to this chapter that the SMT at the ZnO surface can be explained by enhancing the photodoping of the surface in the ultrafast time

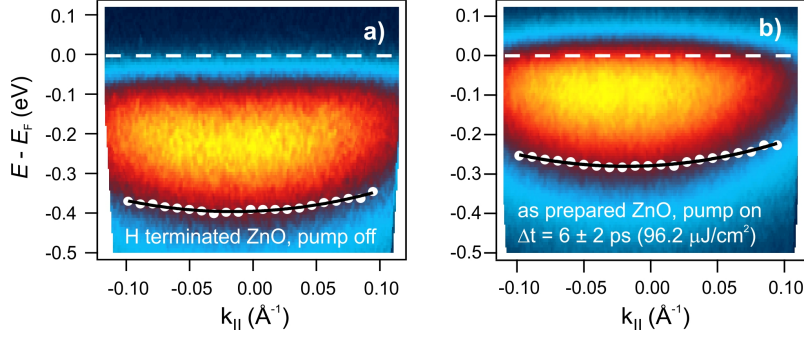


**Figure 6.10:** Comparison of the photoinduced SMT and the H adsorption induced 2DEG at the ZnO surface. a) H terminated ZnO(10-10) (coverage: 150 L). b) Photoexcited as-prepared ZnO(10-10) (pump: 3.4 eV, fluence  $96.2 \mu\text{J}/\text{cm}^2$ , pump-probe delay:  $6 \pm 2$  ps). White markers and black lines: Position of the low energy half maximum and fits with a free electron parabola.

domain. Evidences for the mechanism will be given in the subsequent subsection 6.2. Here I present a direct comparison between the transient metal phase and the 2DEG induced by H adsorption at the ZnO surface. Furthermore, I explore the sensitivity of the transient metal phase to the surface conditions.

**Direct comparison to surface doping with hydrogen** Adsorption of H leads to the formation 2DEG at the ZnO(10-10) surface [Oza10, Dei15, Dei16]: The H atoms act like shallow donors that induce DBB towards the surface, bending the CB below  $E_F$ . At low dosing laterally localized electron pockets isolated each from other are formed [Dei15, Dei16], cf. section 2.2.3. At high dosing the electrons form a metallic surface band [Oza10]. In this subsection the photoinduced SMT is directly compared to H termination in the high dosing regime.

Figure 6.10 a) shows an angle-resolved PE spectrum of ZnO(10-10) terminated with H (dosage: 150 L) and recorded with  $h\nu=6.3$  eV (pump off). Figure 6.10 a) shows that H termination leads to formation of a metallic band with positive dispersion and of several 100 meV width, centered at -0.2 eV below  $E_F$ . I extract the band curvature by determining the position of the low energy half maximum (white markers in Figure 6.10 a), cf. Figure 6.3 for the evaluation). The positions of the half maximum can be described by a free electron parabola (black line, equation 6.98) with an effective mass of  $m_{\text{eff}} = 1.0(1) m_e$ . An evaluation of the positions of the peak maximum gives the same result (not shown).

As a comparison, I show in Figure 6.10 b) an angle-resolved PE spectrum of the transient metallic band induced by resonant photoexcitation with  $96.2 \mu\text{J}/\text{cm}^2$  at the as-prepared ZnO surface. The spectrum is averaged from 4 to 8 ps. Clearly, compared to the H-induced 2DEG, the photoinduced metallic band is shifted by 0.1 eV to higher energies but has a similar width and curvature. Applying the half-maximum method as done above gives  $m_{\text{eff}} = 0.84(4) m_e$ , almost coinciding with the result for the H-induced metallic band.

The comparison suggests that resonant photoexcitation with  $F=96.2 \mu\text{J}/\text{cm}^2$  is equivalent to surface doping with H above the delocalization density and that the photoinduced metallic phase is a transient 2DEG.

It is interesting that, in addition to the curvature and width, the absolute PE intensity of both metallic bands is about identical: In case of the photoinduced metal phase the integrated intensity below  $E_F$  is 270, while for the H-induced feature the integrated intensity below  $E_F$  is 50, but measured with a 9 times lower probe fluence, which yields a ratio of  $9 \cdot (50/270) = 1.7$ . If the PE intensity of the metallic band is proportional to the charge density, the latter must be about the same for both cases. Ozawa et al. estimated the charge density of the 2DEG at a H termination of 200 L to  $n = 1 \times 10^{13} \text{ cm}^{-2}$  based on the size of the Fermi surface measured by ARPES.<sup>33</sup> I therefore conclude that the charge density in the transient 2DEG must be on this order of magnitude. Relating this to the surface atom density of  $11.8 \times 10^{14} \text{ cm}^{-2}$ , the excitation density is on the order of 0.01 per surface atom.

Finally, it can be noted that both metallic bands are rather broad compared other two-dimensional states, e.g. image potential states at metal surfaces [Wei02]. Broadening might occur from a finite  $k_z$  dispersion as a range of final states with different energies is accessed for a given  $k_{\parallel}$  (see section 3.1). A finite  $k_z$  dispersion would be indicative of a bulk component, i.e. no true confinement of the electrons to the surface. Yet, DFT calculations show that the extension into the bulk is less than 2 nm in case of H terminated ZnO. Moreover, broad electronic bands have been observed also in a high-density 2DEG at ZnO(10-10) [Röd18] and at other oxide surfaces, e.g. SrTiO<sub>3</sub> [Mee10], where confinement to the surface was evidenced by the observation of quantized subbands. Recently, the broadening has been attributed to energy-loss structures caused by electron-phonon interaction, which are invisible close to the  $\Gamma$  point due to the limited energy resolution but become apparent at higher  $k_{\parallel}$  [Yuk16]. Such an effect might well be present on the ultrafast time scale considering that the electron-phonon interaction takes place in the first ps (cf. subsection 6.1.2).

### Quenching of the photoinduced metallic phase upon hydrogen termination

The above suggested that the photoinduced metallic phase is alike to a 2DEG at the ZnO surface. As such it should be sensitive to the surface conditions. In this subsection I show that the photoinduced metal phase cannot be generated if the surface is already metallic due to H termination.

Figure 6.11 a) and b) show angle-resolved PE spectra of the as-prepared ZnO surface upon pump photoexcitation above  $F_C$ . The two spectra at large negative (-100 ps) and

<sup>33</sup>Although also in case of Ozawa et al. the 2DEG leads to a broad metallic band similar to the here observed metal phases induced via photoexcitation or H adsorption, a clearer Fermi crossing can be determined in their study.

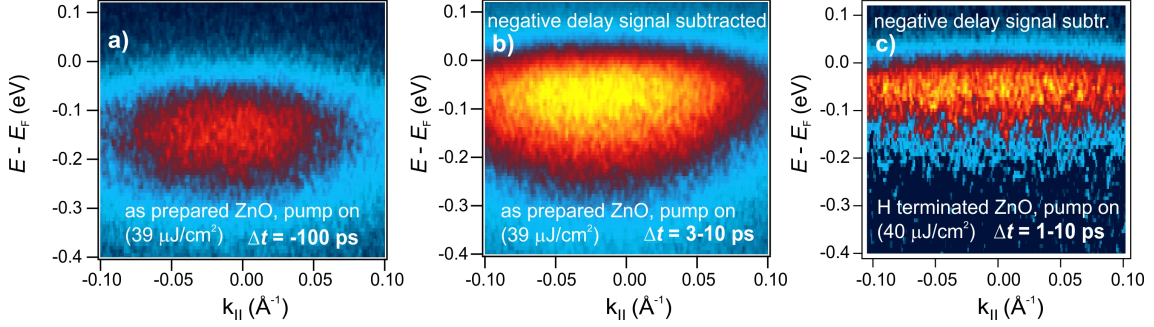


**Figure 6.11:** H termination inhibits the generation of a transient metal phase by photoexcitation. a) The PE signal of the *as-prepared* ZnO surface at a negative pump-probe delay of -100 ps showing the localized photostationary state. b) Pump-induced PE signal averaged from  $\Delta t = 3$  ps to  $\Delta t = 10$  ps showing the photoinduced metallic band. Pump:  $h\nu = 3.4$  eV above  $F_C$  ( $F = 96.2 \mu\text{J}/\text{cm}^2$ ), probe:  $h\nu = 6.3$  eV. The intensity at negative delays displayed in a) was subtracted. c) Pump-induced PE signal averaged from  $\Delta t = 3$  ps to  $\Delta t = 10$  ps under the same pump excitation conditions as in b) but for the *H-terminated* surface (coverage: 150 L). Also here, the signal at negative delays was subtracted, consisting in this case of a metallic band. The photoresponse is clearly different from b).

positive pump-probe delay (averaged from 3-10 ps) show the localized photostationary electron population and the pump-induced metal phase, respectively. The negative delay signal has been subtracted from the spectrum shown in Figure 6.11 b). Clearly, a pump-induced free electron-like band is recognized, characterized by the apparent positive curvature at low energies. Now, the same pump-probe experiment is carried out at the H terminated ZnO surface using a H dosage of 150 L. At this dosage the surface becomes metallic already in the unpumped state, the signal at negative delays is identical to the spectrum without applied pump shown in Figure 6.10 a). Figure 6.11 c) shows the pump-induced PE intensity averaged from 1-10 ps; again, the negative delay signal was subtracted. Clearly, although the same pump fluence above  $F_C$  is used, the photoresponse looks qualitatively different: The signal does not exhibit an apparent positive curvature. Rather, it is flat, somewhat reminiscent of the low fluence response of the *as-prepared* surface (cf. Figure 6.5). Obviously the transient metallic phase cannot be generated. This shows that the transient metal signal is sensitive to the surface termination, consistent with a surface feature. The remaining signal might be a transient filling of the H adsorption-induced 2DEG, as has been observed for the 2DEG at the  $\text{SrTiO}_3$  surface [Weg14a]. Alternatively, the signal could arise from bulk excitons, or from surface excitons in regions of the sample surface, which are not metallized (e.g. because the coverage by H is inhomogeneous).

In summary of this subsection, I showed that the transient metal phase induced by photoexcitation above  $F_C$  at the *as-prepared* ZnO surface and the metal phase induced by Hydrogen termination at the same ZnO surface exhibit very similar spectral signatures

in ARPES. This suggests that resonant photoexcitation acts similar to H surface doping, not only with regard to the metastable time domain explored in chapter 5, but also in the ultrafast time domain. Furthermore I showed that, if the surface is terminated with H, no photoinduced transient metal phase can be generated. This suggests that the transient metal phase is confined to the ZnO surface forming a state similar to a 2DEG induced by chemical doping.

### 6.1.8 Summary

In this section I demonstrated an ultrafast SMT in ZnO using low fluence photoexcitation resonant to the band gap, with sub-ns recovery and feasible up to at least 256 K. The metal phase is identified by a free-electron like band that is partially filled and cut by the equilibrium  $E_F$ . Moreover, hot electron gas cooling alike to photoexcited metals takes place. The metal phase is sensitive to the surface conditions and its spectroscopic signature is similar to the 2DEG induced by H termination, hence forming a surface metal.

## 6.2 The mechanism

The mechanisms leading to PIPTs are usually complicated. Most often, the mechanism cannot be resolved within a single experiment, but requires complementary datasets (e.g. accessing lattice and electron dynamics) and theory input, such as in the case of the photoinduced SMT in  $\text{VO}_2$  [Wal18, Weg15]. In this section I unveil the mechanism leading to the photoinduced SMT at the ZnO surface *en detail* within a single set of experiments exploiting the capabilities of trARPES.

The photoinduced SMT reported above occurs at a threshold photoexcitation fluence  $F_C$  consistent with the excitation density of the Mott transition reported from optical experiments (cf. section 6.1.3) and at a time scale of electronic screening, i.e. within 20(20) fs (cf. section 6.1.5). Especially due to the latter observation, carrier-lattice interactions seem unlikely the cause of the metallization. Instead, most likely, a Mott transition between excitons is observed. The theory of photoexcited semiconductors predicts such a metallic (or metal-like) phase upon the exciton Mott transition. As outlined in the introduction to this thesis, the electron-hole plasma leads to quasi-Fermi levels in the CB and VB, respectively, which do normally not coincide with the equilibrium Fermi level. As the CB is filled upon increasing the photoexcitation fluence, a shift of the Fermi level to higher energies would be expected (Burstein-Moss effect). Complementary, a change of the electronic screening causes band gap renormalization (BGR) leading to a downwards shift of the CB and an upwards shift of the VB, respectively. trARPES is capable of resolving the band positions as well as the position of the quasi Fermi level on an absolute energy scale. As reported in section 6.1, for the here detected metal phase the Fermi level of the

transient metal phase *equals* the equilibrium Fermi level, notably for *all* photoexcitation fluences (cf. Figure 6.5). Within the picture of a transiently occupied CB and the quasi Fermi level that is formed within this band, this observation means that the CB must be shifted below  $E_F$  by virtue of photoexcitation (cf. the energy level sketch in Figure 6.1 a)). The mechanism driving this could be BGR; alternatively, the electronic band structure change could result from photodoping, as outlined in the following paragraph.

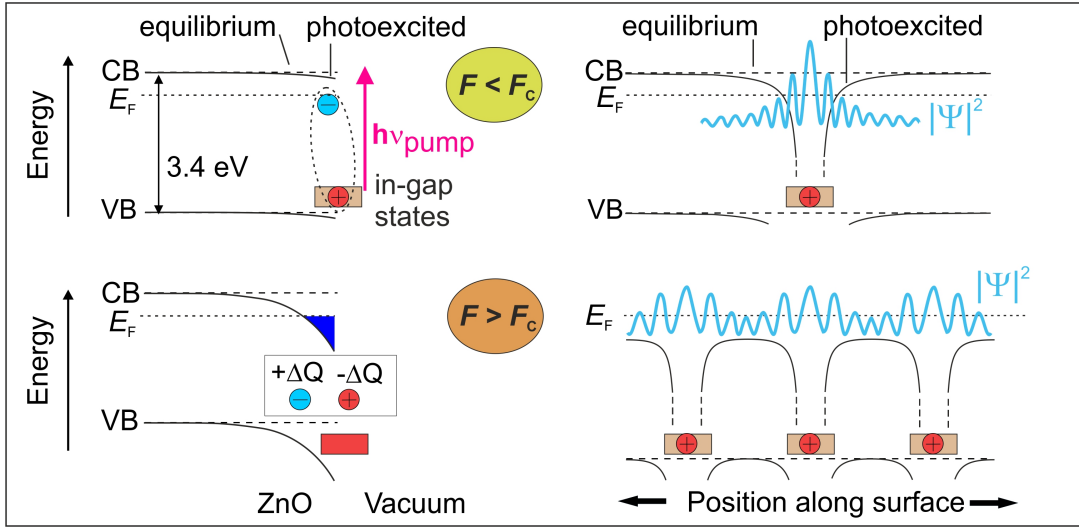


**Figure 6.12:** Sketch of the discussed photodoping mechanism due to the defect exciton formation. The left side presents a surface-averaged view of the band structure, the right side is a lateral view at the surface. For explanation please see text.

### 6.2.1 Concept of the photodoping mechanism

In subsection 6.1.7 a striking similarity between the spectroscopic signatures of the photoinduced metal phase and the 2DEG induced by H surface doping was unveiled. In addition it was noted that the transient metallization must be a surface phenomenon due to the sensitivity to the surface conditions. This is reminiscent of the photostationary state at the ZnO that was unveiled in chapter 5 and which is similar to H surface doping in the low dosing range. Here I outline the proposed photodoping mechanism leading to the SMT due to an elevated photodoping density on ultrafast time scales and derive expectations that will be crosschecked with trARPES in the subsequent sections.

Figure 6.12 presents a sketch of the photodoping mechanism. Prior to photoexcitation, i.e. in the equilibrium, CB and VB are flat with no band bending towards the surface (left side of Figure 6.12) and no lateral corrugation of the bands (right side of Figure 6.12); the CB is above  $E_F$  everywhere. Photoexcitation (with  $h\nu_{\text{pump}}$ ) creates defect excitons at the ZnO surface. Every photohole superimposes a hydrogenic potential to the crystal potential

at the position of the defect and the electron is bound to it; this is conceptually similar to introducing shallow donor dopants in the system (cf. chapter 2.3.3). Because the doping takes place at the surface, DBB occurs, caused by the creation of positive charges localized at the surface. At low fluence  $< F_C$  the electron density is below the Mott limit and the electrons are localized at the defect sites. Above a critical electron density the electrons delocalize and a transient 2DEG is formed. It should be mentioned that photoinduced change of surface band bending is well known in literature [Kro01]. Both, decrease and increase of band bending at semiconductor surfaces have been observed in the ultrafast time domain [Yan14, Ret12]. The decrease of preexisting (equilibrium) band bending is the well-known surface photovoltage effect. The increase of band bending via photoexcitation, which occurs in the photodoping scenario described here, is termed 'photovoltage inversion' [Kro01].

The following expectations from the surface doping analogy can be formulated:

- $m_{\text{eff}}$  is expected to diverge with a power law when lowering the doping density towards the localization threshold at the Mott transition [Cas03, Tok93]. At high enough photodoping levels  $m_{\text{eff}}$  should converge to the CB  $m_{\text{eff}}$ .
- DBB of CB and VB should occur towards the surface upon photoexcitation, as observed upon chemical doping [McK14, Mee10, Dei15]. DBB of the VB is the contrary of what would be expected from BGR, where the VB should shift upward [Liu19, Mor17]
- Besides DBB, surface doping with shallow donors is expected to reduce the work function as observed for H adsorption at ZnO [Dei15].
- Because photodoping results from the photoexcitation of deep donor defects, it should be possible to induce it with below band gap excitation, i.e. by creating photoholes only in defect-induced in-gap states and not in the VB.
- The photoinduced electron and hole density at the surface should depend to the defect density at the surface.

In the following I will crosscheck all these expectations using additional data analysis and data taken with trARPES.

### 6.2.2 Critical behaviour of the effective mass

Upon approaching the Mott (or Mott-Anderson) SMT from the metallic side (by varying the doping density, electron density, the external magnetic field, pressure ...), the electrons localize at the impurity sites. The Mott-Hubbard model predicts that various system properties, including the effective mass, show critical behaviour towards the transition

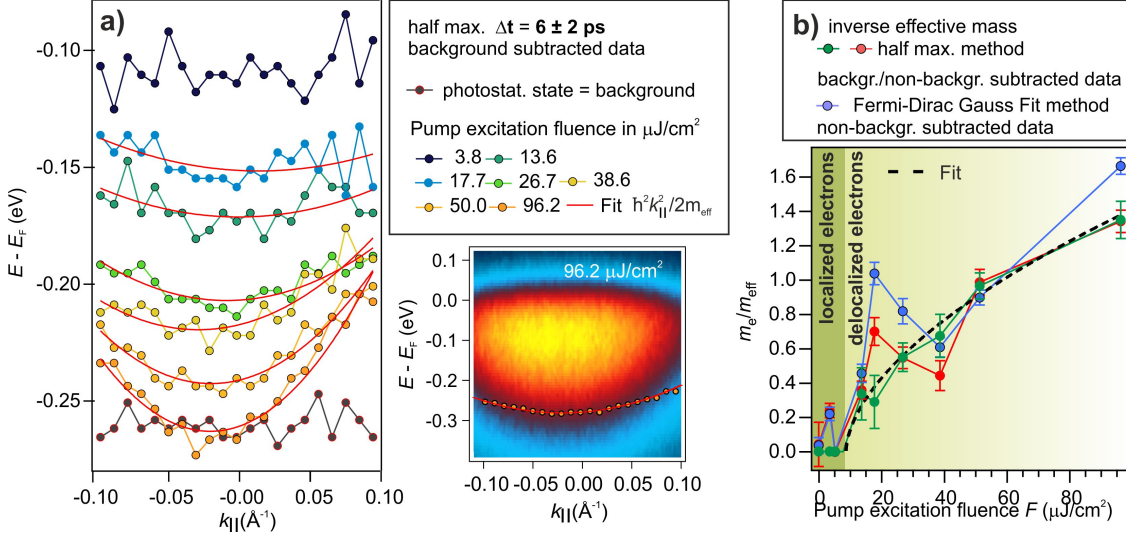


**Figure 6.13:** Evaluation of the effective mass of the transient metallic band. a) Position of the low energy half maximum of the pump-induced electron signal at  $\Delta t = 6 \pm 2$  ps versus parallel momentum  $k_{||}$  for different pump fluences. An exemplary angle-resolved photoelectron spectrum where the half maximum is indicated is seen at the right hand side; the photostationary background was subtracted (cf. Figure 6.5 a)-e) for the full fluence series). The red lines are fits with a free-electron parabola (equation 6.98). b) Inverse effective masses  $m_e/m_{\text{eff}}$  at  $\Delta t = 6 \pm 2$  ps extracted from the parabola fits using different evaluations. Green and red markers: Using the half maximum method, where the position of the low energy half maximum is extracted from angle-resolved spectra with and without subtracting the photostationary background, respectively. Blue markers: Using the Fermi-Dirac Gauss Fit method, cf. subsection 6.1, Figure 6.3. Dashed line: Fit with the inverse of the critical form, equation 6.104.

point, cf. section 2.2.2. In experimental studies of the SMT in 2D and 3D systems the effective mass close to the transition point is found to follow the critical form

$$m_{\text{eff}} \propto (x - x_C)^{-\alpha} \quad (6.103)$$

where  $x$  is the electron [Vit02, Kra04] or doping density [Cas03, Tok93] and  $\alpha$  is the critical exponent.

Figure 6.13 a) shows an evaluation of  $m_{\text{eff}}$  from trARPES measurements of photoexcited ZnO at a fixed pump-probe delay ( $\Delta t$  averaged from 4 to 8 ps) and for different fluences. The data points represent the energetic position of the low energy half maximum of the PE intensity, determined at different  $k_{||}$  from angle-resolved PE data. The trARPES data used for this evaluation was already presented and discussed with regard to the pump fluence threshold of  $F_C = 13.6 \mu\text{J}/\text{cm}^2$  for the photoinduced SMT in subsection 6.1; for the convenience of the reader, I reproduce at the right side of Figure 6.13 a) an angle-resolved spectrum for  $F = 96.2 \mu\text{J}/\text{cm}^2$  and indicate the position of the half maximum. An extended fluence series is displayed in Figure 6.5 a)-e). Note that, for the evaluation, the photosta-

tionary background determined at large negative delays was subtracted from the raw data; the influence of the background subtraction and upon using different evaluation methods is discussed further below. Figure 6.13 a) shows that at low fluence ( $3.8 \mu\text{J}/\text{cm}^2$ ) below  $F_C$ , the half maximum lies at the same energy and is independent of  $k_{\parallel}$ <sup>34</sup>. Above  $F_C$  the position of the half maximum has a parabolic trend. The position shifts to higher energies with increasing fluence and the curvature of the parabola becomes more pronounced. The red lines in Figure 6.13 a) are fits with a free-electron parabola (equation 6.98). These fits are used to extract the curvature  $1/m_{\text{eff}}$  for  $F > F_C$ . The resulting values of  $1/m_{\text{eff}}$  are plotted as green markers as a function of fluence in Figure 6.13 b). For  $F < F_C$  the parabola fit does not converge because the curvature is flat;  $1/m_{\text{eff}}$  is set to 0 here. The curvature shows a distinct monotonous rise that flattens at elevated fluence. The dashed line in Figure 6.13 b) is a fit with the inverse of

$$m_{\text{eff}} = A (F - F_C)^{-\alpha} + m_0, \quad (6.104)$$

where  $A$  is a proportionality constant and  $m_0$  an offset. The offset is introduced because the effective mass should converge to a finite value for high fluence (hence photodoping), namely the CB effective mass [Liu93]. The fit is in excellent agreement with the data. Fixing  $F_C$  at the SMT threshold  $F_C=13.6 \mu\text{J}/\text{cm}^2$ , results in the critical exponent  $\alpha = 0.6(5)$  and  $m_0 = 0.2(6) m_e$ . This suggests that  $m_{\text{eff}}$  follows the critical form expected from theory and experiments on the doping-induced Mott-Anderson transition. Notably,  $m_0$  coincides with the ZnO CB  $m_{\text{eff}}$  of  $0.25 m_e$  [Yan11].

In Figure 6.13 b) I also show  $1/m_{\text{eff}}$  that results when the photostationary background is not subtracted from the raw data using either the half maximum method or by Fermi-Dirac Gauss fits (cf. 6.3 for details on the evaluation). Above  $F=20 \mu\text{J}/\text{cm}^2$ , all data points nearly coincide, independent of the evaluation method and if the background is subtracted or not. At low fluences, however, significant deviations between the evaluation of the background subtracted and the non-background subtracted data are observed. Evaluation of the non-background subtracted data even results in a small positive curvatures  $1/m_{\text{eff}}$  for  $F=3.8 \mu\text{J}/\text{cm}^2$ , i.e. below  $F_C$ . The latter is not only contradicting the evaluation of the background-subtracted data, but also the finding in subsection 6.1.3 that the ultrafast electron thermalization and cooling after photoexcitation indicative of electron delocalization only occurs above  $F_C$ .

To understand the discrepancies between analyzing the background subtracted and the non-background subtracted data, it should be noted that the pump-induced intensity at positive delays with respect to negative delays is smaller or equal to the photostationary state intensity at negative delays until about  $F_C$  and becomes comparably large at high

<sup>34</sup>This also holds for the  $5.2 \mu\text{J}/\text{cm}^2$  data set, which is omitted in Figure 6.13 a) for clarity.

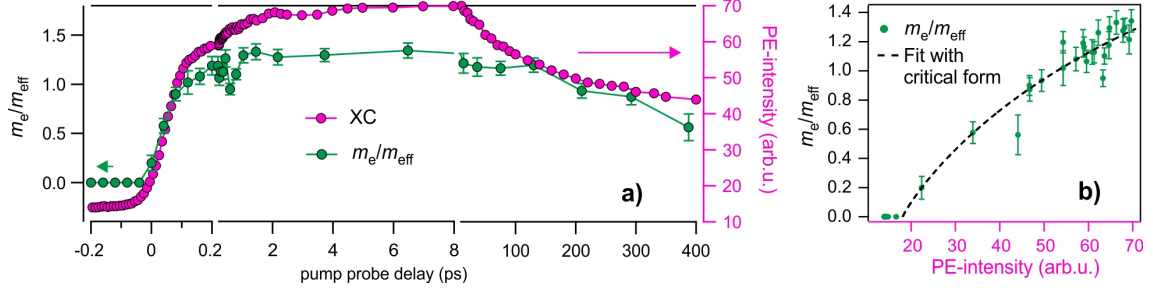


**Figure 6.14:** Determination of the critical exponent from a single pump-probe measurement. a) Integrated PE intensity (-0.63 to 0.12 eV with respect to  $E_F$ ) (photostationary state not subtracted) and effective mass extracted using the half maxima method as a function of pump-probe delay. b) Inverse effective mass plotted versus the integrated PE intensity. Dashed line: Fit with the critical form, equation 6.104.

fluences. It therefore makes sense that at high fluences identical results are observed. The deviation at low fluences, in contrast, is attributed to an artifact in the evaluation: Both, the photostationary background as well as the ultrafast pump-induced signal are flat. Still, the evaluation of the sum both contributions results in a finite  $1/m_{\text{eff}}$ , because the photostationary background lies at a lower energy than the ultrafast pump-induced signal and has a narrower momentum spread (the half maximum positions of an exemplary photostationary background spectrum are given in Figure 6.13 a), a comparison of the angular spread is not shown). The combination of both contributions then may lead to an *apparent* positive curvature, see the discussion of a similar case reported in ref. [Bov03]. Clearly, the photostationary state makes the analysis of ultrafast photoresponse at small positive delays difficult<sup>35</sup>. The trend of  $1/m_{\text{eff}}$  from the background subtracted data is remarkably clear. It is tempting to trust it as it exhibits the expected critical behaviour with respect to  $F_C$ , but a solid conclusion cannot be given from this measurement alone.

To get a grip on the influence of the photostationary contribution, I focused on a lab time where the photostationary state is as small as possible, which is directly after the sample preparation (cf. subsection 5.5). A single pump-probe measurement at high fluence provides a continuous variation of the pump-induced electron density as the latter rises and decays on the ultrafast time scale, with an associated change of the  $1/m_{\text{eff}}$  as discussed previously in subsection 6.1.4. Figure 6.14 a) shows the pump-induced electron density integrated around  $E_F$  together with the effective mass, evaluated by the half maximum

<sup>35</sup>An additional complication comes from changes of the PE intensity with lab time: As show in subsection 5.5, the photostationary state increases with lab time. In subsection 6.2.6 I will show that also the additional pump-induced intensity at positive delays increases with lab time, but at a slower rate. Therefore, the influence of the background on the data analysis depends on the moment (in lab time) when the data was taken. All data points were taken at substantially different lab times and partially on different days, because the angle-resolved spectra are extracted from pump-probe scans that take at least 30-60 minutes. The fluence was not varied monotonously with lab time but in a disordered way, such that the lab time change is likely responsible for the observed scattered values for  $1/m_{\text{eff}}$  at low fluences.

method, versus pump-probe delay for a high pump fluence  $F=96.2 \mu\text{J}/\text{cm}^2$ . In this case, the photostationary state was not subtracted; it only forms a small perturbation of the measurement as can be seen in Figure 6.14 a): The integrated PE intensity at positive delays surpasses the photostationary background at negative delays already few tens of femtoseconds after time zero, and becomes about 6 to 7 times larger at positive delays of few ps. In Figure 6.14 a) it is obvious that both observables, integrated PE intensity and  $1/m_{\text{eff}}$ , show a two-step rise and a decay within hundreds of ps, alike to the measurement presented in subsection 6.1.4. Now, in Figure 6.14 b)  $1/m_{\text{eff}}$  is plotted *versus* the integrated PE intensity. The dashed line is a fit with the critical form, equation 6.104, with replacing  $F$  with  $n$ , where  $n$  is now the electron density in the metallic band. Clearly, the data is well described by the fit. Fixing the critical density  $n_C$  at  $n = 18$  the critical exponent becomes  $\alpha = 0.9 \pm 0.3$  and  $m_0 = 0.3(3)$ . This is in excellent agreement with the evaluation of the background subtracted intensity as function of fluence that was presented above. If I leave  $n_C$  as free parameter and set the offset to  $m_0$  to the ZnO CB effective mass of  $0.25 m_e$  the critical exponent becomes  $\alpha = 0.9 \pm 0.2$ .

I thus conclude that  $1/m_{\text{eff}}$  diverges with a power law towards the localization threshold at  $F_C$ . The extrapolation of  $m_{\text{eff}}$  at elevated electron density yields a value consistent with the ZnO CB  $m_{\text{eff}}$ . This is as expected for the formation of an impurity band in a doping-induced Mott-Anderson SMT, cf. section 2.2.2. The critical behaviour and convergence with the CB  $m_{\text{eff}}$  at elevated doping or electron densities has been observed in 3D systems and 2D systems [Tok93, Cas03, Kra04]. Taking for granted that the band finally reaches the ZnO CB  $m_{\text{eff}}$ , the critical exponent can be determined to  $\alpha = 0.9(2)$ .

### 6.2.3 Valence band dynamics

When chemical doping with shallow donors is carried out in a layer confined to the surface, DBB of CB and VB toward the surface results [McK14, Mee10, Dei15], cf. section 2.2.3. The same would be expected, if photoexcitation would act like doping the surface with shallow donors (cf. subsection 6.2.1). In this subsection, I show by tracking the VB after photoexcitation in the ultrafast time domain that DBB indeed occurs and is directly linked to the formation of the metal phase by photoexcitation. Moreover, DBB can be induced by excitation slightly below the fundamental gap, corroborating that photoexcitation depopulates deep defect states. I also show that BGR is negligible at the threshold fluence of the SMT, but likely becomes an appreciable contribution to the ultrafast band structure changes as the fluence increases.

**Resonant photoexcitation ( $h\nu_{\text{pump}}=3.4 \text{ eV}$ )** The VB is accessed by a 2PPE process using  $h\nu_{\text{pump}}=4.26 \text{ eV}$ ; an energy level sketch and a unpumped VB spectrum have been

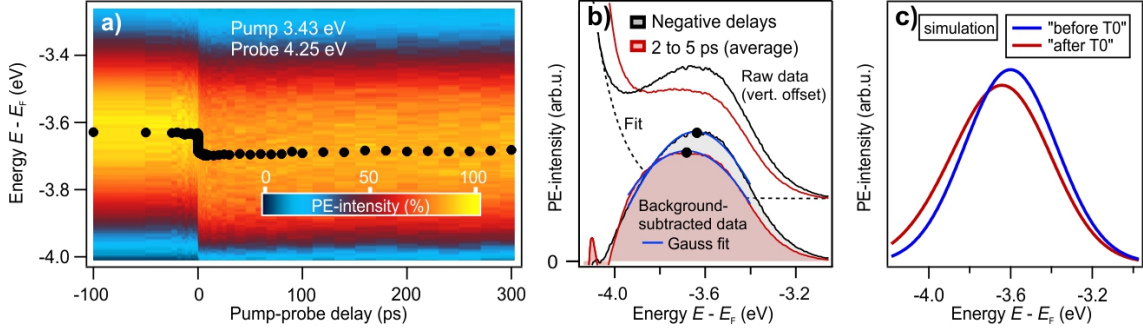


**Figure 6.15:** VB downward shift after resonant photoexcitation ( $h\nu=3.43$  eV). The pump fluence is  $27 \mu\text{J}/\text{cm}^2$ , i.e. above  $F_C$ . a) VB intensity as a function of pump-probe delay and energy. Black markers: peak position from a Gaussian fit to the background subtracted data, see b). b) Exemplary VB spectra, one for large negative delays (black) and one for positive delays of few ps (red). Top: raw data, the subtracted background is indicated with the dashed line for the spectrum at negative delays. Bottom: secondary electron background subtracted data, solid lines are Gaussian fits to track the peak shifting. c) 'Simulation' of the PE-intensity, assuming that not all unit cells experience the same VB downward shift (see text).

presented earlier, cf. section 5.1 Figure 5.1. Figure 6.15 b) compares a VB spectrum at negative delays (black) to one at a positive pump-probe delay of few ps (red) upon resonant photoexcitation above  $F_C$ . Clearly, the VB is transiently shifted to lower energies. Note that VB shift is not entirely rigid but that the peak also appears broadened and has a lower amplitude. This becomes particularly clear after subtracting the secondary electron background at low energies, cf. Figure 6.15 b) bottom.

This observation is consistent with surface DBB, where not all probed unit cells along the surface normal exhibit the same shift, as noted earlier [McK14, Röd18]. The effect is illustrated by the simulated spectra shown in Figure 6.15 c): The total VB intensity is assumed to consist of 100 individual Gaussian functions (representing the signals of different unit cells, the number is arbitrarily chosen). Before arrival of the pump pulse, all Gaussian functions are at the same peak position. Upon arrival of the pump, in case it creates positive charges at the surface by photodoping, the surface unit cell electronic bands experience a stronger shift than sub-surface and bulk unit cells. In the simulation I thus assumed that 50 Gaussians stay at the same peak position, and the other 50 Gaussians experience a downward shift, with a linear distribution from 0 eV to 0.5 eV<sup>36</sup>. The resulting sum of shifted and non-shifted Gaussians shows the experimentally observed peak shape, namely the VB intensity has the shape of a Gaussian function that is shifted to lower energies and exhibits a reduced amplitude and increased width. The above is thus entirely

<sup>36</sup>To demonstrate the principle I assumed that the bands are downward shifted linearly toward the surface. The efficiency to photoemit electrons from different depths is unknown and is not taken into account. In principle surface electrons will contribute more strongly to the signal, because photoemission is surface sensitive (cf. 3.1), but the electron mean free path can be nm to tens of nm depending on the system and electron energy.

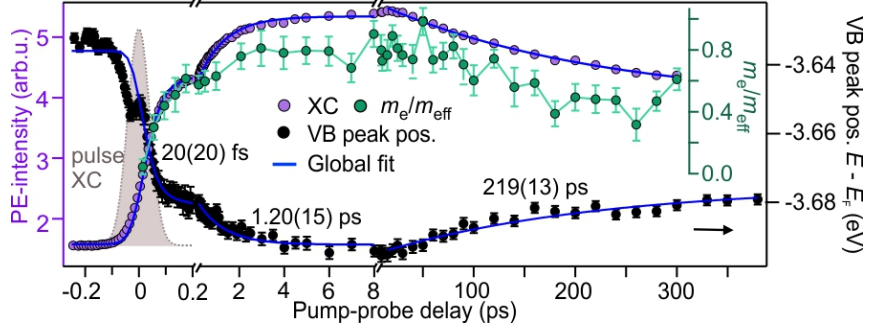


**Figure 6.16:** Comparison of the temporal evolution of the VB downward shift and the surface metallization. Black: VB peak position, determination see Figure 6.15 b). The error bars represent standard deviations. Purple and green: surface electron density in the metallic band and the band curvature  $1/m_{\text{eff}}$ , reproduced from Figure 6.6. The blue line is a global fit with a double exponential rise and a single exponential decay (see text). Grey area: instrument response function (pump-probe cross correlation). The pump is  $h\nu=3.43$  eV, with a fluence of  $27 \mu\text{J}/\text{cm}^2$  for all displayed data.

consistent with photodoping that induces DBB. It clearly shows that BGR, which would shift the VB upward, if it occurs, is overcompensated by this effect.

The false color plot in Figure 6.15 a) shows that the downward shift occurs abruptly and persists for several hundred ps. To explore the relation between DBB and the photoinduced SMT, I show in Figure 6.16 the DBB of the VB as a function of pump probe delay together with the the dynamics of the surface metal phase, i.e. the PE signal of the surface metal phase and the band curvature  $1/m_{\text{eff}}$ . The latter two observables were presented and discussed in section 6.1.4 (cf. Figure 6.6). To extract the VB shift, the secondary electron background-subtracted spectra were fitted with Gaussian functions for each delay (cf. the exemplary spectra and fits in Figure 6.15 b)). The peak position of the Gaussian function is taken as a measure of the band bending, but the evaluation of the amplitude or simply integrating the signal in the depleted region gives the same result (not shown), as expected from the simulation. Note that, because different unit cells exhibit different shifts and their signals are summed by the photoemission measurement, an absolute number of the band bending at the surface cannot be given. The temporal evolution of the VB downward shift shows the same characteristic steps as the surface metal phase: Alike to the rise of the surface metal signal and the band curvature  $1/m_{\text{eff}}$ , the downward shift of the VB has two components, one that occurs within the pump-probe cross correlation (shaded area in Figure 6.16), and one that continues on a timescale of few ps. The downward shift relaxes as the surface metal signal decays.

To make the point that the observed dynamics are in fact identical I employ a global fit analysis. For pump-probe delays up to 10 ps, I fit the surface metal signal and the VB downward shift with a double exponential rise convolved with a Gaussian representing

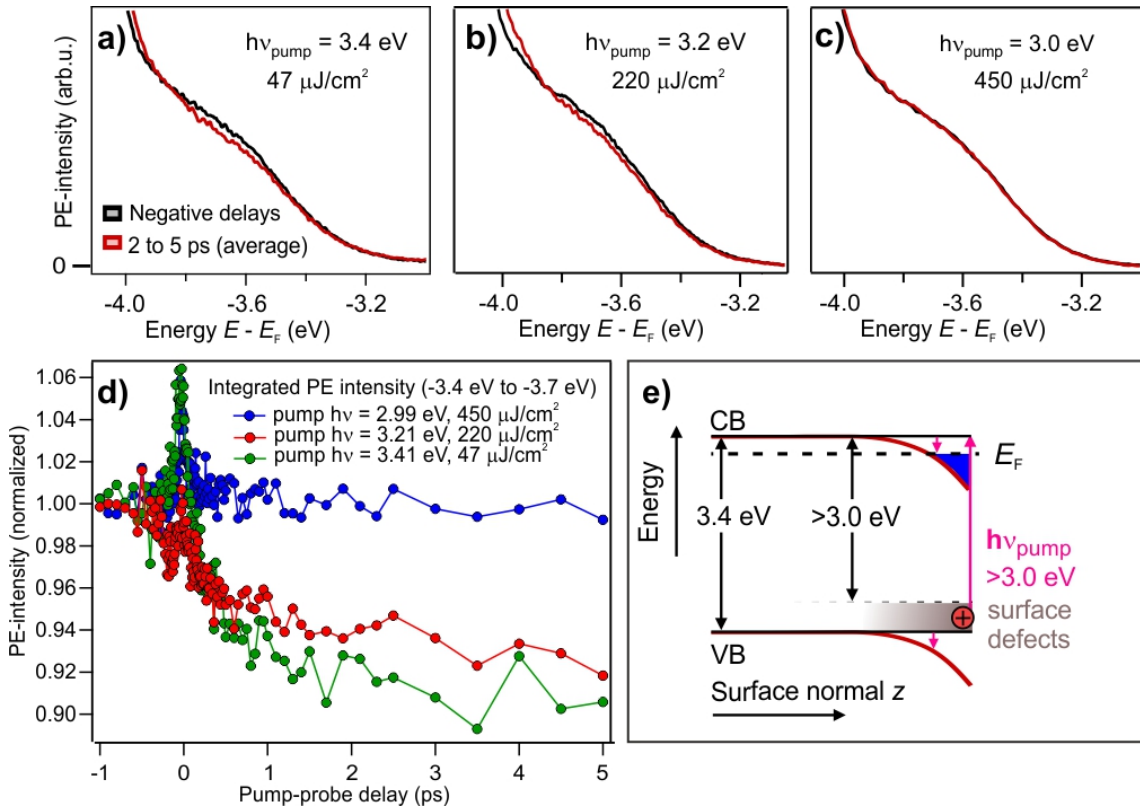


**Figure 6.17:** VB downward shift upon below band gap photoexcitation. a)-c) VB spectrum at positive delays of few ps (red) compared to negative delays (black) for different pump energies: 3.4 eV, 3.2 eV and 3.0 eV. 3.4 eV is resonant to the ZnO band gap, 3.2 eV and 3.0 eV are below, even when considering the width of the laser spectra (FWHM 0.1 eV). d) Temporal evolution of the VB downward shift by integrating the PE-intensity from -3.4 to -3.7 eV with respect to  $E_F$ . e) Energy level diagram. The photon energy dependence shows that defects levels  $< 0.4 \text{ eV}$  above the VB maximum and at the surface must be depopulated, leading to DBB by positive photoholes at the surface.

the pump-probe cross correlation (equation 6.100 in section 6.1.5)<sup>37</sup>. The time constants are optimized globally (i.e. for both data sets simultaneously). As can be seen in Figure 6.16 a), the global fit matches both data sets perfectly. The resulting fit time constants are  $\tau_1 = 20(20) \text{ fs}$  and  $\tau_2 = 1.20(15) \text{ ps}$ , nearly identical to the results obtained by fitting solely the surface metal signal (cf. section 6.1.5). For the decay at late pump-probe delays, I use a single exponential fit (equation 6.101); global variation of the decay time constant gives  $\tau_3 = 219(13) \text{ ps}$ . Also here the global fit matches both data sets nicely, and the resulting decay time constant is nearly identical to the result obtained by fitting solely the surface metal signal. This analysis proves that DBB is *linked* to the photoinduced SMT.

<sup>37</sup>For the VB shift the pump-probe cross correlation was independently determined from the ultrafast PE signal of the metal sample holder, and for the surface metal signal the procedure described in section 6.1.5 was employed.

**Below bandgap excitation ( $h\nu_{\text{pump}} < 3.4 \text{ eV}$ )** The above showed that DBB is directly linked to the photoinduced SMT, as expected from the photodoping mechanism described in subsection 6.2.1. The mechanism is based on the photoexcitation of defect levels in the ZnO band gap. If this was indeed the cause of the photoinduced SMT, then photodoping and thus DBB should be possible with photoexcitation below the fundamental band gap of ZnO of 3.4 eV [Kli10b].

I thus tuned the pump photon energy below 3.4 eV and checked if the VB shifts downward or not. Figure 6.17 a)-c) compares a VB spectrum at negative delays (black) to one at a positive pump-probe delay of few ps (red) upon using three different pump photon energies: 3.4 eV, 3.2 eV, and 3.0 eV. The FWHM of the photon energies is 0.1 eV. Figure 6.17 b) shows that photoexcitation with 3.2 eV clearly shifts down the VB transiently. The effect on the spectra is comparable to the case of resonant photoexcitation, see Figure 6.17 a)<sup>38</sup>. However, it should be noted that the pump fluence is 5 times higher than upon resonant photoexcitation ( $220 \mu\text{J}/\text{cm}^2$  versus  $47 \mu\text{J}/\text{cm}^2$ ). This indicates that the photodoping efficiency reduces rapidly as the pump photon energy is lowered. Indeed, using a photon energy of 3.0 eV, no VB shift can be observed anymore, see Figure 6.17 c), even at fluence as high as  $450 \mu\text{J}/\text{cm}^2$ .

Figure 6.17 d) compares the temporal evolution of the VB downward shift upon using a pump photon energy of 3.4 eV, 3.2 eV, and 3.0 eV in the first 5 ps after incidence of the pump. As a marker of the VB downward shift I simply integrated in the depleted part of the spectrum where a reduction of the PE signal is observed, i.e. in the range from -3.4 eV to -3.7 eV. This should give identical results as evaluating the peak shift with a fit function, see the simulation in the last paragraph. Figure 6.17 d) shows that upon photoexcitation 3.0 eV no change with respect to negative delays is observed, while the temporal evolution upon photoexcitation with 3.4 eV, 3.2 eV is identical. This is consistent with the comparison of spectra at small positive and negative delays (6.17 a)-c)) and shows that the processes related to  $\tau_1$  and  $\tau_2$  are related to the photoexcitation of deep defect levels. The deep defect levels must be situated  $< 0.4 \text{ eV}$  above the VB maximum, cf. the energy level diagram in Figure 6.17 e). The photodepletion of the defect levels induces positive surface charges that induce the DBB. Note that this is identical to the photon energy dependency of the surface-localized defect exciton signal below  $E_F$ , which survives the inverse repetition rate, see section 5.6. In combination with the established link between DBB and the ultrafast SMT, this suggests that the same species is responsible

<sup>38</sup>Note the difference in the spectra displayed in Figure 6.17 a) and 6.15 b). Although the same pump photon energy and a similar pump fluence is used, the effect on the VB displayed in Figure 6.17 a) is not as strong as in 6.15 b). This is attributed to differences in the defect density of the sample surface. The spectra have been recorded in two different beam times using slightly different annealing temperatures during the sample preparation, which creates different surface defect densities and therefore affects the photoresponse, as will be shown in section 6.2.7. The photon energy series displayed in Figure 6.17 a)-c) was recorded under the same surface conditions.

for generating the ultrafast surface metal.

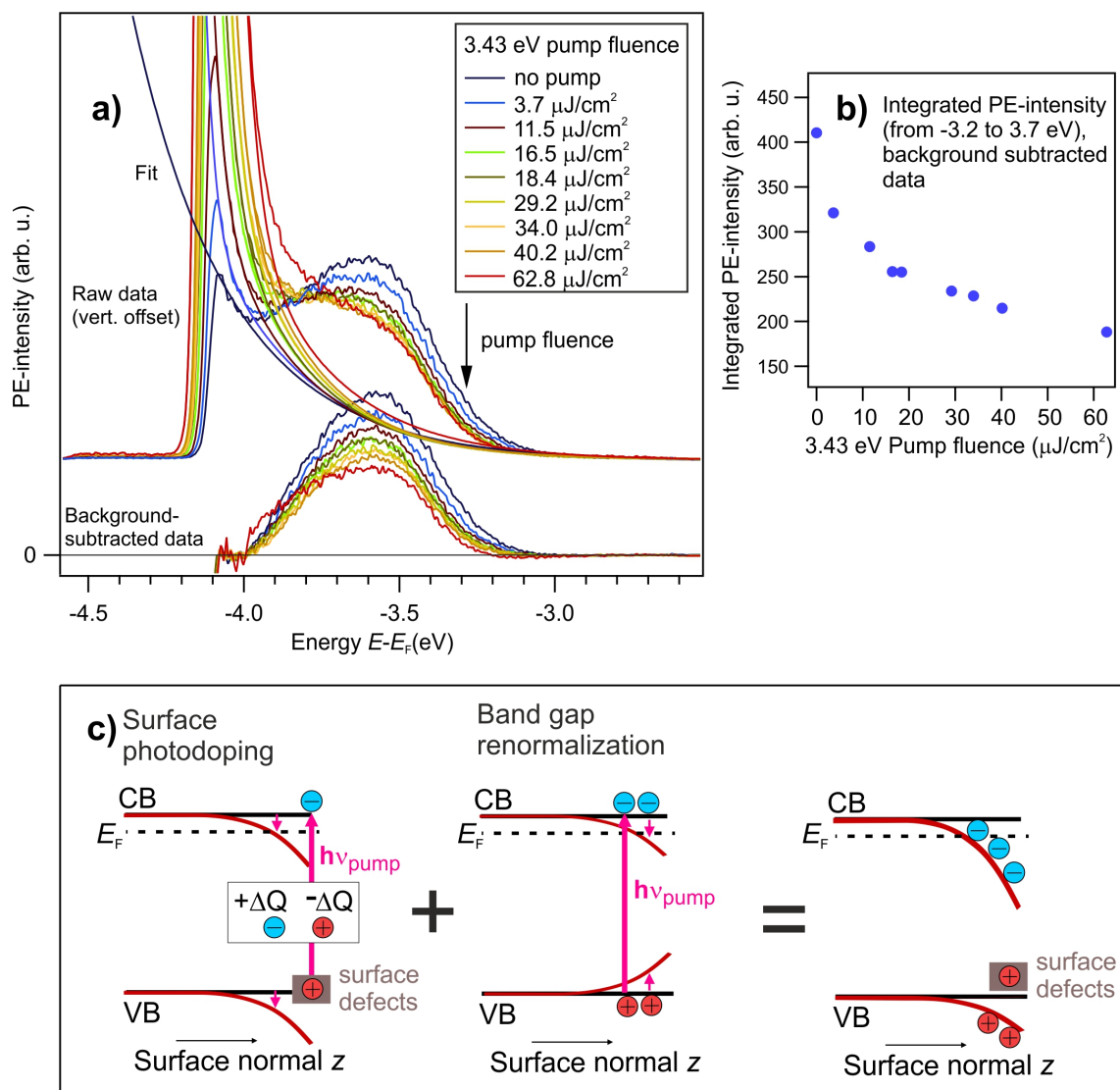


**Figure 6.18:** Saturation of the VB downward shift with increasing fluence. a) VB spectra probed by  $h\nu=4.26$  eV upon different pump fluences. The pump-probe delay is 20 ps, the pump photon energy is 3.43 eV. Top: Raw data with double exponential fits to subtract the secondary electron background that overlaps with the VB signal. Bottom: Background subtracted data. b) VB downward shift, extracted by integrating the background subtracted data from -3.2 to -3.7 eV with respect to  $E_F$ . The downward shift already starts with the lowest pump fluence. The additional shift induced by stronger photoexcitation gets smaller and smaller. c) Illustration of the competition between BGR and photovoltage inversion due to surface photodoping. Free carrier populations contributing to BGR can also result from cross-band gap excitation. Surface photodoping leads to a downward shift of the VB, while the former leads to an upward shift. Both contribute to bend the CB downward. The sum of both leads to a smaller VB downward shift than upon surface photodoping alone.

**The onset of band gap renormalization?** BGR is known to occur in photoexcited semiconductors due to a change of screening [Hau09]. As the band gap shrinks, the VB shifts upward on an absolute energy scale, as observed in refs [Liu19, Mor17]. The downward shift of the VB in the present experiments shows that BGR is, if present, overcompensated by photoinduced band bending. From theory and optical experiments on ZnO, BGR is expected to be on the order of 100 meV at the excitation density of the Mott transition (cf. subsection 6.1.3), increasing superlinearly for excitation densities [Kli10b]. At some excitation density BGR may exceed photoinduced DBB.

Figure 6.18 a) shows VB spectra for different pump fluences. The pump photon energy is  $h\nu=3.43$  eV and the pump-probe delay is 20 ps. Already at the lowest fluence of  $3.7 \mu\text{J}/\text{cm}^2$ , which is below  $F_C$ , the amplitude of the VB signal is reduced and the intensity at lower energies is enhanced, indicative of a downward shift of the VB as discussed above. A part of the intensity at lower energies also stems from the increase of secondary electrons emitted by the pump or probe<sup>39</sup>. With increasing fluence, the trend continues, but at the highest fluences the VB intensity reduction seems to saturate. Because the amplitude reduction results from the VB downward shift, the consequence is that the latter stops shifting down further at elevated fluences. In order to exclude that the observed behaviour of the VB intensity is due to an enhancement of the secondary electron background overlapping with the signature of the VB, I subtracted the background using double-exponential functions as shown in Figure 6.18 a)<sup>40</sup>. The background subtracted data is shown at the bottom of Figure 6.18 a) and exhibits the same saturation of the intensity reduction with increasing fluence, see also the integrated intensity plotted in Figure 6.18 b). There are two possibilities to explain that the VB stops shifting down more and more at higher fluences: First, all defect states could be depopulated at the highest fluence, simply because of a limited amount of these states. Although I cannot exclude this, it seems unlikely considering that the electron density in the metallic band increases linearly with increasing fluence, not showing any indications of a saturation, cf. Figure 6.8. Furthermore, as shown in the next section, the pump-induced positive surface charging can be directly measured with trARPES and it also increases approximately linearly. Secondly, BGR could counteract DBB, as illustrated in Figure 6.18 c). The observed saturation of the VB downward shift is not a proof of this statement, since I do not observe a turning point where the VB starts shifting up again. Nevertheless, the explanation seems plausible considering the above mentioned expectations from optical experiments and theory on BGR in ZnO.

---

<sup>39</sup>The position of the secondary edge shifts down as well. This pump-induced downward shift shows no delay dependency, it equally happens at negative pump-probe delays. The effect is attributed to the enhancement of the photostationary state population by the pump, cf. section 5.

<sup>40</sup>With this procedure I cannot avoid subtracting the part of the signal increase at low energies resulting from the downward shift of the VB, which overlaps with the secondary electron intensity.

In summary of this subsection I showed that the ZnO VB is shifted downward upon photoexcitation and the downward shift evolves simultaneously to the transient metal phase. The spectral shape of the VB after photoexcitation is indicative of surface DBB, where not all unit cells exhibit the same shift. Surface DBB can be induced using a pump photon energy of 3.2 eV, slightly below the fundamental band gap of ZnO, but not with a pump photon energy of 3.0 eV. This shows that the electronic band structure is strongly affected by photoexcitation of deep defect levels  $<0.4$  eV above the VB. The effect exceeds BGR at all pump fluences and is directly linked to the photoinduced SMT. This strongly supports the surface photodoping mechanism presented in section 6.2.1.

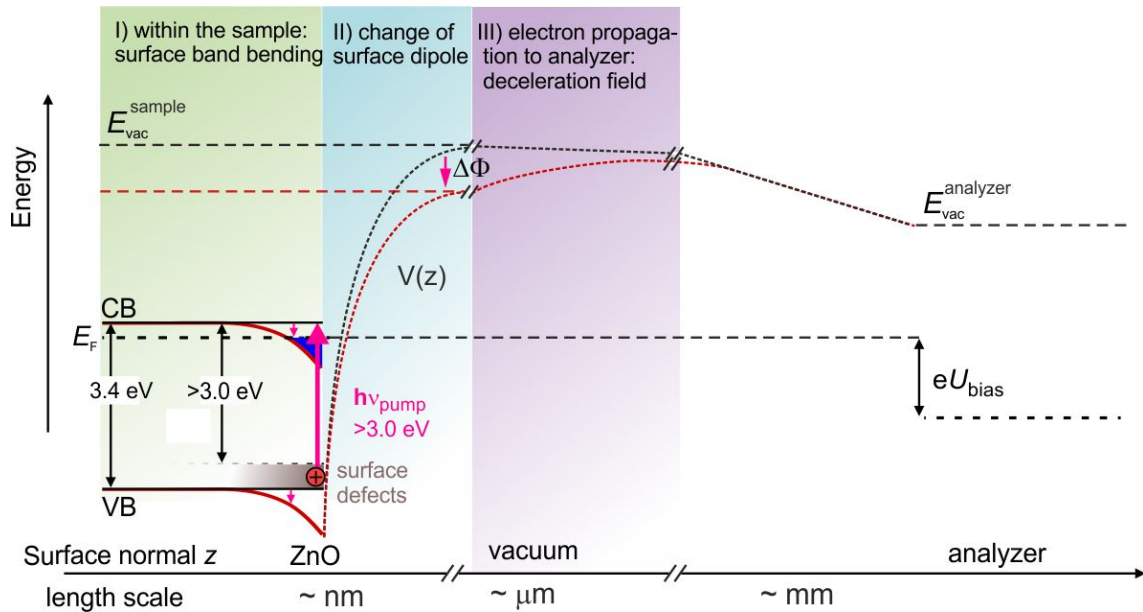


**Figure 6.19:** Pump-induced effects on the electron energies upon the photoexcitation of deep defects at the ZnO surface. I) Within the sample, VB and CB are bent downward towards the surface due to the formation of positive surface charges. II) The resulting dipole (photoholes at defect site plus electrons in the CB) is oriented opposite to the surface dipole that leads to an energy barrier (work function) on a length scale of nm's, cf. section 3.1.2. Photoexcitation of deep defects thus reduces the work function. III) Outside the sample in the near vacuum region a decelerating field exists on a length scale of the pump spot size ( $\mu\text{m}$ 's) that affects photoelectrons propagating to the analyzer.

#### 6.2.4 Pump-induced shifts probed at negative delays

Figure 6.19 summarizes the effects on the electron energies by the photoexcitation of deep defects at the ZnO surface: I) Within the sample, the photoholes localized at surface defect sites lead to DBB toward the surface, which was demonstrated in the previous subsection 6.2.3. II) The formation of dipoles (photoholes plus electrons in the CB) pointing outward the surface normal should reduce the surface dipole, i.e. the work function. This will

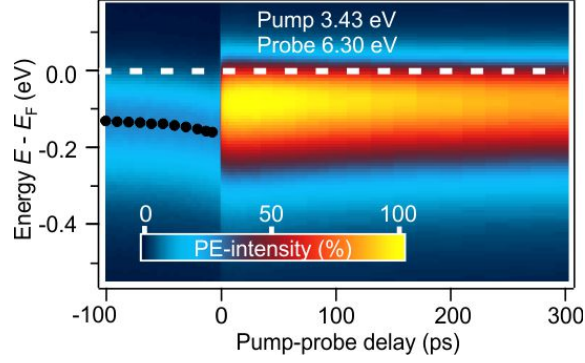


**Figure 6.20:** False color representation of the ultrafast dynamics around  $E_F$ , pump:  $h\nu=3.43$  eV ( $27 \mu\text{J}/\text{cm}^2$ ), probe:  $h\nu=6.3$  eV. The pump-induced increase of the PE signal at positive delays is due to the surface metal. The signal negative delays is due the photostationary defect excitons probed by  $h\nu=6.3$  eV and shows a dynamic shift toward negative delays induced by the pump.

be tackled in the subsequent subsection 6.2.5. III) Because the photoexcitation of deep defects only takes place within the pump spot size of the order of  $\mu\text{m}$ , a decelerating field on this order of magnitude should exist that affects the electron propagation to the analyzer. As described in section 3.1.5, the short-range electrostatic field in the near-surface vacuum region affects photoelectrons that just escaped the sample. Consequently, in a pump-probe experiment, photoelectrons emitted by the probe would be decelerated by the defect exciton formation induced by the pump at small *negative* pump-probe delays  $\Delta t < 0$ , when the photoelectrons are still close to the surface.

Figure 6.20 reproduces the angle-integrated surface metal signal as a function of pump-probe delay that was discussed in section 6.1. The probe photon energy is 6.3 eV, the pump photon energy is  $h\nu=3.43$  eV and the pump fluence is above  $F_C$ . At positive pump probe delays the signal is due to the pump-induced formation of the surface metal. At negative delays the detected signal is due the photostationary defect excitons probed by 6.3 eV, cf. section 5. This signal experiences a shift on a timescale of 100 ps: Close to time zero, the energetic position of the peak is lowered with respect to -100 ps. As shown below, the shift at negative delays also occurs for the VB. **The downward shift at negative delays close to time zero demonstrates unambiguously that positive surface charging by the pump indeed takes place, which decelerates the probe electrons on the way to the detector.**

In what follows I will present an analysis of the negative delay shift. I will demonstrate that the shift can be described by simple electrostatic calculations that encompass the pump-induced retarding field acting on the probe electrons. Thereby, I extract the extent of the pump-induced field extending from the sample surface into the vacuum. The result is in remarkable agreement with the electrostatic field induced by the long-lived defect exciton, mapped by tuning the bias between sample and analyzer (cf. section 5.9).

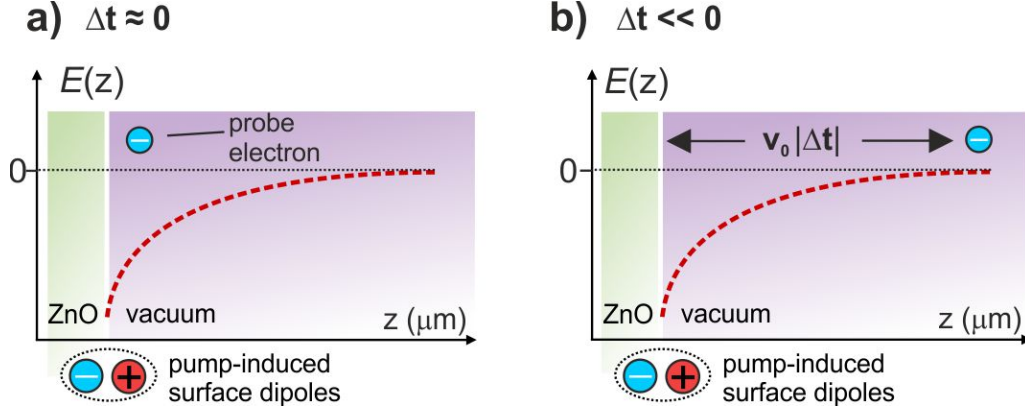


**Figure 6.21:** Origin of the pump-induced shift of the probe signal at negative delays. The pump induces a decelerating field (here displayed: projection onto the unity vector in  $z$  direction) due to a change of the surface dipole upon photoexcitation of deep defects that affects the propagation of the probe electron to the detector. This corresponds to region III in Figure 6.19). For small negative delays  $\Delta t \approx 0$  (a), the probe electron has not propagated and is close to the sample surface, in contrast to larger negative delays (b), where it has traveled the distance  $v_0 |\Delta t|$  ( $v_0$ : speed of the probe electron). The probe electron can be considered as a point charge that maps out the pump-induced electric field extension from the sample surface into the vacuum upon varying the pump-probe delay (see text).

Figure 6.21 illustrates that the extent of the pump-induced electric field is encoded in the negative delay dynamics: When the probe comes just before the pump ( $\Delta t < 0$  but  $\approx 0$ , Figure 6.21 a)), the probe electron senses a stronger field and is decelerated stronger than at larger negative delays (Figure 6.21 b)). This is because in the first case the probe electron is just in front of the sample surface, while in the latter case the electron has traveled a certain distance and does not experience the same deceleration on its propagation to the detector.

The deceleration is related to the short-range electrostatic field  $E(z)$  through the classic equation of motion [Tan12]:

$$m_e \frac{d}{dt} v(z(t), t) = eE(z(t), t) \quad (6.105)$$

Here,  $t$  is the propagation time and  $z(t)$  the position in front of the sample surface. A numerical solution of this differential equation will be performed in the subsequent subsection 6.2.5 to resolve the trajectories of very slow electrons that constitute the secondary edge. Here I just consider a simplified case by assuming

- The deceleration is small so that the position of the probe electron in front of the sample surface can be expressed by  $z = v_0 t$ , where  $v_0$  is the speed the electron has after photoemission.
- $E(z)$  is long-lived, or rather, the probe electron is fast enough to transverse it com-

pletely before it decays.

In this case it is not necessary to solve equation 6.105 to know how fast the probe electron will be upon reaching the detector; the loss of kinetic energy  $\Delta E_{\text{kin}}$  by the pump induced field  $E(z)$  must equal the potential energy

$$\Delta E_{\text{kin}}(z_0) = V(z)|_{z=z_0}^{\infty} = e \int_{z_0}^{\infty} E(z') dz'. \quad (6.106)$$

$z_0$  is the distance which the probe electron has traveled before the pump arrives and creates the field, which depends on the delay as depicted in Figure 6.21<sup>41</sup>. It is given within the approximation of small decelerations by

$$z_0 = v_0 |\Delta t|, \quad (6.107)$$

where  $\Delta t$  is the pump-probe delay, which is  $<0$ . Equation 6.106 thus relates the kinetic energy shift to the (negative) pump-probe delay. For the pump-induced dipole density at the sample surface I assume a Gaussian distribution. This corresponds to the measured intensity distribution of the pump laser pulse. Furthermore, I assume that the probe electrons escape along the center axis of the pumped area at the sample, which is approximately fulfilled, because the probe spot size determined by a beam profiler is a factor of 2-3 smaller than the pump spot size. The electronic potential energy along the center axis of the pumped area is [Tan12]:

$$V_G(z) = \frac{eD}{2\epsilon_0} \int_0^{\infty} \frac{z r}{(r^2 + z^2)^{3/2}} S(r) dr \quad (6.108)$$

Here,  $r$  is the radial distance from the center axis of the disk of pump-induced surface dipoles  $D$ .  $S(r)$  is the spatial envelope of the pump-induced dipoles at the surface. For a Gaussian distribution

$$S(r) = e^{-r^2/[FWHM/2 \ln(2)]^2} \quad (6.109)$$

The integration needs to be carried out numerically. Note that the pump-induced dipole density would also reduce the work function of the sample. The work function change on ultrafast time scales will be analyzed in the subsequent subsection.

In the following I present the data evaluation of the observed pump-induced negative delay shifts and subsequently compare the calculation above to the experimental observations.

Figure 6.22 a) shows the peak position of the PE-signal due to the photostationary

---

<sup>41</sup>The integration can be extended to  $z = \infty$  because the sample-detector distance is 4 mm in the present experiment, and the pump-induced field has a range on the order of the spot size which is on the order of 100  $\mu\text{m}$ .

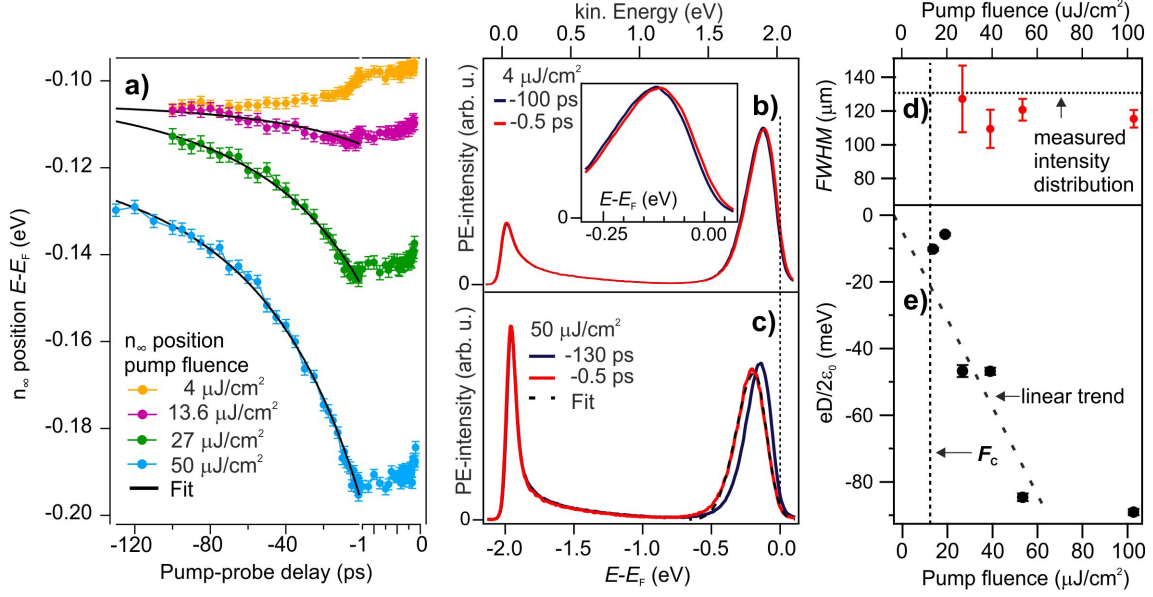


**Figure 6.22:** Pump-induced shift of the photostationary defect excitons probed at negative delays ( $h\nu_{\text{Pump}}=3.43$  eV,  $h\nu_{\text{Probe}}=6.3$  eV). a) Peak position (determination see c)) as a function of negative pump-probe delay for different pump fluences. The black lines are fits with equation 6.106 with  $V(z_0) = V_D(z_0)$ . b) and c): Exemplary PE-spectra of the photostationary defect excitons at large negative and small negative pump-probe delays for low and high pump fluence, respectively. The inset in b) is a magnification around  $E_F$  showing that for low fluences the photostationary defect excitons shows a small upward shift at small negative with respect to large negative delays. At high fluence the shift is downward, as shown in c). Dashed line: Exemplary fit with an asymmetric Gaussian function to extract the peak position of the PE signal. d) and e): Results from fitting the downward shift at negative delay with equation 6.106 and  $V(z_0) = V_D(z_0)$  (FWHM of the Gaussian intensity distribution and pump-induced surface potential change  $\frac{eD}{2\epsilon_0}$ ) for different pump fluences. The dashed line in d) marks the intensity distribution of the pump laser spot measured with a beam profiler (cf. section 3.2.2)

defect excitons versus negative pump-probe delays between 0 and -130 ps for four selected pump fluences. The fluence range from below to above  $F_C$ . The peak position is extracted from a fit with an asymmetric Gaussian function to the PE-intensity at each negative delay, c.f. the exemplary PE-spectra and fits in Figure 6.22 b) and c). Figure 6.22 a) shows that a dynamic shift toward negative delays is observed for all fluences. For the smallest pump fluence ( $F=4$   $\mu\text{J}/\text{cm}^2$ ) the shift is *upward* upon approaching time zero from large negative delays. The effect is very small, on the order of 10 meV or below, but clearly discernable in the raw data, cf. Figure 6.22 b). For all other fluences, which are above  $F_C$ , a *downward* shift is observed. The downward shift gets more pronounced for increasing pump fluence. The upward shift is not further evaluated at this point, its origin is not yet clear at present<sup>42</sup>.

<sup>42</sup>An upwards shift at negative delays indicates that electrons are *accelerated* by the pump induced field, i.e. the surface must be *negatively* charged at low fluences. Possibly, it arises from a SPV effect due to the

The solid black lines in Figure 6.22 a) are fits with equation 6.106 with  $V(z_0) = V_G(z_0)$ .  $z_0$  is calculated for each pump-probe delay  $\Delta t$  using equation 6.107. The velocity  $v_0$  of the photoelectrons can be determined from plotting the PE-intensity versus their kinetic energy, see the top axis in Figure 6.22 b). The fits match the data precisely. The full width of half maximum of the disk of pump-induced dipoles at the ZnO surface that results from the fit is given in Figure 6.22 d) as a function of pump fluence. It is about 120  $\mu\text{m}$  for all pump fluences. This is in nearly perfect agreement with the measured FWHM of the pump laser beam, which is 128-131  $\mu\text{m}$ <sup>43</sup>. This demonstrates that the negative delay shift is due to a short-ranged decelerating field induced by the pump laser pulse, extending from the sample into the vacuum. The pump laser pulse thus evidently creates dipoles pointing outward the surface normal at the ZnO surface, which are also responsible for the downward surface band bending described in the last subsection.

It is interesting to compare the so-determined pump-induced field to the results from mapping the evanescent field in the photostationary state by tuning the bias, cf. section 5.9. In the latter case a constant distribution of photoinduced dipoles

$$S(r) = \text{const.}, \text{ if } r < R, \text{ and } 0 \text{ otherwise} \quad (6.110)$$

was assumed which yields the integral in equation 6.108 analytically tractable. The result of the integration is (cf. equation 3.15 in section 3.1.2 and equation 5.92 in section 5.9):

$$V_D(z) = -\frac{eD}{2\epsilon_0} \left(1 - \frac{z}{\sqrt{R^2 + z^2}}\right) \quad (6.111)$$

The negative delay shift (Figure 6.22 a)) can also be fitted with this potential, i.e. with equation 6.106 with  $V(z_0) = V_D(z_0)$ . These fits match the data as perfectly as upon using a Gaussian intensity distribution (not shown), meaning that the pump-induced potential can be parametrized with  $V_D(z)$ . The resulting  $R$  is about 0.9 of the half width half maximum (HWHM) of the measured pump laser intensity distribution. This value is in perfect agreement with the result of the mapping of the evanescent field in the photostationary

---

preexisting DBB upon incidence of the pump: The charge separation due to the preexisting DBB would drive photoexcited electrons in the CB to the surface and holes in the VB to the bulk [Kro01]. This would charge surface negatively with respect to negative delays, and indeed, there should be such a preexisting DBB due to the photostationary state. However, photoexcitation with the pump should then lead to a weakening of the DBB. Consequently, the VB would shift upward with respect to negative delays. This is in conflict with the observation that the pump induces (or enhances preexisting) DBB shown in section 6.2.3, Figure 6.18. It can be noted that the fluence at which the upward shift is observed is below  $F_C$  (cf. section 6.1.3), but it is not clear whether this is a mere coincidence. The downward shift could be simply too weak to be observed at low fluences. Moreover, looking closely at the data in Figure 6.22 a) it seems that a fast and weak upward shift is superimposed to the downward shift observed for all fluences even above  $F_C$ .

<sup>43</sup>This value results from averaging the FWHM of the long and short axis of the elliptical spot via  $\sqrt{\text{FWHM}_x \cdot \text{FWHM}_y} / \cos(45^\circ)$ , which are determined with a beam profiler as described in chapter 3.2. The factor  $1/\cos(45^\circ)$  accounts for the projection onto the sample surface under  $45^\circ$  grazing incidence.

state by tuning the bias using the parametrization with  $V_D(z)$ , cf. section 5.9. **The observed shift at negative delays suggests that defect excitons of the same kind as those that form the photostationary state revealed in section 5 are created by photoexcitation with  $h\nu_{\text{Pump}}=3.4$  eV on the ultrafast time scale, because the pump creates the same surface potential change.**

Figure 6.22 e) shows the pump-induced surface potential change  $\frac{eD}{2\epsilon_0}$  as a function of pump fluence that results from the fits with equation 6.106 with  $V(z_0) = V_G(z_0)$  (nearly identical values result from using  $V_D(z_0)$ ). The pump reduces the surface potential roughly linearly with increasing pump fluence, only the data point recorded at the highest pump fluence of  $96 \mu\text{J}/\text{cm}^2$  deviates significantly from the trend. In Figure 6.22 e) the critical fluence  $F_C$  is marked with a dashed line. No downward shift is detected for fluences below  $F_C$ , likely because the effect is small. In fact, as mentioned above, a small upward shift is observed at small fluences, of yet unknown origin. A small downward shift at low fluences could be indistinguishable in the data due to this upward shift. A threshold behaviour as a function of pump fluence cannot be discerned, in agreement with the VB downward shift, which also sets on already below  $F_C$ , see section 6.2.3. The surface potential reduction extracted from this procedure amounts to 90 meV at the highest pump fluence. This is on the order of the surface potential reduction by the photostationary defect exciton population, which is 70-195 meV, see section 5.9<sup>44</sup>. Thus, at the highest pump fluence, the amount of defects photoexcited by  $h\nu_{\text{Pump}}=3.4$  eV on the ultrafast time scale roughly equals the photostationary portion (the latter stays almost constant upon different  $h\nu_{\text{Pump}}=3.4$  eV fluences, see section 5.7).

As a crosscheck of the above findings I also evaluated the VB shifts as a function of negative delay. The VB is probed using a different probe photon energy,  $h\nu_{\text{Probe}}=4.26$  eV (cf. section 6.2.3); the same pump photon energy ( $h\nu_{\text{Pump}}=3.43$  eV) and pump spot radius as above was used. Figure 6.23 a) shows two VB spectra, one at -100 ps and one at -1 ps, plotted versus kinetic energy. Clearly, the VB edge is shifted downward at -1 ps with respect to -100 ps. The shift as a function of pump-probe delay is plotted in Figure 6.23 b) for two different pump fluences,  $25 \mu\text{J}/\text{cm}^2$  and  $50 \mu\text{J}/\text{cm}^2$ . The shift was extracted from the data by a Gaussian fit after subtracting the secondary electron background as described

<sup>44</sup>On the one hand, 70 meV results from evaluating the secondary edge position upon varying the repetition rate and corresponds to the difference of the surface potential at 200 kHz with respect to 5 kHz. At 5 kHz, the  $\mu\text{s}$ -long lived component of the photostationary state is practically decayed in between two subsequent laser pulses. On the other hand, a value of 195 meV was extracted from the bias dependency. The bias dependency is sensitive to both, the surface potential reduction from the  $\mu\text{s}$ -long lived component as well as from the quasi-static component that is invariant upon tuning the repetition rate in the kHz regime. Additionally, a resonant pump beam was applied at negative delays during the bias series. As will be shown in the next section also pump-induced fields that are decaying faster than the inverse repetition rate (i.e. are not photostationary) lead to a downward shift of the secondary edge at negative delays. Hence, 70 meV is the minimum surface potential reduction due to the photostationary defect exciton population, and 195 meV is the maximum.

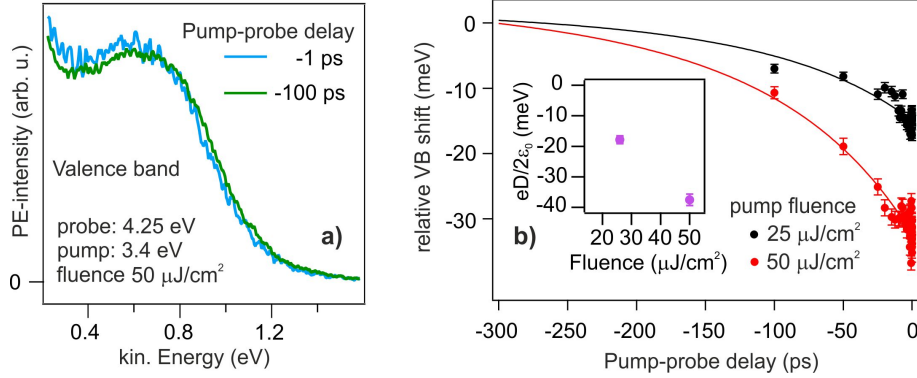


**Figure 6.23:** VB shift probed at negative delays. a) VB spectra probed by  $h\nu_{\text{Probe}}=4.26$  eV at -1 ps and -100 ps ( $h\nu_{\text{Pump}}=3.43$  eV). The VB is shifted down close to time zero with respect to large negative delays. b) Extracted shift as a function of pump-probe delay for two different pump fluences,  $25 \mu\text{J}/\text{cm}^2$  and  $50 \mu\text{J}/\text{cm}^2$ , relative to the value at large negative delays. Solid lines are fits with equation 6.106 with  $V(z_0) = V_G(z_0)$  and fixing  $FWHM$  at the value of  $120 \mu\text{m}$ . Inset: Pump-induced surface potential change  $\frac{eD}{2\epsilon_0}$  resulting from the fit.

in section 6.2.3. For both fluences, the VB is shifted downward at small negative delay with respect to large negative delays and the effect is more pronounced at higher pump fluence. The solid lines in Figure 6.23 a) are fits with equation 6.106 with  $V(z_0) = V_G(z_0)$  and fixing  $FWHM$  at the value of  $120 \mu\text{m}$  that resulted from the analysis of the shift of the PE-signal due to the photostationary defect excitons above. The fits match the data points well and shows that also the VB shift at negative delays is consistent with a pump-induced change of the surface potential. Note that for the VB shift the pump-probe delay axis is extended to -300 ps because the shift is slower: The kinetic energy of the VB is about one fourth the kinetic energy of the electrons arising from the photostationary defect excitons (cf. the PE-intensity as a function of kinetic energy for the VB and the photostationary defect excitons shown in Figure 6.23 a) and Figure 6.22 b), respectively). Therefore the VB shift extends to larger negative delays than the shift of the PE-signal due to the photostationary defect excitons, because the electrons propagate for a longer time in the extent of the pump-induced field. The inset in Figure 6.23 b) shows the extracted pump-induced surface dipole change. Compared to the shift of the defect exciton signal, it is only about half as large at the same pump fluence. This deviation may be attributed to the fact that within the propagation time of the VB electrons the pump-induced change of the surface potential has already partially decayed: the negative delay shift occurs on a time scale of 300 ps and the DBB relaxes partially within  $\tau_3=219(13)$  ps, see subsection 6.2.3. This is expected to diminish the observed shift [Tan12]. Note that the observation of the dynamic shift toward negative delays excludes that the observed shift of the photostationary state signal is due to different photostationary equilibria at varying the pump probe delay (cf. section 4.2). The latter leads to an intensity variation

of the photostationary state signal and not (or not necessarily) to a shift. The intensity increase of the photostationary state signal toward negative delays described in section 4.2 indeed also occurs for the data set evaluated above, *in addition* to the shift, cf. the photostationary state spectra at large versus small negative pump-probe delays in Figure 6.22 c).

In summary of the subsection, photoelectrons emitted by the probe show dynamic shifts toward negative delays induced by the pump pulse. The shifts can be nicely explained by a decelerating potential due to the photoexcitation of deep defects at the ZnO surface by the pump.

### 6.2.5 Measuring work function shifts in the ultrafast time domain

The last subsection showed that photoexcitation by the pump ( $h\nu_{\text{Pump}}=3.43$  eV) creates dipoles at the ZnO surface, attributed to the photoexcitation of deep defects, which cause a decelerating field extending tens of  $\mu\text{m}$  into the vacuum. As shown in chapter 5, the photoexcited defects partially survive the inverse repetition rate and form the photostationary defect exciton population. In case of the photostationary defect excitons, a work function reduction was detected: Upon decreasing of the photostationary state population by reducing the repetition rate an upward shift of the secondary edge occurs, see section 5.2. A work function reduction is expected upon the enhancement of the dipole density by the pump as well (cf. Figure 6.19). In this subsection I show that a shift of the secondary edge does *not* occur in pump-probe scans on the ultrafast time scale, even though the work function is reduced by the formation of dipoles at the ZnO surface upon crossing time zero. This is explained by simulating the trajectories of the slowest electrons constituting the secondary edge. The simulations build an extension of the theoretical work by Tanaka [Tan12], who explicitly did not consider low energy electrons. Finally, I propose that although a *shift* of the secondary edge does not occur in the ultrafast time domain, a pump-induced work function reduction affects its *intensity*. The secondary edge intensity that occurs in the pump-probe scans on ZnO is discussed in this context. It should be noted that this subsection is technical and does not provide additional information on the photodoping mechanism beyond consistency checks. The aim of this subsection is to understand the signatures of ultrafast work function changes in trARPES. The reader interested in the photodoping mechanism may continue with the succeeding subsection 6.2.6.

#### The position of the secondary edge in pump-probe scans on ZnO: Experiment

As shown in the preceding section the pump creates dipoles at the ZnO surface that cause

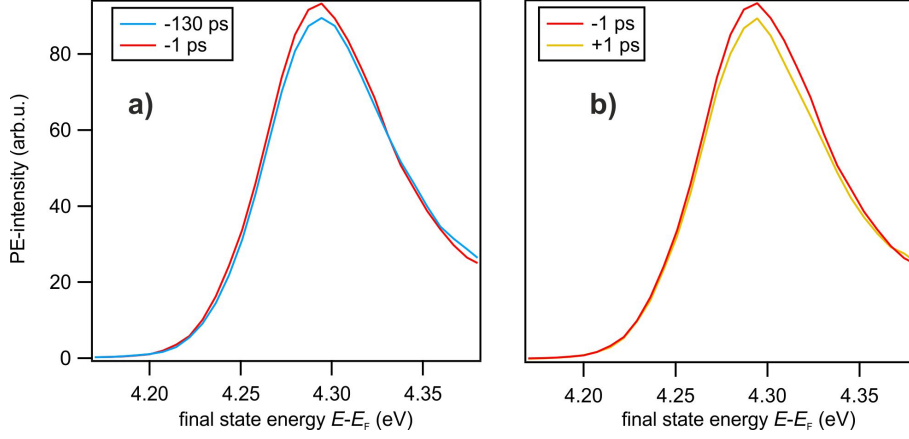


**Figure 6.24:** Comparison of the position of the secondary edge position for a) -130 ps and -1 ps, b) -1 ps and +1 ps. Small changes of the intensity at the secondary edge are detected but no shift occurs. The simulation in this subsection shows that this is expected even when the work function is changed upon incidence of the pump. Probe  $h\nu_{\text{Probe}}=6.3$  eV, pump  $h\nu_{\text{Pump}}=3.43$  eV, pump fluence  $50 \mu\text{J}/\text{cm}^2$ .

a decelerating field of the form

$$V_D(z) = -\frac{eD}{2\epsilon_0} \left(1 - \frac{z}{\sqrt{R^2 + z^2}}\right) \quad (6.112)$$

Accordingly, the work function should be lowered by  $\frac{eD}{2\epsilon_0}$  (cf. section 3.1.2 and 5.9). In static photoemission spectroscopy, the work function can be determined from the secondary edge position, cf. section 3.1.2. Therefore one naively expect that in the pump-probe data on ZnO the position of the secondary edge (consisting of electrons emitted by the probe pulse) would shift to lower energies once the pump pulse has arrived, i.e. at positive with respect to negative delays.

Figure 6.24 compares the secondary edge for ZnO at different pump-probe delays for a) -130 ps and -1 ps and b) -1 ps and +1 ps. The probe photon energy is  $h\nu_{\text{Probe}}=6.3$  eV and the pump photon energy is  $h\nu_{\text{Pump}}=3.43$  eV; the gross of secondary electrons is emitted by the probe pulse (not shown). The pump fluence is  $50 \mu\text{J}/\text{cm}^2$ , at which  $\frac{eD}{2\epsilon_0} = -85$  meV, see Figure 6.22 e). The comparison in Figure 6.24 shows that the secondary edge stays at the same position for all delays. It does not shift for negative delays, unlike the primary electrons constituting the VB and the photostationary state, as described in the last section. Most importantly, it does not shift when crossing time zero, i.e. from -1 ps to +1 ps. Only a slight variation of the secondary edge intensity occurs, which will be discussed further below. As shown in the following, the reason that no ultrafast shift of the secondary edge occurs is that the secondary electrons are very slow and are not detected just after photoemission but need to propagate until the analyzer. The shift is cancelled

due to propagation effects.

### The position of the secondary edge in pump-probe scans on ZnO: Simulations

Figure 6.25 a) recapitulates the experimental situation: Electrons emitted by the probe have to travel 4 mm to arrive at the analyzer entrance. The analyzer then measures the kinetic energy of these electrons and records the number of electrons versus their kinetic energy. This is described in detail in section 3.1.3. Since it is the kinetic energy *at the detector* that matters it is essential to know by how much the probe electron has been accelerated or decelerated on the way to the analyzer. Only then, one can relate the measured kinetic energy to the binding energy of electrons within the solid, or determine work function correctly.

In the following I explain the experimental setting and the ansatz for the simulation. For simplicity, I assume that the secondary edge is constituted exclusively of photoelectrons emitted by the probe laser pulse. In order to simulate the position of the secondary edge in pump-probe scans, I start with the simplest case, where the field between sample and analyzer does not change as a function of time. Then it is sufficient to draw potential energy diagrams to figure out the measured kinetic energy as a function of initial kinetic energy  $E_{\text{kin}}^0$  after photoemission (see section 3.1.3 and Figure 3.5). This situation is encountered for very large negative delays or if the pump is off. In this case, the electron potential sensed by probe electrons on the way to the analyzer can be described by the sum of a decelerating field due to the photostationary defect exciton population and the bias:  $V(z) = V_D(z) + V_C(z)$ . Here,  $V_D(z)$  is given by equation 6.112. The variables entering equation 6.112 are known from the bias series discussed in section 5.9. The radius  $R$  has to be set to 0.9 times the measured pump spot size, which results in  $R = 55 \mu\text{m}$  for the experiment shown in Figure 6.24. Moreover,  $\frac{eD}{2\epsilon_0} = -0.2 \text{ eV}$  is assumed, which is a value that was extracted in section 5.9 with the bias series. The same value is used in the present simulations, because the excitation conditions of both experiments, i.e. the one in Figure 6.24 and Figure 5.12, are almost the same.  $V_C(z)$  is the plate capacitor potential, which is also known as the bias is  $U_{\text{bias}} = -1.5 \text{ V}$  and the analyzer sample distance is 4 mm. The resulting potential is shown in Figure 6.25 b). The potential is the sum of  $V_D(z)$  and  $V_C(z)$ , i.e.  $V(z) = V_D(z) + V_C(z)$ . It the shape of an energy barrier, with a maximum at  $z_{\text{max}}$  at ca.  $100 \mu\text{m}$  in front of the sample surface. Because of the energy barrier, electrons with zero kinetic energy do not arrive at the detector *although* they are photoemitted from the sample: To overcome the barrier by  $V(z) = V_D(z) + V_C(z)$  a minimum kinetic energy of 0.138 eV after photoemission is required, which results from the value of the potential at  $z_{\text{max}}$  with respect to the potential at  $z_0$ , see Figure 6.25 b) and cf. section 5.9.

In this simple case the position of the secondary edge in the photoemission spectrum can be determined by simple energy conservation: If no decelerating potential is present,

the slowest electrons (0 eV kinetic energy after photoemission) are accelerated due to the bias to  $\tilde{E}_{\text{kin}}=0 \text{ eV}+1.5 \text{ eV}=1.5 \text{ eV}$ . In case the photostationary potential is present the 0 eV kinetic energy electrons do not arrive at the detector, but only those with 0.138 eV. They are slowed down to 0 eV at  $z_{\text{max}}$  and then do not experience the full acceleration due to the bias. Their kinetic energy at the detector is given by  $\tilde{E}_{\text{kin}}+V(z_{\text{max}})=1.438 \text{ eV}$ .

However, if photoexcitation by the pump creates time-variant fields in the near-surface vacuum region and the probe electrons are still close to the surface, or not even emitted from the sample (small negative or positive pump probe delays, respectively), the situation becomes more complex: The time-variant fields affect the electron propagation from sample to analyzer as a function of pump-probe delay  $\Delta t$ , the decay time of the pump-induced field and the initial kinetic energy  $E_{\text{kin}}^0$  of the photoemitted electrons. The way to find the kinetic energy of probe electrons at the detector is to solve the classic equation of motion (equation 6.105) [Tan12], which yields the electron speed  $v(t)$  and position  $z(t)$  as a function of propagation time  $t$ .

Figure 6.25 c) and d) shows electron trajectories  $z(t)$  calculated by solving equation 6.105 numerically with just the stationary potentials given above (i.e. no time-variant fields). Different trajectories result depending on the initial kinetic energy of photoelectrons  $E_{\text{kin}}^0$ , the kinetic energy at  $z = 0$ , just after photoemission. The kinetic energy at the detector is determined by propagating the electrons until the analyzer entrance at  $z = 4 \text{ mm}$ , which takes several ns, depending on the initial kinetic energy (cf. Figure 6.25 d)). Determining the position of the secondary edge requires the calculation of the trajectories of very slow electrons. A meaningful value to start with is the  $E_{\text{kin}}^0$  value sufficient to overcome the energy barrier that extends up to  $z_{\text{max}}$ , determined from the energy conservation above. In Figure 6.25 c) the trajectories with this  $E_{\text{kin}}^0$  and with slightly smaller or higher  $E_{\text{kin}}^0$  (1 meV steps) are shown. By this procedure I find that only electrons with  $E_{\text{kin}}^0 = 0.139 \text{ eV}$  can overcome the energy barrier and arrive at the analyzer. The kinetic energy at the analyzer found to be 1.439 eV. This value is in agreement with the energy conservation consideration. Also the numerically determined  $z_{\text{max}}$  marked in Figure 6.25 c) is in excellent agreement with the value for  $z_{\text{max}}$  resulting from drawing  $V(z)$ , cf. Figure 6.25 b). Thus, both approaches are consistent in case of stationary fields. In extension to the pure energy conservation consideration, from this simulation I gain the formation that for overcoming the energy barrier at  $z_{\text{max}}$  the slowest electrons that arrive at the detector need nearly 2 ns (cf. Figure 6.25 c)).

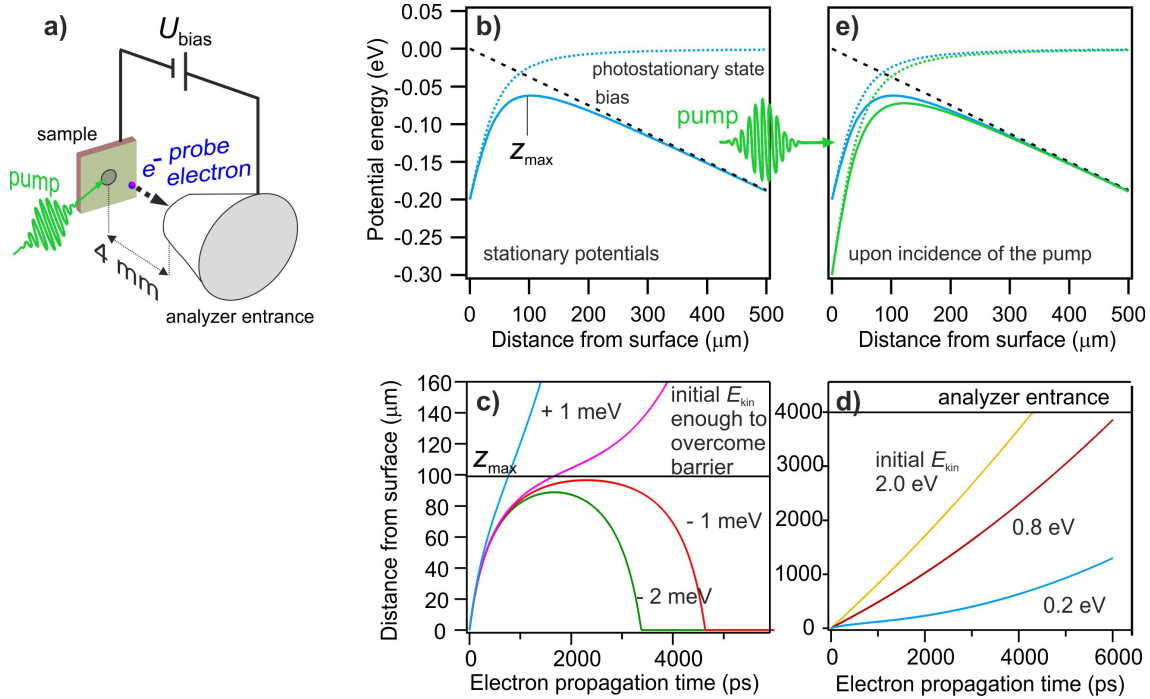


**Figure 6.25:** Setting for the simulations to tackle ultrafast work function changes. a) Sketch of analyzer and sample for the photoemission experiment used in this work. The analyzer-sample distance is 4 mm and a bias voltage  $U_{\text{bias}}$  is applied between sample and analyzer. The bias accelerates photoemitted electrons towards the detector. In addition, both pump and probe pulses induce dipoles at the surface, which lead to short-ranged decelerating fields that affect the propagation, cf. section 6.2.4. In c)-d) the propagation of probe electrons without applied pump is considered. In this case there are only photostationary photoinduced dipoles with a lifetime exceeding  $\mu\text{s}$ , which is very long compared to the time the probe electrons need for reaching the analyzer. b) Potential sensed by probe electrons between ZnO sample and analyzer in the first 500  $\mu\text{m}$ . The electrons sense the photostationary decelerating potential (blue dashed line, cf. section 5.9) and the potential due to the bias between sample and analyzer (black dashed line). The resulting potential (solid blue line) is the sum of both components and has the shape of an energy barrier, with a maximum at  $z_{\text{max}}$ . c) and d) Trajectories of photoelectrons calculated by solving equation 6.105 for different kinetic energies upon photoemission. c) Slow photoelectrons that just overcome the potential barrier that extends up to  $z_{\text{max}}$ . These electrons constitute the secondary edge in the measurement. To reach  $z_{\text{max}}$  they need several nanoseconds. d) The measured kinetic energy of electrons fast enough to overcome the surface barrier is found by propagating the electrons to the analyzer entrance at  $z=4\text{ mm}$ . e) The pump laser is on and reduces the surface dipole. The photoinduced dipoles are created within few ten's of femtoseconds and decay partially within few hundred ps, cf. section 6.2.3, cf. section 5.9. This results in an additional decelerating potential that has the same  $z$ -dependency as the photostationary decelerating potential, but it decays within the time the slowest electrons reach  $z_{\text{max}}$ . The question addressed in this subsection is if such pump-induced time-variant fields lead to a downward shift of the measured secondary edge or not.

I now move on to simulate the measured kinetic energies of photoelectrons in pump-probe scans. The pump induces an additional potential of the form  $V_D(z)$  that is added to the stationary  $V(z)$ . This reduces the work function further and leads to an additional decelerating field in front of the sample surface. For the simulations that follow, the surface potential reduction induced by the pump is assumed to be  $\frac{eD}{2\epsilon_0} = -0.1$  eV; the resulting potential is drawn in Figure 6.25 e). The temporal evolution of the surface potential reduction after incidence of the pump is also known, because it is responsible for the DBB that is experimentally determined in section 6.2.3. The DBB is characterized by a rise with two components ( $\tau_1=20$  fs,  $\tau_2=1.2$  ps) and a single exponential decay ( $\tau_3 = 219$  ps)<sup>45</sup>. To start with, I calculate electron trajectories  $z(t)$  of fast probe electrons for negative pump-probe delays. The final kinetic energy as a function of negative pump probe is displayed in Figure 6.26 a) for different  $E_{\text{kin}}^0$  (0.2 eV, 0.8 eV and 2.0 eV). From -100 ps towards time zero they all show a dynamic downward shift. The shift becomes less pronounced and gets slower for lower  $E_{\text{kin}}^0$ , in qualitative agreement with the experimental data presented in the last subsection and the calculations by Tanaka [Tan12]. As discussed in the last subsection, if the electrons are fast enough to transverse the pump-induced potential completely before it decays and the shift is small compared to  $E_{\text{kin}}^0$ , the kinetic energy shift of the probe electrons at negative delays maps the extension of the pump-induced potential. I showed that the experimentally observed shift is described by  $V_D(z_0)$  with  $z_0 = \Delta t v_0$  ( $v_0 = \sqrt{2E_{\text{kin},0}/m_e}$ ). In the simulations, the fastest electrons with  $E_{\text{kin}}^0 = 2$  eV represent probe electrons photoemitted from the photostationary state. These electrons transverse the pump-induced field within approximately 100 ps which is faster than  $\tau_3=219$  ps. Furthermore, the kinetic energy shift is small compared to  $E_{\text{kin}}^0$  (cf. Figure 6.26 a)). Correspondingly, I find an excellent fit of  $V_D(z_0)$  with  $z_0 = \Delta t v_0$ , see Figure 6.26 a). This shows that the simulations are able to describe the experimentally observed shift at negative delays.

Having ascertained this consistency, I turn to the main interest of this subsection: The position of the secondary edge in pump-probe scans for positive and negative delays. This is determined by finding the trajectory of the slowest electron that can overcome the surface barrier at  $z_{\text{max}}$  (cf. Figure 6.25 c) and propagating it through the time-variant fields in front of the surface to the analyzer. Figure 6.25 b) shows the result of the simulation for different cases: No photostationary fields at all, only the photostationary decelerating field, and then a pump-induced surface potential reduction that rises with  $\tau_1=20$  fs,  $\tau_2=1.2$  ps and decays with  $\tau_3=219$  ps. While the photostationary decelerating field creates the above-mentioned downward shift of the secondary edge, a pump-induced surface potential reduction that decays  $\tau_3=219$  ps does not affect the secondary edge

<sup>45</sup>Plus a long-lived portion, namely the offset of the single exponential decay. For simplicity I assume that the long lived component  $y_0$  is zero in the simulations.

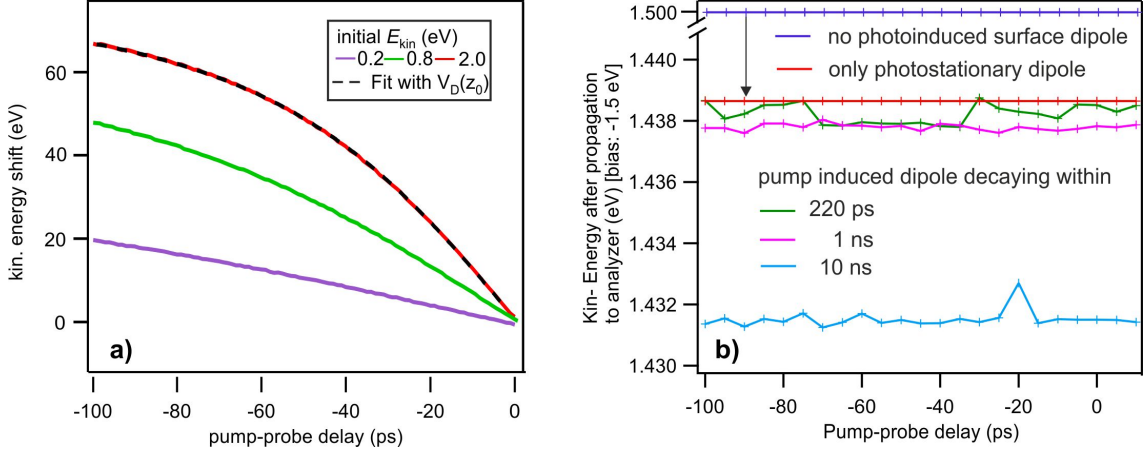


**Figure 6.26:** Results from simulating electron trajectories. a) Kinetic energy shift of probe electrons due to the pump at negative pump-probe delays. The shift is calculated for probe electrons with three different kinetic energies just after photoemission and gets weaker for slower probe electrons within the given delay window. The pump-induced potential is  $V_D(z)$  (equation 6.108) with  $R=55 \mu\text{m}$ . The dashed line is a fit with equation 6.106 with  $V(z_0) = V_D(z_0)$  with  $R=55 \mu\text{m}$  and  $z_0 = \Delta t v_0$  and is a consistency check (see text). b) To calculate the shift for the slowest electrons that constitute the secondary edge, the trajectory of the electron that just overcomes the energy barrier at  $z_{\text{max}}$  needs to be found (cf. Figure 6.25 d)). Doing this for different pump-probe delays gives the position of the secondary edge as a function of pump-probe delay. Different parameters for the pump-induced potential are considered (see legend and text).

position. If the field is longer lived (1 ns, 10 ns), the secondary edge shifts further down. Interestingly, however, the shift occurs for all pump-probe delays, irrespective of negative or positive.

The explanation of this result is as follows: The secondary cutoff measured experimentally is, in case of a photoinduced reduction of the surface potential, determined by the energy barrier that extends up to  $z_{\text{max}}$ . This was shown experimentally in section 5.9 and also results from the theoretical considerations (either energy conservation-based or simulation-based) above. Notably, the electrons that have just enough energy to overcome the barrier require about 2 ns to propagate to  $z_{\text{max}}$  after they start from the sample surface (cf. Figure 6.25 c)). It is for this reason that the timing of the electron emission with respect to the incidence of the pump on a ps time scale does not matter. Firstly, for short decay times (case  $\tau_3=219$  ps), the propagation time of 2 ns exceeds the time frame of few hundred ps by far in which pump-induced modulations of the surface dipoles rise and decay. Therefore, the probe electrons always find the same energy barrier at  $z_{\text{max}}$  as without the pump laser pulse. Secondly, in case of longer decay times of the pump-induced field that are on the order of the propagation time of the probe electrons (case  $\tau_3=1$  ns or 10 ns), the electrons find a different energy barrier at  $z_{\text{max}}$  compared to without applied pump. However, in this case the variation of the pump-probe timing a timescale of

hundred's of picoseconds does not matter, because this time span is much shorter than the propagation time: As the pump-induced field determines the value of the potential at  $z_{\max}$  instantaneously (with the speed of light), the electrons find the same barrier at  $z_{\max}$  independent of the pump-probe timing. A delay-dependent shift could only be observed for pump-probe timings that are on the order of the propagation time, i.e. ns in this case.

It should be noted that the situation might be quite different if no decelerating field in front of the surface but an accelerating field due an increase of the surface potential upon photoexcitation was created. In this case  $V(z)$  would not have the shape of an energy barrier at  $z_{\max}$ . The simulations show that a *dynamic* downward shift of the secondary edge in the present experimental setting does not occur upon a pump-induced work function decrease in the ultrafast time domain, in agreement with the experimental observation. Instead, the simulation predicts that if the work function reduction is sufficiently long lived, it leads to a downward shift of the secondary edge at negative and positive delays likewise with no change when crossing time zero.

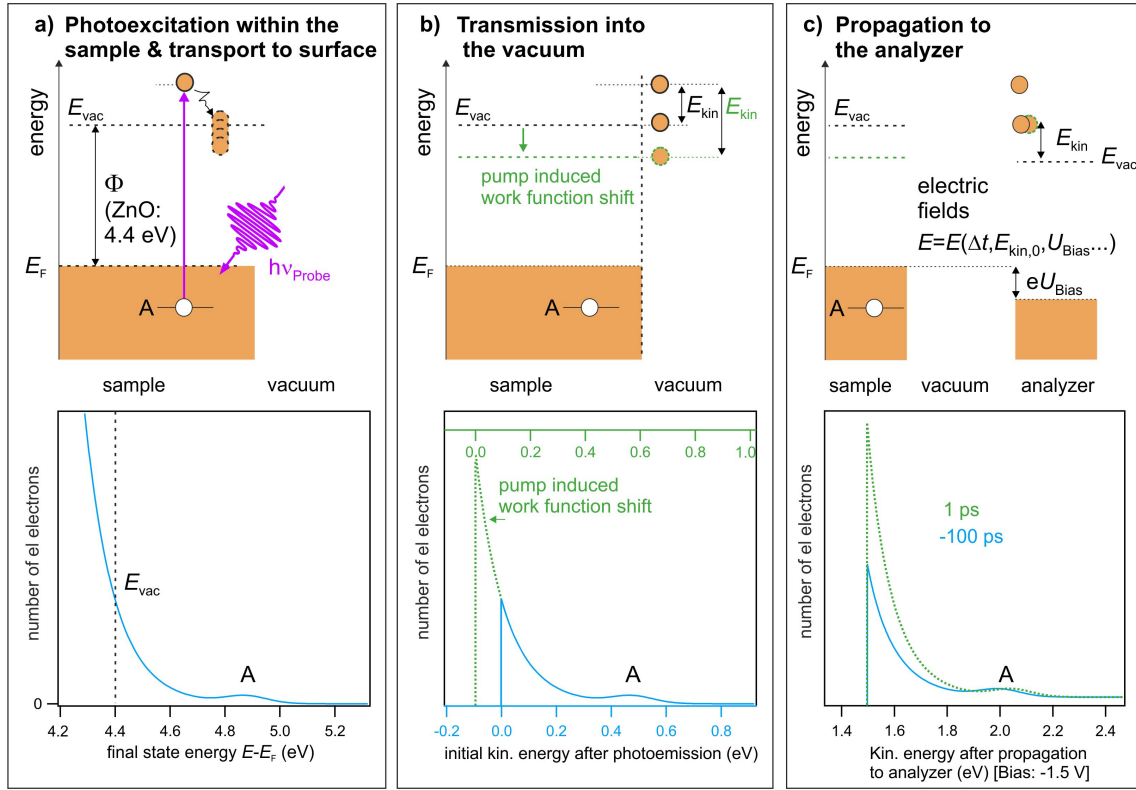


**Figure 6.27:** Simulation of the secondary edge intensity based on the three-step-model of photoemission (cf. section 3.1) *plus* an additional step that accounts for the propagation to the analyzer. The respective processes are illustrated at the top and the simulated electron distribution as a function of energy is displayed in the bottom. a) Photoexcitation of an occupied initial state A into an unoccupied final state within the bulk due to the probe pulse and accumulation of secondary electrons at low energies due to inelastic scattering. The electron distribution is most sensibly displayed versus a final state energy axis with respect to  $E_F$ . The energy of the vacuum level  $E_{vac}$  of the ZnO is indicated as reference, but does not come into play at this point. The amount of secondary electrons is assumed to increase exponentially towards lower energies. b) Upon transmission through the surface, overcoming the surface dipole leads to the low energy cutoff at  $E_{vac}$ . If the work function is reduced by photoexcitation by the pump *before* the secondary electrons are transmitted through the surface, the cut off is at a lower energy and overall more electrons are emitted. The electron distribution is displayed versus kinetic energy after photoemission  $E_{kin}^0$ . The zero point of this energy axis is at the low energy cut off, therefore two energy axis are displayed, in case the work function is modified by the pump pulse or not (top and bottom axis, respectively). c) Resulting electron distribution after propagation to the analyzer, displayed versus kinetic energy. The two spectra are electron distributions where the probe electrons are emitted before (blue line,  $\Delta t = -100$  ps) or after the pump arrives and changes the work function (green line,  $\Delta t = 1$  ps). The propagation to the analyzer is influenced by electrostatic fields such as the bias voltage as well as pump-induced fields, which depend on the pump-probe delay  $\Delta t$ , the temporal evolution of the pump-induced field  $\tau$  etc. In case of ZnO, the temporal evolution of the pump-induced field is characterized by a rise with  $\tau_1 = 20$  fs,  $\tau_2 = 1.2$  ps and a decay with  $\tau_3 = 219$  ps after photoexcitation with the pump laser pulse (see text). The effect of this field on the propagation of secondary electrons emitted by the probe laser pulse is tackled in this subsection with solving the equation of motion (equation 6.105). The result of the simulation is that, in case of ultrafast pump-induced work function changes, the measured kinetic energy of the secondary edge is the same at positive with respect to negative delays. However, the secondary edge intensity is higher, as overall more electrons are emitted from the sample and arrive at the detector.

**Measuring ultrafast work function changes by the secondary edge intensity**

The last paragraph showed that an ultrafast work function *reduction* cannot be measured by the position of the secondary electron cutoff such as done in static photoemission (cf. section 3.1.2). Here I simulate the changes to the intensity of secondary electrons induced by a pump-induced work function reduction for the present case of photoexcited ZnO. The expectations are compared to experimental observations.

To simulate the secondary edge intensity upon a pump-induced work function reduction I assume the three-step-model of photoemission (cf. section 3.1) *plus* an additional step that accounts for the propagation to the analyzer. Figure 6.27 a) top depicts the photoexcitation of an electron from an occupied initial state A into an unoccupied final state above  $E_{\text{vac}}$  within the bulk of the sample by the probe pulse. On the way to the surface a part of these primary electrons undergo inelastic scattering, creating a tail of low energy electrons. This corresponds to step 1 and 2 of the three-step-model. At the bottom the distribution of electrons as a function of final state energy above  $E_F$  is shown. Beside the peak due to the primary electrons, low energy electrons accumulate, even below  $E_{\text{vac}}$ . The number of secondary electrons is assumed to increase exponentially towards lower energies, as observed often experimentally in PE spectra (see for example the PE spectra in section 6.2.3, Figure 6.18). The transmission through the surface, corresponding to step 3 of the three-step-model, is depicted in Figure 6.27 b). Only the electrons with a final state energy above  $E_{\text{vac}}$  have sufficient energy to overcome the surface dipole and this induces a cut in the photoelectron spectrum at low energy, as shown in the bottom of Figure 6.27 b). Electrons that have just overcome the surface have now 0 eV kinetic energy  $E_{\text{kin}}^0$ . At this point, the position of the low energy cutoff depends on the pump-probe timing. If the pump arrives *before* emission of the secondary electrons and induces a work function reduction, i.e. at positive pump-probe delays, the cutoff is at a lower energy. If the pump arrives *after* the emission of secondary electrons, the pump does not affect the cutoff energy. Note that shifting the cutoff means that in total a larger amount of secondary electrons is emitted, simply because the number of secondary electrons increases exponentially towards lower energies. Finally the electrons propagate to the analyzer, see Figure 6.27 c). For both, positive and negative delays, the pump-induced work function reduction affects the propagation by the decelerating field extending into the vacuum. The field the probe electrons senses depends on the pump-probe delay  $\Delta t$ , the initial  $E_{\text{kin}}^0$ , the applied bias and the temporal evolution of the pump-induced field. For knowing the kinetic energy of the electrons at the detector, the classic equation of motion has to be solved for each electron at a given  $E_{\text{kin}}^0$ , as described in the last paragraph. This yields the spectra displayed at the bottom of Figure 6.27 c) for two pump-probe delays, +1 ps and -100 ps. For the simulation, I took into account the temporal evolution the pump-induced work function reduction (rise with  $\tau_1=20$  fs,  $\tau_2=1.2$  ps, decay with  $\tau_3=219$  ps) and omitted

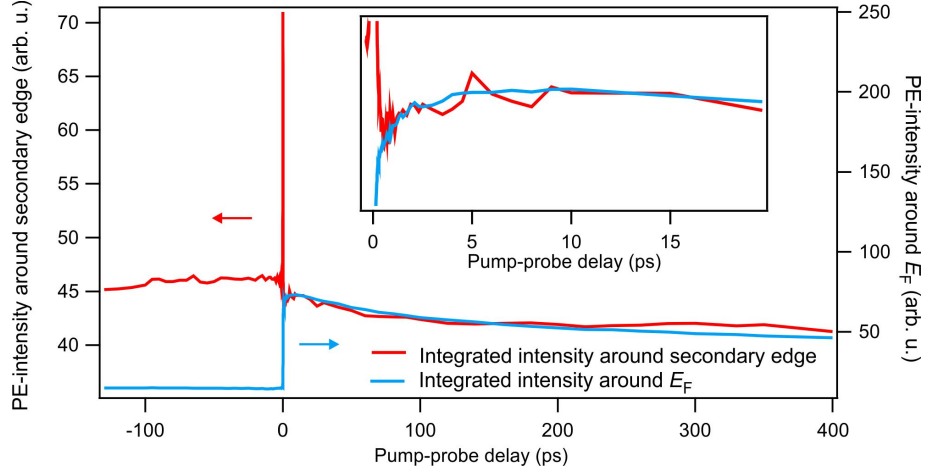


**Figure 6.28:** Measured secondary edge intensity as a function of pump-probe delay (red). Overlaid is the integrated PE intensity from  $-0.62$  to  $0.12$  eV with respect to  $E_F$ . The latter is proportional to the electron density of the surface metal phase, which has the identical temporal evolution as the (hypothesized) pump-induced work function reduction (see text).

the photostationary field. The simulated spectra are displayed as a function of the kinetic energy they have upon arriving at the analyzer. As a consequence of the propagation the low energy cutoff now lies at the very same energy, as already shown in the last paragraph. However, the number of electrons at low energies is different for negative and positive delays. **Because more electrons are emitted upon a pump-induced reduction of the work function, the intensity of the secondary edge is enhanced, albeit its position stays the same. This suggests that the intensity of the secondary edge could be used as a marker for ultrafast work function changes.**

In practice the secondary edge intensity requires a very careful analysis, since photoemitted secondary electrons caused by pump *or* probe or even a combination of them upon temporal overlap are isoenergetic. An analysis of the secondary edge intensity for the case of photoexcited ZnO is given in the following. Figure 6.28 shows the secondary edge intensity as a function of pump-probe delay with  $h\nu_{\text{Probe}}=6.3$  eV and  $h\nu_{\text{Pump}}=3.43$  eV; the pump fluence is  $50 \mu\text{J}/\text{cm}^2$ . At time zero the PE signal shows a spike that is attributed to secondary electron emission upon two-photon photoexcitation by  $h\nu_{\text{Pump}}+h\nu_{\text{Probe}}$  at temporal overlap. There are also dynamic changes at positive as well as negative delays. Notably, at positive delays, a rise of few ps can be discerned, followed by a decay of the order of few hundred ps. This is reminiscent of the dynamics of the VB downward shift and the associated surface metal phase, respectively, which evolves concomitantly; the VB downward shift is attributed to DBB due to the reduction of the surface potential, see section 6.2.3. Associated to this, there should be a modification of the work function of the sample: It should first decrease with  $\tau_1$ ,  $\tau_2$  and then increase again with  $\tau_3$ , which should

then be reflected in the secondary edge intensity according to the simulations above. For a comparison of the dynamics, the signal of the surface metal for the present pump-probe experiment is overlaid on top of the secondary edge intensity in Figure 6.28. Clearly, both traces exhibit the same evolution on the ps time scale: They have the same decay and show the same rise of few ps, see the inset in Figure 6.28. Thus, within this pump-probe delay range, the secondary edge intensity indeed evolves concomitantly to the work function modification on the ultrafast time scale. From negative to positive delays, there is a clear deviation: Overall, the intensity of secondary electron intensity is decreased at positive with respect to negative delays. If the secondary electrons would be emitted solely due to the probe, the secondary edge intensity should increase upon time zero, as the pump arrives and creates the work function decrease. I attribute this deviation to increased secondary electron emission by the pump, which is isoenergetic with the signal arising from the probe.

In summary of this subsection, by simulating electron trajectories in the time-variant field between sample and analyzer, I showed that a pump-induced ultrafast work function reduction does not lead to a shift of the secondary edge trARPES. This is in agreement with the experimental data on ZnO. Furthermore, the simulations show that a work function reduction should be reflected in an increase of the secondary edge intensity. The ZnO data shows such a variation of the secondary edge intensity for positive pump-probe delays. Further work is necessary to incorporate the effect of a pump-induced work function increase, and an evaluation of experimental data on different systems would be desirable.

### 6.2.6 Versus lab time change of the ultrafast photoresponse

In this subsection I provide further evidence that the photoexcitation of defects is at origin of the SMT. The species must be the same as the one that is at the origin of the photostationary state population. As discussed in chapter 5, section 5.5, the photostationary state population increases as a function of UV illumination time. In this subsection I show that the signal of the surface metal is enhanced likewise as a function of UV illumination time, and so does the pump-induced ultrafast DBB.

Figure 6.29 a) and b) show the evolution of the transient surface metal phase as a function of 'lab time'. Displayed is the PE-intensity versus  $k_{\parallel}$  and energy with respect to  $E_F$ , averaged over  $\Delta t=1$  ps to  $\Delta t=10$  ps. The pump is  $h\nu_{\text{Pump}}=3.43$  eV and the probe is  $h\nu_{\text{Probe}}=6.3$  eV. Since both beams are incident on the sample for recording the PE data, the 'lab time' equals the UV exposure time. At the 'start' (Figure 6.29 a)), which is an arbitrary time on the order of an hour after the preparation of the surface with sputtering and annealing, a free electron like band is observed, comparable to the data presented and analyzed in Figure 6.3. This is because the pump fluence is above  $F_C$ , in both cases

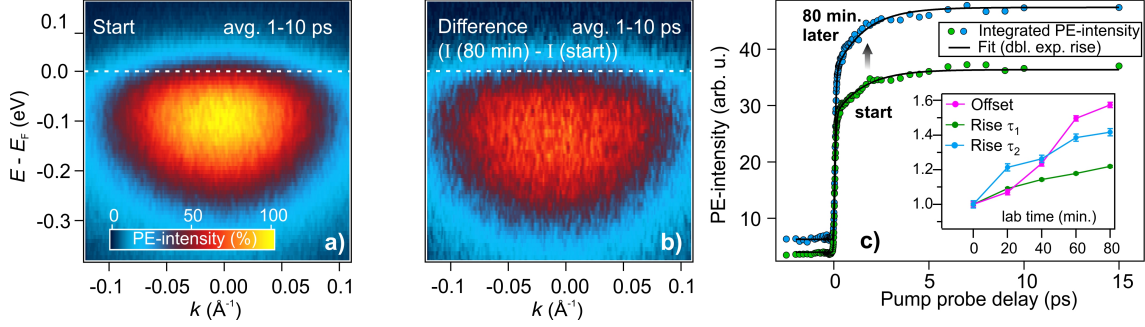
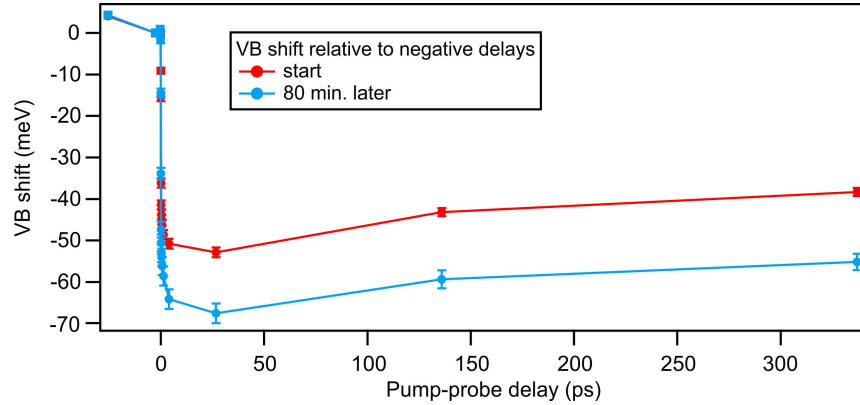


**Figure 6.29:** Changes of the transient metallic state as a function of lab time. a) Angle-resolved PE intensity averaged from 1 ps to 10 ps at an arbitrary point of lab time ('start'). The pump is 3.4 eV with a fluence of  $26 \mu\text{J}/\text{cm}^2$ , which is above the metallization threshold  $F_C$ . The probe is 6.3 eV. b) Intensity change after 80 minutes. The intensity of the metallic band below  $E_F$  increases as a function of lab time. c)

$F=26 \mu\text{J}/\text{cm}^2$ . Figure 6.29 b) displays the difference in detected PE intensity between a measurement taken at the time 'start+80 minutes later' and 'start'. Although the probe fluence stays the same, the measured intensity increases. The intensity increase occurs at the energy of the surface metal, and amounts to about 50 % of the intensity measured at the 'start'.

To exclude that this is solely an effect of the increasing photostationary background, I evaluated the temporal evolution of the PE signal from negative delays to positive delays of few ps. Figure 6.29 c) shows the PE intensity integrated from -0.62 eV to 0.12 eV with respect to  $E_F$  as a function of pump-probe delay for the two different lab times 'start' and 'start+80 minutes later'. Clearly, the signal at negative delays, which is due to the photostationary state, increases, but the signal at positive delays increases even stronger. To investigate the lab time change in more detail, both traces are fitted with a double exponential rise convoluted with the pump probe cross correlation (equation 6.100) plus a delay-independent offset that accounts for the photostationary background. The time constants of the double exponential rise are optimized globally, i.e. by fitting both traces simultaneously and the results  $\tau_1$ ,  $\tau_2$  are identical to those reported in subsection 6.1.5. The fits match the data perfectly, showing that the temporal evolution is identical for both lab times. The inset in Figure 6.29 c) shows how the amplitude of the individual contributions to the delay dependent PE intensity develop with lab time. The offset due to the photostationary state, as well as the amplitudes of both components of the double exponential rise increase monotonously with lab time. **This shows that the formation of the surface metal is associated to the same species as the photostationary state. The species can be created by UV illumination.**

The photoinduced metal phase is directly linked to DBB as shown in subsection 6.2.3. As a consistency check, I also analyzed how the latter changes as a function of lab time.



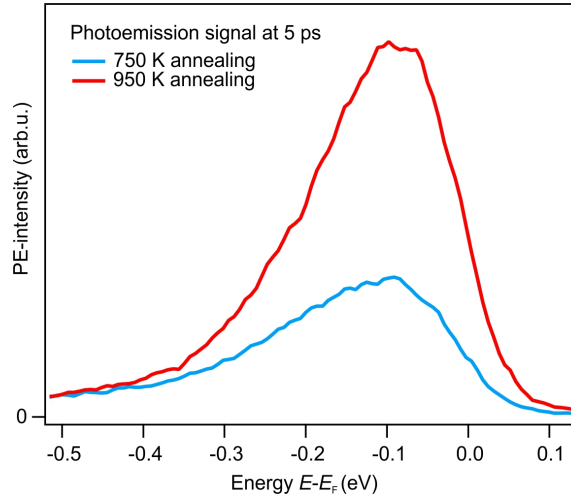
**Figure 6.30:** VB position measured as a function of pump probe delay at an arbitrary point of lab time ('start') and 80 minutes later (each measurement itself results from integrating spectra over 80 minutes). The pump photon energy is  $h\nu_{\text{Pump}}=3.4$  eV with identical power for both measurements. Shown is the shift relative to negative delays. The transient downward band bending becomes stronger as a function of lab time.

Figure 6.30 shows the VB position versus pump-probe delay at 'start' and 80 minutes later. The evaluation of the VB shift was done as described in section 6.2.3, i.e. by fitting a Gaussian peak to the secondary electron background-subtracted data. In both measurements the VB is shifted down at positive with respect to negative delays, but the downward shift is about a factor of 1.4 stronger after 80 minutes, although the same pump fluence was used ( $h\nu_{\text{Pump}}=3.4$  eV,  $27 \mu\text{J}/\text{cm}^2$ ). This once more demonstrates that DBB and the metal phase are intimately connected and can be associated with the photoexcitation of the same species as the one that is at the origin of the photostationary state.

In summary of this subsection, the electron density in the surface metal phase, as well as the transient DBB induced by photoexcitation with the pump increase as a function of lab time. This finding corroborates that the PIPT is not intrinsic to the ZnO crystal, but requires certain defects that are created upon UV illumination. The latter must be the same as those for the photostationary state, which likewise increases as a function of labtime. The most likely defects are surface oxygen vacancies as discussed in section 5.5 and 5.6 in context of the photostationary state. In the subsequent subsection I show that the corresponding defect species can be also created by high-temperature treatment of the sample surface, which likewise suggests that the defects are surface oxygen vacancies.

### 6.2.7 Influence of the annealing temperature on the photoresponse

Beside by UV illumination, deep defects at the ZnO surface could be created during the surface preparation process consisting of sputtering and annealing cycles (cf. section 3.2.6). Indeed the transient surface metal generation can be realized promptly after starting to



**Figure 6.31:** Dependence of the ultrafast photoresponse on the annealing temperature. PE-spectra recorded with  $h\nu_{\text{Probe}} = 6.3$  eV and  $h\nu_{\text{Pump}}$  (fluence  $140 \mu\text{J}/\text{cm}^2$ ) at a pump-probe delay of 5 ps using two different annealing temperatures during the sample preparation. The same fluence of pump as well as probe laser pulses is used for both shown spectra, hence the absolute PE-intensity can be compared. After annealing at 750 K (blue), the photoelectron intensity of the pump-induced metal phase is by a factor of 2-3 smaller than after annealing at 950 K (red).

measure at a spot, when no significant UV illumination-induced change of the surface has occurred. This indicates a significant contribution for the deep defects from another source.

Figure 6.31 shows two angle-integrated photoemission spectra probed with  $h\nu_{\text{Probe}} = 6.2$  eV, recorded just after the sample preparation with two different annealing temperatures and within few minutes after addressing a previously not illuminated spot<sup>46</sup>. A pump beam of the same fluence ( $h\nu_{\text{Pump}} = 3.4$  eV,  $140 \mu\text{J}/\text{cm}^2$ ) is applied in both cases, and the pump-probe delay is 5 ps. Thus, the probed photoemission signal arises from the transient surface metal phase induced by the pump laser pulse. Clearly, the photoresponse after annealing at 950 K is larger than after annealing at 750 K, by a factor of 2-3<sup>47</sup>. This shows that the ultrafast surface metal generation is driven by the photoexcitation of a species that cannot only be induced by UV illumination, but also by sputtering and subsequent annealing in UHV at elevated temperatures. There are three possible sources for this species:

- As mentioned before in section 3.2.6, during annealing at high temperatures, desorption of lattice atoms may occur, creating oxygen and zinc vacancies (above sample

<sup>46</sup>The shown spectra are averaged measurements over five different spots at the sample surface. The spots are addressed one after each other and the signal is integrated for about 5 minutes on each spot. The whole set of measurements is carried out within 1-2 hours after surface preparation using sputtering at 300 K and subsequent annealing at either 950 K or 750 K. This procedure excludes that the UV illumination-induced increase of the surface defect density and potential contamination processes that happen in the dark interfere with the here made comparison of different annealing temperatures.

<sup>47</sup>Note that an increase of the signal also occurs with the pump is switched off, because of an increase of the photostationary state population, which originates from the same defect species (not shown).

temperature of 700 K, and 900 K, respectively [Göp77, Göp80]). Annealing may also promote the formation of other defects, such as lattice interstitials. The native point defects with the lowest formation energies are the lattice vacancies, followed by the zinc interstitial (an extra zinc occupying interstices in the lattice) and the zinc antisite (a zinc atom occupying an oxygen lattice site) [Jan09].

- Annealing may lead to the diffusion of impurities from the bulk crystal to the surface. For example, calcium and magnesium segregation is reported [Die04]. Furthermore, nitrogen and hydrogen form common impurities in ZnO crystals [Jan09].
- Different annealing temperatures after sputtering could lead to a different surface roughness, leading to structural defects such as step edges and kinks.

First of all, structural defects such as step edges and kinks can be excluded: Figure 6.32 presents LEED measurements of the sample surface recorded after annealing at different temperatures. A sharper diffraction pattern is obtained after 950 K annealing than after 750 K annealing. This indicates a better ordered surface after annealing with 950 K, with lower roughness and less step edges and kinks, contrary to the experimental trend that the photoresponse is larger at higher annealing temperature.

Another option is that annealing leads to the segregation of impurities at the surface. This cannot be excluded, but it can be noted that hydrogen and nitrogen and several other impurities form shallow donor or acceptor levels [Jan09]. Subsection 6.2.3 showed that photoexcitation charges the surface positively by depleting occupied in-gap states just above the VB edge. This cannot be caused by photoexciting shallow impurities: Firstly, shallow *donors* would most likely be unoccupied due to thermal activation, cf. section 2.2.1. Even if this would not be the case, because all present measurements are carried out at cryogenic temperatures (100 K), shallow donors would form an occupied in-gap state just below the CB minimum, i.e. far away from the VB edge. Secondly, the photoexcitation of shallow acceptors can also not be at the origin of the positive surface charging. If shallow acceptors form an occupied state deep in the band gap, they would be *negatively charged* in thermodynamic equilibrium, as ZnO is an n-doped sample with the equilibrium Fermi energy 0.2 eV below the CB minimum. The photoexcitation of a negatively charged state at the surface would not lead to a *net positively charged* surface and could not lead to photoinduced DBB.

Finally, native defects could be created. Notably, among the native defects with low formation energy, the oxygen vacancy is the only deep donor. The zinc vacancy forms a deep acceptor, which is, again, negative charged in an n-doped sample [Jan09]. The oxygen vacancy, in contrast, is neutral in thermodynamic equilibrium and the deep defect level is just above the VB maximum. Oxygen vacancies are also created already upon heating the sample to 750 K as suggested by mass spectroscopy [Göp77] and the efficiency

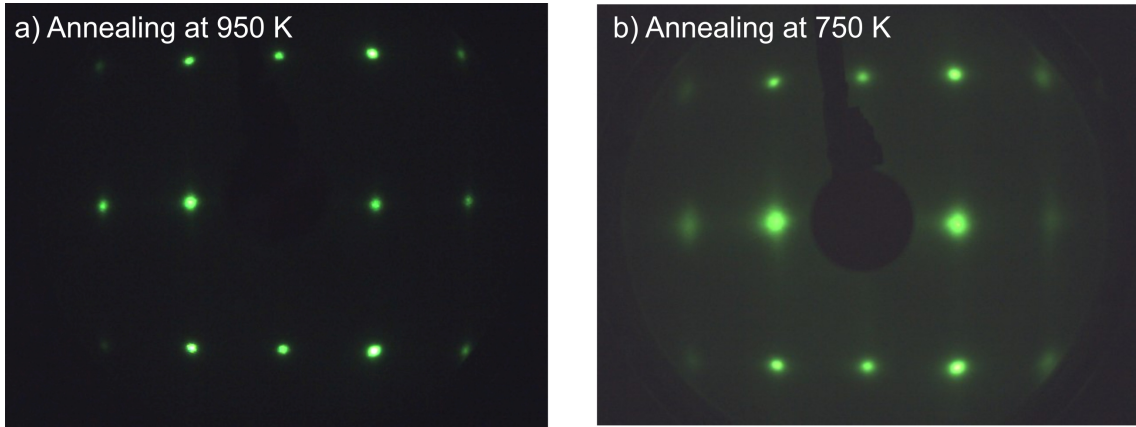


**Figure 6.32:** LEED of the ZnO(10-10) surface upon different annealing temperatures. The diffraction pattern is sharper after 950 K annealing (a)) than after 750 K annealing (b)), indicating a better ordered surface after 950 K annealing.

to create oxygen vacancies should increase upon using higher annealing temperatures, thus explaining the observed trend in the experiment.

In summary of this subsection, the transient photoresponse of the ZnO surface depends on the surface preparation process. A lower photoresponse is observed when the annealing temperature is decreased. Oxygen vacancies created during annealing explain this finding.

### 6.2.8 Summary and discussion

The preceding section 6.2 is devoted to the mechanism responsible for the SMT driven by photoexcitation resonant to the band gap. As shown in section 6.1, the metal phase rises on a femtosecond time scale and decays within few hundred picoseconds. Due to the fast rise, carrier-lattice interactions are excluded as the origin of the PIPT. Instead, it seems likely that an exciton Mott transition takes place. However, the SMT goes beyond an exciton Mott transition without changes of the equilibrium band structure as outlined in the introduction to this section: Because the quasi Fermi level of the photoinduced metallic phase *equals* the equilibrium  $E_F$ , the CB must be shifted *below*  $E_F$ . This band structure change could be either band gap renormalization (BGR) or photoinduced downward band bending upon photodoping of the ZnO surface due to the photodepletion of occupied deep defect states. In the latter case, the Mott transition would occur among defect excitons, where the hole is located at a defect site at the ZnO *surface*, and not between free excitons (cf. Figure 6.12 in section 6.2.1 for an illustration).

Here, I summarize the results of this section, which show that the SMT can be understood very well within this 'photodoping' framework. Photoexcitation efficiently excites defect excitons at the ZnO surface that behave in remarkable analogy with shallow donor dopants. Finally, I discuss the observed time constants within the framework of the

photodoping mechanism and the contribution of free and defect excitons to the ultrafast photoresponse.

A crucial experimental evidence for the photodoping scenario is the observation of the VB *downward* shift upon photoexcitation (section 6.2.3). It shows that BGR is not the dominant mechanism that changes the electronic band structure, as in that case the VB would shift *upward*. On the contrary, the downward shift is expected for the photodoping mechanism, as photoholes at photoexcited deep defects located at the ZnO surface create positive surface charging and hence downward band bending (DBB) toward the surface. The temporal evolution of the DBB exactly matches the evolution of the surface metal phase, i.e. the electron density as well as the effective mass, showing that DBB is *linked* to the SMT. Furthermore, negative delay shifts observed in trARPES (subsection 6.2.4) unambiguously show that the surface is positively charged upon photoexcitation by the pump laser pulse.

To corroborate even further that photoexcitation addresses deep defect states, several test experiments are carried out: Firstly, it is shown that the DBB is not only caused by resonant photoexcitation but also by below bandgap photoexcitation with  $h\nu_{\text{Pump}} = 3.2$  eV (subsection 6.2.3). This excludes optical transitions across the fundamental band gap of 3.4 eV as the origin of the band structure change. Note that, using  $h\nu_{\text{Pump}} = 3.0$  eV no DBB is observed anymore, i.e. this photon energy is not sufficient to depopulate the relevant defect states. This shows that the in-gap states responsible for the SMT must lie deeply in the band gap, closer than 0.4 eV above the VB maximum.

Secondly, the photoresponse is sensitive to the surface defect density, which can be engineered by UV illumination as well as high temperature treatment (subsections 6.2.6 and 6.2.7 respectively). The electron density of the photoinduced metallic band as well as the transient positive surface charging increase as a function of UV illumination time (subsection 6.2.6). UV illumination most likely causes surface photolysis and creates oxygen vacancies as discussed in section 5.5. Moreover, the surface electron density is increased by high temperature annealing that is part of the sample preparation (subsection 6.2.7). This high temperature treatment also likely creates oxygen vacancies, as discussed in section 6.2.7. Hence, the findings of subsections 6.2.6 and 6.2.7 not only corroborate that photoexcitation by the pump laser pulse addresses defect states at the ZnO surface but also show how these defect states can be created. Moreover, the experiments suggest that the defect responsible for the transient surface metal is the oxygen vacancy.<sup>48</sup>

---

<sup>48</sup>Indeed, oxygen vacancies are deep donors, lying just above the VB maximum according theory (0.4 eV above the VB maximum to hybrid DFT calculations [Pat06]) and previous experimental work, as discussed in detail in sections 5.5 and 5.6. To give a definite answer whether oxygen vacancies are the responsible deep donor-type defects, additional experiments sensitive to such vacancies (microscopy, chemical sensitive methods such as X-Ray spectroscopy) would be desirable. The present experiments do, however, specify the requirements such defects must have to be able to induce a photoinduced SMT: The defects must create a neutral, occupied state deep in the band gap. Beside the oxygen vacancy in ZnO, such requirements are

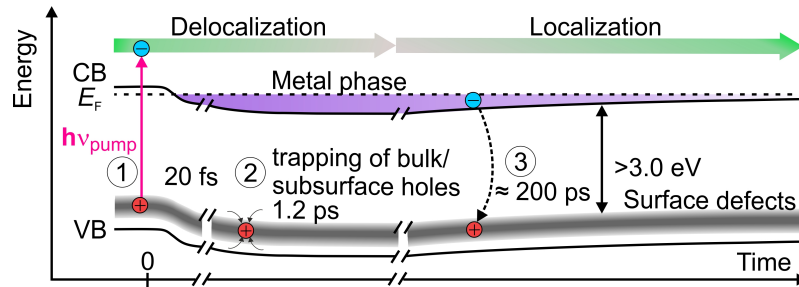


**Figure 6.33:** Overview of the observed time constants and associated processes upon resonant photoexcitation of ZnO. Photoexcitation by the pump populates the CB and depopulates surface defect states leading to DBB toward the surface; the electrons delocalize and form the metal phase (process 1). Delayed increase of the DBB occurs due to hole trapping at surface defect sites (process 2). The semiconducting state is recovered the surface charge is reduced by electron-hole recombination (process 3).

The above summarized experimental findings show that the SMT is intimately linked to photoinduced DBB, caused by photoexcitation of deep donor-type defects at the ZnO surface. This link between the formation of a metallic phase and DBB is exactly what is observed upon 2DEG formation, when oxide surfaces are doped with shallow donors (cf. section 6.2.1 and section 2.2.3). The analogy between chemical doping with shallow donors and photoexcitation of deep donors is completed by the finding that the effective mass  $m_{\text{eff}}$  of the transiently created metallic band shows diverging behaviour when lowering the photoexcitation fluence towards the localization threshold at  $F_C$  (subsection 6.2.2). Complementarily, the extrapolation to *high* fluences yields a value consistent with the CB  $m_{\text{eff}}$ . Such critical behaviour of the  $m_{\text{eff}}$  is predicted by the Mott-Hubbard theory of the doping-induced SMT and has been observed upon chemical doping in three as well as in two dimensions. Hence photoexcited deep donors indeed behave like shallow donors, and notably, do so under highly non-equilibrium conditions, i.e. in the ultrafast time domain, on a timescale of femto- to picoseconds. Based on these findings, **the photoinduced metal phase at the ZnO surface is identified as transient 2DEG, created by the photodepletion of deep defects which acts like doping the surface with shallow donors.**

In the following I discuss the time constants of the photoinduced SMT within the surface photodoping mechanism. Finally, I discuss the contribution of free and defect-bound excitons to the photoresponse.

**Time constants of rise and decay of the metal phase.** Figure 6.33 shows an overview of the temporal evolution of the metal phase and the associated DBB on the

met by e.g. the titanium vacancy in SrTiO<sub>3</sub> [Tar13] or Si dopands in GaAs [Kat87]. Similar photoinduced phase transitions could thus be reached for other systems based on this work.

ultrafast time scale. The electron density in the metallic band, the degree of delocalization ( $1/m_{\text{eff}}$ ) and the DBB evolve concomitantly, see subsection 6.2.3. The temporal evolution has been analyzed in subsection 6.1.5. It is characterized by an exponential rise with two components  $\tau_1 = 20$  fs and  $\tau_2 = 1.2$  ps and a single exponential decay of few hundred picoseconds. While the time constants  $\tau_1$  and  $\tau_2$  are independent of the pump laser fluence, the amplitude of the first component increases linearly with pump laser fluence and the amplitude of the second component exhibits a kink at  $F_C$ . The decay is more pronounced and slightly accelerated upon increasing the pump laser fluence (clearly discernable only above  $F_C$ ). For all pump laser fluences, a part of the population survives the accessed time window and eventually funnels into the photostationary state.<sup>49</sup> Within the surface photodoping mechanism the temporal evolution can be explained by three different processes:

**The first process** ( $\tau_1$ ) is the immediate reaction of the electronic system to the photoexcitation that occurs on a time scale of electronic screening: The pump laser pulse depopulates deep donor defects at the surface and populates the CB with electrons. Subsequently DBB toward the surface builds up, shifting the CB below  $E_F$ . In the regime of low fluence photoexcitation by the pump laser pulse, defect excitons are formed as the electrons are localized to the photodepleted defects. The electrons form isolated electron pockets at the surface, as is known from ZnO doped with H, see ref. [Dei15] and section 2.2.3. The DBB is, in this fluence regime, a *local* effect, concentrated around the ionized deep defect sites. Above  $F_C$  the electrons delocalize as they undergo a Mott transition. The surface electron density created within this process increases linearly as a sufficient amount of deep defects is present that can be depopulated.

**The second process** ( $\tau_2$ ) occurs long after ( $>1$  ps) the abrupt laser excitation and is attributed to trapping of bulk or sub-surface photoholes at the surface. As illustrated in Figure 6.34 the pump laser pulse not only photoexcites defects at the surface, but also in the subsurface or bulk. The so-created photoholes are trapped at surface defect sites. Consequently, the DBB increases and more electrons can be accommodated in the 2DEG. Concomitant with electron density increase, the degree of electron delocalization increases (decreasing  $m_{\text{eff}}$ ). The kink of the amplitude of the second process indicates that the hole trapping process is sensitive to the character of the surface electrons, i.e. whether they are delocalized or not. Possibly, it is the screening due to quasi-free electrons at the surface that affects the trapping efficiency of bulk or subsurface holes at remaining *unexcited* surface defects. As the most likely candidate for the surface defects, the oxygen vacancy has long been said to be a very efficient hole trap [Zha01]. A resolution-limited upper boundary of 80 ps for hole trapping at the ZnO surface was recently identified by X-

---

<sup>49</sup>The proof that a part of the pump-induced defect excitons survive the inverse laser repetition rate and form a photostationary state is given in section 5.8.

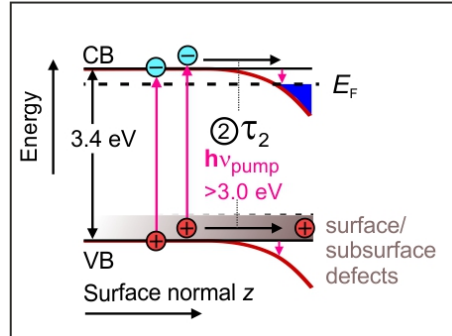


**Figure 6.34:** The origin of process 2: Hole trapping at surface defect sites. Photoexcitation by the pump does not only excite surface defects but also creates holes in the bulk and subsurface due to the depopulation of defects and the VB.  $\tau_2$  is attributed to the trapping of holes at surface defect sites leading to an increase of the photodoping density at the surface long after the abrupt laser excitation.

ray absorption spectroscopy [Pen18] and few-ps time constants were determined by optical spectroscopy [Fog19].

**The third process** is attributed to the recombination of CB electrons with the photoholes at the surface defect sites. As the doping density is reduced, the DBB relaxes and the electrons localize (increasing  $m_{\text{eff}}$ ). The process is more efficient at elevated fluences (hence the decay is more pronounced and slightly accelerated). This is most likely because a larger number photogenerated electrons and holes increases the rate of pairwise recombination, because the (delocalized) electrons in the CB have a higher probability to encounter a hole at a defect. A part of the defect excitons remain and survive up to  $\mu\text{s}$ , eventually forming the photostationary state. The assignment of the third process to defect exciton recombination is consistent with literature, as a multi-step recombination of defect excitons with lifetimes of hundreds of ps up to  $\mu\text{s}$  is also found by photoluminescence studies on ZnO [Fog19].

Thus, all time constants can be explained within the surface photodoping framework. The number of photoexcited deep defects at the ZnO surface is increased (decreased) thereby increasing (decreasing) the number of states that behave like shallow donor dopants. This determines the surface band bending as well as the character of the surface electrons, i.e. whether they are delocalized or localized. It is noteworthy that the trapping of bulk or subsurface photoholes at the surface (process 2) and the inherent increase of surface electron density leads to an *overall increase* of the photoelectron intensity (cf. Figure 6.16 in subsection 6.2.3). This is explained as electrons move into the region that is most efficiently probed, namely the surface of the sample (as photoelectron spectroscopy is a surface sensitive technique). This, once again, demonstrates the surface character of the metallic phase.

Finally, the question remains if the photoresponse is *exclusively* due to the photoex-

citation of deep defects. The SMT was demonstrated using photoexcitation resonant to the band gap (section 6.1). Thus, both defect excitons and free excitons should be formed below the Mott density and the electrons arising from photoexcitation across the band gap may contribute to the electron-hole plasma that is created above  $F_C$ .

In this context it is interesting to note that the amount of newly photoexcited defects by the pump pulse is approximately doubled with respect to the photostationary state at the strongest pump fluence  $F=96\mu\text{J}/\text{cm}^2$ . This finding is based on the mapping the dipolar field due to the newly photoexcited defects by its effect on the probe electron propagation in subsection 6.2.4. Because the photostationary state can be regarded as a mildly varying background as a function of pump-probe delay, one can also say that the amount of photoexcited defects is doubled at positive with respect to negative delays. The electron signal integrated around  $E_F$ , which rises by a factor of ca. 7 with respect to negative delays (cf. Figure 6.14), can therefore not solely arise from the photoexcitation of deep defect levels at the ZnO surface, but must be of different origin. Most likely, part of the transient electron population originates from resonant photoexcitation of the VB, filling the downward bent CB up to  $E_F$ . In contrast to the photoexcitation of deep defects, this does not imply a surface dipole change. Since the quasi- $E_F$  of the transient metal phase equals the equilibrium  $E_F$  for all photoexcitation fluences, cf. Figure 6.5, an electron flow must take place that equilibrates the electron reservoirs at the surface and in the rest (bulk) of the n-doped sample.

This consideration suggests that the effect of the photodoping is mainly to induce DBB toward the surface, bending the CB below the Fermi level  $E_F$ , in analogy to chemical doping of transition metal oxide surfaces with shallow donor dopants. At first, the CB bends below  $E_F$  only locally leading to the formation of isolated electron pockets, such as upon surface doping with H [Dei15]. Above a critical electron density, delocalization occurs generating the metallic band at the surface, which is filled up to  $E_F$ . The critical electron density can be estimated from the comparison with the H-induced 2DEG in section 6.1.7. From this comparison, the electron density in the surface metal is  $n = 1 \times 10^{13} \text{ cm}^{-2}$  at a pump fluence of  $F=96 \mu\text{J}/\text{cm}^2$ . Extrapolated to the threshold fluence  $F_C=13.6 \mu\text{J}/\text{cm}^2$  the electron density at the delocalization threshold is ca.  $n = 1 \times 10^{12} \text{ cm}^{-2}$ . This is indeed in the range at which SMTs in two dimensions occur [Kra04]: In 2DEGs induced by band bending via electrical fields a critical electron density of  $1.6 \times 10^{12} \text{ cm}^{-2}$  was reported for Si surfaces with relatively strong disorder. This agrees well with the estimation for the transient 2DEG at photoexcited ZnO.<sup>50</sup>

Summing up, the photoinduced SMT in ZnO is a transient 2DEG, created by photoexcitation of deep donor-type defects at the surface, most likely oxygen vacancies. These

---

<sup>50</sup>As ZnO and Si have similar Bohr radii [Ell16, Cox87], the SMT in the two systems should take place at approximately the same electron density according to the Mott criterion (equation 2.11 in section 2.3.4).

photoexcited defects behave like shallow donors in the ultrafast time domain. As upon chemical doping of oxide surfaces with shallow donors, they lead to downward surface band bending. Above a threshold electron density, a Mott transition occurs and a transient metallic band filled up to the equilibrium Fermi level is formed.

### 6.3 Final summary

Sufficiently strong photoexcitation resonant to the band gap causes a SMT at the surface of ZnO(10-10). Compared to SMTs in other inorganic compounds, it can be induced with an extraordinarily low threshold fluence. The metallic phase is generated and decays on the ultrafast time scale. The mechanism is simple and universal: Photodoping due to excitation of deep defects causes DBB toward the surface, bending the CB below the Fermi level  $E_F$ , in analogy to chemical doping of transition metal oxide surfaces with shallow donor dopants. Electron delocalization occurs above a critical electron density only. Notably, the exploration of the photodoping on the ultrafast time scale unveiled the continuous transition from localized to delocalized electrons and the back-transition as a function of the electron density in the ultrafast time domain (subsection 6.1.4). The electron delocalization, measured by the curvature of the metallic band, follows the critical form expected from the theory of Mott-Anderson transitions (subsection 6.2.2). For this PIPT no other effects are needed than photoinduced band bending induced by the photoexcitation of deep donor defects. As such defects can be found in many semiconductors, the demonstrated mechanism is a general pathway for controlling metallicity confined to semiconductor interfaces on ultrafast timescales.

## 7 Summary and conclusions

This thesis focuses on the response of vacuum-annealed ZnO(10-10) to ultrafast photoexcitation resonant to and slightly below the fundamental band gap. Using trARPES it is shown that the photoresponse is governed by the photoexcitation of deep donor-type defect states localized at the ZnO surface, most likely oxygen vacancies. This 'photodoping' has the same effect as doping of oxide surfaces with shallow donors: It induces severe changes to the surface electronic band structure, causing downward surface band bending of CB and VB, respectively, as well as a reduction of the work function. In the regime of low fluence photoexcitation and at low density of deep donor-type defect states, spatially isolated electron pockets at the ZnO surface are formed. An electron bound to a charged defect is part of a defect exciton, a 'photodopant'. Above a certain density of photodopants, a Mott transition occurs and the surface becomes metallic: Photoexcitation drives a semiconductor-to-metal transition (SMT), analogous to 2DEG formation induced by chemical doping with shallow donors at oxide surfaces.

The photoinduced SMT is revealed on two largely different time scales: On femto- to picosecond time scales, photodoping causes an *ultrafast* SMT. The transient phase shows all defining properties of a metal: Density of states around the equilibrium Fermi energy  $E_F$  resulting from a partially filled dispersive band and an electron distribution following Fermi-Dirac statistics. Because the quasi-Fermi level of the transient metal equals the equilibrium Fermi level, this effect could be exploited for novel devices, e.g. to drive currents in the ultrafast time domain as outlined in the introduction. This is in particular so as the required photon flux for the SMT is extraordinarily low compared to hitherto known photoinduced SMTs that occur in the bulk of inorganic semiconductors.

Complementary to the ultrafast generation and decay of a surface metal described above, a part of the photoexcited deep defects has a lifetime that exceeds the inverse laser repetition rate and leads to the buildup of a photostationary state. This results in *metastable* photodoping of the ZnO surface on time scales compatible with the those of persistent photoconductivity (PPC) in ZnO, i.e. microseconds to minutes/hours. For low defect densities, the photodoping concentration is below the Mott density rendering the ZnO surface photostationarily n-type doped. For large defect densities, which are reached by sustained UV illumination, a photostationary SMT results. The long-lived fraction of the defect excitons forms an important modification to the surface electronic structure under realistic application conditions. Devices based on ZnO, which are exposed to UV light are intrinsically n-doped by photoexcitation, leading to PPC. For lifetime determination of the photostationary population and to understand ultrafast pump-probe measurements carried out on a sample that is in a photostationary state, a new mathematical model is developed. In the framework of these two main effects, the photodoping-induced metal-

---

lization at ultrafast and metastable time scales, many exciting and interesting results were obtained. The results are summarized step-by-step below.

**Model for photostationary populations** The model takes into account the full 'history' of the sample, which is originally in equilibrium and then exposed to repetitive laser excitation. Assuming that every laser pulse can populate as well as depopulate the long-lived state, a rapid saturation of the photostationary state population is reached. With this, the photostationary state population can be calculated and evaluated with respect to changing the laser repetition rate and fluence. By tuning the repetition rate, the model allows to extract lifetimes on the order of the time between two subsequent laser pulses (microseconds for the laser used in this work), hence going well beyond the temporal range commonly accessed by today's pump-probe spectroscopy.

At a sufficient strength of the repetitive excitation, i.e. laser fluence, the photostationary state is established within few excitation events. This has consequences for pump-probe scans, where data points at individual pump-probe delays are averaged over several (in the present experiments many thousand) excitation events. At each pump-probe delay a different photostationary population is reached. It is shown for the example of ZnO that unexpected delay-dependent spectral changes in pump-probe scans result, in which the ultrafast formation dynamics of the photostationary population is encoded.

**Metastable photodoping of the ZnO surface** Static and time-resolved ARPES data recorded upon a systematic variation of the laser repetition rate, laser fluence, photon energy and defect density unveiled a photostationary defect exciton population at the ZnO surface. The defect excitons consist of an electron bound to a charged deep donor-type defect, most likely an oxygen vacancy. The defect excitons are evidently confined to the surface, as they modify the surface potential, causing a photoinduced work function reduction. The spectroscopic signatures due to the photostationary defect exciton population are identical to those observed after surface doping with hydrogen, which leads to n-type doping of the surface. With the help of the model for photostationary states, the defect exciton lifetime is determined. The photostationary defect exciton population decays partially within tens of microseconds, but a longer-lived component with a lifetime exceeding the microsecond regime is also deduced from the data. Such long lifetimes are concomitant with the observation of PPC at ZnO surfaces [Col58, Hei55, Bao11]. Moreover, the threshold photon energy needed to excite the defect excitons is the same as the one that is needed to induce PPC.

This work shows, in agreement with previous theoretical studies, that this well-known effect is the result of *two* effects of the UV light at the ZnO surface: Firstly, UV light creates deep donor-type surface defects, most likely oxygen vacancies via photolysis. Secondly,

UV light excites these vacancies to form defect excitons that behave like shallow donor dopands.

**Photostationary metallization of the ZnO surface** The electrons that form part of the photostationary defect excitons are localized at low densities of deep donor-type defect states at the surface. This holds true for all photoexcitation fluences used within this thesis. With the help of the model for photostationary populations, it is shown that this results from a balance between population and depopulation with repetitive laser pulses. However, for sufficiently high densities of deep donor-type defect states at the surface, a dispersive metallic band is observed, indicating that a photoinduced *photostationary* SMT occurs.

**Ultrafast generation and decay of a surface metal** For low defect densities, where the surface is photostationarily n-doped but below the Mott density, a *reversible* ultrafast SMT occurs. The SMT is driven within 20 femtoseconds by increasing the density of defect excitons above the Mott limit. The semiconducting state is resumed as a substantial part of the photoexcited electrons recombine with the photoholes at the deep defects within few hundred picoseconds. Only a part of the photodopants survives longer than the inverse repetition rate and lead to metastable photodoping of the ZnO surface as described above.

The photodoping mechanism leading to the ultrafast SMT is evidenced by a multitude of experimental findings: Firstly, as upon chemical doping of oxide surfaces with shallow donors, photoexcitation creates downward band bending (DBB) toward the surface, resulting from positive surface charging upon photodepletion of deep defects at the ZnO surface. The photoinduced DBB is monitored by the downward shift of the VB, which evolves in exact temporal correlation with the rise and decay of the metal phase in the ultrafast time domain. Positive surface charging as the origin of this band structure change is unambiguously confirmed by the observation of characteristic shifts of the probe electron spectra at negative pump-probe delays. These shifts are caused by the short-ranged field extending into the vacuum created upon positive surface charging with the pump laser pulse, as is well known from previous trARPES studies.

Secondly, several test experiments show that photoexcitation must address deep defect states: DBB is induced by photoexcitation below the fundamental band gap of 3.4 eV. The effect is observed with  $h\nu=3.2$  eV but not with even lower photon energies. This shows that in-gap states just above the VB maximum are responsible for the SMT. Furthermore, it is demonstrated that the corresponding defect species can be created by UV illumination as well as by high-temperature annealing in ultrahigh vacuum. As for the photostationary photodopants, the most likely deep defect is the oxygen vacancy.

Thirdly and finally, the analogy between photoexcitation and chemical doping is com-

---

plemented by the finding that the effective mass of the transient metallic band diverges upon approaching the excitonic phase, as the electrons localize at the charged defects. The observed critical behaviour is predicted by the Mott-Hubbard model for the doping-induced Mott SMT and observed for chemical doping in three as well as in two dimensions. As an order parameter for the phase transition, the effective mass is used to characterize the ultrafast rise and decay of the metallic phase. With this, for the first time, the delocalization upon 2DEG formation and localization upon the 2DEG decay is monitored in the time domain at an oxide surface.

Alltogether, these findings demonstrate that the photoexcitation of deep defects lies at the origin of the SMT and that this has the same effect as chemical doping with shallow donors. While shallow donors are *ionized spontaneously*, forming a thermally activated defect exciton, deep donors require *photoionization*. This way, the number of states that behave like shallow donors is controlled deliberately on a timescale of femto- to picoseconds, leading to 'ultrafast photodoping' of the ZnO surface.

Notably, compared to hitherto known ultrafast SMTs in other inorganic materials, the here demonstrated SMT has extraordinary properties. Firstly, an extremely low threshold fluence is required to drive the SMT: It amounts to only few  $\mu\text{J}/\text{cm}^2$ , while typically, laser fluences on the order of  $\text{mJ}/\text{cm}^2$  are necessary to drive photoinduced SMTs. The reason for this is, on the one hand, the large photoinduced band structure change resulting from positive surface charging: Photoinduced DBB exceeds band gap renormalization in ZnO by far. On the other hand, the lateral delocalization of the surface electrons (the Mott transition) occurs at low photodoping densities. The sum of both effects leads to a transient metal, i.e. a photoinduced metallic phase below the equilibrium Fermi level at comparably low laser fluence.

Secondly it is remarkably that the back-transition to the semiconducting state occurs on a sub-nanosecond time scale. This is at least one order of magnitude faster than the decay of the famous photoinduced SMT in  $\text{VO}_2$  [Wen13]. The reason is that, in ZnO, purely electronic transitions are responsible for the decay of the metal phase, while in the example of  $\text{VO}_2$ , the metallic phase is stabilized thermally, and the back-transition speed is limited by thermal diffusion processes of nanosecond duration. A thermal stabilization of the metallic phase in ZnO cannot occur, because there is no metallic phase in the equilibrium phase diagram as a function of temperature [Lie11].

Thirdly, this is the first demonstration of a surface-confined photoinduced SMT. The surface confinement results from the photoexcitation of deep defects *localized at the ZnO surface*, created by UV illumination and high temperature annealing. It is confirmed by the photoinduced surface potential changes and the observation that the SMT cannot be driven when the surface is terminated with hydrogen.

Low threshold fluence and fast back-transition are favourable for device applications.

Such applications would also benefit from the material properties of ZnO, such as transparency to visible light and ease of nanostructuring. Besides technological implementations of this low-fluence SMT, future work may explore the low-dimensionality effects beyond metallicity that are known to occur in 2DEGs at oxide surfaces.

### **Measuring photoinduced work function reductions with (time-resolved) ARPES**

The pump pulse changes the surface potential on the ultrafast time scale, leading to photoinduced downward band bending. An associated photoinduced work function reduction is expected, leading to a downward shift of the secondary edge in ARPES spectra. In the present thesis I show that such a downward shift can only be observed if the pump-induced surface potential change is sufficiently long-lived, such as is the case of the photostationary defect exciton population. There, the magnitude of the photoinduced work function shift measured with inspecting the secondary edge in ARPES data depends strongly on the electronic potential between sample and analyzer. As a function of pump-probe delay in the ultrafast time domain, a shift of the secondary edge position due to a pump-induced work function reduction does not occur as shown by numerical modeling and an evaluation of the trARPES data on ZnO data. This is simply because secondary electrons are too slow. However, the model suggests that a work function reduction leads to an increase of the intensity of the secondary edge, which may still allow the detection of ultrafast work function changes.<sup>51</sup> Note that such work function changes are not unique to the present system, but, in contrary, are expected to occur quite often, as transient band bending due to surface photovoltage phenomena are common to semiconductor surfaces.

In summary, the present work shows that a photoinduced Mott transition can be driven in ZnO. The Mott transition occurs between surface-confined defect excitons that behave like shallow donors. As a result a transient surface metal arises and decays in the ultrafast time domain. Partially, defect excitons exhibit lifetimes that are compatible with PPC in ZnO, thus giving a microscopic explanation of this phenomenon. A model for tackling photostationary state populations in pump-probe spectroscopy and concepts of analyzing photoinduced work function changes with trARPES are developed.

**Outlook** Ultrafast and long-lived surface charges at the ZnO surface are likely relevant in the context of photochemistry. Future experiments could test if, e.g., water splitting at the ZnO surface can be driven. The presence of oxygen vacancies was shown to be favourable for this photochemical reaction [Lee16].

Beyond ZnO, a sufficiently large number of deep donor-type defects should enable ultrafast photoinduced surface metallicity and related effects at the surfaces of many semi-

---

<sup>51</sup>It should be noted that the present calculations and measurements are exclusively done for photoinduced work function *reductions*. A photoinduced work function increase might lead to different effects.

---

conductors. The generality of the ultrafast photodoping mechanism could be tested for other oxide surfaces, e.g. for  $\text{SrTiO}_3$ , which also exhibits PPC [Tar13].

It would be interesting to see how the optical response changes above the SMT threshold. Optical experiments on ZnO have been mostly carried after exposure to air, which saturates the surface with adsorbants such as oxygen, water and hydrogen. Experiments under UHV conditions or using protective adlayers are highly desirable and may eventually lead to an application of the effect in photonic devices [Ryc13]. A challenge for such experiments is that they are not inherently surface-sensitive, unlike to photoelectron spectroscopy. Thus the signal of the surface metal has to be separated from any potential bulk signal.

The SMTs here presented photoinduced are confined to the surface. Just like static 2DEGs, the transient surface metal may exhibit intriguing properties beyond metallicity, such as superconductivity or surface magnetism that are driven by their low-dimensionality. To explore how the system properties change beyond the metallization of the electronic system, additional experiments are necessary, e.g. using spin-resolved trARPES, ultrafast transport measurements and ultrafast magneto-optical spectroscopy. The present study is just the starting point for future work in this direction.

## 7 Summary and conclusions

---

---

## Appendix: Sample holder and sample mount

The custom-built sample holder, as used and described before in refs [Weg14a, Hag09], is depicted in Figure 7.1 a). It consists of a part that is attached permanently to the manipulator cryostat (*Cryovac GmbH*) in the UHV system and a detachable sample 'ship', which can be removed to transfer the sample in and out the UHV environment. The part of the sample holder that stays permanently in the UHV system consists of a copper (Cu) rod and two gold-plated Cu parts that are isolated with Sapphire plates against the central Cu rod. These parts are connected via electrical feedthroughs to a power supply for resistive heating (not shown). The current is then passed through the Ta wires of the sample ship to heat the sample.

The sample ship is separately depicted in Figure 7.1 b). It consists of two halves separated with a sapphire plate against each other for the resistive heating and has a TC pin which is connected to the female part in the sample holder upon sliding the sample ship in. The TC wires are connected to the sample mount as described below in order to measure the sample temperature. From the sample holder the TC reaches via another electrical feedthrough the temperature PID controller (*Lake Shore Cryotronics, Inc.*), which is then used to monitor and control the sample temperature via the resistive heating.

A photograph of the ZnO sample mounted in the sample ship is shown in Figure 7.2. Two different designs are displayed. In the design shown in Figure 7.2 a) a Mo frame is used which enables to fix the sample via a Ta mask that is screwed down at the top and bottom of the Mo frame. In the alternative design displayed in Figure 7.2 b) and c) a single Ta sheet is bent such that the sample is held in place. Heating works in both cases via the Ta wires. In the first design, the Ta wires are spot-welded to a Ta sheet of the size of the ZnO sample, pressed tightly against its back (backside not shown in Figure 7.2 a)). In the second design the wires are directly spot-welded to the back of the Ta pocket. To measure the sample temperature a TC is placed at the sample mount. In the first design it is clamped beneath the Ta mask to the sample surface. In the second it is spot-welded to the back of the Ta pocket, as shown in Figure 7.1 c). Both designs work well to control the temperature of the sample. The first design has the advantage that the mount can be reused, e.g. after removing the sample for characterization *ex situ*. In contrast the design consisting of a single Ta sheet does not endure taking the sample in and out, as the sheet gets irreversibly bent. However, the Mo frame imposes a challenge for the cooling of the sample due to the additional thermal mass: In order to efficiently cool the sample, the sample holder must have good thermal contact to the cryostat. In practice the contact often loses over time upon repeated heating/cooling cycles and has to be renewed accordingly. This problem does not arise upon using the second design.

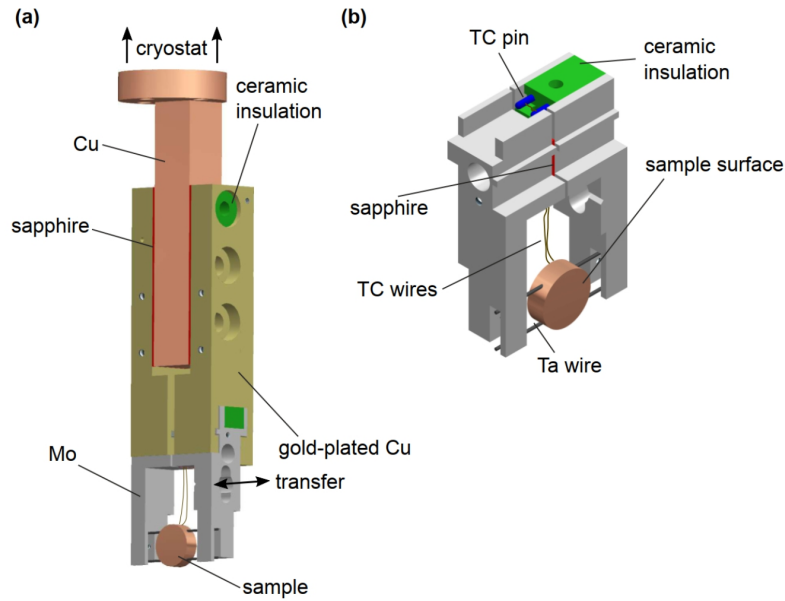


**Figure 7.1:** Sample holder, drawing from ref. [Weg14a]. a) Part of the sample holder permanently attached to the manipulator cryostat in the UHV system and removable sample ship. The sample is mounted with two Ta wires in the sample ship. b) The sample ship consists of two halves that are electrically insulated against each other for the resistive heating via the Ta wires and is equipped with a TC pin. The TC wires are fixed to the sample to measure the sample temperature.

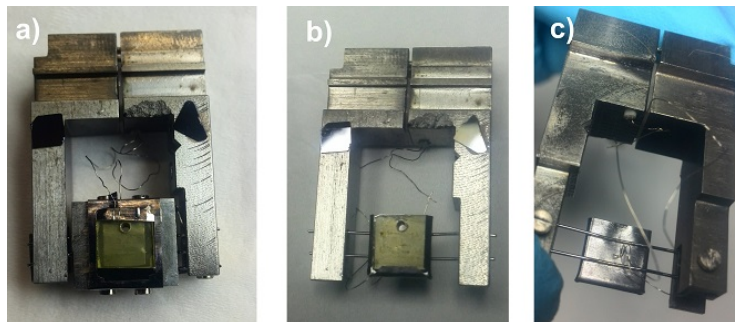


**Figure 7.2:** Photograph of the ZnO sample mounted in the sample ship. Two different designs are shown. a) A Mo frame allows to use screws at the top and bottom of the frame that fix a Ta mask to hold the sample in place. b) and c) Ta envelope design. The mount consists of a single folded Ta sheet. b) Front side and c) back side, showing the position of the TC. The hole in the ZnO sample has historic reasons resulting from a different approach of fixing the TC.

---

## References

- [And05] I. Andrianov, T. Klamroth, P. Saalfrank, U. Bovensiepen, C. Gahl, & M. Wolf. *Quantum theoretical study of electron solvation dynamics in ice layers on a Cu(111) surface*. Journal of Chemical Physics **122**, 234710 (2005). 106, 107
- [Bao11] J. Bao, I. Shalish, Z. Su, R. Gurwitz, F. Capasso, X. Wang, & Z. Ren. *Photoinduced oxygen release and persistent photoconductivity in ZnO nanowires*. Nanoscale Research Letters **6**, 404 (2011). 25, 26, 98, 109, 195
- [Bas11] D. N. Basov, R. D. Averitt, D. Van Der Marel, M. Dressel, & K. Haule. *Electrodynamics of correlated electron materials*. Reviews of Modern Physics **83**, 471-541 (2011). 35, 36, 139
- [Bog15] L. Bogner. *Ultrafast Relaxation Dynamics after Optical Excitation of Hybrid Inorganic/Organic Systems*. Dissertation, Freie Universität Berlin (2015). 47, 59
- [Bov03] U. Bovensiepen, C. Gahl, & M. Wolf. *Solvation Dynamics and Evolution of the Spatial Extent of Photoinjected Electrons in D<sub>2</sub>O/Cu(111)*. Journal of Physical Chemistry B **107**, 8706 (2003). 46, 106, 107, 154
- [Bov09] U. Bovensiepen, C. Gahl, J. Stähler, M. Bockstedte, M. Meyer, F. Baletto, S. Scandolo, X. Y. Zhu, A. Rubio, & M. Wolf. *A dynamic landscape from femtoseconds to minutes for excess electrons at ice - metal interfaces*. Journal of Physical Chemistry C **113**, 979-988 (2009). 66
- [Bri70] W. F. Brinkman & T. M. Rice. *Application of Gutzwiller's variational method to the metal-insulator transition*. Physical Review B **2**, 10 (1970). 16
- [Cah03] D. Cahen & A. Kahn. *Electron energetics at surfaces and interfaces: Concepts and experiments*. Advanced Materials **15**, 4, (2003) 271. 42, 43
- [Cas03] A. Casey, H. Patel, J. Nyéki, B. P. Cowan, & J. Saunders. *Evidence for a Mott-Hubbard Transition in a Two-Dimensional <sup>3</sup>He Fluid Monolayer*. Physical Review Letters **90**, 11 (2003). 19, 151, 152, 155
- [Cha] N. A. Charipar, H. Kim, S. A. Mathews, & A. Piqué. *Broadband terahertz generation using the semiconductor-metal transition in VO<sub>2</sub>*. AIP Advances **6**, 015113 (2016). 4, 128
- [Che15] A. Chernikov, C. Ruppert, H. M. Hill, A. F. Rigosi, & T. F. Heinz. *Population inversion and giant bandgap renormalization in atomically thin WS<sub>2</sub> layers*. Nature Photonics **9**, 466-471 (2015). 31

## References

---

- [Chr19] D. Christiansen, M. Selig, E. Malic, R. Ernstorfer, & A. Knorr. *Theory of exciton dynamics in time-resolved ARPES: Intra- and intervalley scattering in two-dimensional semiconductors*. Physical Review B **100**, 205401 (2019). 108
- [Chu99] E. V. Chulkov, V. M. Silkin, & P. M. Echenique. *Image potential states on metal surfaces: Binding energies and wave functions*. Surface Science **437**, 330–352 (1999). 41
- [Col58] R. J. Collins & D. G. Thomas. *Photoconduction and surface effects with zinc oxide crystals*. Physical Review **112**, 2 (1958). 25, 98, 109, 111, 113, 127, 195
- [Cor18] C. Corder, P. Zhao, X. Li, M. Kershis, M. White, & T. Allison. *Development of a tunable high repetition rate XUV source for time-resolved photoemission studies of ultrafast dynamics at surfaces*. Bd. 10015. **2018** . 65
- [Cox87] P. A. Cox. *The electronic structure and chemistry of solids*. Clarendon Press, 1st edition, (1987). 1, 12, 14, 15, 21, 192
- [Cui14] X. Cui, C. Wang, A. Argondizzo, S. Garrett-Roe, B. Gumhalter, & H. Petek. *Transient excitons at metal surfaces*. Nature Physics **10**, 505–509 (2014). 108, 144
- [Dam04] Andrea Damascelli. *Probing the Electronic Structure of Complex Systems by ARPES*. Physica Scripta **T109**, 61-74 (2004). 38, 39, 40
- [De 13] S. De Jong, R. Kukreja, C. Trabant, N. Pontius, C. F. Chang, T. Kachel, M. Beye, F. Sorgenfrei, C. H. Back, B. Bräuer, W. F. Schlotter, J. J. Turner, O. Krupin, M. Doehler, D. Zhu, M. A. Hossain, A. O. Scherz, D. Fausti, F. Novelli, M. Esposito, W. S. Lee, Y. D. Chuang, D. H. Lu, R. G. Moore, M. Yi, M. Trigo, P. Kirchmann, L. Pathey, M. S. Golden, M. Buchholz, P. Metcalf, F. Parmigiani, W. Wurth, A. Föhlisch, C. Schüßler-Langeheine, & H. A. Dürr. *Speed limit of the insulator-metal transition in magnetite*. Nature Materials **12**, 882–886 (2013). 128, 139
- [Dei11] J.-C. Deinert. *Zeit- und winkelaufgelöste Zweiphotonen-Photoemissionsspektroskopie: Aufbau und Charakterisierung des Experiments anhand der Cu(111)- und der D<sub>2</sub>O/Cu(111)-Oberfläche*. Diplomarbeit, Freie Universität Berlin (2011). 44, 59, 60
- [Dei14] J.-C. Deinert, D. Wegkamp, M. Meyer, C. Richter, M. Wolf, & J. Stähler. *Ultrafast Exciton Formation at the ZnO(10 $\bar{1}$ 0) Surface*. Physical Review Letters **113**, 057602 (2014). 23, 89, 90, 111, 113, 134, 142

- [Dei15] J.-C. Deinert, O. T. Hofmann, M. Meyer, P. Rinke, & J. Stähler. *Local aspects of hydrogen-induced metallization of the ZnO(10 $\bar{1}$ 0) surface*. Physical Review B **91**, 235313 (2015). 1, 19, 20, 24, 99, 101, 103, 110, 146, 151, 155, 190, 192
- [Dei16] J.-C. Deinert. *Zinc oxide surfaces and interfaces: Electronic structure and charge carrier dynamics*. Dissertation, Technische Universität Berlin (2016). 9, 19, 24, 39, 60, 64, 89, 90, 100, 101, 146
- [Den20] M. Dendzik, R. P. Xian, E. Perfetto, D. Sangalli, D. Kutnyakhov, S. Dong, S. Beaulieu, T. Pincelli, F. Pressacco, D. Curcio, S. Y. Agustsson, M. Heber, J. Hauer, W. Wurth, G. Brenner, Y. Acremann, P. Hofmann, M. Wolf, A. Marini, G. Stefanucci, L. Rettig, & R. Ernstorfer. *Observation of an Excitonic Mott Transition through Ultrafast Core-cum -Conduction Photoemission Spectroscopy*. Physical Review Letters **125**, 96401 (2020). 3, 31
- [Die04] U. Diebold, L. V. Koplitz, & O. Dulub. *Atomic-scale properties of low-index ZnO surfaces*. Applied Surface Science **237**, 336–342 (2004). 64, 186
- [Dul02] O. Dulub, L. A. Boatner, & U. Diebold. *STM study of the geometric and electronic structure of ZnO(0001)-Zn, (000 $\bar{1}$ )-O, (10 $\bar{1}$ 0), and (11 $\bar{2}$ 0) surfaces*. Surface Science **519**, 201-217 (2002). 63, 64
- [Eck13] M. Eckstein & P. Werner. *Photoinduced states in a Mott insulator*. Physical Review Letters **110**, 126401 (2013). 24
- [Edw81] Peter P. Edwards & M. J. Sienko. *Phase Separation in Metal Solutions and Expanded Fluid Metals*. Journal of the American Chemical Society **103**, 2967–2971 (1981). 13
- [Edw85] P. P. Edwards & C. N. R. Rao (editors). *The metallic and nonmetallic states of matter*. Taylor & Francis, London and Philadelphia, 1st edition, (1985). 14, 16
- [Ell16] K. Ellmer & A. Bikowski. *Intrinsic and extrinsic doping of ZnO and ZnO alloys*. Journal of Physics D: Applied Physics **49**, 413002 (2016). 12, 98, 111, 192
- [Fan92] W. S. Fann, R. Storz, H. W.K. Tom, & J. Bokor. *Direct measurement of nonequilibrium electron-energy distributions in sub-picosecond laser-heated gold films*. Physical Review Letters **68**, 18 (1992). 46, 134
- [Fog15] L. Foglia. *Ultrafast dynamics and energy loss channels at a hybrid inorganic/organic interface*. Dissertation, Technische Universität Berlin (2015). 47
- [Fog19] L. Foglia, S. Vempati, B. T. Bonkano, L. Gierster, M. Wolf, & J. Stähler. *Revealing the competing contributions of charge carriers, excitons, and defects to*

- the non-equilibrium optical properties of ZnO*. Structural Dynamics **6**, 034501 (2019). 22, 27, 65, 108, 138, 191
- [For84] R. L. Fork, O. E. Martinez, & J. P. Gordon. *Negative dispersion using pairs of prisms*. Optics Letters **9**, 5 (1984). 55
- [Fra17] E. Frantzeskakis, T. C. Rödel, F. Fortuna, & A. F. Santander-Syro. *2D surprises at the surface of 3D materials: Confined electron systems in transition metal oxides*. Journal of Electron Spectroscopy and Related Phenomena **219**, 16–28 (2017). 1, 17
- [Gah04] C. Gahl. *Elektronentransfer- und Solvatisierungsdynamik in Eis adsorbiert auf Metalloberflächen*. Dissertation, Freie Universität Berlin (2004). 66, 67, 74
- [Gia16] C. Giannetti, M. Capone, D. Fausti, M. Fabrizio, F. Parmigiani, & D. Mihailovic. *Ultrafast optical spectroscopy of strongly correlated materials and high-temperature superconductors: a non-equilibrium approach*. Advances in Physics **65**, 2 (2016). 36
- [Göp77] W. Göpel. *Oxygen interaction of stoichiometric and non-stoichiometric ZnO prismatic surfaces*. Surface Science **62**, 165-182 (1977). 64, 186
- [Göp80] W. Göpel & U. Lampe. *Influence of defects on the electronic structure of zinc oxide surfaces*. Physical Review B **22**, 12 (1980). 64, 110, 186
- [Gor10] P. Gori, M. Rakel, C. Cobet, W. Richter, N. Esser, A. Hoffmann, R. Del Sole, A. Cricenti, & O. Pulci. *Optical spectra of ZnO in the far ultraviolet : First-principles calculations and ellipsometric measurements*. Physical Review B , 125207 (2010). 138
- [Gue19] D. Guerci, M. Capone, & M. Fabrizio. *Exciton Mott transition revisited*. Physical Review Materials **3**, 054605 (2019). 3, 16, 30
- [Gur14] R. Gurwitz, R. Cohen, & I. Shalish. *Interaction of light with the ZnO surface: Photon induced oxygen "breathing," oxygen vacancies, persistent photoconductivity, and persistent photovoltage*. Journal of Applied Physics **115**, 033701 (2014). 25, 26, 98, 109, 127
- [Hö5] S. Hüfner. *Photoelectron Spectroscopy*. Springer, Heidelberg, (1995). 38, 41
- [Hag09] S. Hagen. *Isomerization behavior of photochromic molecules in direct contact with noble metal surfaces*. Dissertation, Freie Universität  $\frac{1}{2}$ t Berlin (2009). 201

- 
- [Hau09] H. Haug & S. W. Koch. *Quantum Theory of the Optical and Electronic Properties of Semiconductors*. World Scientific, 5th edition, (2009). 162
- [Hei55] G. Heiland. *Die elektrische Leitfähigkeit an der Oberfläche von Zinkoxydkristallen*. Zeitschrift für Physik **142**, 415-432 (1955). 109, 195
- [Hen07] E. Hendry, M. Koeberg, & M. Bonn. *Exciton and electron-hole plasma formation dynamics in ZnO*. Physical Review B **76**, 045214 (2007). 138
- [Her96] T. Hertel, E. Knoesel, M. Wolf, & G. Ertl. *Ultrafast electron dynamics at Cu(111): Response of an electron gas to optical excitation*. Physical Review Letters **76**, 3 (1996). 46, 47
- [Hof02] Ph Hofmann, Ch Søndergaard, S. Agergaard, S. V. Hoffmann, J. E. Gayone, G. Zampieri, S. Lizzit, & A. Baraldi. *Unexpected surface sensitivity at high energies in angle-resolved photoemission*. Physical Review B - Condensed Matter and Materials Physics **66**, 245422 (2002). 40
- [Hör18] U. Hörmann, S. Zeiske, F. Piersimoni, L. Hoffmann, R. Schlesinger, N. Koch, T. Riedl, D. Andrienko, & D. Neher. *Stark Effect of Hybrid Charge Transfer States at Planar ZnO/Organic Interfaces*. Physical Review B **98**, 155312 (2018). 98
- [Hua98] L. Huang, J. P. Callan, E. N. Glezer, & E. Mazur. *GaAs under Intense Ultrafast Excitation: Response of the Dielectric Function*. Physical Review Letters **98**, 1 (1998). 5, 33
- [Hub01] R. Huber, F. Tauser, A. Brodschelm, M. Bichler, G. Abstreiter, & A. Leitenstorfer. *How many-particle interactions develop after ultrafast excitation of an electron-hole plasma*. Nature **414**, 286-289 (2001). 3, 31, 144
- [Hwa12] H. Y. Hwang, Y. Iwasa, M. Kawasaki, B. Keimer, N. Nagaosa, & Y. Tokura. *Emergent phenomena at oxide interfaces*. Nature Materials **11**, 103-113 (2012). 1, 17
- [Iwa03] S. Iwai, M. Ono, A. Maeda, H. Matsuzaki, H. Kishida, H. Okamoto, & Y. Tokura. *Ultrafast Optical Switching to a Metallic State by Photoinduced Mott Transition in a Halogen-Bridged Nickel-Chain Compound*. Physical Review Letters **91**, 5 (2003). 1, 4, 24
- [Jac84] K. Jacobi, G. Zwicker, & A. Gutmann. *Work function, electron affinity and band bending of zinc oxide surfaces*. Surface Science **141**, 109-125 (1984). 101, 110

## References

---

- [Jan09] A. Janotti & C. G. Van de Walle. *Fundamentals of zinc oxide as a semiconductor*. Reports on Progress in Physics **72**, 126501 (**2009**). 10, 18, 27, 98, 111, 126, 186
- [Jan14] A. Janotti, J. B. Varley, M. Choi, & C. G. Van De Walle. *Vacancies and small polarons in SrTiO<sub>3</sub>*. Physical Review B - Condensed Matter and Materials Physics **90**, 085202 (**2014**). 18
- [Kat87] S. Katsumoto, F. Komori, N. Sano, & S. Kobayashi. *Fine Tuning of Metal-Insulator Transition in Al<sub>0.3</sub>Ga<sub>0.7</sub>As Using Persistent Photoconductivity*. Journal of the Physical Society of Japan **56**, 7 (**1987**). 3, 27, 28, 114, 116, 189
- [Kaz] T. Kazimierczuk, D. Fröhlich, S. Scheel, H. Stolz, & M. Bayer. *Giant Rydberg excitons in the copper oxide Cu<sub>2</sub>O*. Nature **514**, 343-347 (**2014**). 22
- [Kin11] P. D. C. King & T. D. Veal. *Conductivity in transparent oxide semiconductors*. Journal of Physics: Condensed Matter **23**, 334214 (**2011**). 98
- [Kin12] P. D. C. King, R H He, T Eknapakul, P Buaphet, S Mo, Y Kaneko, S Harashima, Y Hikita, M S Bahramy, C Bell, Z Hussain, Y Tokura, Z Shen, H Y Hwang, F Baumberger, & W Meevasana. *Subband Structure of a Two-Dimensional Electron Gas Formed at the Polar Surface of the Strong Spin-Orbit Perovskite KTaO<sub>3</sub>* **108**, 117602 (**2012**). 18
- [Kin17] S. B. King, D. Wegkamp, C. Richter, M. Wolf, & J. Stähler. *Trapped Electrons at the Amorphous Solid Water/Vacuum Interface as Possible Reactants in a Water Splitting Reaction*. Journal of Physical Chemistry C **121**, 7379-7386 (**2017**). 66, 67
- [Kin19] S. B King, K. Broch, A. Demling, & J. Stähler. *Multistep and multiscale electron transfer and localization dynamics at a model electrolyte/metal interface*. Journal of Chemical Physics **150**, 041702 (**2019**). 46, 62, 139
- [Kli10a] C. Klingshirn, J. Fallert, H. Zhou, J. Sartor, C. Thiele, F. Maier-Flaig, D. Schneider, & H. Kalt. *65 years of ZnO research - old and very recent results*. Physica Status Solidi B **247**, 6 (**2010**). 22, 113
- [Kli10b] C. Klingshirn, B. K. Meyer, A. Waag, A. Hoffmann, & J. Geurts. *Zinc Oxide - From Fundamental Properties Towards Novel Applications*. Springer Series in Materials Science, 1st edition, (**2010**). 4, 9, 10, 98, 100, 159, 162
- [Kli12] C. Klingshirn. *Semiconductor Optics*. Springer Series in Materials Science, 4th edition, (**2012**). 3, 5, 30, 31, 33

- [Koc07] N. Koch. *Organic electronic devices and their functional interfaces*. ChemPhysChem **8**, 10, (2007) 1438. 41
- [Kra04] S. V. Kravchenko & M. P. Sarachik. *Metal-insulator transition in two-dimensional electron systems*. Reports on Progress in Physics **67**, 1-44 (2004). 18, 152, 155, 192
- [Kro99] L. Kronik & Y. Shapira. *Surface photovoltage phenomena: theory, experiments and applications*. Surface Science Reports **37**, 1-206 (1999). 5, 34
- [Kro01] L. Kronik & Y. Shapira. *Surface photovoltage spectroscopy of semiconductor structures: at the crossroads of physics, chemistry and electrical engineering*. Surface and Interface Analysis **31**, 10 (2001). 35, 151, 168
- [Lak10] G. Lakhwani, R. F. H. Roijmans, A. J. Kronemeijer, J. Gilot, R. Janssen, & S. C. J. Meskers. *Probing charge carrier density in a layer of photodoped ZnO nanoparticles by spectroscopic ellipsometry*. Journal of Physical Chemistry C **114**, 14804–14810 (2010). 98
- [Lan05] S. Lany & A. Zunger. *Anion vacancies as a source of persistent photoconductivity in II-VI and chalcopyrite semiconductors*. Physical Review B **72**, 035215 (2005). 3, 26, 27, 95, 98, 111, 126, 127
- [Lan07] S. Lany & A. Zunger. *Dopability, intrinsic conductivity, and nonstoichiometry of transparent conducting oxides*. Physical Review Letters **98**, 045501 (2007). 3, 26, 29, 98, 127
- [Lee16] K. M. Lee, C. W. Lai, K. S. Ngai, & J. C. Juan. *Recent developments of zinc oxide based photocatalyst in water treatment technology: A review*. Water Research **88**, 428–448 (2016). 198
- [Lei03] F. Leiter, H. Alves, D. Pfisterer, N. G. Romanov, & D. M. Hofmann. *Oxygen vacancies in ZnO*. Physica B **340-342**, 201-204 (2003). 27
- [Lie11] C.-C. Lien, C.-Y. Wu, Z.-Q. Li, & J.-J. Lin. *Electrical conduction processes in ZnO in a wide temperature range 20-500 K*. Journal of Applied Physics **110**, 063706 (2011). 197
- [Lim03] P. Limelette, A. Georges, D. Jérôme, P. Wzietek, P. Metcalf, & J. M. Honig. *Universality and critical behavior at the Mott transition*. Science **302**, 5642 (2003). 14, 16
- [Lis04] M. Lisowski, P. A. Loukakos, U. Bovensiepen, J. Stähler, C. Gahl, & M. Wolf. *Ultra-fast dynamics of electron thermalization, cooling and transport effects in*

## References

---

- Ru(001)*. Applied Physics A: Materials Science and Processing **78**, 165–176 (2004). 46, 134
- [Liu93] S. Liu, K. Karrai, F. Dunmore, H. D. Drew, R. Wilson, & G. A. Thomas. *Thermal activation of carriers from a metallic impurity band*. Physical Review B **48**, 15 (1993). 16, 153
- [Liu09] P. Liu, G. She, Z. Liao, Y. Wang, Z. Wang, W. Shi, S.-T. Lee, & D. Chen. *Observation of persistent photoconductance in single ZnO nanotube*. Applied Physics Letters **94**, 063120 (2009). 98, 111, 113
- [Liu19] F. Liu, M. E. Ziffer, K. R. Hansen, J. Wang, & X.-Y. Zhu. *Direct Determination of Band-Gap Renormalization in the Photoexcited Monolayer MoS<sub>2</sub>*. Physical Review Letters **122**, 246803 (2019). 33, 151, 162
- [Mah67] G. D. Mahan. *Excitons in degenerate semiconductors*. Physical Review **153**, 3 (1967). 22, 32
- [Mäh16] S. Mährlein. *Nonlinear Terahertz Phononics: A Novel Route to Controlling Matter*. Dissertation, Freie Universität Berlin (2016). 65
- [McK14] S. McKeown Walker, A. De La Torre, F. Y. Bruno, A. Tamai, T. K. Kim, M. Hoesch, M. Shi, M. S. Bahramy, P. D. C. King, & F. Baumberger. *Control of a Two-Dimensional Electron Gas on SrTiO<sub>3</sub> (111) by Atomic Oxygen*. Physical Review Letters **113**, 177601 (2014). 1, 17, 18, 151, 155, 156
- [Mee10] W. Meevasana, P. D. C. King, R. H. He, S. K. Mo, M. Hashimoto, A. Tamai, P. Songsiriritthigul, F. Baumberger, & Z. X. Shen. *Creation and control of a two-dimensional electron liquid at the bare SrTiO<sub>3</sub> surface*. Nature Materials **10**, 1-4 (2010). 1, 17, 18, 147, 151, 155
- [Mil01] T. Miller & T. C. Chiang. *Lineshape effects in photoemission from the valence states of metals*. Journal of Physics Condensed Matter **13**, 11115-11132 (2001). 41
- [Mor14] V. R. Morrison, R. P. Chatelain, K. L. Tiwari, A. Hendaoui, A. Bruhács, M. Chaker, & B. J. Siwick. *A photoinduced metal-like phase of monoclinic VO<sub>2</sub> revealed by ultrafast electron diffraction*. Science **346**, 6208 (2014). 4
- [Mor17] S. Mor, M. Herzog, D. Golez, P. Werner, M. Eckstein, N. Katayama, M. Nohara, H. Takagi, T. Mizokawa, C. Monney, & J. Stähler. *Ultrafast Electronic Band Gap Control in an Excitonic Insulator*. Physical Review Letters **119**, 086401 (2017). 33, 151, 162

- 
- [Mot61] N. F. Mott. *The transition to the metallic state*. Philosophical Magazine **6**, 62 (1961). 14
- [Mot74] N. F. Mott. *Semiconductor-to-metal transitions*. Taylor & Francis, London, 1st edition, (1974). 1, 2, 4, 12, 14, 15, 16, 30
- [Naj19] M. N. Najafi. *An electronic avalanche model for metal-insulator transition in two dimensional electron gas*. The European Physical Journal B **92**, 172 (2019). 19
- [Nep16] S. Neppel, J. Mahl, A. S. Tremsin, B. Rude, R. Qiao, W. Yang, J. Guo, & O. Gessner. *Towards efficient time-resolved X-ray absorption studies of electron dynamics at photocatalytic interfaces*. Faraday Discussions **194**, 659 (2016). 65
- [Nic18] C. Nicholson, A. Lücke, W. G. Schmidt, M. Puppinger, L. Rettig, R. Ernstorfer, & M. Wolf. *Beyond the molecular movie: Dynamics of bands and bonds during a photoinduced phase transition*. Science **362**, 821–825 (2018). 46
- [Oka11] H. Okamoto, T. Miyagoe, K. Kobayashi, H. Uemura, H. Nishioka, H. Matsuzaki, A. Sawa, & Y. Tokura. *Photoinduced transition from Mott insulator to metal in the undoped cuprates  $Nd_2CuO_4$  and  $La_2CuO_4$* . Physical Review B - Condensed Matter and Materials Physics **83**, 125102 (2011). 24
- [Oza03] K. Ozawa, K. Sawada, Y. Shirotori, & K. Edamoto. *Angle-resolved photoelectron spectroscopy study of the anion-derived dangling-bond band on  $ZnO(10\bar{1}0)$* . Physical Review B **68**, 125417 (2003). 100
- [Oza05] K. Ozawa, K. Sawada, Y. Shirotori, & K. Edamoto. *Angle-resolved photoemission study of the valence band structure of  $ZnO(10\bar{1}0)$* . Journal of Physics: Condensed Matter **17**, 1271 (2005). 100
- [Oza10] K. Ozawa & K. Mase. *Metallization of  $ZnO(10\bar{1}0)$  by adsorption of hydrogen, methanol, and water: Angle-resolved photoelectron spectroscopy*. Physical Review B **81**, 205322 (2010). 1, 19, 64, 99, 146
- [Oza11] K. Ozawa & K. Mase. *Comparison of the surface electronic structures of H-adsorbed  $ZnO$  surfaces: An angle-resolved photoelectron spectroscopy study*. Physical Review B **83**, 125406 (2011). 101
- [Pal20] T. Palmieri, E. Baldini, A. Steinhoff, A. Akrap, M. Kollár, E. Horváth, L. Forró, F. Jahnke, & M. Chergui. *Mahan excitons in room-temperature methylammonium lead bromide perovskites*. Nature Communications **11**, 850 (2020). 32, 138

## References

---

- [Pat06] C. H. Patterson. *Role of defects in ferromagnetism in  $Zn_{1-x}Co_xO$ : A hybrid density-functional study*. Physical Review B - Condensed Matter and Materials Physics **74**, 144432 (2006). 26, 111, 126, 188
- [Pat10] J. Patterson & B. Bailey. *Solid-State Physics: Introduction to the Theory*. Springer-Verlag, Heidelberg, Germany, 2nd edition, (2010). 122
- [Pen18] T. J. Penfold, J. Szlachetko, F. G. Santomauro, A. Britz, W. Gawelda, G. Doumy, A. M. March, S. H. Southworth, J. Rittmann, R. Abela, M. Chergui, & C. J. Milne. *Revealing hole trapping in zinc oxide nanoparticles by time-resolved X-ray spectroscopy*. Nature Communications **9**, 478 (2018). 191
- [Per06] L. Perfetti, P. A. Loukakos, M. Lisowski, U. Bovensiepen, H. Berger, S. Biermann, P. S. Cornaglia, A. Georges, & M. Wolf. *Time evolution of the electronic structure of  $1T-TaS_2$  through the insulator-metal transition*. Physical Review Letters **97**, 067402 (2006). 46
- [Pet98] H. Petek & S. Ogawa. *Femtosecond time-resolved two-photon photoemission studies of electron dynamics in metals*. Progress in Surface Science **56**, 4 (1998). 46, 57
- [Pup17] M. Puppín. *Time- and angle-resolved photoemission spectroscopy on bidimensional semiconductors with a 500 kHz extreme ultraviolet light source*. Dissertation, Freie Universität Berlin (2017). 23, 33
- [Pup19] M. Puppín, Y. Deng, C. W. Nicholson, J. Feldl, N. B.M. Schröter, H. Vita, P. S. Kirchmann, C. Monney, L. Rettig, M. Wolf, & R. Ernstorfer. *Time- and angle-resolved photoemission spectroscopy of solids in the extreme ultraviolet at 500 kHz repetition rate*. Review of Scientific Instruments **90**, 023104 (2019). 46
- [Ret12] L. Rettig, P. S. Kirchmann, & U. Bovensiepen. *Ultrafast dynamics of occupied quantum well states in  $Pb/Si(111)$* . New Journal of Physics **14**, 023047 (2012). 35, 48, 151
- [Ric20] S. Richter, O. Herrfurth, S. Espinoza, M. Rebarz, M. Kloz, J. A. Leveillee, A. Schleife, S. Zollner, M. Grundmann, J. Andreasson, & R. Schmidt-Grund. *Ultrafast dynamics of hot charge carriers in an oxide semiconductor probed by femtosecond spectroscopic ellipsometry*. New Journal of Physics **22**, 083066 (2020). 31, 32, 138
- [Röd15] T. C. Rödel, F. Fortuna, F. Bertran, M. Gabay, M. J. Rozenberg, A. F. Santander-Syro, & P. Le Fèvre. *Engineering two-dimensional electron gases at*

- the (001) and (101) surfaces of TiO<sub>2</sub> anatase using light.* Physical Review B - Condensed Matter and Materials Physics **92**, 041106(R) (2015). 1, 18
- [Röd18] T. C. Rödel, J. Dai, F. Fortuna, E. Frantzeskakis, P. Le Fèvre, F. Bertran, M. Kobayashi, R. Yukawa, T. Mitsuhashi, M. Kitamura, K. Horiba, H. Kumigashira, & A. F. Santander-Syro. *High-density two-dimensional electron system induced by oxygen vacancies in ZnO.* Physical Review Materials **2**, 051601(R) (2018). 18, 147, 156
- [Roh18] G. Rohde, A. Stange, A. Müller, M. Behrendt, L. Oloff, K. Hanff, T. J. Albert, P. Hein, K. Rossnagel, & M. Bauer. *Ultrafast Formation of a Fermi-Dirac Distributed Electron Gas.* Physical Review Letters **121**, 256401 (2018). 135
- [Ros01] K. Rossnagel, L. Kipp, M. Skibowski, C. Solterbeck, T. Strasser, W. Schattke, D. Voß, P. Krüger, A. Mazur, & J. Pollmann. *Three-dimensional Fermi surface determination by angle-resolved photoelectron spectroscopy.* Physical Review B - Condensed Matter and Materials Physics **63**, 125104 (2001). 41
- [Rot10] E. Rotenberg. *Many-Body Interactions in Nanoscale Materials by Angle-Resolved Photoemission Spectroscopy.* Pages 169-209 in X-Rays in Nanoscience, J. Guo (Editor), Wiley, 2010 . 38, 41
- [Ryc13] J. D. Ryckman, K. A. Hallman, R. E. Marvel, R. F. Haglund, & S. M. Weiss. *Ultra-compact silicon photonic devices reconfigured by an optically induced semiconductor-to-metal transition.* Optics Express **21**, 9 (2013). 128, 199
- [Sch08] F. Schmitt, P. S. Kirchmann, U. Bovensiepen, R. G. Moore, L. Rettig, M. Krenz, J. H. Chu, N. Ru, L. Perfetti, D. H. Lu, M. Wolf, I. R. Fisher, & Z. X. Shen. *Transient electronic structure and melting of a charge density wave in TbTe<sub>3</sub>.* Science **321**, 5896 (2008). 41, 46, 128, 139
- [Sch11] A. Schleife, C. Rödl, F. Fuchs, K. Hannewald, & F. Bechstedt. *Optical Absorption in Degenerately Doped Semiconductors: Mott Transition or Mahan Excitons?* Physical Review Letters **107**, (2011) 236405 (2011). 32, 138
- [Sek17] F. Sekiguchi, T. Mochizuki, C. Kim, H. Akiyama, L. N. Pfeiffer, K. W. West, & R. Shimano. *Anomalous Metal Phase Emergent on the Verge of an Exciton Mott Transition.* Physical Review Letters **118**, 067401 (2017). 3, 31
- [Sez15] H. Sezen, H. Shang, F. Bebensee, C. Yang, M. Buchholz, A. Nefedov, S. Heissler, C. Carbogno, M. Scheffler, P. Rinke, & C. Wöll. *Evidence for photogenerated intermediate hole polarons in ZnO.* Nature Communications **6**, 6901 (2015). 108

## References

---

- [Shk84] B. I. Shklovskii & A. L. Efros. *Electronic properties of doped semiconductors*. Springer-Verlag Berlin Heidelberg, 1st edition, (**1984**). 11, 14
- [SPE] SPECS GmbH (Hrsg.): *PHOIBOS Hemispherical Energy Analyzer Series*. Version 2.2. Specs GmbH, (**2008**). 57
- [Spe13] B. F. Spencer, D. M. Graham, S. J. O. Hardman, E. A. Seddon, M. J. Cliffe, K. L. Syres, A. G. Thomas, S. K. Stubbs, F. Sirotti, M. G. Silly, P. F. Kirkham, A. R. Kumarasinghe, G. J. Hirst, A. J. Moss, S. F. Hill, D. A. Shaw, S. Chattopadhyay, & W. R. Flavell. *Time-resolved surface photovoltage measurements at n-type photovoltaic surfaces: Si(111) and ZnO(10-10)*. *Physical Review B - Condensed Matter and Materials Physics* **88**, 195301 (**2013**). 32, 65, 98, 111, 127
- [Stä07] J. Stähler. *Freezing Hot Electrons, Electronic Transfer and Solvation Dynamics at D<sub>2</sub>O and NH<sub>3</sub>-Metal Interfaces*. PhD Thesis, Freie Universität Berlin, **2007**. 66
- [Stä16] J. Stähler & P. Rinke. *Global and local aspects of the surface potential landscape for energy level alignment at organic-ZnO interfaces*. *Chemical Physics* **486**, 485-486 (**2016**). 34, 41, 42
- [Str03] V. N. Strocov. *Intrinsic accuracy in 3-dimensional photoemission band mapping*. *Journal of Electron Spectroscopy and Related Phenomena* **130**, 65-78 (**2003**). 41
- [Szy05] P. Szymanski, S. Garrett-Roe, & C. B. Harris. *Time- and angle-resolved two-photon photoemission studies of electron localization and solvation at interfaces*. *Progress in Surface Science* **78**, 1–39 (**2005**). 49
- [Tan12] S. I. Tanaka. *Utility and constraint on the use of pump-probe photoelectron spectroscopy for detecting time-resolved surface photovoltage*. *Journal of Electron Spectroscopy and Related Phenomena* **185**, 152–158 (**2012**). 48, 50, 51, 52, 120, 165, 166, 170, 171, 174, 176
- [Tan19] H. Tanimura, K. Tanimura, & P. H. M. Van Loosdrecht. *Dynamics of incoherent exciton formation in Cu<sub>2</sub>O : Time- and angle-resolved photoemission spectroscopy*. *Physical Review B* **100**, 115204 (**2019**). 23, 108
- [Tar13] M. C. Tarun, F. A. Selim, & M. D. McCluskey. *Persistent photoconductivity in strontium titanate*. *Physical Review Letters* **111**, 187403 (**2013**). 189, 199
- [Tok93] Y. Tokura, Y. Taguchi, Y. Okada, Y. Fujishima, T. Arima, K. Kumagai, & Y. Iye. *Filling dependence of electronic properties on the verge of metal-Mott*

- insulator transition in  $Sr_{1-x}La_xTiO_3$* . Physical Review Letters **70**, 14 (1993). 151, 152, 155
- [Ulb11] R. Ulbricht, E. Hendry, J. Shan, T. F. Heinz, & M. Bonn. *Carrier dynamics in semiconductors studied with time-resolved terahertz spectroscopy*. Reviews of Modern Physics **83**, 2 (2011). 23
- [Uls15] S. Ulstrup, J. C. Johannsen, F. Cilento, A. Crepaldi, J. A. Miwa, M. Zacchigna, C. Cacho, R. T. Chapman, E. Springate, F. Fromm, C. Roidel, T. Seyller, P. D. C. King, F. Parmigiani, M. Grioni, & P. Hofmann. *Ramifications of optical pumping on the interpretation of time-resolved photoemission experiments on graphene*. Journal of Electron Spectroscopy and Related Phenomena **200**, 340–346 (2015). 48
- [Vem12] S. Vempati, J. Mitra, & P. Dawson. *One-step synthesis of ZnO nanosheets: a blue-white fluorophore*. Nanoscale Research Letters **7**, 470 (2012). 22
- [Ver11] M. A. M. Versteegh, T. Kuis, H. T. C. Stoof, & J. I. Dijkhuis. *Ultrafast screening and carrier dynamics in ZnO: Theory and experiment*. Physical Review B **84**, 035207 (2011). 138
- [Ver12] M. A. M. Versteegh, A. J. van Lange, H. T. C. Stoof, & J. I. Dijkhuis. *Observation of preformed electron-hole Cooper pairs in highly excited ZnO*. Physical Review B **85**, 195206 (2012). 33
- [Vit02] S. A. Vitkalov, M. P. Sarachik, & T. M. Klapwijk. *Spin polarization of strongly interacting two-dimensional electrons: The role of disorder*. Physical Review B **65**, 201106 (R) (2002). 152
- [Vit17] R. Vittal & Kuo Chuan Ho. *Zinc oxide based dye-sensitized solar cells: A review*. Renewable and Sustainable Energy Reviews **70**, 920–935 (2017). 4
- [Wal18] S. Wall, L. Vidas, T. A. Miller, S. Yang, O. Delaire, M. Chollet, J. M. Glowacka, M. Kozina, T. Henighan, M. Jiang, D. A. Reis, M. Trigo, T. Katayama, & L. A. Boatner. *Ultrafast disordering of vanadium dimers in photoexcited  $VO_2$* . Science **362**, 572-576 (2018). 128, 139, 149
- [Wan97] K. Wandelt. *The local work function: Concept and implications*. Applied Surface Science **111**, 1-10 (1997). 41
- [Wan12] J. Wang, Z. Wang, B. Huang, Y. Ma, Y. Liu, X. Qin, X. Zhang, & Y. Dai. *Oxygen vacancy induced band-gap narrowing and enhanced visible light photocatalytic activity of ZnO*. ACS Applied Materials and Interfaces **4**, 4024–4030 (2012). 111

## References

---

- [Weg14a] D. Wegkamp. *Ultrafast electron dynamics and the role of screening*. Dissertation, Freie Universität Berlin (2014). 41, 53, 55, 56, 66, 67, 148, 201, 202
- [Weg14b] D. Wegkamp, M. Herzog, L. Xian, M. Gatti, P. Cudazzo, C. L. McGahan, R. E. Marvel, R. F. Haglund, A. Rubio, M. Wolf, & J. Stähler. *Instantaneous band gap collapse in photoexcited monoclinic VO<sub>2</sub> due to photocarrier doping*. Physical Review Letters **113**, 216401 (2014). 1, 4, 36, 46
- [Weg15] D. Wegkamp & J. Stähler. *Ultrafast dynamics during the photoinduced phase transition in VO<sub>2</sub>*. Progress in Surface Science **90**, 464–502 (2015). 4, 36, 149
- [Wei02] M. Weinelt. *Time-resolved two-photon photoemission from metal surfaces*. Journal of Physics: Condensed Matter **14**, R1099-R1141 (2002). 147
- [Wei04] M. Weinelt, M. Kutschera, T. Fauster, & M. Rohlfing. *Dynamics of exciton formation at the Si(100) c(4x2) surface*. Physical Review Letters **92**, 12 (2004). 23, 65
- [Wen13] H. Wen, L. Guo, E. Barnes, J. H. Lee, D. A. Walko, R. D. Schaller, J. A. Moyer, R. Misra, Y. Li, E. M. Dufresne, D. G. Schlom, V. Gopalan, & J. W. Freeland. *Structural and electronic recovery pathways of a photoexcited ultrathin VO<sub>2</sub> film*. Physical Review B **88**, 165424 (2013). 36, 128, 197
- [Wid03] W. Widdra, D. Bröcker, T. Gießel, I. V. Hertel, W. Krüger, A. Liero, F. Noack, V. Petrov, D. Pop, P. M. Schmidt, R. Weber, I. Will, & B. Winter. *Time-resolved core level photoemission: surface photovoltage dynamics of the SiO<sub>2</sub>/Si(100) interface*. Surface Science **543**, 87–94 (2003). 47, 48
- [Wöl07] C. Wöll. *The chemistry and physics of zinc oxide surfaces*. Progress in Surface Science **82**, 55–120 (2007). 9, 10
- [Yan11] Q. Yan, P. Rinke, M. Winkelkemper, A. Qteish, D. Bimberg, M. Scheffler, & C. G. Van De Walle. *Band parameters and strain effects in ZnO and group-III nitrides*. Semiconductor Science and Technology **26**, 014037 (2011). 153
- [Yan14] S. L. Yang, J. A. Sobota, P. S. Kirchmann, & Z. X. Shen. *Electron propagation from a photo-excited surface: Implications for time-resolved photoemission*. Applied Physics A: Materials Science and Processing **116**, 85–90 (2014). 35, 48, 151
- [Yu91] G. Yu, C. H. Lee, A. J. Heeger, N. Herron, & E. M. McCarron. *Transient photoinduced conductivity in single crystals of YBa<sub>2</sub>Cu<sub>3</sub>O<sub>7-δ</sub>: 'Photodoping' to the metallic state*. Physical Review Letters **67**, 18 (1991). 1

- [Yuk16] R. Yukawa, K. Ozawa, S. Yamamoto, H. Iwasawa, K. Shimada, E. F. Schwier, K. Yoshimatsu, H. Kumigashira, H. Namatame, M. Taniguchi, & I. Matsuda. *Phonon-dressed two-dimensional carriers on the ZnO surface*. Physical Review B **94**, 165313 (2016). 147
- [Zha01] S. B. Zhang, S. H. Wei, & Alex Zunger. *Intrinsic n-type versus p-type doping asymmetry and the defect physics of ZnO*. Physical Review B **63**, 075205 (2001). 190
- [Zha12] Z. Zhang & Jr. J. T. Yates. *Band Bending in Semiconductors: Chemical and Physical Consequences at Surfaces and Interfaces*. Chemical Reviews **112**, 5520 - 5551 (2012). 34
- [Zha13] K. H. L. Zhang, R. G. Egdell, F. Offi, S. Iacobucci, L. Petaccia, S. Gorovikov, & P. D. C. King. *Microscopic origin of electron accumulation in In<sub>2</sub>O<sub>3</sub>*. Physical Review Letters **110**, 056803 (2013). 18
- [Zha14] Y. Zhang & J. Wang. *Bound exciton model for an acceptor in a semiconductor*. Physical Review B - Condensed Matter and Materials Physics **90**, 155201 (2014). 13, 21
- [Zha18] Y. Zhang. *Electronic structures of impurities and point defects in semiconductors*. Chinese Physics B **27**, 117103 (2018). 2, 12, 13, 21
- [Zhu04] X.-Y. Zhu. *Electronic structure and electron dynamics at molecule-metal interfaces: Implications for molecule-based electronics*. Surface Science Reports **56**, 1-83 (2004). 41, 43
- [Zhu10] V. P. Zhukov, P. M. Echenique, & E. V. Chulkov. *Two types of excited electron dynamics in zinc oxide*. Physical Review B **82**, 094302 (2010). 23
- [Zhu14] X.-Y. Zhu. *How to draw energy level diagrams in excitonic solar cells*. Journal of Physical Chemistry Letters **5**, 2283-2288 (2014). 22
- [Zhu15] X.-Y. Zhu. *Photoemission from excitons in organic semiconductors*. Journal of Electron Spectroscopy and Related Phenomena **204**, 75-79 (2015). 23

## Acronyms

<b>1PPE</b>	one-photon photoemission.
<b>2D</b>	two dimensions.
<b>2DEG</b>	two-dimensional electron gas.
<b>2PPE</b>	two-photon photoemission.
<b>3D</b>	three dimensions.
<b>Al</b>	Aluminum.
<b>ARPES</b>	Angle-resolved photoelectron spectroscopy.
<b>BBO</b>	$\beta$ -barium borate.
<b>BGR</b>	band gap renormalization.
<b>CB</b>	conduction band.
<b>Cu</b>	copper.
<b>DBB</b>	downward band bending.
<b>DFT</b>	density functional theory.
<b>fs</b>	femtoseconds.
<b>FWHM</b>	full width at half maximum.
<b>GaAs</b>	gallium arsenide.
<b>H</b>	hydrogen.
<b>IOPA</b>	internal optical parametric amplifier.
<b>IR</b>	infrared.
<b>L</b>	Langmuir.
<b>LEED</b>	low-energy electron diffraction.
<b>LV</b>	leak valve.
<b>Mo</b>	Molybdenum.
<b>MOSFET</b>	metal-oxide semiconductor field-effect transistor.
<b>ms</b>	milliseconds.
<b>nm</b>	nanometer.
<b>NOPA</b>	non-collinear optical parametric amplifier.
<b>PE</b>	Photoemission.
<b>PES</b>	photoelectron spectroscopy.
<b>PIPT</b>	photoinduced phase transition.
<b>PPC</b>	persistent photoconductivity.
<b>ps</b>	picoseconds.
<b>Si</b>	Silicon.
<b>SMT</b>	semiconductor-to-metal transition.
<b>SPV</b>	surface photovoltage.

<b>STM</b>	Scanning tunneling microscopy.
<b>Ta</b>	tantalum.
<b>TC</b>	thermocouple.
<b>tr2PPE</b>	time-resolved two-photon photoemission.
<b>trARPES</b>	time-resolved ARPES.
<b>UHV</b>	ultrahigh vacuum.
<b>UV</b>	ultraviolet.
<b>VB</b>	valence band.
<b>VO<sub>2</sub></b>	Vanadium dioxide.
<b>ZnO</b>	zinc oxide.



# Thank you

First and foremost, thank you Julia Stähler for teaching me and guiding me through this time. You were always there when I needed it. Thank you for your trust in me, which was there from the beginning. You gave me the chance to pursue what interested me, and you were always so enthusiastic about my findings.

To my beloved wife Marie. You always believed in me. All these morning coffees that we shared, all the soul food that you provided me with. All your love. That's what carried me.

To all the edynamiX group members, Boubacar, Angelika, Stefano, Sarah, Joachim, Elsie, Ines, Marco, Sam, Sabrina, Johannes, ... You are a wonderful group. Special thanks to Boubacar and Sam for enjoyable shared office hours and discussions, and for always closing the door.

To Sessa Vempati, Postdoc from 2015-2018, thank you for teaching me all the patience and lab-related skills. Thank you for all these endless hours in the lab that we shared. These years were filled with laser alignment and a lot of ZnO preparation cycles. But they were also filled with plenty of fun and, most importantly, friendship. I am very grateful for all the memorable moments that we had.

To Selene Mor, PhD student in the EdynamiX group 2014-2019, you are such an enthusiastic and warm person, I am glad to have met you. Unforgettable the Fritz summer parties with Kartoffelsalat, your magic laser alignment skills and tireless helpfulness with everything.

To Jan Deinert, PhD student in the EdynamiX group 2011-2016, for being always in reach to answer all my numerous questions on ZnO and the experimental setup.

Thanks to the Fritz-Haber-Institute, in particular the PC department under the guidance of Martin Wolf, for providing such a friendly work atmosphere. To Daniel, Albrecht, Marcel and Sven, for all the technical support. Thanks to the PC secretary, Manuel, Ines and Daria for organizing, and always thinking ahead.

Corona special times in the Reichenberger writing refuge are greatly acknowledged. Thank you for going through this year with me.

Finally, to my dear flatmate Max for his patience with me.



## List of publications

### Publications within this thesis

L. Gierster, S. Vempati and J. Stähler, *Ultrafast generation and decay of a surface metal*. Nature Communications (accepted), preprint at <https://arxiv.org/abs/2005.13424>

### Publications concerning other topics

S. Vempati, J.-C. Deinert, L. Gierster, L. Bogner, C. Richter, N. Mutz, S. Blumstengel, A. Zykov, S. Kowarik, Y. Garmshausen, J. Hildebrandt, S. Hecht and J. Stähler, *Uncovering the (un-)occupied electronic structure of a buried hybrid interface*. Journal of Physics: Condensed Matter **31**, 094001 (2019). <https://doi.org/10.1088/1361-648X/aaf98a>

L. Foglia, S. Vempati, B. T. Bonkano, L. Gierster, M. Wolf, S. Sadofev and J. Stähler, *Revealing the competing contributions of charge carriers, excitons, and defects to the non-equilibrium optical properties of ZnO*. Structural Dynamics **6**, 034501 (2019). <https://doi.org/10.1063/1.5088767>

S. Vempati, L. Bogner, C. Richter, J.-C. Deinert, L. Foglia, L. Gierster and J. Stähler, *Photoexcited organic molecules en route to highly efficient autoionization*, Journal of Chemical Physics **152**, 074715 (2020). <https://doi.org/10.1063/1.5136075>

L. Gierster, A.A. Ünal, L. Pape, F. Radu, and F. Kronast *Laser induced magnetization switching in a TbFeCo ferrimagnetic thin film: discerning the impact of dipolar fields, laser heating and laser helicity by XPEEM*, Ultramicroscopy **159**, 508-512 (2015). <https://doi.org/10.1016/j.ultramic.2015.05.016>

L. Gierster, L. Pape, A.A. Ünal, and F. Kronast *A sample holder with integrated laser optics for an ELMITEC photoemission electron microscope*, Review of Scientific Instruments **86**, 023702 (2015). <http://dx.doi.org/10.1063/1.4907402>